University of Nottingham

UK | CHINA | MALAYSIA

Investigations of Hollow Carbon Nanoshell Structures

Julie A. Watts, BSc(hons), MSc.

Thesis submitted to the University of Nottingham for the degree of doctor of Philosophy

August 2018

Abstract

Discrete, uniform < 10 nm sized hollow carbon nanoshells (HCNS) have been formed via a facile, one-step heat induced transformation of alkane thiol stabilised silver nanoparticles (AgNP). Direct evidence for the templated formation of predominantly complete, spherical HCNS, from rapid heating to > 650 °C, *in situ* inside a transmission electron microscope with a microelectromechanical system (MEMS) system is presented, with the size of the resultant HCNS being slightly larger than that of the AgNP template. Further, *ex situ* heating of AgNP on carbon nanotube supports has revealed the defining features of these very stable HCNS structures: hollow interiors and very thin graphitised, yet highly disordered walls.

A formation mechanism is proposed for the thermal transformation of stabilising layer alkane thiol molecules during HCNS synthesis, occurring in advance of AgNP template removal. Accordingly, the AgNP core acts both as a physical template for HCNS and catalyses the graphitisation of carbon. It is considered that one-step thermal processing of thiol stabilised AgNP provides for excellent size control of the HCNS product, via appropriate AgNP template selection.

In particular, a fast heating rate is found to be crucial for the formation of well-defined graphitic <10 nm sized HCNS, whilst intermediate and slow heating rates give rise to products that reflect competition between HCNS formation and AgNP ripening. Significantly, a range of AgNP starting materials, stabilised by ligands containing F or N, also produce similar HCNS following a fast rate of heating , reflecting starting material morphology . The presence of F in HCNS has been demonstrated, but evidence for inclusion of N is more tentative. However, the addition of heteroatoms to AgNP presents challenges for sample handling due to aggregation and changes to the dispersion of AgNP in solvents.

Publications List

Watts, J. A., Fay, M. W., Rance, G. A., Brown, P. D., Khlobystov, A. N., *Formation of hollow carbon nanoshells from thiol stabilised silver nanoparticles via heat treatment*, Carbon 139 (2018) pp538-544.

Watts, J. A., Fay, M. W., Khlobystov, A. N., Brown, P. D. B., Effect of TEM grid deposition method on the dispersion of thiol-stabilised silver nanoparticles, J. Phys. Conf. Ser. 902(1) (2017) 012030.

Acknowledgements

Firstly, this research would not have been possible without the academic expertise, guidance and pastoral care of my supervisors, Professors Paul Brown and Andrei Khlobystov. I am extremely grateful for the many insights, support, and challenges they have provided; thank you for introducing me to TED lectures and reminding me of the importance of the Pauli Exclusion Principle. The project has been very challenging at times and your sage advice has been most appreciated. I value the time you have spent with me, discussing results, teaching me to write with appropriate technical language, at the transmission electron microscope (TEM), or in the chemistry laboratories. I thoroughly enjoy electron microscopy (but not always temperamental, truculent electron microscopes!), it really is amazing to collect images on an almost atomic scale, of individual carbon nanotubes, or to watch twinkling dark field images appear from crystallites in moving samples, I am very happy, and grateful that you have given me the opportunity to learn this unique technique. On a more personal note, thank you both for the multifarious frequent supervision meetings, for broadening my horizons and making my time as a PhD student in Nottingham both productive and fun.

Thanks are due to Dr Graham Rance, for training within Chemistry, Raman spectroscopy data collection and interpretation, and guiding me through the somewhat lengthy paper submission process, Dr Emily Smith for XPS advice, data collection and interpretation, Dr Nigel Neate for XRD training and assistance and for TEM training and to Dr Mike Fay for continuing TEM training, collecting in situ spectroscopy data and working with me on the proof of concept *in situ* heating experiment, maintaining professionalism under duress.

Credit is due to Mick Cooper and Graham Coxhill for MALDI mass spectrometry, Dr Adriana Davies and Shazad Aslam for NMR, Clive Dixon in the glass blowing workshop, and technical and support staff within Chemistry; also to Engineering technical and support staff in the Wolfson building and L2, particularly Martin Rowe and Nicola Weston, with whom I spent an hour watching paint dry – seemingly ridiculous, but I (unexpectedly) learnt a lot about environmental scanning electron microscopy.

I am also grateful to Professor Amalia Patane and her research group at the School of Physics & Astronomy for allowing access to the laser suite, for training and data interpretation, which has proved invaluable, to Dr Alessandro La Torre for useful discussions, creativity and attempting to teach me to speak Italian, and to Professor Philip Moriarty for advice regarding NP self-assembly processes.

One of the joys of multidisciplinary projects is being involved with, and supported by, different, diverse research groups: Advanced Materials within Engineering, and Nottingham Nanocarbon; I am particularly grateful to past and present members of the latter group, for generally being fabulous, and also for advice, occasional hilarity, nights out etc, Dr Craig Stoppiello deserves particular credit.

Lastly, and most importantly, I would like to express my appreciation for the support, encouragement and welcome distractions provided by my family.

The financial support of the ESPRC, Grant number EP/M506588/1, is also gratefully acknowledged.

Definition of Symbols

Symbol	Definition
~	approximately
<	Less than
=	Equal to
>	Greater than
Δ	Difference
°C	Degrees centigrade
Å	1×10^{-10} m
At %	Atomic percentage
B	Full Width at Half Maximum
B_0	Magnetic field strength
cm^{-1}	Wavenumber
D1	Disordered graphitic lattice (A_{1g} symmetry)
D2	Disordered graphitic lattice (E_{2g} symmetry)
D3	Amorphous carbon Raman band assignment
D4	Disordered graphitic lattice (A_{1g} symmetry), polyenes, ionic impurities
eV	Electron volts
G	Ideal graphitic lattice Raman band assignment (E_{2g} symmetry)
h	Hour
I	Intensity
k	Crystallite shape constant
n	Number
nm	1×10^{-9} m
PPM	Parts per million
s	Seconds
T	Temperature
t	Time
t	Crystallite size
Wt %	Weight percentage
Θ	Scattering angle
λ	wavelength
σ	Standard deviation
χ^2	Sum of the square of the difference between observed and expected value, divided by the expected value

Definition of Abbreviations and Acronyms

Acronym	Definition
AgNP	Silver Nanoparticles
BF	Bright Field Contrast
CCD	Charge Coupled Device
CNS	Carbon Nanoshell
CNT	Carbon Nanotube
DDM	1-Dodecanethiol
DF	Dark Field Contrast
DLS	Dynamic Light Scattering
EDS	Electron Dispersive Spectroscopy
EELS	Electron Energy Loss Spectroscopy
FAT	Fixed Analyser Transmission
FEG	Field Emission Gun
FLG	Few Layered Graphene Flakes
FTIR	Fourier Transform Infrared Spectrophotometry
FWHM	Full Width At Half Maximum
G-HCNS	Graphitised Hollow Carbon Nanoshell
GO	Graphene Oxide
HAADF	High Angle Annular Dark Field
HCNS	Hollow Carbon Nanoshell
HFT	3,3,4,4,5,5,6,6,7,7,8,8,9,9,10,10,10 Heptadecafluoro-1-decanethiol
MEMS	Micro-Electro-Mechanical-System
MRI	Magnetic Resonance Imaging
MWCNT	Multi-Walled Carbon Nanotube
NMR	Nuclear Magnetic Resonance Spectroscopy
NP	Nanoparticles
OM	1-Octanethiol
PL	Photoluminescence
PTFE	Polytetrafluoroethylene
PUT	11-(1*H*-Pyrrol-1-Yl) Undecane-1-Thiol
SAED	Selected Area Diffraction
SPR	Surface Plasmon Resonance
TEM	Transmission Electron Microscopy
TGA	Thermogravimetric Analysis
TLC	Thin Layer Chromatography
TS-AgNP	Thiol Stabilised Silver Nanoparticles
UV/Vis	Ultraviolet-Visible Spectroscopy
XPS	X-Ray Photon Spectroscopy
XRD	X-Ray Powder Diffractrometry

Table of Contents

Chapter 1 Introduction

Carbon is an abundant, non-toxic element forming a diverse range of allotropes from macro-scale diamond and graphite to nano-scale graphene, nanotubes, quantum dots, fullerenes and many others [1], whilst nanoscale materials have functional properties arising from their size. Indeed, nano-carbons have significant and diverse potential applications in nanoscale electronics, structural materials or imaging, due to the ballistic conduction of graphene [2], exceptional strength of carbon nanotubes (CNT) [3], and fluorescence of carbon quantum dots (CQD) [4], respectively. Hollow carbon materials have shown promise for gas storage [5], drug containment and delivery [6], catalysis [7], or as electrode materials [8]. However, CNT are not readily soluble and tend to bundle [9], whilst the small interior diameters of fullerenes, 0.7 nm for C_{60}, [10], limit their potential for containment to ions, atoms or small molecules [11].

Hollow carbon nano shells (HCNS) have larger interior dimensions than fullerenes, and potential applications for catalysis [12], gas storage [13], targeted delivery and release of drugs [14] or as electrode materials [15]. Most HCNS structures are > 70 nm diameter [16], and current multi-step synthetic strategies typically involve carbon coating a hard template and thermal graphitisation, followed by template removal, often achieved with harsh chemicals [17]. There is a recognised need for smaller structures to improve functional properties such as electrochemical performance and catalysis [18], and for lower toxicity drug delivery systems [19]; additionally, simplifying methods of production would be advantageous. Modifications to HCNS functional properties have been achieved through the addition of heteroatoms, e.g. the addition of nitrogen, to improve catalytic performance [20]. The smallest hollow carbon materials to date are ~20 nm, but these have a very wide size distribution of 20 – 40 nm and large variations in interior cavity dimensions, additionally the

formation strategy involves lengthy heating at very high temperatures (1250°C for 10h) [21].

The purpose of this research is to develop a synthetic route for the controllable formation of < 10 nm sized hollow carbon structures. Metal nanoparticles (NP), known to catalyse thermal graphitisation [22], may be stabilised by organic molecules [23], therefore these materials contain both a source of carbon and catalyst for HCNS formation. Additionally, control of NP size is readily achievable in the < 50 nm range [24]. Graphitisation of stabilising molecules at the NP surface during heating, with the metal core acting as a HCNS template, should produce structures commensurate with the size, and shape, of starting NP. However, the competing thermally mediated processes of NP ripening [25] presents issues for template stability and retention, which were overcome by use of very fast rates of heating. The principle finding is that well-defined hollow graphitic carbon structures may be formed from heating silver nanoparticles (AgNP) stabilised by alkane thiol molecules, given a sufficiently fast heating rate. Slower rates of heating favour NP ripening processes over HCNS formation and produce large accumulations of Ag and disordered carbon structures. Further, modification of AgNP starting materials to include the heteroatoms nitrogen or fluorine with subsequent heating, also leads to the formation of well-defined HCNS.

The thesis states the aims and objectives of the research, followed by a survey of existing literature in Chapter 2, the materials and methods applied are described in Chapter 3, whilst Chapter 4 describes the formation of HCNS from heating AgNP, with characterisation of starting materials and products formed. Chapter 5 considers

the effects of heating regimes on AgNP, particularly the rate of heating, with Chapter 6 considering the effect of heteroatom inclusion to AgNP before heating to form HCNS. A critical review of the studies undertaken comprises Chapter 7, with a discussion of future work set out in Chapter 8. Finally, conclusions and a summary are presented, with two appendices – the first containing the rationale behind choice of AgNP stabilising agents, and the second presenting additional supplementary data to Chapter 6.

References

1 Pokropivny, V.V., Ivanovskii, A.L., *New nanoforms of carbon and boron nitride*, Russ. Chem. Rev. 77 (10) (2008) pp837 -873.

2 Geim, A., K., *Graphene: Status and Prospects*, Science 324 (5934) (2009) pp1530-1534.

3 Popov, V., *Theoretical study of the doping effect on the phonon dispersion of metallic carbon nanotubes*. Physica E: Low Dimens. Syst. Nanostruct. 44 (6) (2012) pp1032-1035.

4 Baker, S. N., Baker, G. A., *Luminescent Carbon Nanodots: Emergent Nanolights*, Angew. Chem. Int. Ed. 49 (38) (2010) pp6726-6744.

5 Rode, A. V., Elliman, R. G., Gamaly, E. G., Veinger, A. I., Christy, A. G., Hyde, S. T., Luther-Davies, B., *Electronic and magnetic properties of carbon nanofoam produced by high-repetition-rate laser ablation*, Appl. Surf. Sci. 197 (2002) pp 644-649.

6 Jong, W. H. De., Borm, P. J. A., *Drug delivery and nanoparticles: Applications and hazards*, Int. J Nanomedicine 3 (2) (2008) pp133–149.

7 Zhong, M.J., Kim, E.K., Natesakhawat, S., McGann, J.P., Whitacre, J.F., Matyjaszewski, K., Kowalewski, T., *Nitrogen-rich porous nanocarbon from block copolymer precursors for CO_2 capture and electrocatalysis of oxygen reduction*, Abstr. Pap. Am. Chem. (2012) S 244.

8 Hu, D., Chen, C., Liu, Q., *Fabrication of hollow carbon spheres with robust and significantly enhanced capacitance behaviors*, J Mater. Sci. 53 (17) (2018) pp12310-12321.

9 Azoubel, S., Magdassi, S., *The formation of carbon nanotube dispersions by high pressure homogenization and their rapid characterization by analytical centrifuge*, Carbon 48 (12) (2010) pp3346-3352.

10 Lebedeva, M. A., Chamberlain, T. W., Khlobystov, A. N., *Harnessing the Synergistic and Complementary Properties of Fullerene and Transition-Metal Compounds for Nanomaterial Applications*, Chem. Rev. 115 (20) (2015) pp11301-11351.

11 Vougioukalakis, G., Roubelakis, M., Orfanopoulos, M., *Open-cage fullerenes: Towards the construction of nanosized molecular containers*, Chem. Soc. Rev. 39 (2) (2010) pp817-844.

12 Mahmoud, M. A., O'Neil, D., El-Sayed, M. A., *Hollow and Solid Metallic Nanoparticles in Sensing and in Nanocatalysis*, Chem. Mater. (26) (2014) pp44-58.

13 Blinc, R., Arcon, D., Umek, P., Apih, T., Milia F., Rode, A. V., *Carbon nanofoam as a potential hydrogen storage material,* Phys.Status Solidi 244 (11) (2007) pp4308-4310.

14 Zhao, Q., Wang, S., Yang, Y., Li, Z., Di, D., Zhang, C., Jiang, T., Wang, S., Hyaluronic acid and carbon dots-gated hollow mesoporous silica for redox and enzyme-triggered targeted drug delivery and bioimaging, Mater. Sci. Eng C, 78 (2017) pp475-484.

15 Yang, S., Feng, X., Zhi, L., Cao, Q., Maier, J., Müllen, K., *Nanographene-Constructed Hollow Carbon Spheres and Their Favorable Electroactivity with Respect to Lithium Storage,* Adv. Mater. 22 (7) (2010) pp838-842.

16 Xu, F., Tang, Z., Huang, S., Chen, L., Liang, Y., Mai, W., et al., *Facile synthesis of ultrahigh-surface-area hollow carbon nanospheres for enhanced adsorption and energy storage,* Nat. Comm. 6 (2015) pp7221.

17 Wang, Y., Su, F., Lee, J., Zhao, X., *Crystalline Carbon Hollow Spheres, Crystalline Carbon−SnO 2 Hollow Spheres, and Crystalline SnO 2 Hollow Spheres: Synthesis and Performance in Reversible Li-Ion Storage,* Chem. Mater. 18 (5) (2006) pp1347-1353.

18 Li, S., Pasc, A., Fierra, V., Celzard, A., *Hollow carbon spheres, synthesis and applications – a review,* J Mater. Chem A 4 (2016) pp12686-12713

19 Liu, J., Qiao, S., Chen, J., Lou, X., Xing, X., Lu, G. Yolk/shell nanoparticles: *New platforms for nanoreactors, drug delivery and lithium-ion batteries.* Chem. Comm. (2011) 47 (47) pp12578-12591.

20 Li, Y., Zhou, C., Xie, X., Shi, G., Qu, L., *Spontaneous, catalyst-free formation of nitrogen-doped graphitic carbon nanocages,* Carbon (2010) 48 (14) pp4190-4196.

21 Huang, Q., Wang, S., Zhang, Y., Yu, B., Hou, L., Su, G., Ma, S., Zou, L.u., Huang, H., *Hollow Carbon Nanospheres with Extremely Small Size as Anode Material in Lithium-Ion Batteries with Outstanding Cycling Stability,* J Phys. Chem. C 120 (6) (2016) pp3139-3144.

22 Sengupta, J., Jacob, C., *The effect of Fe and Ni catalysts on the growth of multiwalled carbon nanotubes using chemical vapor deposition,* J Nanopart. Res. (2010) 12 (2) pp457-465.

23 Zhao, P., Li, N., Astruc, D., *State of the art in gold nanoparticle synthesis,* Coord. Chem. Rev. (2013) 257 (3-4) pp638-665.

24 Arvizo, R. R., Bhattacharyya, S., Kudgus, R. A., Giri, K., Bhattacharya, R., Mukherjee, P., *Intrinsic therapeutic applications of noble metal nanoparticles: past, present and future,* Chem. Soc. Rev. (2012) 41 (7) pp2943-2970.

25 Ji, H., Wang, S., Li, M., Kim, J., *Deep crystallisation induced high thermal conductivity of low-temperature sintered Ag nanoparticles,* Mater. Lett. (2014) 116 pp.219-222.

Aims and Objectives

Aims

Creation and implementation of processing techniques for the bottom-up formation of < 10 nm sized, well-defined, hollow carbon shells from thiol stabilised silver nanoparticles.

Objectives

Synthesise silver nanoparticles, using molecular self-assembly to create thiol-stabilised metal nanoparticles, with a narrow size distribution. Further synthesise silver nanoparticles with mixed thiol layers, to incorporate the heteroatoms fluorine or nitrogen.

Perform heating experiments to reliably produce novel hollow carbon structures from silver nanoparticles on a range of support materials. Investigate the possibility of incorporating heteroatoms into these hollow carbon structures by heating suitable starting materials containing nitrogen or fluorine.

Characterise these materials using appropriate techniques, including transmission electron microscopy.

2.0 Literature review

2.1 Introduction

The literature review begins with an overview of nanomaterials and a precis of nanostructured carbon, followed by details concerning the main theme of this research: Hollow carbon nanoshells (HCNS). Synthetic routes for HCNS formation are then summarised, leading on to starting material selection and synthetic route rationale.

2.2 Nanomaterials

Nanomaterials are important because they have functional properties that differ from bulk matter and molecular species. Whilst the official definition of a nanomaterial is still being debated by UK government [1], recommendations to the European Commission have suggested a "Nanomaterial" is:

"A natural, incidental or manufactured material …. where, for 50% or more of the particles in the number size distribution, one or more external dimensions is in the size range 1 nm - 100 nm …. fullerenes, graphene flakes and single wall carbon nanotubes with one or more external dimensions below 1 nm should be considered as nanomaterials." [2]

Indeed, governments world-wide consider nanoscience, nanotechnology and nanomaterials to be strategically important, in terms of research and development and for future economic growth, whilst acknowledging the disruptive potential of this technology. In this context, the European Commission has identified six strategically important Key Enabling Technologies, four of which include nanomaterials; *i.e.* micro-nanoelectronics, nanotechnology, advanced materials and photonics [3]. In terms of scale of investment, in the U.S., for example, the National Nanotechnology Initiative Research Federal Budget (4), in 2018, was $1.5 billion.

2.3 Nanocarbon

Carbon is abundant and non-toxic, and all known life is carbon-based [5]. Carbon is the single, most intensely researched element, due to the variety of bonds carbon can form, both with other carbon atoms and virtually all known elements, giving rise to a vast number of carbon compounds [6]. In addition, there are a diverse range of carbon allotropes [7]: On the macro-scale, diamond and graphite; whilst on the nanoscale, graphene, nanofibres, nanotubes, quantum dots and fullerenes (Figure 2.1), along with nano-forms of diamond and graphite, and other nanoscale carbon structures (Table 2.1). Several Nobel prizes have been awarded to researchers of nanoscale carbon [8], constituting evidence for the potential impacts of nanocarbon.

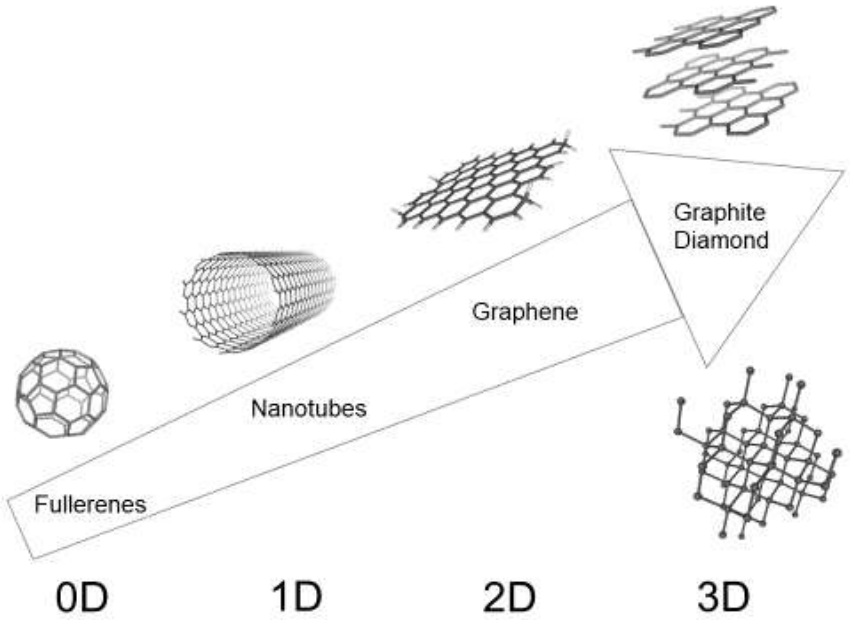

Figure 2.1 Examples of carbon allotropes as a function of dimension. Nanoscale forms are quasi 0D, 1D or 2D: 3D diamond or graphitic structures may also exist on the nanoscale.

In addition to the low toxicity of most carbon nanomaterials [9], with the exception of carbon nanotubes which are considered toxic due to their very high aspect ratio and hydrophobicity [10], nanoscale forms of carbon have significant potential for a variety of applications due to their diverse functional properties, arising from their structural differences and dimensionality. By way of example, electrochemically active quasi zero dimensional (0D) functionalised fullerenes may form molecular electronic components [11, 12]. Further, optically active carbon quantum dots (CQD) are promising for combined bioimaging and drug delivery [13, 14]; additionally, CQD exhibit biocompatibility, quick *in vivo* excretion, good environmental credentials and stability compared to existing agents. Nanoscale diamonds are also promising candidates for medical applications, *e.g.* with single nano-diamond particle fluorescence tracking becoming possible in real-time; their high adsorption capacities could enable drug delivery, and the surface functionalisation of nano-diamonds should further extend their range of applications [15].

Table 2.1 Key carbon allotropes, in terms of dimension, bonding structure, properties and chemistry.

Allotrope	Dimen-sion	Bonding structure	Properties	Chemistry
Diamond	3D	sp^3; bond length 1.54 Å	Very hard; insulator; band gap 5.47eV	Reacts with oxygen at high temperatures
Graphite	3D	sp^2; bond length 1.42 A; inter-layer distance 3.35 Å	High electrical & thermal conductivity along layers	Forms intercalates
Graphene	2D	sp^2; bond length 1.42 Å; one graphite layer thick	Very high electron mobility & low resistivity; spin coherent electron transport; semi-metallic	Reacts with oxygen at high temperatures to form graphene oxide
Nanotubes: single-walled; multi-walled; graphitised nanofibres	1D	sp^2; conceptually an extended cylindrical fullerene from rolled-up 2D graphene	Exceptional strength; thermal & electrical conductor; molecular container or test tube, confinement produces stereo selective products	Reactivity lower than fullerenes, but can be functionalised; enhances the performance of catalysts due to lower ΔG, or by modifying electronic states
Hollow structures; nanofoam, aerogel, shells	1D or quasi 0D	Varies, but has regions of sp^2	May conduct, donate, or accept electrons	Little studied to date
Quantum dots; nano-diamonds; core-shell structures	quasi 0D	Varies, but has regions of sp^3 and sp^2	Photoluminescence; electron donating	Surface alteration possible to enhance properties or enable attachment of dyes *etc*
Fullerenes; C_{60} C_{70}	quasi 0D	sp^2, but with sp^3 character; bond length 1.38 - 1.45 Å	Electron acceptor; molecular container; superconducting at <30K.	Nucleophilic addition; hydrogenation; halogenation; cycloaddition and others

For the case of two dimensional (2D) graphene, the polycyclic aromatic hydrocarbon monolayer produces exceptional electrical and thermal conductance, combined with material strength and malleability [16], suggesting potential applications as transistors or batteries, or within optoelectronics or sensing; and many others, such as embedded wearable technology, with a recent 3D printing technique producing graphene aerogels [17] extending the many potential uses into energy storage, absorbents, catalysts, or tissue scaffolds [18].

Carbon nanotubes (CNT) have immense mechanical strength, combined with very high Young's modulus and remarkable flexibility [19], leading to potential

applications as structural materials, with even theoretical suggestions of a CNT-based space elevator [20]. The electronic properties of CNT range from metallic to semiconducting, depending on the chirality of CNT, with potential applications as field effect transistors or diodes [21]. Further, their confined internal dimensions and hollow nature have enabled the formation of ordered molecular arrays during chemical syntheses, inside these nanoscale "test-tubes" [22], producing highly unusual structures, unique to these materials [23].

2.4 Hollow nanocarbon

Hollow, nanostructured carbons, such as carbon nanotubes (CNT), nanofoams, aerogels, fullerenes and nanoshells, provide for a wide variety of applications including catalysis [24] and supercapacitance [25], by exploiting the large internal and external surface areas available, combined with their electron accepting or donating properties. Gas-storage is another promising application, particularly for carbon nanofoams / aerogels, with their intrinsically high porosity and low mass [26]. Further, the use of quasi zero dimensional carbon materials as molecular hosts for drug delivery systems [27], and for cell imaging and cancer therapy have been reported [28].

However, fullerenes have limited sizes (~ 3.5 Å diameter) for use as containers, being suitable only for small atoms, molecules or ions [29], whilst quasi one dimensional CNT and nanofibers (NF) with larger volumes have limited solubilities and tend to bundle [30]. Additionally, there is market pull for improved gas storage systems [31], electrode materials [32] and for lower toxicity drug delivery systems [27]; all of which could potentially be provided for by hollow nanoscale carbon materials.

Interest in HCNS arises due to the properties afforded by the combination of their size and functional properties, *e.g.* in catalysis, the surfaces of HCNS, whilst providing a very large surface area, also have the capacity to accumulate reaction materials and intermediates inside interior cavities, and have been shown to improve reaction rates for catalysts supported inside double shell, hollow nanoparticles [33] without contributing significantly to increased weight or volume. Indeed, the high chemical and thermal stability and good biocompatibility of hollow nanomaterials suggest many applications for environmental remediation; *e.g.* to detect toxins, or adsorb or degrade heavy metal ions or organic pollutants [34]. Further, the intrinsic low toxicity of carbon could find applications as a container for drug delivery systems, with open ended, elongated structures having internal diameters as low as ~ 5 - 30 nm [35], encapsulating therapeutic agents, with functionalisation enabling targeted release [36]. A significant number of publications focus on the potential of hollow carbon spheres as electrode materials [37, 38], where the conductivity of the material is crucial for functional performance.

HCNS structures, of size ~ 200 nm, were documented originally as by-products from the carbon-arc processing of CNT [39]. More recently, HCNS structures with sizes ranging from ~ 70 – 800 nm have been produced using a variety of sacrificial templating and annealing processes [40-43]. The generic approach is that of hydrocarbon templating of mesoporous shell SiO_2 nanoparticles (NP) [44] and thermal processing (at ~ 450 - 1000°C in an inert atmosphere) to create graphitic C, followed by template removal (using dilute HF or NaOH) to create bespoke HCNS structures, typically at least 200 nm in diameter. Carbon sources vary depending on the templating strategy adopted: In the case of chemical vapour deposition (CVD) onto SiO_2 particles, small hydrocarbon molecules such as methane [45], ethylene [46],

benzene or acetonitrile [47] have been employed successfully. Alternatively, sugars have provided a source of carbon, *e.g.* in the case of liquid impregnation of sucrose [48], or polymerisation of glucose [49] onto mesoporous Si, whilst co-condensation of resorcinol, formaldehyde and tetrapropyl orthosilicate have been utilised [50]; hexa-*peri*-hexabenzocoronene, known to self-assemble into graphitic nanotube-shaped structures [51], has led to the production of an interesting mesoporous shell structure containing 2 nm diameter channels arranged perpendicularly to the Si template surface [42].

Alternative strategies for creating HCNS structures (50 – 150 nm) include soft-templating, involving micelles or droplets [52], or template-free methods of production [53], however, in the latter case, coating HCNS with polyaniline was required for electrical conductance, additionally, these routes still present significant challenges, as the high temperatures required for the graphitisation of HCNS are likely to disrupt micelles or droplets. Further, these strategies generally lack scalability and require particular processing conditions and starting materials, therefore limiting flexibility [54]. Schematic representations of hard-templating, soft templating and template free-syntheses of HCNS are illustrated in Figure 2.2 [Adapted from 48, 52, 55].

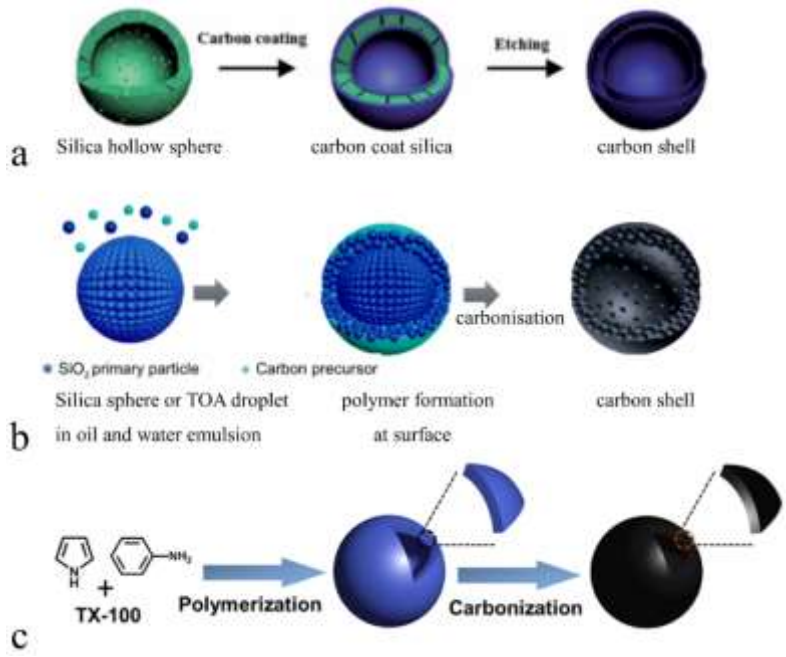

Figure 2.2 Schematics illustrating synthetic strategies for HCNS formation: (a) Soft templating from the carbonisation of hollow or solid SiO_2 spheres, adapted from [48]; (b) soft-templating, typically with an oil-in-water emulsion, self-assembly of a carbon source at the surface with carbonisation simultaneously removing the template (TOA, trioctylamine), adapted from [52] and; (c) template free methods from carbonisation of self-assembled polymers (TX-100, surfactant), adapted from [55].

A summary of synthetic methods for HCNS production, and HCNS products obtained is provided, Table .2.2. Depending on the application, the size distribution of products is clearly important, and where known is reported in Table 2.2.

Table 2.2 Summary of HCNS synthesis details and products formed.

Author	Year	Template	Coating method / Carbon source	Template removal	Preparation steps	Product Size / nm
Arif [40]	2018	polystyrene latex particles	hexamethoxymethylmelamine	n/a	3	220
Arnal [44]	2006	SiO_2 or ZrO_2	thermal polymerisation, polymer carbon source	NaOH or HF	5	400
Chen [32]	2016	SiO_2 particles	3-aminophenol/formaldehyde	HF	3	130 - 290
Chen [56]	2012	SiO_2 coating on Si particles	polymerisation of dopamine, mixing dopamine hydrochloride and template, 20 h.	HF	4	150 - 300
Han [57]	2011	template free	sucrose	n/a	1	50 - 100
Huang [58]	2016	metal-organic Cu NP	acetylacetonate	n/a	2	20 - 40
Katcho [54]	2007	ferrocene	ferrocene, $Fe(C_5H_5)_2$	n/a	1	50 - 150
Lei [41]	2010	Si particles	CVD, 550°C 60 min	HF	4	190
Li [54]	2018	template free	polyaniline	H_2SO_4	4	200
Liu [59]	2011	SiO_2 particles	self-polymerisation of dopamine	HF	5	400
Su [47]	2006	Si particles	CVD, 1000 or 900, benzene, 4 h	HF	4	400, 650, 730
Sun [48]	2015	hollow SiO_2 spheres	hydrothermal polymerisation of glucose, 180°C, 4 h	HF	3	80 - 120
Tan [60]	2013	MnO particles	polyaniline	HNO_3	3	30, foam type

Tun [45]	2014	SiO_2 particle,	CH_4 source	HF	3	50 - 450
Wang [46]	2006	SiO_2 particles	CVD, 1000, benzene, 4 h	HF	3	750
Wickramaratne [43]	2013	soft template	resorcinol-formaldehyde	n/a	4	60 -100
Xu [52]	2015	TX-100 micelle	aniline and pyrrole (confined interfacial co-polymerisation)	n/a	2	70
Yang [42]	2010	Si core-mesoporous shell	hexa-peri-hexabenzo-coronene, stir at 40°C	NaOH	4	380
Zang [61]	2015	SiO_2	resorcinal / formaldehyde resin	HF	4	350
Zhang [50]	2016	SiO_2 particle	condensation of resorcinol-formaldehyde oligomers	HF	3	210 - 320 tuneable
Zhao [62]	2016	TX-100 micelles	Triton X-100, pyrrole, aniline	n/a	2	70
Zhong [63]	2012	poly (n-butyl acrylate)	polyacrylonitrile	n/a	3	fused HCNS

CVD = chemical vapour deposition,
MC = mesoporous carbon
TX-100 = 4-(1,1,3,3-Tetramethylbutyl)phenyl-polyethylene glycol, t-Octylphenoxypolyethoxyethanol, Polyethylene glycol tert-octylphenyl ether

Inherent to these processing routes, it is noted that a processing temperature of ~ 800°C is considered necessary for the effective graphitisation of HCNS [43], this contrasts with the formation temperature of bulk graphite at ~3000°C [64]. HCNS formed at 400°C were comprised of mostly amorphous carbon [27], whilst the lowest temperature leading to graphitised HCNS was 550°C [55] (Table 2.3), with effective graphitisation of HCNS products mostly achieved during extended heating times (up to 24 h), in an inert atmosphere.

Table 2.3 Heating conditions and degree of HCNS product graphitisation.

Author	**Temperature & Duration, °C / h**	**Atmosphere**	**Carbon Structure**
Chen [56]	600 / 3	N_2	assumed graphitic
Han [58]	550 / 10	not specified	0.37 nm lattice spacing, expansion and graphitisation
Huang [59]	1250 / 10	vacuum	graphitic
Katcho [54]	900 / 0.5 -3	Cl_2	disordered, some graphitic regions
Lei [41]	800 / 1.5	not specified	graphitised, but also amorphous
Li [53]	800 / 2	Ar	not graphitic
Su [47]	900 or 1000 / 4	N_2	graphitic
Sun [48]	800 / 4	Ar	disordered, reasonable graphitic
Wang.[46]	400 / 0.3	Ar	mostly amorphous
Xia [49]	1000	N_2	graphitic and disordered
Xiong [65]	190 / 24	not specified	well graphitised
Yang [42]	700 or 1000 / 5	Ar	graphitic
Zhao [63]	800 / 2	Ar	low graphitic levels
Zhong [64]	700 / 5	N_2	not graphitic

Indeed, the thermally induced graphitisation of alkanes has been observed at temperatures of ~ 800°C [66] which may be catalysed by metallic surfaces [67, 68].

In more detail, for alkane molecules bonded to Au(1 1 1) surfaces, graphitisation has been shown to occur following dehydrogenation of terminal CH bonds, with restricted motion and templated molecular arrangements resulting in well-graphitised products; CH bonds start to be broken at around 367°C, with almost all CH bonds absent at 526°C, combined with the appearance of unsaturated features due to double bonds, (and a notable absence of triple bonds); in this case the graphitised plane was noted to be perpendicular to the Au surface [69]. Further, simulations have indicated that the growth of graphene at catalyst surfaces proceeds via sequential addition of carbon hexagons to graphene domain edges, with the catalyst both adsorbing carbon atoms and stabilising carbon chains and small graphene flakes [70].

2.5 Heteroatom addition to / doping of nano-carbon

Several nanoscale forms of carbon, including graphene, nano-diamonds, CQD and HCNS have been substitutionally doped with nitrogen to modify the electronic or optical properties of these materials [71]. Nitrogen doping generally aims to modify material properties by inducing structural changes [72] and for graphitic lattices, N may substitute in quaternary, pyridinic or pyrrolic positions, (Figure 2.3). Incorporation of nitrogen into carbon nanostructures is known to enhance catalytic activity via modification of the electronic structure, similar to that observed in graphene [73], due to the electron donating properties of the lone pair of electrons on the nitrogen atom and to electron-hole asymmetry.

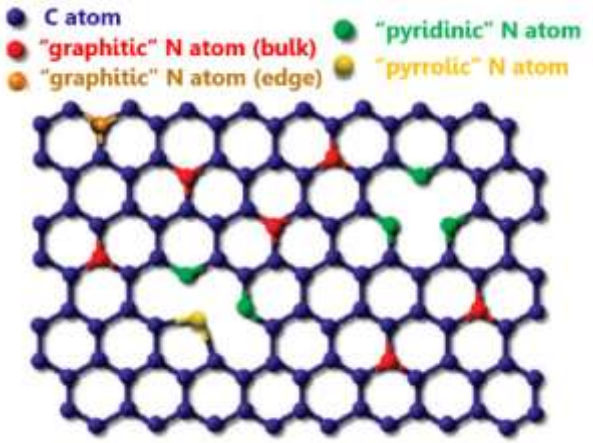

Figure 2.3 Doping graphitic structures with N may result in three different types of substitutions. From [74].

In addition to potential catalytic activity, N-doping has been shown to improve the electronic properties [24] of carbon nano-cage structures, suggesting potential as electrode materials, or supercapacitors which bridge the gap between rechargeable batteries and capacitors whilst being high performance, low cost and environmentally friendly. By way of example, the synthesis of an ultra-thin graphitic nano-cage material [60] doped with nitrogen, with a large surface area and high porosity, facilitating very high charge storage, with connectivity between carbon structures allowing for rapid movement of electrons (Figure 3.4). Whilst the material is cubed, rather than spherical, at around 30 nm, it is smaller than reported hollow shell or spherical structures, and is synthesised via a three step process to form a connected foam-type structure.

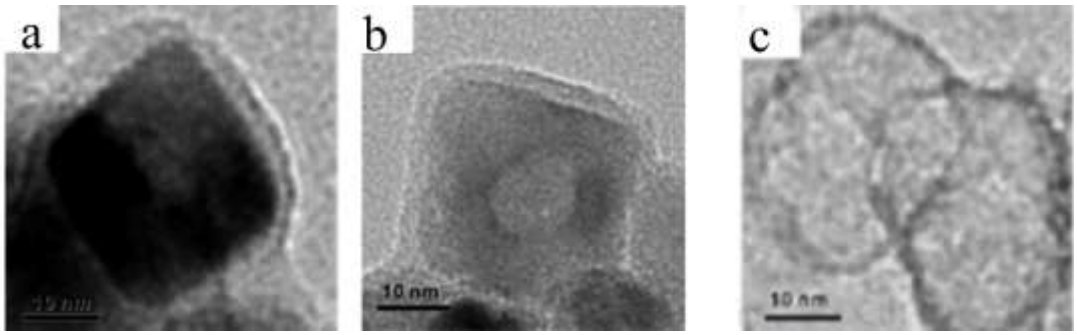

Figure 2.4 TEM images of hollow C-cage synthesis steps: a) Mn_3O_4@PANI core-shell NP, synthesised from a hydrothermal procedure. b) MnO@C cores surrounded by graphitic outer layers. c) Hollow C-cages formed after removal of MnO cores by HNO_3 [60].

Additionally, CNT doped with B, N or P have been shown to improve catalytic performance [75], and carbon nanospheres have been co-doped with N, S and P with the same aim [76]. To date, the doping of HCNS has been achieved generally through pyrolosis or thermal processing of suitably doped starting materials [56].

Substitution of H atoms with halogens such as F, Cl, Br is also possible, with F offering several advantages over the larger halogens. Fluorine is the most electronegative of all elements, with good potential for orbital overlap between electrons of other second row elements such as carbon, boron, nitrogen or oxygen [77]. Additionally, fluorinated compounds are biocompatible, inert and stable [78] and have varied and important applications such as Teflon coatings, propellants, as insulating gasses in high voltage switchgear, and as additives in fire-retardant foams. These applications are due to the unique properties of fluorinated materials [10]: Insolubility in water and oils, and their wettability and frictional properties; *e.g.* the increasing frictional properties of fluorinated monolayers on Au [79] and the formation of super-hydrophobic surfaces [80]. Further, substituting F for H does not induce pronounced structural alterations [81].

The high electron affinity of F has been shown to affect electronic properties of materials, *e.g.* p-type organic semiconductors are changed to n-type in the case of fluorinated analogues (pentacene/perfluoropentacene) [82]; and speculatively, F-doped HCNS may have useful applications in electronics. Further, the electronegativity of F has been shown to lead to self-assembly of materials via supramolecular interactions [83] including solid state self-assembly [84], suggesting the addition of fluorine may potentially promote the self-assembly of HCNS structures with long range order.

It is noted that fluorinated NP are promising fluorescent bio-imaging probes [85], due to their inertness, stability and biocompatibility. As ^{19}F nuclei have a spin quantum number of ½, their use as magnetic resonance imaging agents is being investigated [86], and whilst a patent exists for F-nanodot emulsions as optically active magnetic resonance imaging agents [87], the development of hollow F-doped structures would be novel.

The formation of bespoke HCNS has been achieved to date typically via the use of multi-step processing, e.g. carbon coating a hard template material, necessitating a synthetic step prior to thermal treatment, followed by chemical template removal [57, 24]. Whilst most HCNS formed to date are > 70 nm diameter [52], there is a clear need for smaller structures [88], particularly for electrode materials. However, the smallest HCNS reported in the literature are of average size ~ 20 nm with poor control over size distribution observed, with a spread of 20 – 40 nm diameter [58]. These small HCNS were formed from $Cu(acac)_2$, high temperatures and extended heating times (1250°C for 10h) required for formation. The research undertaken in this thesis aims to reduce the number of synthetic steps and reduce the size distribution of HCNS products to < 10%.

Stabilised metal nanoparticles, as an alternative starting material for HCNS formation, intrinsically contain a carbon source, since these particles may be stabilised with a variety of organic molecules [89], thus negating the requirement for a carbon coating synthetic step before graphitisation. With the metal NP core providing a hard template for HCNS formation, these starting materials provide a self-contained system. Additionally, metal nanoparticles are known to catalyse thermally mediated graphitisation [90]. Further, in contrast to existing HCNS templates, Au or Ag stabilised nanoparticles have size distributions below 20 nm, with narrow size distributions, which may be easily controlled in the 2 - 50 nm range [91]. The bulk melting points (mp) of Ag (962°C) and Au (1064°C) are significantly higher than the temperatures required for graphitisation of the carbon source (550 - 800°C). Since NP species also exhibit lower melting points compared to bulk materials, in accordance with the Gibbs-Thomson equation (which predicts decreased melting points with smaller NP radii, Equation 2.1, Figure 2.5, [92], heating of Ag / Au stabilised nanoparticles could lead to the formation of very small HCNS, with removal of the Ag / Au templates induced by raising the processing temperature higher, if required. Ag nanoparticles were preferred due to the lower melting point of this metal compared to Au.

$$\mathrm{Tm}(r) = Tm(\infty) - \frac{2Tm(\infty)\sigma}{\Delta H(\infty)\rho r}$$

Equation 2.1. Tm(r) is the melting point of a spherical particle with radius r, Tm(∞), ΔH(∞) and ρ are the bulk melting temperature, bulk latent heat of fusion and the solid state density, respectively, whilst σ is the solid-liquid interface energy.

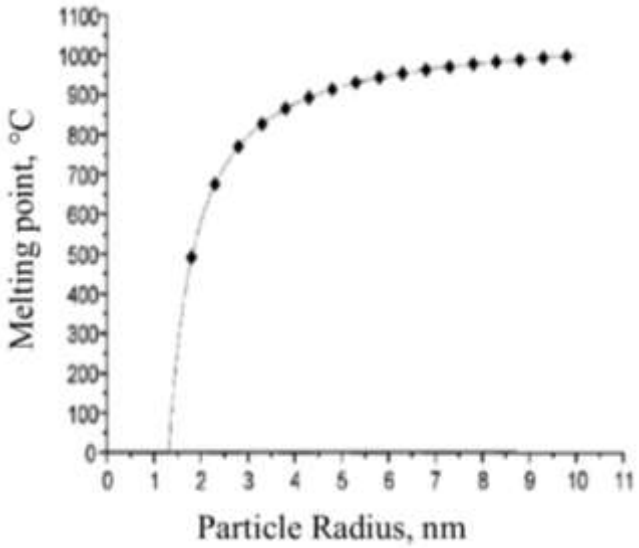

Figure 2.5 Relationship between melting point and radius of spherical Au NP, showing a lowering of melting temperature with reduction in radius [92].

Thiol stabilised AgNP are known to be stable, and have strong covalent Ag-S bonds at Ag surfaces [93], additionally, modification of the relative molarities of Ag and thiol enables the facile formation of < 10nm sized AgNP, therefore1-dodecanethiol was selected as the stabilising AgNP ligand.

Modification of the AgNP starting material to include heteroatoms was intended to result in good spatial distribution of heteroatoms within the final graphitised product [72], without the need for additional processing steps and has been achieved during chemical synthesis of AgNP [94]. Functional properties of AgNP starting materials are known to be influenced by the stabilising layer composition and chemistry [95]. The incorporation of more than one thiol into the AgNP stabilising layer affords additional flexibility for control of heteroatom amounts, and has led to the production of AgNP with properties intermediate between singly stabilised entities, different from either mono-ligand stabilised NP [96].

With N-doping successfully achieved in larger hollow carbon structures [75], the synthesis of HCNS from AgNP starting materials stabilised with a nitrogen containing ligand was a preferred starting option, with formation of fluorinated AgNP, and HCNS offering functional changes, with minimal structural disruption anticipated. Functionalised HCNS are of potential interest as building blocks for future complex networks or self-assemblies. However, there are challenges with this approach since there is a pronounced tendency for highly fluorinated AgNP to aggregate, producing AgNP that are difficult to purify and characterise, due to low dispersion in solvents [97], and whilst the use of supercritical CO_2 has been shown to limit aggregation [98], a mixed hydrogenated and fluorinated AgNP stabilising layer may overcome this issue.

2.6 Synthesis of AgNP starting materials

AgNP synthesis may be grouped into top-down or bottom-up approaches, *i.e.* etching bulk material or growth of molecular (or atomic) constituents, respectively [99]. Alternatively, synthesis may be classified by method: Chemical, physical or biological. Chemical syntheses produce high yields, but can be expensive and may use toxic or hazardous chemicals, whilst physical methods are low yield, require high energy inputs and may also involve harsh chemicals. More recent bio-inspired syntheses have greener credentials and are increasingly used to produce materials for biological applications, but are less easily adapted to form bespoke AgNP (Figure 2.6).

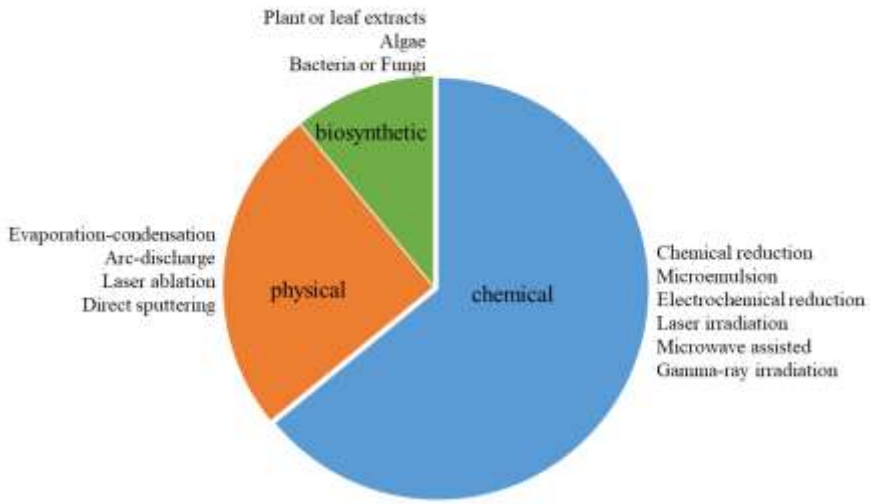

Figure 2.6 Classification of AgNP production methods.

In more detail, physical production methods include evaporation-condensation techniques [100] in which aerosols are formed by electrically heated tube furnaces, over which carrier gasses are passed, with NP condensation at cooler furnace locations; NP are subsequently size-selected and range from 2 – 300 nm diameter. The disadvantages of this synthetic route are the high power costs and time taken, however, smaller more efficient heating systems are available [101] which overcome this limitation. Laser-ablation has produced AgNP as colloids in aqueous media [102] or in air, with femtosecond laser pulses producing improved size dispersions [103], whilst arc-discharge methods [104] or direct metal sputtering [105] are alternative physical approaches to AgNP synthesis. The main advantage of NP produced via these top-down synthetic routes is considered to be the lack of solvent contamination, however, as NP produced by this method do not have a stabilising layer, *i.e.* a source of carbon for HCNS formation, this production method does not provide a suitable HCNS precursor.

Biosynthetic approaches to AgNP production aim to lower costs and improve environmental credentials, with the use of bacterial cells [106], fungi [107], and plants [108] reported, but drawbacks arise due to optimisation of the many parameters involved in these synthetic approaches, such as selection of the most appropriate organism, controlling cell growth, enzyme activity and reaction conditions; however, these approaches are relatively new and likely to improve in the future.

The most popular AgNP synthetic routes are bottom-up chemical syntheses; amongst the different options are two-phase micro-emulsion techniques [109] during which metal clusters form at the interface between two immiscible liquid phases which, when stabilised, are transferred away from the interface into the organic phase - this synthetic route is particularly applicable for applications requiring AgNP dissolved in non-polar solvents, but the main drawbacks are the large amounts of solvents involved and the aggregation of AgNP once removed from the micro-emulsion. Microwave-assisted technology offers time savings over traditional approaches, when combined with the use of plant-based reducing and capping agents [110], these offer a greener approach, but studies to optimise control of processing parameters continue. Other more specialised routes include laser irradiation to produce stabilised spherical AgNP, triangular AgNP and interconnected networks [111]. Whilst γ-ray irradiation has been employed for tailoring AgNP properties [112], photo-induced routes are considered more versatile [113], with photo-generated radical generation enabling AgNP synthesis in emulsion, polymer films and glasses. Further, synthetic approaches involving electrochemical reduction may produce stabiliser free AgNP [114], or stabilised AgNP, but tend to produce somewhat widely sized dispersed AgNP [115], in this example 39 ± 15 nm.

The most widely applied AgNP synthesis approach is chemical reduction, although the precise mechanism of AgNP formation is debated [116], but in general terms, Ag^+ ions in solution are reduced to Ag atoms which undergo nucleation to form increasingly larger NP in a non-equilibrium, dynamic process [117]. Surface stabilisation of AgNP formed by this method prevents agglomeration, with good size control and distribution of products, and allows for surface functionalisation. Some important reducing and stabilising agents are summarised in Table 2.4, with AgNP sizes, adapted from [99].

Table 2.4 Reducing and stabilising agents used for the production of AgNP via chemical reduction, adapted from [99].

Reducing Agent	**Stabilising Agent**	**AgNP size, nm**
M-Hydroxy Benzaldehyde	Sodium Dodecyl Sulphate	15 - 260
Ethylene Glycol	Polyvinyl Pyrrolidone	5 -115
Dextrose	Polyvinyl Pyrrolidone	18 - 27
Glucose	Gluconic Acid	40 - 80
Ascorbic Acid	-	200 -650
Trisodium Citrate	Trisodium Citrate	30 -60
Dimethyl Formaldehyde	-	< 25
Sodium Borohydride	Thiols	3

Chemical synthesis via a modified one-phase synthetic route affords high yields, good size distributions and stable AgNP with facile size control [118]. In addition, a range of stabilising ligands may be incorporated, *e.g.* citrate [119], alcohols, phosphines or polymers, with mixed thiol syntheses offering a route to further tailor functional groups at the AgNP surface. Additionally, the use of a single phase eliminates the need for large amounts of organic solvents, with associated environmental costs.

2.7 Concluding remarks

There is need for very small (< 10 nm) HCNS structures, providing for anticipated improvements in electrical performance and catalytic activity. The smallest reported HCNS to date are ~ 20 nm, with most being significantly larger (~ 300 nm). Additionally, improved control of size distribution is desirable, whilst maintaining the formation of a well-defined graphitised product, for good structural integrity. In particular, there is a market pull for < 10 nm nanoscale confinement materials, for applications in catalysis, drug delivery or environmental remediation. However, most HCNS formation strategies involve multi-step processes and chemical removal of templates, or very high temperatures for several hours, and the associated environmental costs should be considered.

The proposed formation strategy involves a self-contained templated carbon source, and a single heating step, to both produce HCNS and remove the templates. The use of AgNP stabilised with small organic molecules, as novel starting materials for HCNS formation, are investigated here, as these provide a convenient source of carbon, good size control (< 10 nm), and an in-built template. Thermal processing aims to promote HCNS formation and the removal of the AgNP template in a one-step process, negating the need for harsh chemicals. Good size control of AgNP starting materials is easily achievable, with narrow size distributions, hypothesised to lead to the formation of commensurate HCNS structures, following thermal processing.

Further, the thiol stabilising of AgNP templates offer the possibility of introducing heteroatoms into the HCNS, with N and F selected due to the many, varied

applications afforded by these elements; it is considered this will demonstrate the flexibility of this approach.

References

1 GUV.UK (2015). Nanomaterial definition: final European Commission report. G. Chemist.

2 Nano.gov. (2015). "National Nanotechnology Initiative." Retrieved 8.12.15, from http://www.nano.gov/.

3 Research & Innovation - Key Enabling Technologies. from http://ec.europa.eu/growth/industry/key-enabling-technologies/european-strategy/high-level-group/index_en.htm accessed 09-02-2018

4 Nano.gov, National Nanotechnology Initiative, President's 2019 Budget, from https://www.nano.gov/about-nni/what/funding accessed 17-08-2018.

5 Reece, J. B., Urry, L. A., Cain, M. A., Wasserman, S. A., Minorsky, P. V., Jackson, R. B., (2008). Biology. San Francisco, Pearson Education.

6 Carey, A. F. (2008). Organic Chemistry. Boston Mass; London, McGraw-Hill Higher Education.

7 Pokropivny, V.V., Ivanovskii, A.L., *New nanoforms of carbon and boron nitride*, Russ. Chem. Rev. 77 (10) (2008) pp837 -873.

8 Nobel prize in Chemistry, 1996 Retrieved 19/12/2016 from https://www.nobelprize.org/nobel_prizes/chemistry/laureates/.

Nobel prize in Physics, 2010 Retrieved 19/12/2016 from https://www.nobelprize.org/nobel_prizes/physics/laureates/2010/index.html.

9 Royal Society of Chemistry. (2016). Periodic Table. http://www.rsc.org/periodic-table/element/6/carbon, Retrieved 19/12/2016

10 Lin, S., Yu, T., Yu, Z., Hu, X., Yin, D., *Nanomaterials Safer-by-Design: An Environmental Safety Perspective. Advanced Materials*, 30 (17) (2018) pp1705691.

11 Kroto, H. W., Heath, J. R., O'Brien, R. F., Smalley, R. E., *C60: Buckminsterfullerene,* Nature 318 (1985) pp162-163.

12 Carroll, J. B., Cooke, G., Garety, J., Jordan, B. J., Mabrukb, S., Rotelloa, V. M., *The electrochemically-tuneable interactions between flavin-functionalised C60 derivatives and 2,6-diethylamidopyridine,* Chem. Commun. (2005) pp3838–3840.

13 Yang, S. T., Cao, L., Luo, P. G. J., Lu, F. S., Wang, X., Wang, H. F., Meziani, M. J., Liu, Y. F., Qi, G., Sun, Y. P., *Carbon Dots for Optical Imaging in Vivo*, J. Am. Chem. Soc. 131 (32) (2009) pp11308-11309.

14 Baker, S. N., Baker, G. A., *Luminescent Carbon Nanodots: Emergent Nanolights,* Angew. Chem. Int. Ed. 49 (38) (2010) pp6726-6744.

15 Barnard, A., *Diamond standard in diagnostics: Nanodiamond biolabels make their mark.* The Analyst, 134 (9) (2009) pp1751-1764.

16 Geim, A., K., *Graphene: Status and Prospects*, Science 324 (5934) (2009) pp1530-4.

17 Jiang, Y., Xu, Z., Huang, T., Liu, Y., Guo, F., Xi, J., Gao, C., Direct 3D Printing of Ultralight Graphene Oxide Aerogel Microlattices, Adv. Funct. Mater. 28 (16) (2018) pp170702.

18 Mazzaglia, A., Scala,A., Sortino, G., Zagami, R., Zhu, Y., Sciortino, M. T., Pennisi, R., Pizzo, M. M., Musarra, M., Giulia, N., Grassi, G., Piperno, A., *Intracellular trafficking and therapeutic outcome of multiwalled carbon nanotubes modified with cyclodextrins and polyethylenimine*, Colloids Surf. B: Biointerfaces 163 (2018) pp55-63.

19 Demczyk, B. G., Wang, M., Cumings, J., Hetman, M., Han, W., Zettl, A., Ritchie, R. O., *Direct mechanical measurement of the tensile strength and elastic modulus of multiwalled carbon nanotubes*, Mat. Sci. Eng. A-struct. 334 (1-2) (2002) pp173-178.

20 NASA.gov, 2000, from https://science.nasa.gov/science-news/science-at-nasa/2000/ast07sep_1, accessed 13-08-2018.

21 Popov, V., *Theoretical study of the doping effect on the phonon dispersion of metallic carbon nanotubes*. Physica E: Low Dimens. Syst. Nanostruct. 44 (6) (2012) pp1032-1035.

22 Chamberlain, T.W., Lebedeva, M.A., Abuajwa, W., Suyetin, M., Lewis, W., Bichoutskaia, E., Schröder, M., Khlobystov, A. N., *Switching intermolecular interactions by confinement in carbon nanotubes*. Chem. Comm. 51 (2015) pp 648-651.

23 Khlobystov, A. N., *Carbon nanotubes: From nano test tube to nano-reactor,* ACS Nano 5 (12) (2011) pp9306-12.

24 Zhong, M.J., Kim, E.K., Natesakhawat, S., McGann, J.P., Whitacre, J.F., Matyjaszewski, K., Kowalewski, T., *Nitrogen-rich porous nanocarbon from block copolymer precursors for CO_2 capture and electrocatalysis of oxygen reduction*, Abstr. Pap. Am. Chem. (2012) S 244.

25 Ramakrishnan, P., Shanmugam, S., *Nitrogen-doped carbon nanofoam derived from amino acid chelate complex for supercapacitor applications*, J. Power Sources 316 (2016) pp60-71.

26 Rode, A. V., Elliman, R. G., Gamaly, E. G., Veinger, A. I., Christy, A. G., Hyde, S. T., Luther-Davies, B., *Electronic and magnetic properties of carbon nanofoam produced by high-repetition-rate laser ablation*, Appl. Surf. Sci. 197 (2002) pp 644-649.

27 Jong, W. H. De., Borm, P. J. A., *Drug delivery and nanoparticles: Applications and hazards*, Int. J Nanomedicine 3 (2) (2008) pp133–149.

28 Wang, Q., Huang, X., Long, Y., Wang, X., Zhang, H., Zhu, R., Liang, L., Teng, P., Zheng, H., *Hollow luminescent carbon dots for drug delivery*, Carbon 59 (2013) pp192-199.

29 Vougioukalakis, G., Roubelakis, M., Orfanopoulos, M., *Open-cage fullerenes: Towards the construction of nanosized molecular containers,* Chem. Soc. Rev. 39 (2) (2010) pp817-844.

30 Azoubel, S., Magdassi, S., *The formation of carbon nanotube dispersions by high pressure homogenization and their rapid characterization by analytical centrifuge*, Carbon 48 (12) (2010) pp3346-3352.

31 Blinc, R., Arcon, D., Umek, P., Apih, T., Milia F., Rode, A. V., *Carbon nanofoam as a potential hydrogen storage material,* Phys.Status Solidi 244 (11) (2007) pp4308-4310.

32 Chen, A. B., Li, Y. Q., Yu, Y. F., Ren, S. F., Wang, Y. Y., Xia K. C., Li, S. H., *Nitrogen-doped hollow carbon spheres for supercapacitors application,* J. Alloys Compd. 688 (2016) pp878-884.

33 Mahmoud, M. A., O'Neil, D., El-Sayed, M. A., *Hollow and Solid Metallic Nanoparticles in Sensing and in Nanocatalysis,* Chem. Mater. (26) (2014) pp44-58.

34 Zhang, Y., He, Y., Wang, H., Lu, Q., Liu, G., Zhang, X.,. *Applications of hollow nanomaterials in environmental remediation and monitoring: A review*. Front. Env. Sci. Eng. 9 (5) (2015) pp770-783.

35 Yokoi, H., Hatakeyama, K., Taniguchi, T., Koinuma, M., *Novel pot-shaped carbon nanomaterial synthesized in a submarine-style substrate heating CVD method,* J Mater. Sci. 31 (1) (2016) pp117-126

36 Zhao, Q., Wang, S., Yang, Y., Li, Z., Di, D., Zhang, C., Jiang, T., Wang, S., *Hyaluronic acid and carbon dots-gated hollow mesoporous silica for redox and enzyme-triggered targeted drug delivery and bioimaging,* Mater. Sci. Eng C, 78 (2017) pp475-484.

37 Hu, D., Chen, C., Liu, Q., *Fabrication of hollow carbon spheres with robust and significantly enhanced capacitance behaviors,* J Mater. Sci. 53 (17) (2018) pp12310-12321.

38 Li, M., Zhang, Y. Q., Yang, L. L., Liu, Y. K., Yao, J. S., *Hollow melamine resin-based carbon spheres/graphene composite with excellent performance for supercapacitors,* Electrochimica Acta 166 (2015) pp310-319.

39 Cowley, J. M., Kiang, C. H., *The structure of near-spherical carbon nano-shells,* 38 (10) (2000) pp1437-1444.

40 Arif, A. F., Kobayashi, Y., Schneider, E. M., Hess, S. S., Balgis, R., Izawa, T., Stark, W. J., *Selective Low-Energy Carbon Dioxide Adsorption Using Monodisperse Nitrogen-Rich Hollow Carbon Submicron Spheres,* Langmuir 34 (1) (2017) pp30-35.

41 Lei, Z.B., Chen, Z.W., Zhao, X.S., *Growth of Polyaniline on Hollow Carbon Spheres for Enhancing Electrocapacitance*, J Phys. Chem. C 114 (46) (2010) pp19867-19874.

42 Yang, S., Feng, X., Zhi, L., Cao, Q., Maier, J., Müllen, K., *Nanographene-Constructed Hollow Carbon Spheres and Their Favorable Electroactivity with Respect to Lithium Storage,* Adv. Mater. 22 (7) (2010) pp838-842.

43 Wickramaratne, N.P., Perera, V.S., Park, B.-W., Gao, M., McGimpsey, G.W., Huang, S.D., et al., *Graphitic Mesoporous Carbons with Embedded Prussian Blue-Derived Iron Oxide Nanoparticles Synthesized by Soft Templating and Low-Temperature Graphitization*, Chem. Mater. 25 (14) (2013) pp2803-2811.

44 Arnal, P.M., Schuth, F., Kleitz, F., *A versatile method for the production of monodisperse spherical particles and hollow particles: Templating from binary core-shell structures,* Chem. Comm. (11) (2006) pp1203-1205.

45 Tun, N.M., Morozov, A. N., Izvol'skii, I.M., Rakov, E.G., *Preparation and characterisation of hollow carbon nanospheres,* Inorg. Mater. 51 (5) (2015) pp445-450.

46 Wang, Y., Su, F., Lee, J., Zhao, X., *Crystalline Carbon Hollow Spheres, Crystalline Carbon−SnO 2 Hollow Spheres, and Crystalline SnO 2 Hollow Spheres: Synthesis and Performance in Reversible Li-Ion Storage,* Chem. Mater. 18 (5) (2006) pp1347-1353.

47 Su, F., Zhao, X. S., Wang, Y., Wang, L., Lee, J. Y., *Hollow carbon spheres with a controllable shell structure,* J Mater. Chem. 16 (45) (2006) pp4413-4419.

48 Sun, Z., Song, X., Zhang, P., Gao, L., *Template-assisted synthesis of multi-shelled carbon hollow spheres with an ultralarge pore volume as anode materials in Li-ion batteries,* RSC Adv. 5 (5) (2015) pp3657-3664.

49 Xia, Y., Yang, Z., Mokaya, R., *Mesostructured Hollow Spheres of Graphitic N-Doped Carbon Nanocast from Spherical Mesoporous Silica*, J Phys. Chem. B 108 (50) (2004) pp19293-19298.

50 Zhang, H., Noonan, O., Huang, X., Yang, Y., Xu, C., Zhou, L., Yu, C., *Surfactant-Free Assembly of Mesoporous Carbon Hollow Spheres with Large Tunable Pore Sizes,* ACS Nano. 10 (4) (2016) pp4579-86.

51 Hill, J., Jin, W., Kosaka, A., Fukushima, T., Ichihara, H., Shimomura, T., Ito, K., Tomihiro, H., Ishii, N., Aida, T., *Self-assembled hexa-peri-hexabenzocoronene graphitic nanotube,* Science 304 (5676) (2004) pp1481-3.

52 Xu, F., Tang, Z., Huang, S., Chen, L., Liang, Y., Mai, W., et al., *Facile synthesis of ultrahigh-surface-area hollow carbon nanospheres for enhanced adsorption and energy storage*, Nat. Comm. 6 (2015) pp7221.

53 Li, X., Xiang, X., Liu, Y., Xiao, D., *Template-free fabrication of hollow N-doped carbon sphere (h-NCS) to synthesize h-NCS@PANI positive material for MoO3//h-NCS@PANI asymmetric supercapacitor*, Appl. Surf. Sci. 442 (2018) pp476-486.

54 Katcho, N.A., Urones-Garrote, E., Ávila-Brande, D., Gómez-Herrero, A., Urbonaite, S., Csillag, S., et al., *Carbon hollow nanospheres from chlorination of ferrocene,* Chem. Mater. 19 (9) (2007) pp2304-2309.

55 Li, S., Pasc, A., Fierra, V., Celzard, A., *Hollow carbon spheres, synthesis and applications – a review,* J Mater. Chem A 4 (2016) pp12686-12713.

56 Chen, S., Gordin, M., Yi, R., Howlett, G., Sohn, H., Wang, D., *Silicon core hollow carbon shell nanocomposites with tunable buffer voids for high capacity anodes of lithium-ion batteries*, Phys. Chem. Chem. Phys. 14 (37) (2012) pp12741-12745.

57 Han, F. D. , Bai, Y. J., Liu, R., Yao, B., Qi, Y. X., Lun, N., Zhang, J. X., *Template-Free Synthesis of Interconnected Hollow Carbon Nanospheres for High-Performance Anode Material in Lithium-Ion Batteries,* Adv. Energy Mater. 1 (2011) pp798-801.

58 Huang, Q., Wang, S., Zhang, Y., Yu, B., Hou, Li., Su, G., Ma, S., Zou, J., Huang, H., *Hollow Carbon Nanospheres with Extremely Small Size as Anode Material in Lithium-Ion Batteries with Outstanding Cycling Stability*, J Phys. Chem. C 120 (6) (2016) pp3139-3144.

59 Liu, R., Mahurin, S., Li, C., Unocic, R., Idrobo, J., Gao, H., Pennycook, S. J., Dai, S., *Dopamine as a Carbon Source: The Controlled Synthesis of Hollow Carbon*

Spheres and Yolk-Structured Carbon Nanocomposites, Angew. Chem. Int. Ed. 50 (30) (2011) pp6799-6802.

60 Tan, Y. M., Xu, C. F., Chen, G. X., Liu, Z. H., Ma, M., Xie, Q. J., Zheng, N. F., Yao, S. Z., *Synthesis of Ultrathin Nitrogen-Doped Graphitic Carbon Nanocages as Advanced Electrode Materials for Supercapacitor*, ACS Appl. Mater. Interfaces 5 (6) (2013) pp2241-2248.

61 Zang, J., An, T., Dong, Y., Fang, X., Zheng, M., Dong, Q., Zheng, N., *Hollow-in-hollow carbon spheres with hollow foam-like cores for lithium–sulfur batteries*, Nano Research 8 (8) (2015) pp2663-2675.

62 Zhou, C., Geng, S., Xu, X., Wang, T., Zhang, L., Tian, X., Fan, Y., Yang, H., Li, Y., *Lightweight hollow carbon nanospheres with tunable sizes towards enhancement in microwave absorption*, Carbon 108 (2016) pp234-241.

63 Zhong, M., Kim, E. K., McGann, J. P., Chun, S. E., Whitacre, J. F., Jaroniec, M., Matyjaszewski, K., Kowalewski, T., *Electrochemically Active Nitrogen-Enriched Nanocarbons with Well-Defined Morphology Synthesized by Pyrolysis of Self-Assembled Block Copolymer,* J. Am. Chem. Soc. 134 (36) (2012) ..4846-14857.

64 Murakami, M., Nishiki, N., Nakamura, K., Ehara, J., Okada, H., Kouzaki, T., Watanabe, K., Hoshi, T., Yoshimura, S., *High-quality and highly oriented graphite block from polycondensation polymer films*, Carbon 30 (2) (1992) pp255-262.

65 Xiong, Y., Xie, Y., Li, Z., Wu, C., Zhang, R., *A novel approach to carbon hollow spheres and vessels from CCl_4 at low temperatures,* Chem. Comm. 7 (2003) pp904-905.

66 Endo, O., Nakamura, M., Amemiya, K., Ozaki, H., *Graphene nanoribbons formed from n-alkane by thermal dehydrogenation on Au(111) surface*, Surf. Sci., (2015) pp44-47.

67 Ramirez, A. G., Itoh, T., Sinclair, R., *Crystallization of amorphous carbon thin films in the presence of magnetic media,* J. App. Phy 85 (3) (1999) pp1508-1513.

68 Cai, J., Ruffieux, P., Jaafar, R., Bieri, M., Braun, T., Blankenburg, S., Muoth, M., Seitsonen, A.P., Saleh, M., Feng, X., Müllen, K., Fasel, R., *Atomically precise bottom-up fabrication of graphene nanoribbons*, Nature 466 (2010) pp470-473.

69 Zhong, D., Franke, J.-H., Podiyanachari, S.K., Blomker, T., Zhang, H., Kehr, G., Erker, G., Fuchs, H., Chi, L., *Linear Alkane Polymerization on a Gold Surface,* Science 334 (2011) pp213-216.

70 Haghighatpanah, S., Börjesson, A., Amara, H., Bichara, C., Bolton, K., *Computational studies of graphene growth mechanisms,* Phys. Rev. B 85 (2012) 205448

71 Zhao, Y., Nakamura, R., Kamiya, K., Nakanishi, S., Hashimoto, K., *Nitrogen-doped carbon nanomaterials as non-metal electrocatalysts for water oxidation,* Nature Comm. 4 (1) (2013) pp2390.

72 Zabet-Khosousi, A., Zhao, L., Pálová, L., Hybertsen, M. S., Reichman, D. R., Pasupathy, A. N., Flynn, G. W., *Segregation of Sublattice Domains in Nitrogen-Doped Graphene*, J Am. Chem. Soc. 136 (4) (2014) pp1391-1397.

73 Zhao, L., He, R., Rim, K. T., Schiros, T., Kim, K. S., Zhou, H., Gutiérrez, C., Chockalingam, S. P., Arguello, C. J., Pálová, L., Nordlund, D., Hybertsen, M. S., Reichman, D. R., Heinz, T. F., Kim, P., Pinczuk, A., Flynn, G. W., Pasupathy, A. N., *Visualizing Individual Nitrogen Dopants in Monolayer Graphene,* Science 333 (6045) (2011) pp999-1003.

74 Wei, D.; Liu, Y.; Wang, Y.; Zhang, H.; Huang, L.; Yu, G., *Synthesis of N-doped graphene by chemical vapor deposition and its electrical properties*, Nano Lett. 9 (2009) pp1752–1758.

75 Alsawat, M., Altalhi, T., Santos, A., Losic, D., *Facile and controllable route for nitrogen doping of carbon nanotubes composite membranes by catalyst-free chemical vapour deposition*, Carbon 106 (2016) pp295-305.

76 Yang, S., Peng, L., Huang, P., Wang, X., Sun, Y., Cao, C., Song, W., *Nitrogen, Phosphorus, and Sulfur Co-Doped Hollow Carbon Shell as Superior Metal-Free Catalyst for Selective Oxidation of Aromatic Alkanes,* Angew. Chem. *128* (12) (2016) pp4084-4088.

77 Smart, B. E., *Fluorine substituent effects (on bioactivity),* J Fluor. Chem. 109 (1) (2001) pp3-11.

78 Kurczy, M. E., Zhu, J.Z. J., Ivanisevic, J., Schuyler, A. M., et al, *comprehensive bioimaging with fluorinated nanoparticles using breathable liquids,* Nat. Commun. 6 (33) (2015) pp5998.

79 Kim, H. I., Koini, T., Lee, T. R., Perry, S. S., *Systematic Studies of the Frictional Properties of Fluorinated Monolayers with Atomic Force Microscopy: Comparison of CF3- and CH3-Terminated Films,* Langmuir 13 (1997) pp7192-7196.

80 Song, X., Zhai, J., Wang, Y., Jiang, L., *Fabrication of superhydrophobic surfaces by self-assembly and their water-adhesion properties,* J. Phys. Chem. B 109 (2005) pp4048-4052.

81 Shimizu, T. K., Jung, J., Otani, T., Han, Y. K., Kawai, M., Kim, Y., *Two-dimensional superstructure formation of fluorinated fullerenes on Au(1 1 1): A scanning tunnelling microscopy,* ACS Nano 6 (3) (2012) pp2679-2685.

82 Sakamoto, Y., Suzuki, T., Kobayashi, M., Gao, Y., Fukai, Y., Inoue, Y., Sato, F., Tokito, S., *Perfluoropentacene: High-Performance p−n Junctions and Complementary Circuits with Pentacene*, J. Am. Chem. Soc.126 (26) (2004) pp8138–8140.

83 Lu, G. L., Jiang, X. J., Li, Y. J., Lu, X. L., Huang, X. Y., *Synthesis and self-assembly of PMBTFVB-g-PNIPAM fluorine-containing amphiphilic graft copolymer*, RSC Adv. 5 (91) (2015) pp74947-74952.

84 Pervez, H., Ahmad, M., Hadda, T. B., Toupet L., Naseer, M. M., *Synthesis and fluorine-mediated interactions in methanol-encapsulated solid state self-assembly of an isatin-thiazoline hybrid,* J Mol. Struct. 1098 (2015) pp124-129.

85 Bhunia, S. K., Saha, A., Maity, A. R., Ray, S. C., Jana, N. R., *Carbon Nanoparticle-based Fluorescent Bioimaging Probes,* Scientific Reports 3 (2013) pp1473.

86 Taylor, A. J., Granwehr, J., Lesbats, C., Krupa, J., Six, J. S., Pavlovskaya, G. E., Thomas, N. R., Auer, D. P., Meersmann, T., Faas, H. M., *Probe-Specific Procedure to Estimate Sensitivity and Detection Limits for 19F Magnetic Resonance Imaging, Magnetic Resonance Imaging,* PLoS ONE 11 (10) (2016) e0163704.

87 Chung, B. H., Lim, Y. T., Choi, B. S., Han, J. H., (2010) *Perfluorocarbon nano-emulsion containing quantum dot nanoparticles and method for preparing the same, 8734762* United States, Korea Research Institute of Bioscience and Biotechnology (Daejeon, KR).

88 Feynman, R. *There's plenty of room at the bottom* [data storage]. J Microelectromech. Syst. 1 (1) (1992) pp60-66. (Alternatively from http://calteches.library.caltech.edu/1976/1/1960Bottom.pdf)

89 Smetana, A. B., Klabunde, K. J., Sorensen, C. M., *Synthesis of spherical silver nanoparticles by digestive ripening, stabilization with various agents, and their 3-D and 2-D superlattice formation,* J Colloid Interface Sci. 284 (2) (2005) pp521-526.

90 Yaakob, Y., Yusop, M. Z. M., Takahashi, C., Rosmi, M. S., Kalitaa, G., Tanemura, M., *In situ transmission electron microscopy of Ag-incorporated carbon nanofibers: the effect of Ag nanoparticle size on graphene formation*, RSC Advances 8 (5) (2015) pp5647-5651.

91 Jana, N. R., Gearheart, L., Murphy, C. J., *Seeding growth for size control of 5-40 nm diameter gold nanoparticles,* Langmuir 17 (22) (2001) pp6782-6786.

92 Sun, J., Simon, S. L., the melting behaviour of aluminium nanoparticles, Thermochim. Acta. 463 (1-2) (2007) pp32-40.

93 Love, C. J., Estroff, L. A., Kriebel, J. K., Nuzzo, R. G., Whitesides, R. G., *Self-Assembled Monolayers of Thiolates on Metals as a Form of* Nanotechnology, Chem. Rev. 105 (2005) pp1103−1169.

94 Bigioni, T. P., Lin, X.-M., Nguyen, T. T., Corwin, E. I., Witten, T. A., Jaeger, H. M., *Kinetically driven self assembly of highly ordered nanoparticle monolayers,* Nat. Mater. 5 (4) (2006) pp265-270.

95 Battocchio, C., Meneghini, C., Fratoddi, I., Venditti, I., Russo, M., Aquilanti, G., Maurizio, C., Federica, B., Matassa, R., Rossi, M., Settimio, M., Polzonetti, G., *Silver Nanoparticles Stabilized with Thiols: A Close Look at the Local Chemistry and Chemical Structure,* J Phys. Chem. C, 116 (36) (2012) pp19571-19578.

96 Stewart, A., Zheng, S., Mccourt, M., Bell, S., *Controlling assembly of mixed thiol monolayers on silver nanoparticles to tune their surface properties,* ACS Nano 6 (5) (2012) pp3718-26.

97 Shah, P. S., Holmes, J. D., Doty, C. R., Johnston, K. P., Korgel, B. A., *Steric Stabilization of Nanocrystals in Supercritical CO 2 Using Fluorinated Ligands*, J. Am. Chem. Soc. 122 (2000) pp4145-4246.

98 Yonezawa, T., Onoue, S., Kimizuka, N., *Formation of Uniform Fluorinated Gold Nanoparticles and Their Highly Ordered Hexagonally Packed Monolayer*, Langmuir 17 (8) (2001) pp2291–2293.

99 Irvani, S., Korbekandi, H., Mirmohammadi, S. V., Zolfaghari, B., *Synthesis of silver nanoparticles: chemical, physical and biological methods,* Res. Pharm. Sci. 9 (6) (2014) pp385-406.

100 Scheibel, H. G., Porstendo¨rfer, J. *Generation of monodisperse Ag- and NaCl-aerosols with particle diameters between 2 and 300 nm,* J Aerosol Sci. 14 (2) (1983) pp113-126.

101 Jung J, Oh H, Noh H, Ji J, Kim S. *Metal nanoparticle generation using a small ceramic heater with a local heating area,* J Aerosol Sci. 37 (2006) pp1662–1670.

102 Procházka, M., *Probing applications of laser-ablated Ag colloids in SERS spectroscopy: Improvement of ablation procedure and SERS spectral testing,* Analytical Chem. 69 (24) (1997) pp5103-5108.

103 Tsuji, T., Kakita, T., Tsuji, M., *Preparation of nano-size particles of silver with femtosecond laser ablation in water,* Applied Surf. Sci. 206 (1–4) (2003) pp314-320.

104 Tien, D-C., Tseng, K-H., Liao, C-Y., Huang, J-C., Tsung, T. T., *Discovery of ionic silver in silver nanoparticle suspension fabricated by arc discharge method,* J Alloys and Compounds. 463 (2008) pp408–411.

105 Siegel, J., Ondřej, K., Pavel, U., Kolská, Z., Slepička, P., Švorčík, V., *Progressive approach for metal nanoparticle synthesis,* Materials Letters 89 (2012) pp47–50.

106 Klaus, T., Joerger, R., Olsson, E., Granqvist, C. G., *Silver-based crystalline nanoparticles, microbially fabricated,* Proc Natl Acad Sci U S A. 96 (24) (1999) pp13611-4.

107 Ahmad, A., Senapati, S., Khan, M. I., Kumar, R., Ramani, R., Srinivas, V., et al. *Intracellular synthesis of gold nanoparticles by a novel alkalotolerant actinomycete, Rhodococcus species,* Nanotechnology, 14 (2003) pp824–828.

108 Iravani, S., *Green synthesis of metal nanoparticles using plants,* Green Chem. 13 (2011) pp2638–2650.

109 An, J., Luo, Q., Li, M., Wang, D., Li, X., Yin, R., *A facile synthesis of high antibacterial polymer nanocomposite containing uniformly dispersed silver nanoparticles,* Colloid Polym. Sci. 293 (7) (2015) pp1997-2008.

110 Chen, J., Wang, J., C., Zhang, X., Jin, Y., *Microwave-assisted green synthesis of silver nanoparticles by carboxymethyl cellulose sodium and silver nitrate,* Mater. Chem. Phys. 108 (2) (2008) pp421-424.

111 Shweta, V., Tirumala, R. B., Srivastava, A. P., Srivastava, D., Kaul, R., Singh, B., *A facile synthesis of broad plasmon wavelength tunable silver nanoparticles in citrate aqueous solutions by laser ablation and light irradiation,* Colloids Surf. A: Physicochemical Eng. Asp. 527 (2017) pp23-33.

112 Dehghani, Z., Vejdani-Noghreiyan, A., Nadafan, M., Majles Ara, M. H., *The effect of different doses of γ –ray irradiation on the third order nonlinear optical properties, molecular structure and mass attenuation coefficients of synthesized colloidal silver nanoparticles,* Physica E: Low Dimens. Syst. Nanostruct. 103 (2018) pp423-429.

113 Maretti, L., Billone, P., Liu, Y., Scaiano, J., *Facile photochemical synthesis and characterization of highly fluorescent silver nanoparticles,* J Am. Chem. Soc. 131 (39) (2009) pp13972-80.

114 Treshchalov, A., Erikson, H., Puust, L., Tsarenko, S., Saar, R., Vanetsev, A., Tammeveski, K., Sildos, I., *Stabilizer-free silver nanoparticles as efficient catalysts for electrochemical reduction of oxygen,* J Colloid Interf. Sci. 491 (2017) pp358-366.

115 Nasretdinova, G., Fazleeva, R., Osin, Y., Gubaidullin, N., Yanilkin, A., *Methylviologen-mediated electrochemical synthesis of silver nanoparticles via the reduction of AgCl nanospheres stabilized by cetyltrimethylammonium chloride,* Russ. J. Electrochem. 53 (1) (2017) pp25-38. Gomes, J., Garcia, A., Ferreira, E., Pires, C.,

116 Oliveira, V., Tremiliosi-Filho, G., Gasparotto, L., *New insights into the formation mechanism of Ag, Au and AgAu nanoparticles in aqueous alkaline media: Alkoxides from alcohols, aldehydes and ketones as universal reducing agents,* Phys. Chem. Chem. Phys. 17 (33) (2015) pp21683-21693.

117 Krutyakov, Y. A., Kudrinskiy, A. A., Olenin A. Y., Lisichkin, G. V., *Synthesis and properties of silver nanoparticles: advances and prospects,* Russ. Chem. Rev. 77 (3) (2008) pp233-257

118 Kang, S. Y. and K. Kim *Comparative study of dodecanethiol-derivatized silver nanoparticles prepared in one-phase and two-phase systems,* Langmuir 14 (1) (1998) pp226-230.

119 Bastus, N. G., Comenge, J., Puntes, V., *Kinetically Controlled Seeded Growth Synthesis of Citrate-Stabilized Gold Nanoparticles of up to 200 nm: Size Focusing versus Ostwald Ripening,* Langmuir 27 (17) (2011) pp11098-11105.

3.0 Experimental methodology and materials

This Chapter describes the processing steps and instrumentation used for the investigation of hollow carbon nanoshells (HCNS) from thiol stabilised AgNP. The Chapter is divided into two parts; *i.e.* processing steps and instrumentation. The processing section is concerned with the chemical synthesis of AgNP starting materials; the deposition of AgNP onto suitable supports; and the thermal processing of AgNP to form HCNS. The instrumentation section outlines the characterisation techniques used to investigate the starting materials and resultant products.

3.1 Methodology overview

Conceptually, HCNS may be formed from a single-step thermal procedure, starting with a hard spherical template encapsulated by carbon, in the form of aliphatic chain molecules, which cross-link and undergo graphitisation prior to template removal (Figure 3.1).

Figure 3.1. Schematic representation of the transformation of AgNP, to HCNS-AgNP, to HCNS via heat-treatment. Thiol molecules stabilises the surface of AgNP prior to graphitisation, and subsequent removal of the Ag template.

Accordingly, the synthesis of starting AgNP materials, their deposition onto appropriate supports, and their thermal processing under vacuum (either *in situ* within

a TEM, or *ex situ* within a furnace) is described initially. The experimental design was concerned primarily with the effects of thermal processing conditions, with emphasis on temperature and rate of heating, along with the possible role of different support materials, on the development of the HCNS product. Consideration is then given to the prospects for including other species into the HCNS product via the incorporation of heteroatoms of N or F into the thiol, prior to AgNP transformation. The overall approach to experimentation, linking in to the presentation of Results (Chapters 4 – 6), is depicted by Figure 3.2.

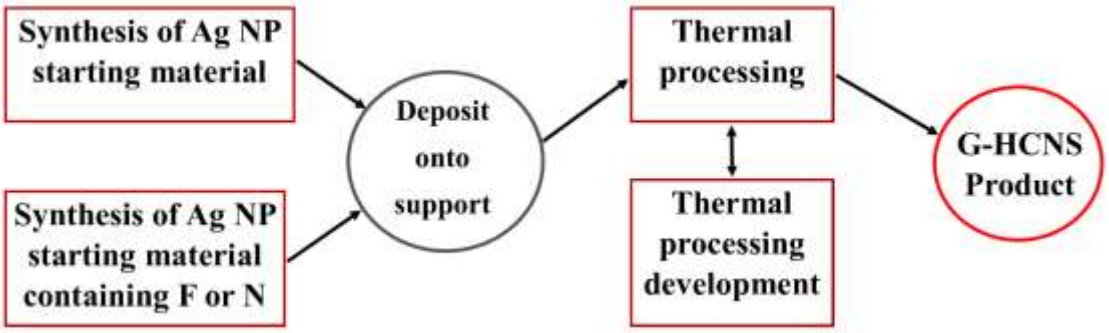

Figure 3.2 Overview of the approach to produce graphitised HCNS (G-HCNS) via thermal processing of AgNP on various supports. The formation of G-HCNS from AgNP is detailed in Chapter 4. Chapter 5 reports on the effect of thermal processing conditions on the development of the product. Chapter 6 is concerned with the prospects for incorporating heteroatoms of N or F into the product.

3.2 G-HCNS production

This section details (i) the synthesis of AgNP, and modified AgNP to include nitrogen or fluorine in the thiol layer; (ii) the procedures to deposit AgNP onto suitable support materials; and (iii) the thermal processing conditions, for both *in situ* and *ex situ* experiments.

3.2.1 Chemical synthesis of thiol stabilised AgNP

AgNP stabilised with 1-dodecanethiol (DDM) were synthesised via a modified Brust-Schiffrin reduction [1] as follows: to a solution of silver nitrate (0.3 mmol / 30 mL ethanol), DDM (0.37 mmol / 100 uL) was added slowly with vigorous stirring for 15 minutes. This was followed by dropwise addition of excess sodium borohydride (saturated / 60 mL ethanol) and the solution stirred vigorously for 2 h. After addition of 250 mL ethanol and refrigeration for 20 h, the thiol stabilised AgNP (TS-AgNP) product was isolated by vacuum filtration using a 0.2 μm PTFE membrane, washed with 10 mL toluene, followed by washing with 200 mL acetone and drying under vacuum for 16 h (Figure 3.3). Syntheses were repeated to check the reproducibility of the method with DDM and 1-octanethiol (OM, 0.37 mmol / 64 uL). All reagents were used as purchased from Sigma Aldrich without further purification and syntheses were performed at room temperature (RT) using standard glassware and laboratory equipment.

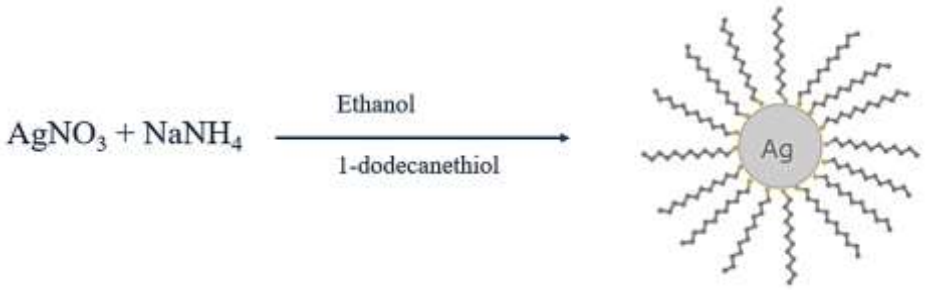

Figure 3.3. Depiction of the chemical reaction to synthesise AgNP stabilised with 1-dodecanethiol (TS-AgNP), as starting material for the production of HCNS.

For the synthesis of AgNP containing fluorine or varying amounts of nitrogen, the thiols 3,3,4,4,5,5,6,6,7,7,8,8,9,9,10,10,10-heptadecafluoro-1-decanethiol (HFT), or 11-(1H-pyrrol-1-yl) undecane thiol (PUT), were added with DDM, using the synthetic route described above, whilst adjusting relative amounts to maintain the total overall thiol molarity. In the case of fluorinated thiol, the AgNP product was isolated after removal of ethanol by rotary evaporation, suspension of AgNP in acetone (~ 40 mL) and vacuum filtration (0.2 μm PTFE membrane), followed by washing with toluene (20 mL), then acetone (20 mL), and drying under vacuum for 16 h.

The syntheses performed provided a range of AgNP starting materials, containing various thiols, with the inclusion of fluorine (F-AgNP) or varying amounts of nitrogen (N-AgNP) in the amounts indicated in Table 3.1, as utilised for HCNS production via thermal processing. Heteroatom percentages were calculated as molar percentage in the NP stabilising layer using Equation 3.1.

$$X\% = \frac{m(X)}{m(thiol)} \; x \; \frac{100}{1}\%$$

Equation 3.1. Heteroatom molar percentage, where X represents the heteroatom, m(X) and m(thiol) are the molecular mass of the heteroatom and thiol molecule respectively.

Table 3.1. AgNP starting materials synthesised from different thiol mixtures, with heteroatom amounts given as a percentage of the stabilising layer, excluding the AgNP core.

Sample name	Stabilising layer / %	Thiol / %			
		DDM	PUT	HFT	OM
F-AgNP	**F 47.3**	50	0	50	0
TS-AgNP	**none**	100	0	0	0
N2-AgNP	**N 1.6**	75	25	0	0
N3-AgNP	**N 3.1**	50	50	0	0
N4-AgNP	**N 4.4**	25	75	0	0
N5-AgNP	**N 5.5**	0	100	0	0
TS-AgNP	**none**	0	0	0	100

HFT = 3,3,4,4,5,5,6,6,7,7,8,8,9,9,10,10,10-heptadecafluoro-1-decanethiol;
DDM = 1-dodecanethiol;
PUT = 11-(1H-pyrrol-1-yl) undecane-1-thiol, ($C_{15}H_{27}NS$);
OM = 1-octanethiol.

3.2.2 Deposition of thiol stabilised AgNP onto support materials for characterisation and/or thermal processing

AgNP were deposited on support materials to facilitate the characterisation of starting materials by transmission electron microscopy (TEM), and associated spectroscopy, and for both *in situ* and *ex situ* heating experiments to form HCNS products.

Typically, samples for TEM were prepared by suspension of TS-AgNP (0.5 mg / mL solvent), drop casting onto a TEM grid, commonly consisting of a 3 mm diameter metal grid overlaid with an electron transparent carbon film, with drying at room temperature (RT). Details are provided with appropriate results. Preparation artefacts, observed by TEM, arising from deposition process [2], were investigated by varying deposition conditions of TS-AgNP to consider the effects of sonication [3], and the addition of surfactant DDM molecules to TS-AgNP solutions[4,5], Table 3.2.

Table 3.2 TEM sample (TS-AgNP) deposition details to investigate the effects of sonication and addition of surfactant molecules on TEM observations.

Solution concentration /mg/ 1ml	**Solvent**	**Sonication**	**Addition of DDM surfactant**
0.5	hexane	N	N
0.5	hexane	0 – 30s	N
0.5	chloroform	N	N
0.5	chloroform	5 min	N
0.5	cyclohexane	N	N
0.5	cyclohexane	N	30 %

DDM = 1-dodecanethiol.

Thiol stabilised AgNP starting materials containing F or N required modified sample deposition conditions due to changes in dispersion characteristics, details are provided, Table 3.3.

Table 3.3. AgNP starting materials, synthesised from different thiol mixtures (heteroatom amounts given as a percentage of the stabilising layer, excluding the AgNP core) with summary of the dispersion conditions onto TEM supports (which was altered by the addition of F and varying amounts of N).

Sample name	Stabilising layer / %	Dispersion conditions			
		Solvent	Sonication	Support	Drops cast
F-AgNP	F 47.3	hexane*[a]	N	GO/Cu	1
F-AgNP	F 47.3	ethanol	N	Si_3N_4	5
F-AgNP	F 47.3	cyclohexane*[b]	5 min	C/Cu	5
N2-AgNP	N 1.6	cyclohexane	N	GO/Cu	5
N2-AgNP	N 1.6	chloroform	N	GO/Cu	5
N2-AgNP	N 1.6	toluene*[b]	Y	Si_3N_4	5
N3-AgNP	N 3.1	cyclohexane	N	C/Cu	5
N3-AgNP	N 3.1	toluene*[b]	Y	Si_3N_4	1
N3-AgNP	N 3.1	cyclohexane**[c]	N	GO/Cu	5
N4-AgNP	N 4.4	acetone	N	Si_3N_4	1
N5-AgNP	N 5.5	cyclohexane*[b]	Y	GO/Cu	5
N5-AgNP	N 5.5	chloroform	N	Si_3N_4	1
TS-AgNP	none	chloroform	N	Si_3N_4	5
TS-AgNP	none	hexane	N	C/Cu	5

**[a]F-AgNP did not dissolve, but were suspended by fluid agitation, with immediate drop casting; *[b]Sonication required due to sample insolubilities in these solvents;*
[c] ~ 1 % DDM added, solution filtered.

Samples of TS-AgNP required deposition onto appropriate supports for both *in situ* and *ex situ* thermal processing. TEM experiments *in situ* required supports capable of withstanding heating to 850°C *in vacuo*, whilst also enabling spectroscopic analyses without contributing to the sample signals. Accordingly, TEM grids comprising graphene oxide film supports on Cu grids (EM Resolutions) or MEMS-based

EMheaterchip^{TM} (Si_3N_4 support film; DENSolutions (Figure 3.4), were used as purchased. Alternatively, Mo grids with boron nitride (BN) supports, or Cu or Au grids with graphene or BN-flake supports, deposited in-house [6], were used as supports for thermal processing. Table 3.4.

Figure 3.4 TEM supports: a), Cu grid (3 mm diameter); and b) Si_3N_4 DENSolutions heating chip (width 3 mm).

For the case of *ex situ* thermal processing, TS-AgNP samples were supported on GO/Cu TEM grids, or on multi-walled carbon nanotubes (MW-CNT). In the latter case, these were prepared by mixing TS-AgNP (3.6 mg in 1.5 ml cyclohexane) with MW-CNT (3.9 mg; Nanothinx S. A.), with brief sonication required for adhesion of AgNP to MWCNT, followed by shaking for 15 minutes. After filtration (0.2 μm PTFE membrane) and washing with cyclohexane, ethanol and acetone (10 mL), the resultant solid (AgNP@CNT) was dried for 16 h.

Table 3.4 Thermal processing support materials for *in situ* experiments consisted of TEM grids coated with supports, deposited in-house [6] or commercially available.

Source	TEM grid material	Supplier	Support film	Supplier	Temperature limit, °C
Deposited in-house	Au	Agar Scientific	FLG	Graphene supermarket	1064[*1]
	Au	Agar Scientific	BN	Graphene supermarket	1064
	Mo	Agar Scientific	FLG	Graphene supermarket	1300[*2]
	Mo	Agar Scientific	BN	Graphene supermarket	unknown
Proprietary	Cu	EMResolution	GO	-	850
	Si_3N_4	DENSolutions	N/A	-	1300

*FLG = few layered graphene, GO = graphene oxide. *1 [7], *2 [8]*

3.2.3 Thermal processing of TS-AgNP to form G-HCNS

TS-AgNP deposited onto various supports were thermally processed, *in situ* and *ex situ*, to produce G-HCNS, with experimental parameters being modified to appraise the process – structure interrelationship. *In situ* TEM experiments were designed to investigate the effects of rate of heating and choice of support materials, whilst *ex situ* heating investigations provided for thermal processing in the absence of the imaging electron beam. Figure 3.5 provides an overview of parameters modified, with details in Results chapters.

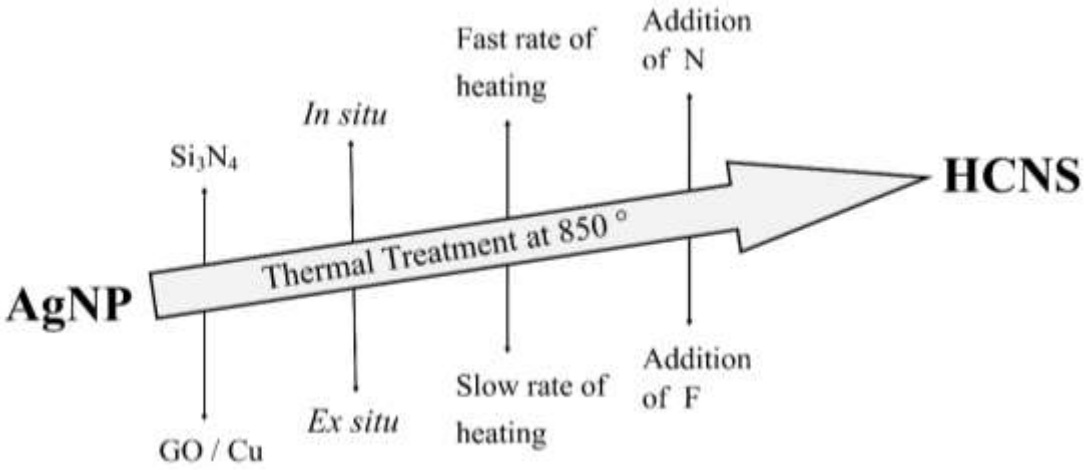

Figure 3.5 Parameters changed to investigate the effects of support material, heating method, heating rate and addition of heteroatoms to AgNP starting materials processing on HCNS structures formed from thermal processing TS-AgNP at 850 °C.

The effects of different support materials on G-HCNS formation was probed using a furnace type holder (Gatan 652 double tilt) and hot stage controller unit (SmartSet 901), allowing thermal processing of samples deposited onto BN or graphene flakes, on Au or Mo grids, or GO/Cu TEM grids, Table 3.6. Heating programmes involved a temperature increase from ambient to a fixed value (typically 850°C, at ~ 14°C/s or ~ 18°C/s), then a hold time followed by a fast cool down period to ambient (Figure 3.6), details are outlined in Table 3.5 and presented with appropriate results.

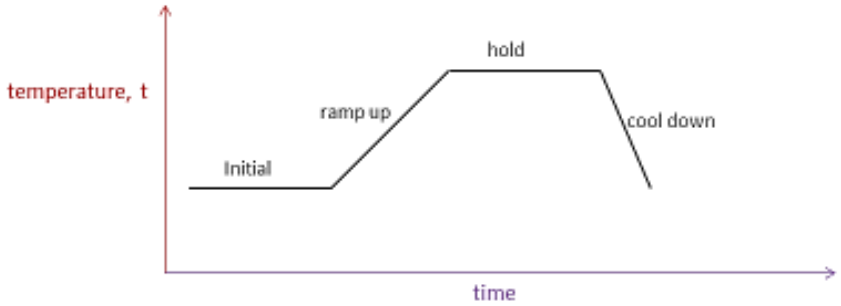

Figure 3.6 Representation of temperature profile for *in situ* thermal processing of TS-AgNP with a Gatan heating system. In this example, temperature is increased from an initial ambient temperature of 21 °C to 850 °C (at 14°C/s), with a hold time (45 min) at 850 °C, followed by cool down to ambient within 2 min.

Thermal processing TS-AgNP *in situ*, in the presence and absence of an electron beam was investigated by blanking the beam prior to commencement of heating.

Table 3.5 Overview of parameters to investigate the effect of heating rate on HCNS formation.

Support	Heating system	Heating rate / °C.s^{-1}	Initial temp / °C	Final temp / °C	Hold time / minutes
FLG / Mo	Gatan *in situ*	**~ 14**	23	850	-
GO / Cu	Gatan *in situ*	**~ 18**	23	750	-
			750	850	~ 20
GO / Cu	Gatan *ex situ*	**~ 14**	23	850	5
MWCNT	muffle furnace	**~ 20**	20	850*	180
Si_3N_4	MEMS	**92**	23	850	-
Si_3N_4	MEMS	**1.5**	23	650	-
		2	650	900	-

**Pre-set furnace temperature, hence ramp rate was estimated.*
FLG = few layered graphene flakes, GO = Graphene oxide flakes.

Further *ex situ* heating experiments on TS-AgNP deposited onto CNT enabled images of G-HCNS to be obtained free from supports, where these formed on CNT edges in appropriate orientations, and were performed on three AgNP samples as follows: the TS-AgNP@CNT (3 mg) was sealed inside a quartz ampoule under vacuum (10^{-5} mbar) (figure 3.7), and placed inside a pre-heated furnace at 850°C for 180 minutes (Nabertherm GmbH P330 muffle furnace), before cooling naturally, outside the furnace to room temperature.

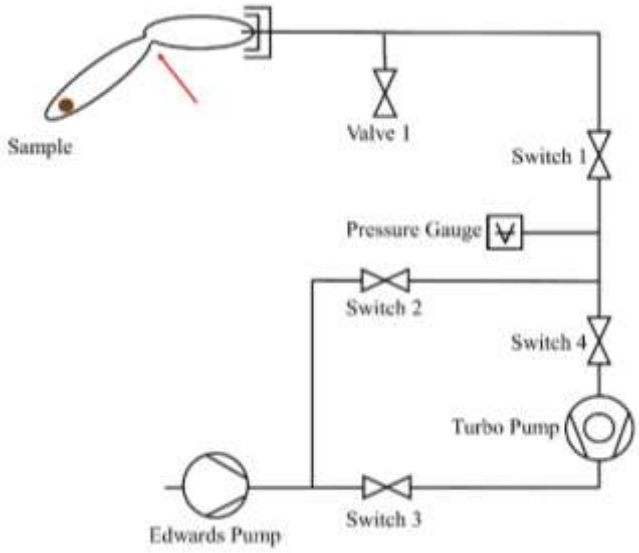

Figure 3.7 Experimental setup of the system for evacuation of ampoules, which were then sealed (indicated by the arrow) prior to removal.

To elucidate the effect of heating rate on the formation of G-HCNS structures *in situ*, two different Micro-Electro-Mechanical Systems (MEMS) heating protocols, with a based heating holder (DENSolutions; SH30), control box (DENS-E-03-00 Digiheater) and software (Wildfire Digiheater 3.0), were developed. Firstly, rapid heating from 23°C to 850°C (at 92°C/s), followed by a hold time of 80 minutes, then cool down to 23°C within 30 s (TP-1). Secondly, slow heating from 23°C to 650°C (at 1.5°C/s), followed by a hold time of 2 minutes, then slow heating to 900°C (at 2°C/s) and a further hold time of 15 minutes, followed by cool down to 23°C within 30 s (TP-2). Further, *in situ* and *ex situ* heating experiments (GO/Cu, Gatan) at intermediate heating rates were performed, Table 3.5.

Investigating the effect of temperature on AgNP template removal was achieved via *in situ* experiments of TS-AgNP (Si_3N_4 MEMS) with rapid heating from room

temperature (20°C) to 650 °C (at 92°C/s), then a hold time of 3 1/2 min, followed by further step-wise heating, and lastly cool down to room temperature within 30 s.

To produce HCNS doped with heteroatoms, the five different AgNP starting materials detailed in section 3.2.1, Figure 3.3, were thermally processed using the MEMS rapid heating protocol (TP-1) previously described, or heated ex situ on MWCNT, outlined in Table 3.5.

3.3 Materials characterisation

This section describes techniques and specifies equipment, methods and sample handling to enable characterisation of AgNP and HCNS. No single characterisation technique can provide detailed, unambiguous information regarding all aspects of these nanomaterials. A more robust approach is to draw together pieces of evidence from individual techniques and use these to form a unified picture of the whole, Table 3.6 summarises advantages, limitations and information content of the techniques applied.

By way of example, for TS-AgNP starting materials, thiol stabilising layer structure may be probed by infrared (IR), and nuclear magnetic resonance (NMR), and together these provide a compelling case for an organic molecules' structure, but neither of these techniques yield information regarding the nanoparticle core. In contrast, X-ray diffraction (XRD) selectively collects data from the metallic nanoparticle core, as the randomly-orientated organic molecules will not contribute to peaks. Information from all three techniques is thus required for the structural determination of nanoparticles,

however, neither IR, NMR, nor XRD will provide nanoparticle size data. For evaluating TS-AgNP size and size distribution, further techniques need to be adopted and several options are available; UV/visible light spectroscopy is the fastest and cheapest, but only provides a broad guide to size distribution; while dynamic light scattering (DLS), tends to overestimate the number of larger particles and nanoparticle sizes include the hydration layer; finally, transmission electron microscopy (TEM), provides exquisite detail with sub-nanometre resolution, but over a very small field of view from a specimen of the sample, which may not be representative, and results may be affected by sample handling protocols. By comparing nanoparticle size and size distribution data from bulk techniques (UV, DLS) to those from TEM we attain greater confidence in the accuracy of results. A complete, robust characterisation of TS-AgNP therefore requires a combination of these six complementary techniques.

Table 3.6 Characterisation techniques, summarising advantages, limitations and information content obtained.

Technique	Advantages	Limitations	Information content
UV/Visible spectroscopy	Fast, easy to use. Non-destructive	Samples require dissolution.	Presence of surface plasmon resonance (SPR) indicative of NP.
Fourier transform infrared spectroscopy (FTIR)	For solid, liquid or gas samples. Simple, reliable, widely used. Non-destructive.	The FT function may affect the results. FTIR instruments use a single beam, changes in CO_2 or water concentration in the instrument chamber may affect results.	Structural information, functional groups present give characteristic bands. Fingerprint region diagnostic of molecules.
Nuclear magnetic resonance spectroscopy	Fast, non-destructive, variety of experiments possible.	Low sensitivity.	Detailed molecular structure of NP stabilising layer.
Dynamic light scattering	Fast, large particle size measurement range. Non-destructive.	Not selective to NP, low resolution. Models tend to over-estimate larger particle contribution.	Particle size information in solution. Estimates of polydispersity.
Transmission electron microscopy (TEM)	Variety of information content available. Very high resolution.	Small specimen from sample imaged, representative of the 'population'? Images are 2D projections of 3D samples in a vacuum. Preparation artefacts may arise.	Images of specimens, size, shape. For crystal samples, diffraction patterns, d spacing. Graphitic lattice distances.
Electron energy-loss spectroscopy (EELS)	High spatial resolution, complementary to TEM images.	Care required during experimental set-up and data interpretation to avoid artefacts; background subtraction required. Peak overlaps. Small specimen from sample, representative? Samples require preparation, and are in vacuum.	Elements present, and element ratios, electronic state. Potential to determine elemental concentration (via edge intensities) and plasmon energy.
Energy dispersive spectroscopy (EDS)	Fast, high spatial resolution, elemental mapping possible. Complementary to TEM images.	Peaks may overlap. Cannot detect light elements. Based on modelling, which requires checking for best fit. Samples require preparation, and are in vacuum.	Element identification and semi-quantitative composition, at% or wt%.
X-ray diffraction	Non-destructive. Comparison with a standard allows identification.	Samples must be crystalline powdered solids, has a lower detection limit.	Crystal state, including d-spacing and composition, crystallite size.
Raman spectroscopy	Does not require sample preparation.	Low sensitivity, background fluorescence may mask signals.	Chemical composition, bonding state. Diagnostic of molecular structure.

X-ray Photon Spectroscopy	Good sensitivity, spatial resolution.	Samples in vacuum, results may require expert analysis. Charging effects may confound data interpretation.	Chemical composition, oxidation state and chemical environment at the sample surface.
Thin Layer Chromatography	Simple, quick.	Requires optimising solvent mixtures for effective separation.	Separation technique, e.g. for detection of free thiol molecules that may be associate with AgNP.

Theory and details of techniques follow, beginning with those most applicable to TS-AgNP starting materials, focusing on TEM and associated spectroscopies and finishing with techniques used to characterise G-HCNS products on support media.

3.3.1. Ultraviolet-visible spectroscopy

Ultraviolet-visible spectroscopy (UV/Vis) provides a quick method to evaluate AgNP synthesis, as the presence of a peak due to surface plasmon resonance (SPR) is indicative of nanoparticles, the wavelength of which is dependent on the particle size and shape [9], with narrow peaks indicating narrow size distribution.

UV/Vis measures the attenuation of a beam of light passing through a sample in solution, with electromagnetic energy in this frequency range corresponding to the SPR of nanosized particles, and with electron energy transitions between bonding (lower energy) and anti-bonding (higher energy) molecular orbitals.

In more detail, plasmon resonance results from interactions between conduction electrons at the nanoparticle surface and incoming electromagnetic radiation, and will only occur if the nanoparticle is capable of forming a dipole *and* the size of the nanoparticle is much smaller than the wavelength of incoming electromagnetic radiation, Figure 3.8.

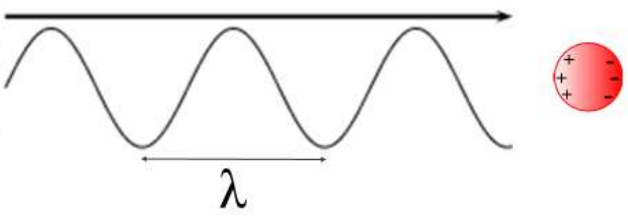

Figure 3.8 Interaction of a nanoparticle with an electromagnetic wave. An incident electromagnetic wave creates an imbalance in nanoparticle surface electron density. Collective oscillation of the nanoparticle surface electron density, coupled to the electromagnetic wave gives rise to surface plasmon resonance.

When particle sizes are equal to or less than the wavelength of incoming electromagnetic radiation, the near side of the particle surface effectively experiences a single phase of incoming radiation - leading to electrons at this physical location migrating to the opposite surface. This movement of electrons increases electron density at the opposite side of the nanoparticle and creates positive ion density at the near side. The resulting charge separation induces an electric field, which acts on the electrons and moves them back toward their original locations, thus the electrons will oscillate around a central point as this process repeats. Because the incoming light and nanoparticle electron density both oscillate, resonance leads to an amplitude increase.

UV/Vis spectroscopy was performed using a Perkin-Elmer Lambda 25 UV-vis spectrophotometer; at a scan rate of 240 nm min^{-1} over the range 220 - 900 nm. Samples were dissolved in cyclohexane, or ethanol in the case of fluorinated AgNP, (1mg mL^{-1}) and filtered prior to data collection.

3.3.2. Dynamic light scattering

Information content yielded with dynamic light scattering (DLS), includes AgNP particle size which includes hydration layer, and size distribution in solution, however nanoparticles are known to aggregate when solvated [10].

In dynamic light scattering monochromatic light is passed through a sample in solution and the resulting constructive and destructive interference patterns are measured as a function of time. From these measurements the velocity of Brownian motion of particles in suspension can be determined, and application of the Stokes-Einstein relationship may be used to predict particle size.

Dynamic and phase analysis light scattering was performed using a Malvern Instruments Nano-ZS Zetasizer (660 nm laser). Samples were dissolved in cyclohexane (1mg mL^{-1}) and filtered (PTFE membrane, 0.2 μm pore size) to remove impurities prior to collection of data.

3.3.3. X-ray powder diffraction

X-ray powder diffraction (XRD) provides information on solid crystalline samples, including d-spacing, crystallite size, crystal state, and composition. Comparison with a standard database may also allow unambiguous identification.

XRD is a technique whereby an X-ray beam, of known frequency, is used to probe the internal structure of crystals in powdered solid samples. The regularly spaced atoms in crystalline samples may be conceptually considered as a 3D diffraction grating, with interactions between the beam and sample producing destructive and constructive interference leading to signals only when Bragg conditions are met

(figure 3.9). Spectra are obtained by scanning and collecting data through a wide range of angles which enables all lattice planes to be detected, as samples are assumed to be randomly orientated.

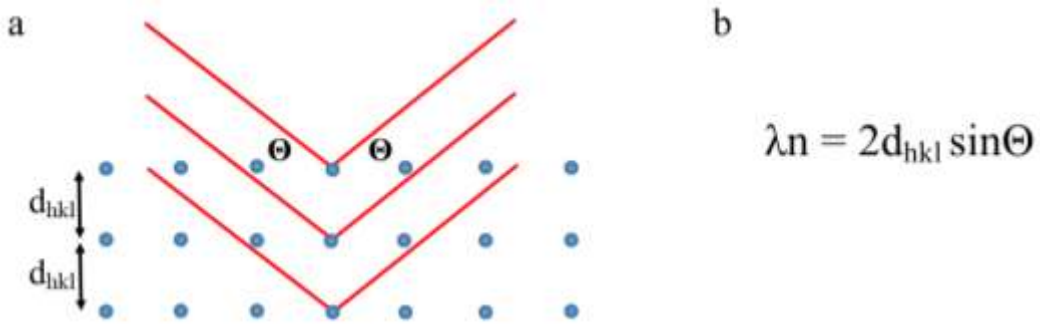

Figure 3.9 Crystalline samples having atoms in parallel planes, (blue lines), with distance d_{hkl} between planes, X-rays (red arrows) will produce diffraction peaks at values of 2Θ, a), when Bragg's law conditions, b), are satisfied.

Spectra are plotted as 2Θ (scattering angle) against signal intensity, with application of Bragg's law enabling d-spacings to be determined from the peak positions, since these are unique to each material, XRD enables identification. Peak widths provide information regarding crystallite size, via application of the Scherrer equation, Equation 3.2, however, contributions to peak widths due to instrument broadening should be removed. It should be noted that crystallite size may differ from particle size, as individual particles may be composed of more than one crystallite.

$$crystallite\ size, t\ = \frac{k.\lambda}{B * Cos\theta B}$$

Equation 3.2 The Scherrer equation, k, θB and B are the crystallite shape constant, Bragg angle of the peak and full width at half maximum (FWHM), respectively.

A value of 0.9 [11] was assumed for the crystallite shape constant, k, and instrument broadening, (0.12 2θ) was calculated from experimental data from a LaB6 standard, assuming a Gaussian peak shape.

X-ray powder diffraction was carried out on a D8 Bruker Advance, Cu-Kα operating at 40kV, 35mA, ($\lambda = 0.15406$ nm), parallel beam geometry with a scintillation counter and x-ray detector, θ and FWHM values were obtained using EVA version 10.0.1.0 software, samples were deposited onto a zero-background Si wafer.

3.3.4 Fourier transform infrared spectroscopy

Fourier transform infrared spectroscopy (FTIR) provides functional group assignment of the molecules in the TS-AgNP stabilising layer, with comparison to a standard providing structural confirmation.

IR measures the vibrational stretching or bending energy of chemical bonds, induced by infrared radiation, and molecules will be infrared active if they possess a dipole, with the intensity of absorption depending on the change of dipole moment during vibration. FTIR measures interferograms, which require a Fourier transformation to produce spectra, but this function may produce artefacts.

FTIR spectrophotometry was performed using a Bruker Tensor 27 or a Bruker Alpha. Approximately 0.5 mg of solid sample was ground with 100 mg KBr and pressed to form a disc.

3.3.5. Nuclear magnetic resonance spectrometry

For TS-AgNP, nuclear magnetic resonance spectroscopy (NMR) allows structural determination and confirmation of the thiol molecules present, but does not yield direct information regarding the Ag core.

NMR involves placing samples in a strong magnetic field, and subjecting them to radiofrequency pulses; the energies emitted provide exquisite diagnostic information of molecular structure. In brief, nuclei with a spin quantum number (s) not equal to zero, placed in a strong external magnetic field ($_{B0}$), have available energy states corresponding to alignment of nuclei with (spin down) or against (spin up) the field (Figure 3.10), the case for ^{1}H, ^{13}C and ^{19}F, where s =½.

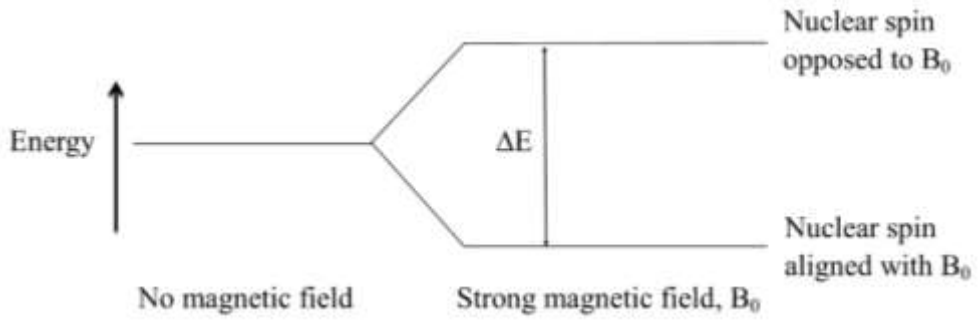

Figure 3.10 Energy states of nuclei with spin quantum number ½, in the presence or absence of a strong external magnetic field, ΔE corresponding to radiofrequency radiation dependent on the strength of B_0 and individual nuclear environments.

The small energy difference (ΔE) in states may be supplied by radiofrequency (RF) pulses, which 'flip' nuclei away from alignment with B_0. The excited, higher energy nuclei return to the lower energy state by a process known as relaxation, giving rise to a time based free induction decay which contains those frequencies attributable to nuclei returning to the lower energy state. Using Fourier transformation, frequency

based information is obtained that, when plotted against signal intensity, produces the NMR spectrum, frequency is expressed in the dimensionless units of parts per million.

Each nucleus in a molecule is usually in a unique magnetic environment and has a slightly different resonance frequency, known as the chemical shift and measured relative to a reference material. This arises because nuclei in molecules are bonded to other atoms through electrons which have a negative charge and, since they are moving, produce small secondary magnetic fields. These influence the local magnetic field around the nucleus, subtly modifying the externally applied magnetic field experienced by the nucleus, a process known as shielding, which changes the RF wavelength absorbed by individual nuclei. In addition, peaks in an NMR spectrum are often split into two, or more, lower intensity peaks, due to coupling between magnetically different nuclei. Coupling occurs through bonding electrons between nuclei and depends on the magnetic moments of the nuclei involved, with splitting patterns in addition to chemical shift enabling molecular structure determination.

In the case of TS-AgNP in solution, thiol nuclei bonded to or neighbouring, the solid Ag core will exhibit relaxation times similar to solid samples, and will not be visible in the NMR experiment, while nuclei at the thiol chain ends, which are more able to tumble in solution will be visible.

A Bruker AV(III) 500 MHz or DPX 400 MHz Nuclear Magnetic Resonance spectrometer was used to acquire data, samples were dissolved in $CDCl_3$ (2 mg / 4.0 ml) and filtered prior to data collection.

3.3.6 Thin layer chromatography

Thin layer chromatography (TLC) is a simple separation and identification technique for non-volatile mixtures. A sheet of aluminium foil (or glass or plastic), coated with a thin layer of silica gel, has samples deposited near to one end. The sheet is then placed into a solvent which is drawn up the plate by capillary action, the sample will move with the solvent at a rate that depends on solubility and the attraction of the sample to the silica gel.

TLC was performed by placing a small spot of TS-AGNP, stabilised with DDM and PUT, in cyclohexane, and placing spots of DDM and PUT in adjacent positions, 0.5 cm from one end of a TLC plate, using a glass capillary. After drying, the plate was placed into a beaker containing a small amount of solvent and covered with a watch glass, the plate being removed when the solvent was 1 cm from the top edge of the plate. The solvent front and positions of DDM, PUT and TS-AgNP were marked in pencil.

3.3.7 Transmission electron microscopy

TEM uses electrons to obtain images of thin samples with very high resolution, the microscopes used for this research can resolve two points ~ 0.19 nm apart, and more sophisticated systems are capable of distinguishing individual atoms [12, 13]. A wide variety of materials may be imaged in TEM, in part due to the different contrast mechanisms available; and the technique is enhanced by *in situ* spectroscopic techniques, which provide chemical information about samples [14]. With systems available to enable thermal or electrical measurements to be performed, or chemical

reactions monitored in liquid cells, in real-time while obtaining images, [15], the technique is widely applied in diverse subject areas [16-18].

TEM may be considered analogous to visible-light microscopy, since many of the concepts and terminologies apply to both; ray diagrams representing wavepaths aiding comprehension of both techniques can be seen in Figure 3.11. However, since electrons possess wave-particle duality, there are some significant differences which will be discussed later in this section.

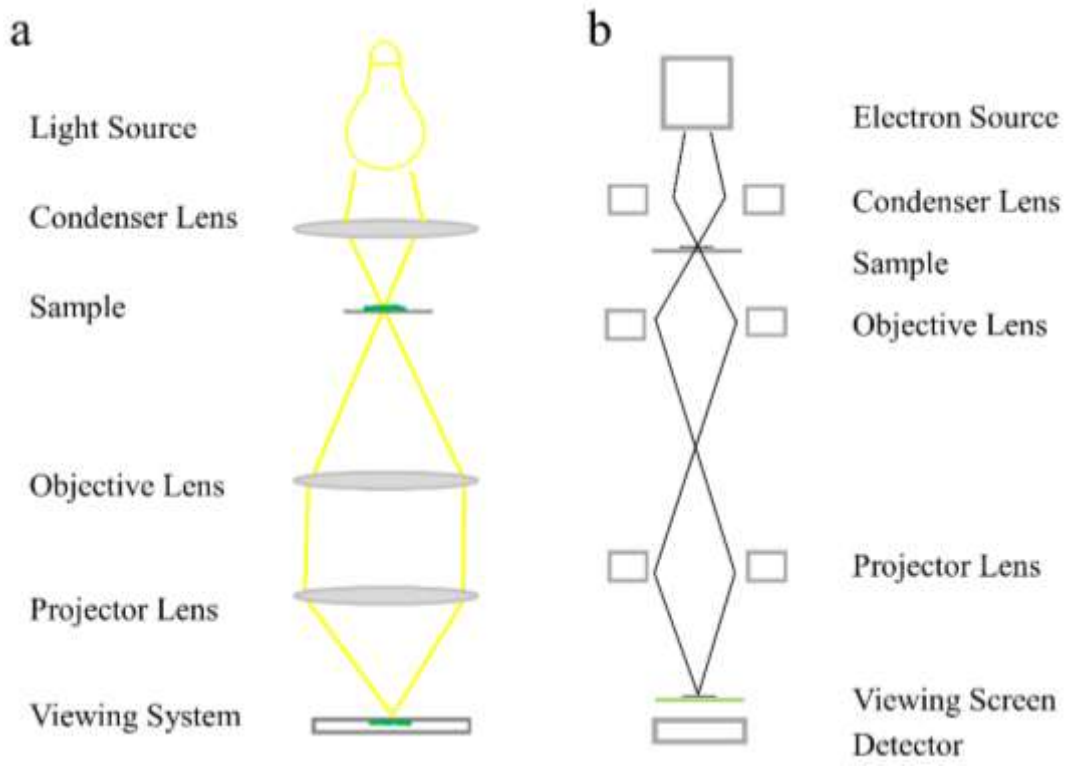

Figure 3.11 Simplified schematic diagrams of principle components of a) light microscope, and b) electron microscope, including wavepaths from source to viewing system or screen.

In the case of visible-light microscopes, glass lenses magnify and focus the rays from a light source to produce images of samples; electron microscopes also require a wave source and lenses that act to magnify and focus images of samples.

Operating principles

Briefly, transmission electron microscopes generate electrons which pass down a microscope column, where electromagnetic lenses focus the electrons which pass through an electron transparent sample. The electrons are then detected to produce images, with the system kept *in vacuo* to avoid unwanted collisions between electrons and gas particles. In more detail, starting with the top of the column, electrons may be generated via thermionic (LaB_6) or field-emission (FEG) sources, producing electrons when heated in the former case, or when a suitable electric potential is applied between the source and an anode in the latter. While FEG sources produce much greater current density, a more coherent electron beam with less energy spread and are more stable compared to LaB_6 sources, they are not necessarily the preferred option, depending on sample requirements [15].

Moving down the column, following beam generation, electromagnetic condenser lenses are arranged to focus the electron beam before it interacts with the sample, with a condenser aperture inserted to select the most coherent part of the beam. Magnification of images is achieved by electromagnetic lenses, at the sample position (objective lenses), and before reaching the screen or camera (projector lenses), with some microscopes having additional intermediate lenses between the objective and projector systems. Changing the lens strengths may produce underfocus, focus or overfocus conditions, with slight underfocus conditions often optimal for imaging since this results in convergent rays that are more parallel in comparison wto the divergent rays of overfocus conditions, illustrated in Figure 3.12a, b, c. Operating slightly out of focus also results in Fresnel fringes at the edges of samples with the

bright Fresnel fringes observed during underfocus allowing edges to be clearly distinguished, Figure 3.12d,e,f,. At the base of the column, images are projected onto fluorescent screens for viewing, or onto detectors for image capture.

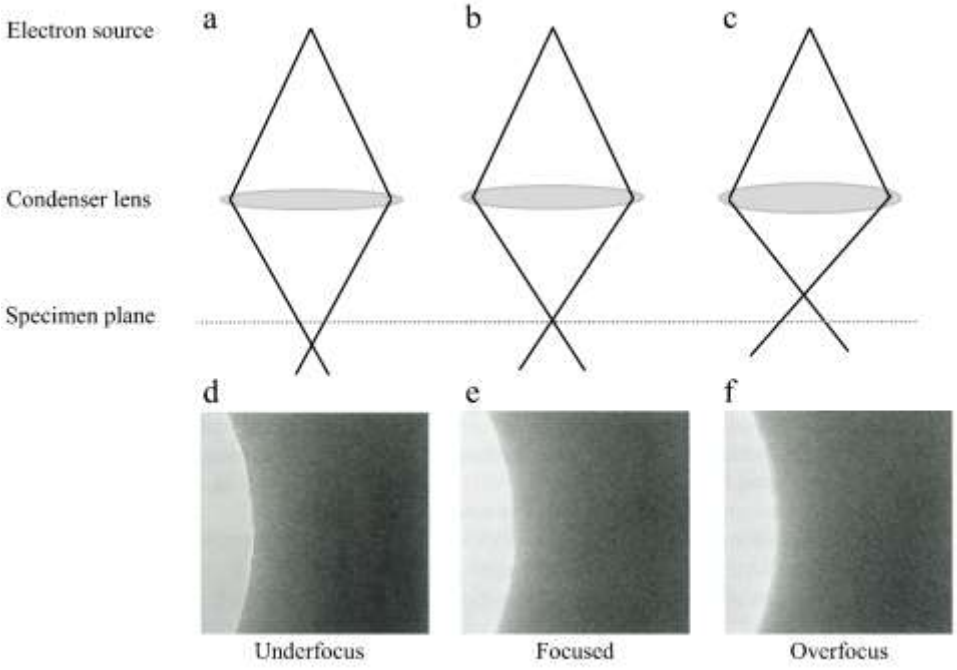

Figure 3.12 Ray diagrams illustrate a) underfocus conditions with a weak lens producing a focal point below the sample plane, b) focused lens conditions and c) overfocus conditions, with a strong lens bringing the focal point above the sample plane. TEM images showing the edge of an amorphous carbon support film during d), slight underfocus conditions, e) focused lens conditions and f), marginally overfocus conditions, the clearest images being obtained with conditions of underfocus, adapted from [19].

Image contrast in TEM can be achieved via three mechanisms, mass-thickness, diffraction or phase contrast. Mass thickness contrast arises due to the amount of sample present, i.e. thickness, and the mass of the elements present, figure 3.13. In practice, it follows that a large volume of a light element may have the same signal intensity as a small quantity of a heavier element.

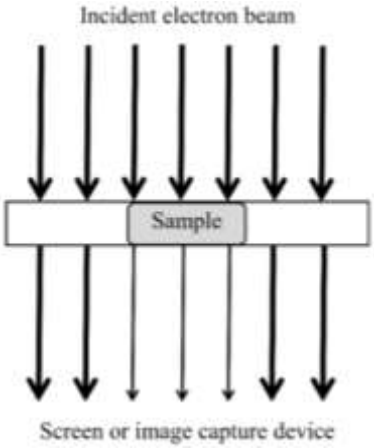

Figure 3.13 Illustration of TEM image contrast due to the mass and / or thickness of a sample. Dark regions will be visible due to samples absorbing electrons from the incident beam.

Diffraction of the electron beam, occurring in crystalline materials, produces diffraction patterns which may be observed by changing the relative strengths of the lenses to project diffraction patterns onto the viewing screen or detector, Figure 3.14.

Although diffraction occurs in both TEM and XRD, there are important differences because electrons have much smaller wavelengths than X-rays and possess charge. High energy electrons in a TEM interact both with electrons and nuclei in a sample, whereas X-rays interact *only* with electrons in samples. In addition, electron beams are scattered more strongly than X-rays, and electrons may be directed since they comprise of charged particles. These differences mean that in TEM selected area diffraction is achievable, data collection is much faster in TEM compared to XRD, and TEM produces many diffractions; there is no requirement to scan through a wide range of angles as in XRD.

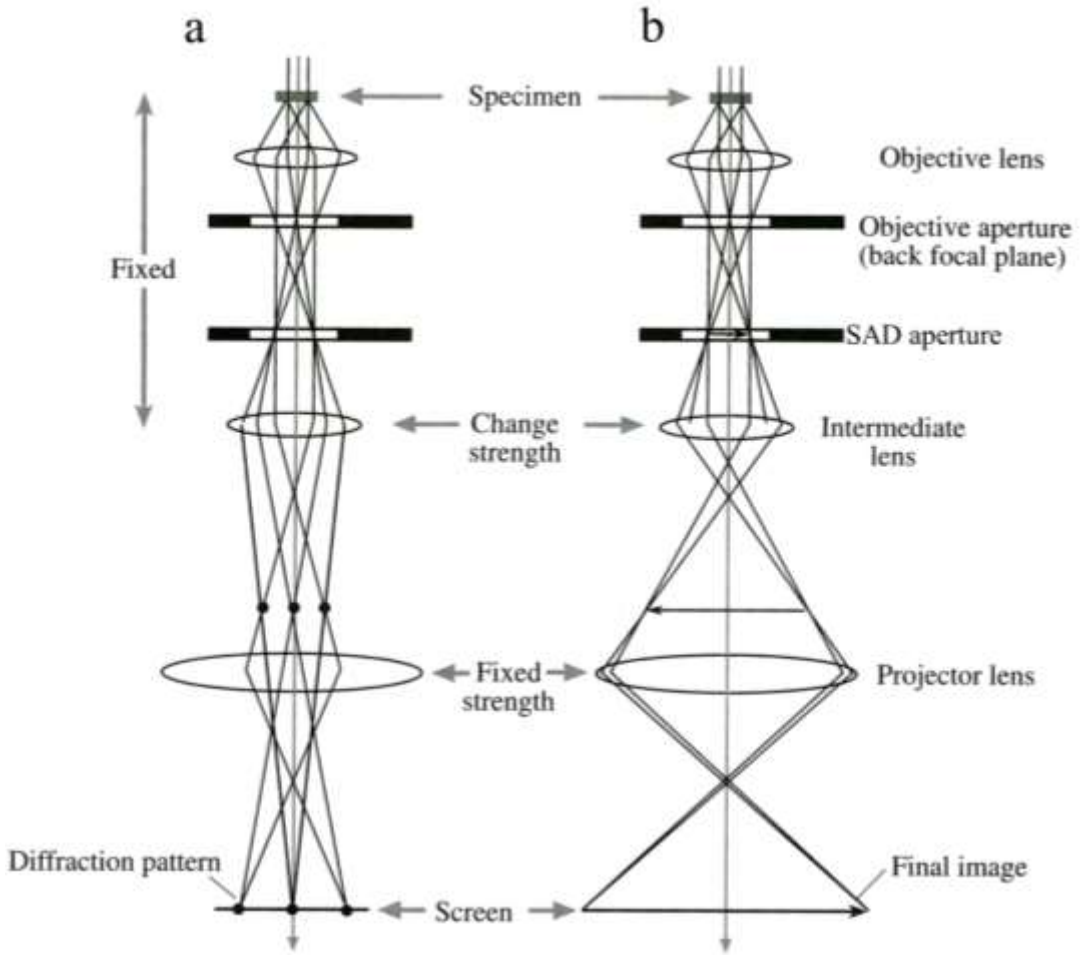

Figure 3.14. Ray diagrams illustrating how adjusting the strength of the intermediate lens system may result in the observation of either; a) diffraction patterns or; b) images on a viewing screen or image capture device, (SAD, selected area diffraction) adapted from [15].

Diffraction contrast may produce bright field (BF) images, generated by selecting only those electrons that pass through the sample, Figure 3.15a. Whilst selection of those electrons that are highly diffracted generates dark field (DF) images, Figure 3.15c, and may be achieved by inserting an objective aperture over a single spot of the diffraction pattern, Figure 3.15b, which represents a portion of possible diffractions

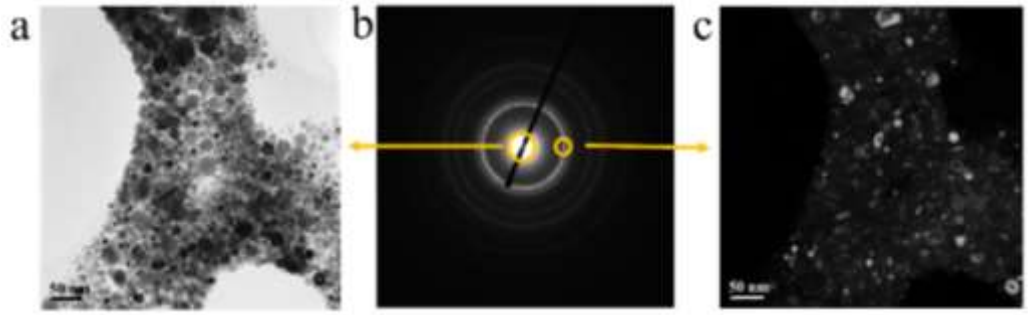

Figure 3.15 TEM image contrast may arise from mass-thickness contrast, producing a) bright field images, via selection of electrons that pass through the sample, i.e. the area inside the region indicated in b). Diffraction contrast may be used to generate either b), diffraction patterns, or c), dark field images, by selecting those electrons that are highly scattered by the sample from a single point.

Phase contrast arises due to differences in the phase of samples to produce high resolution TEM (HRTEM) images, for which a very stable electron beam is required. HRTEM allows individual columns of metal atoms to be observed, or graphitic lattice spacings to be measured, figure 3.16.

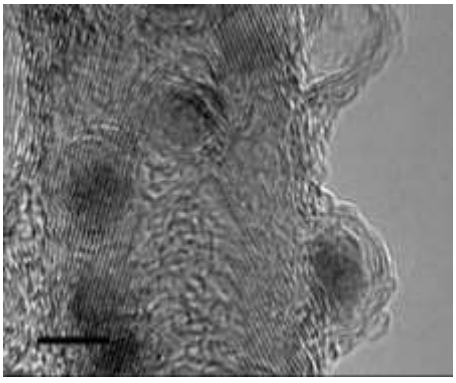

Figure 3.16 Phase contrast achieved in high resolution TEM via insertion of an objective aperture, enables graphitic planes and individual column of metal atoms to be observed, scale bar is 5 nm.

Scanning transmission electron microscopy (STEM) uses a very finely focused beam of electrons to scan a sample in a raster pattern, recording signals from individual points to create an image. The signals generated may be collected with either a bright field, an annular dark field (ADF), or a high angle annular dark field (HAADF) detector, to generate images from the direct beam, or from scattered electrons, an example of the latter is presented in Figure 3.17. In addition to image generation, STEM enables spatial correlation of other signals, such as characteristic X-rays and electron energy loss, producing elemental maps.

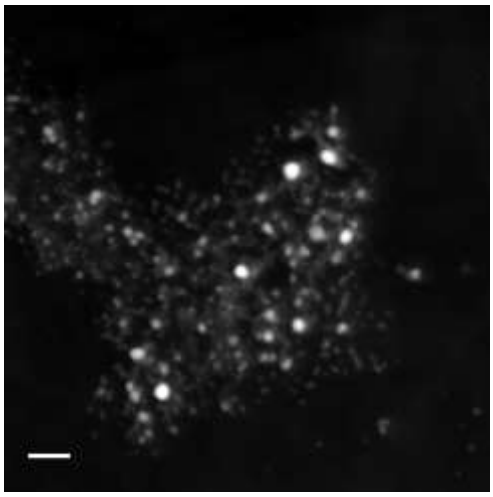

Figure 3.17 Example STEM HAADF image, scale bar is 200 nm.

Determination of NP size and resultant G-HCNS sizes and size distributions were determined from TEM micrographs using ImageJ 1.48v [20], Java 1.6.0-20 (64-bit), Excel and OriginPro 8 software, with the following procedure: ‘dm3’ files were opened in ImageJ, and ‘measurements’ set to include ‘display label’, after enlarging the image, ‘measure’ and then ‘line tool’ were selected and a line drawn across the nanoparticle. The command ‘control / m’ added the measurement to a data table and

labelled the image with a numbered line, unambiguously indicating the nanoparticle measured. After measuring all nanoparticles, the data table was imported into excel, particle diameter measurements were then sorted by size, and the frequency of each diameter range counted before exporting into OriginPro and plotting as histograms.

Contrast enhancement of TEM images was performed, where stated, using ImageJ 1.48v [20], Java 1.6.0-20 (64-bit), by converting images to 16 bit data, selecting 'process', then 'enhance contrast', and equalising the histogram (Saturated pixels set at 0.3%).

Analytical TEM

Since electrons behave as particles in addition to exhibiting wave-like behaviour, they may interact with thin samples to produce many different signals, figure 3.18, which can enable energy dispersive spectroscopy or electron energy loss spectroscopy to be performed *in situ*, within a TEM.

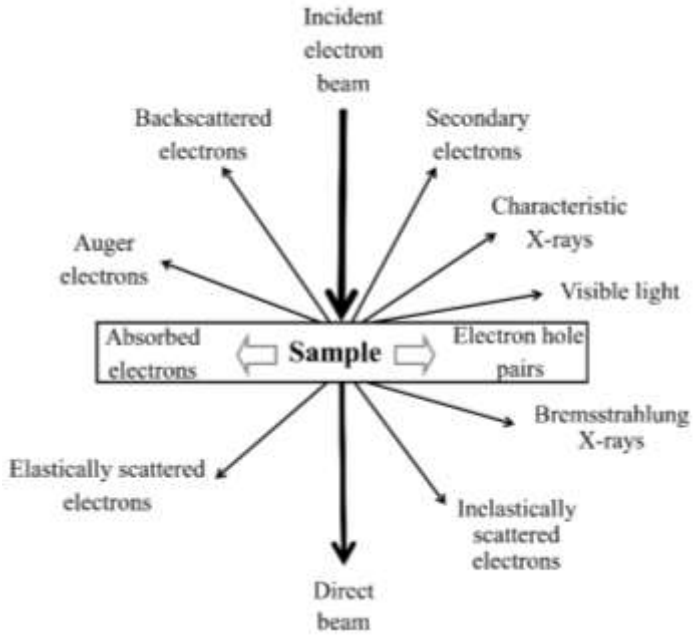

Figure 3.18 Interactions between high energy electrons, such as those generated by TEM, and thin samples produce a range of signals useful for in situ spectroscopic analysis, angles are illustrative only.

In the case of energy dispersive spectroscopy (EDS), the chemical composition of samples may be determined over localised areas or, by combining EDS with STEM elemental maps may be produced. The removal of inner electrons by high energy incident radiation leads to the formation of electron holes. Electrons from higher energy, outer shells will then move to fill the vacancies, emitting X-rays in the process, Figure 3.19 illustrates the process. These X-rays are detected by an energy-dispersive spectrometer and since the energy dispersions are highly sensitive to atomic number, elemental composition may be derived via peak fitting with dedicated software.

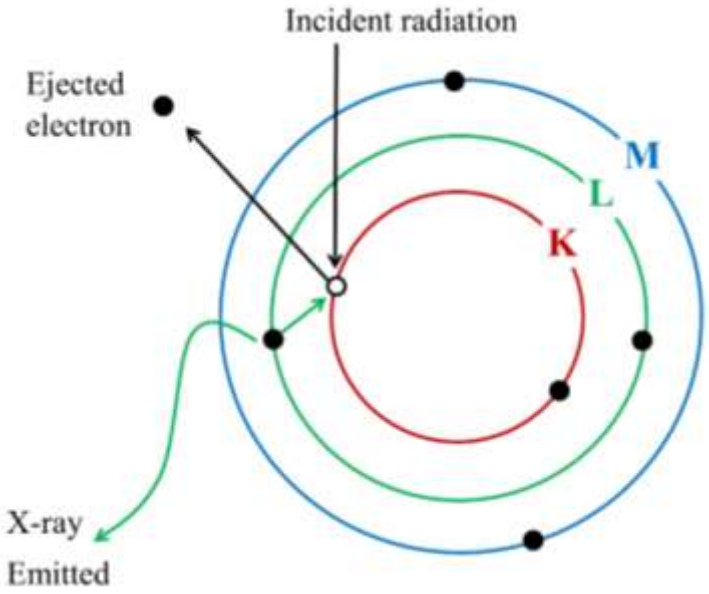

Figure 3.19 High energy incident radiation may lead to the removal of inner k electrons, leaving an electron hole. This is filled by the movement of outer shell electrons, which emit X-rays characteristic of the energy transition involved, providing elemental identification.

A further *in situ* TEM spectroscopy technique, electron energy-loss spectroscopy (EELS), measures the energy distribution of electrons that have passed through a sample. Loss of energy occurs due to inelastic interactions between the electrons and the sample, which may be due to inner shell ionisation, or to plasmon excitation. While plasmon peaks occur at energies close to the zero loss peak and are difficult to resolve, EELS is sensitive to energies required to remove core electrons, which differ between elements and shells within elements, therefore this technique provides information regarding the elements present in a sample, with bonding and electronic state.

TEM was carried out with either a JEOL 2000FXll electron microscope, a single tilt holder with a LaB_6 source operated at 200kV, micrographs were recorded on a Gatan Orius camera or on photographic plates then digitised using an Epson perfection 4870 flatbed scanner, or a JEOL 2100F field emission analytical electron microscope,

operated at 100 or 200 kV, with a Gatan Orius SC1000 camera, Oxford Instruments energy dispersive X-ray spectrometer (X-Max 80T), and electron energy loss spectrometer, with either single tilt (JEOL 21010/21020) or high tilt (GATAN 916) holders to facilitate tomographic imaging, or a JEOL 2100 Plus with a LaB_6 source operating at 80 or 200 kV, with a Gatan Ultrascan 1000XP camera and Oxford Instruments energy dispersive X-ray spectrometer (X-Max 100 TLE). INCA or AZtec software packages were used for EDS elemental identification and quantification.

3.3.6 Raman Spectroscopy

Raman Spectroscopy involves exposing samples to monochromatic radiation, which interact and will, for a small fraction of photons (1×10^{-7}), be at frequencies shifted in respect to the incident beam, due to inelastic Stokes or Anti-Stokes scattering. These energy shifts are associated with particular molecular vibrational or rotational modes. Because signals due to Raman scattering are very weak compared to the more intensely scattered Rayleigh radiation, notch or edge filters are used to remove unwanted signals. The technique provides chemical identification, molecular characterisation, and bonding state.

Micro Raman spectroscopy was performed using a Horiba Jobin Yvon LabRAM HR Raman spectrometer equipped with an automated xyz stage (Märzhäuser). Spectra were acquired using a 532 nm laser at 0.3 mW power, a 100x objective lens and a 50 µm confocal pinhole. The spectral resolution in this configuration is ~1.6 cm-1. To simultaneously scan a range of Raman shifts, a 600 lines mm-1 rotatable diffraction grating along a path length of 800 mm was employed. Spectra were acquired using a

Synapse CCD detector (1024 pixels), thermoelectrically cooled to −60°C. Before the collection of spectra, the instrument was calibrated using the zero-order line and a standard Si(100) reference band at 520.7 cm-1. Point spectra were acquired over the range 800-2000 cm-1 with an acquisition time of 60 s and 16 accumulations to improve signal to noise ratio. The DuoScanTM functionality was employed to confer an effective laser spot size of 20x5x4 microns in the xyz directions, respectively. Spectra were baseline-corrected using a third-order polynomial subtraction and fit with a five-band model analogous to that described by Sadezky et al. [21] using Lapspec 6.4.3 software. The G and D2 bands are described by Lorenzian peak shapes, whereas the D1, D3 and D4 bands are Gaussian.

3.3.7 X-ray photoelectron spectroscopy

X-ray Photon Spectroscopy (XPS) involves the interaction of X-rays in an ultra-high vacuum with a sample, which results in the emission of inner shell electrons, the kinetic energies of which are measured by a detector. XPS is a surface sensitive technique and provides chemical composition, oxidation states and chemical environment, with a spatial resolution of around 5 mm and an elemental sensitivity of 0.1 At %, the lightest elements, hydrogen and helium cannot be detected by XPS.

Samples were analysed using the Kratos AXIS ULTRA with a mono-chromated Al kα X-ray source (1486.6eV) operated at 10 mA emission current and 12 kV anode potential (120 W). A charge neutralizer filament was used to prevent surface charging. Hybrid –slot mode was used measuring a sample area of approximately 0.5 mm^2. The analysis chamber pressure was better than 5 x 10^{-9} mbar.

Three areas per sample were analysed. A wide scan at low resolution (1400 - -5 eV binding energy range, pass energy 80 eV, step 0.5 eV, sweep time 20 minutes) These were used to estimate the total atomic % of the detected elements. High resolution spectra at pass energy 20 eV with step of 0.1 eV, sweep times of 5, 10 or 20 minutes each were also acquired for photoelectron peaks from the detected elements and these were used to model the chemical composition. The high resolution spectra were charge corrected to the C 1s peak set to 285 eV, [22].

Casaxps (version 2.3.18dev1.0x) software was used for quantification and spectral modelling.

The ULTRA detector was used in FAT (fixed analyser transmission) mode, with pass energy of 80eV for wide scans and pass energy 20 eV for high resolution scans. A Hybrid magnetic/electrostatic lens mode is used for maximum electron signal. The magnetic immersion lens system allows the area of analysis to be defined by apertures, a 'slot' aperture of 300 x 700 μm for wide/survey scans and high resolution scans. The take-off angle for the photoelectron analyser is 90˚ and acceptance angle of 9˚ for hybrid lens mode utilised.

The energy range of the XPS was calibrated using Cu, Ag and Au samples. The resolution for the photoelectron detector was based on Ag $3d_{5/2}$ peak FWHM of less than 0.55 eV at PE 20 in hybrid slot mode. The transmission function of the instrument was calibrated using a clean gold sample for all lens modes and pass energies. Last date of calibrations: Energy range, resolution check and Transmission function, July 2013, Kratos Factory settings.

3.4 Summary

This materials and methodology chapter has described the steps required for the formation of G-HCNS from TS-AgNP, with details of the techniques, instrumentation, and sample handling required for processing and materials characterisation. The project follows a logical framework starting with the chemical synthesis of TS-AgNP, then the deposition of this starting material onto supports, followed by thermal processing to form G-HCNS - via *in situ* or *ex situ* heating methods. All stages of the process have been described in this chapter, with details of characterisation performed, and results are reported in chapter four.

The process-structure relationship of G-HCNS formation has then been investigated, achieved by changing individual thermal processing parameters, such as temperature, rate of heating or support material, as described in this chapter, with chapter five presenting experimental results. The addition of heteroatoms to TS-AgNP starting materials, with subsequent processing to form G-HCNS, and characterisation has been described and is reported in chapter six.

References

1 Brust, M., Walker, M., Bethell, D., Schiffrin, D. J., Whyman, R., *Synthesis of thiol-derivatised gold nanoparticles in a two-phase liquid-liquid system*, J Chem. Soc. Chem. Comm., (1994) 7 pp801-802.

2 Deegan, R. D., Bakajin, O., Dupont, T. F., Huber, G., Nagel, S. R., Witten, T. A., *Capillary flow as the cause of ring stains from dried liquid drops*, Nature (1997) 389 (6653) pp827-829.

3 Albanese, A., Chan, W. C., *Effect of gold nanoparticle aggregation on cell uptake and toxicity,* ACS nano (2011) 5 (7) pp5478-5489.

4 Ma, H., Hao, J., *Ordered patterns and structures via interfacial self-assembly: superlattices, honeycomb structures and coffee rings,* Chemical Society Reviews (2011) 40 (11) pp5457-5471.

5 Watts, J. A., Fay, M. W., Khlobystov, A. N., Brown, P. D., *Effect of TEM grid deposition method on the dispersion of thiol-stabilised silver nanoparticles,* IOP Conf. Series: J Physics: Conf. Series (2017) 902 pp012030.

6 Korolkov, V. V., Svatek, S. A., Summerfield, A., Kerfoot, J., Yang, L., Taniguchi, T., Beton, P. H., *Van der Waals-induced chromatic shifts in hydrogen-bonded two-dimensional porphyrin arrays on boron nitride*, ACS Nano (2015) 9 (10)). pp10347-10355.

7 Dick, K., Dhanasekaran, T., Zhang, Z. and Meisel, D., *Size-dependent melting of silica-encapsulated gold nanoparticles,* J Am. Chem. Soc. (2002) 124 (10) pp2312-2317.

8 Balandin, A.A., Thermal properties of graphene and nanostructured carbon materials, Nature materials (2011) 10 (8) pp569.

9 Lee, K-S., El-Sayed, M. A., *Gold and Silver Nanoparticles in Sensing and Imaging: Sensitivity of Plasmon Response to Size, Shape, and Metal Composition*, J Phys. Chem. B (2006) 110 (39) pp19220-19225.

10 Doty, C. R., Tshikhudo, R. T., Brust, M., Fernig, D. G., *Extremely Stable Water-Soluble Ag Nanoparticles*, *Chem. Mater*. (2005) *17* (18) pp4630-4635.

11 Holzwarth, U., Gibson, N., The Scherrer equation versus the 'Debye-Scherrer equation', Nat. Nanotech. [1748-3387] (2011) 6 (9) pp534 -534.

12 Durán, N., Marcato, P.D., De Souza, G.I., Alves, O.L., Esposito, E., *Antibacterial effect of silver nanoparticles produced by fungal process on textile fabrics and their effluent treatment*, J biomed. Nanotechnol. (2007) 3 (2) pp203-208.

13 Batson, P. E., Dellby, N., Krivanek, O. L., *Sub-ångstrom resolution using aberration corrected electron optics*, Nature (2002) 418 pp617-620.

14 Börrnert, F., *Thoughts about next-generation (S)TEM instruments in science*, Micron (2016) 90 pp1-5.

15 Williams D.B., Carter C.B., *Transmission Electron Microscopy*. Springer, Boston, MA, second edition (2009) ISBN 978-0-387-76500-6.

16 Zhu, C., Liang, S., Song, E., Zhou, Y., Wang, W., Shan, F., Shi, F., Hao, C., Yin, K., Zhang, T., Liu, J., Zheng, H., Sun, L., *In-situ liquid cell transmission electron microscopy investigation on oriented attachment of gold nanoparticles,* Nat. Commun. *(*2018) 9 pp421.

17 Penen, F., Malherbe, J., Isaure, M-P., Dobritzsch, D., Bertalan, I., Gontier, E., Le Coustumer, P., Schaumlöffel, D., *Chemical bioimaging for the subcellular localization of trace elements by high contrast TEM, TEM/X-EDS, and NanoSIMS,* J Trace Elem. Med. Biol. (2016) 37 pp62-68.

18 Wu, J., Shan, H., Chen, W., Gu, X., Tao, P., Song, C., Deng, T., *In Situ Environmental TEM in Imaging Gas and Liquid Phase Chemical Reactions for Materials Research*, Adv. Mater. (2016) 28 (44) pp9686-9712.

19 JEOL 2100 Plus manual available from https://www.jeolusa.com/RESOURCES/Electron-Optics/Documents-Downloads?EntryId=560

20 Schneider, C. A.; Rasband, W. S., Eliceiri, K. W. *NIH Image to ImageJ: 25 years of image analysis*, Nat. methods 9 (7) (2012) pp671-675.

21 Sadezky, A., Muckenhuber, H., Grothe, H., Niessner, R., Pöschl, U., *Raman microspectroscopy of soot and related carbonaceous materials: Spectral analysis and structural information*, Carbon (2005) 43 (8) pp1731-1742.

22 Putz, B., Milassin, G., Butenko, Y., Völker, Gammer, G., Semprimoschnig, C., Cordill, M. J., *Combined TEM and XPS studies of metal - polymer interfaces for space applications*, Surf. Coat. Techn. (2017) 332 pp368-375.

4.0 Formation of hollow carbon nanoshells

4.1 Introduction

This Chapter concerns the formation of < 10 nm sized HCNS from the thermal processing of alkane thiol stabilised silver nanoparticles (TS-AgNP), and is broken down into discrete themes, as illustrated in Figure 4.1, corresponding to the experimental design outlined in Chapter 3.

Figure 4.1 Themes in this chapter: (i) Characterisation of starting materials; (ii) thermal protocol development; and (iii) characterisation of HCNS products.

Initially, this chapter reports on the characterisation of TS-AgNP starting materials, then moves onto the deposition of TS-AgNP on various supports, followed by thermal processing experiments and the characterisation of hollow carbon nanoshell (HCNS) products.

4.2 Characterisation of starting TS-AgNP

As-synthesised TS-AgNP samples (Section 3.2.1) were characterised to enable changes to be evaluated after *in situ* and *ex situ* thermal processing. Attention is given to the overall morphology and chemistry of the samples, with emphasis on the AgNP template and the carbon source, *i.e.* the thiol stabilising layer. Accordingly, starting TS-AgNP samples were evaluated using a combination of X-ray diffractometry (XRD), transmission electron microscopy (TEM), and UV / visible light (UV/vis) spectroscopy. The chemistry was investigated using the complementary techniques of Fourier transform infrared (FTIR) and nuclear magnetic resonance (NMR) spectroscopy.

Figure 4.2 shows XRD data for TS-AgNP, with characteristic peaks at 2θ = 38.1°, 44.3°, 64.6°, 77.5° and 82° corresponding to the {111}, {200}, {220}, {311} and {222} lattice planes of Ag. Comparison with the standard powder diffraction card of the Joint Committee on Powder Diffraction Standards (JCPDS) silver file No. 004–0783 confirmed the presence of face centred cubic (FCC) metallic Ag. Further, the calculated d_{hkl} values from this data set of d_{111} = 2.360 Å, d_{200} = 2.044 Å, d_{220} = 1.441 Å and d_{311} = 1.230 Å are in very good agreement with standard values for metallic Ag [1]. Peak shapes are broader than expected particularly at low intensities, and are asymmetric, suggesting a bimodal size distribution, with crystallite sizes estimated from the Scherrer equation of 6.1 ± 2 nm (averaged from 2θ = 38.1, 64.6 and 77.5° peaks).

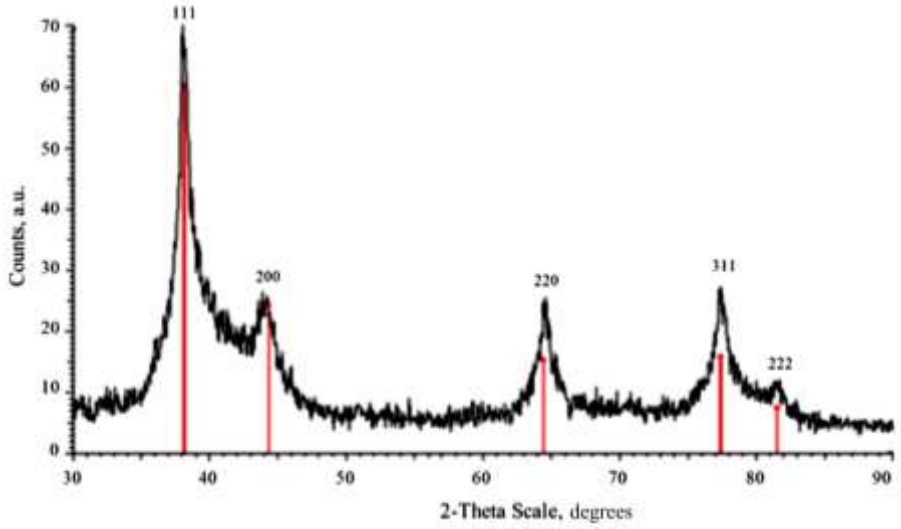

Figure 4.2 XRD data for DDM stabilised silver nanoparticles (Sample NP005) and associated database values (red lines) for face centred cubic Ag, with appropriate Miller indices.

Figures 4.3a,b present representative conventional, bright field, diffraction contrast TEM images of dodecanethiol stabilised AgNP revealing the crystalline AgNP templates, which appeared circular in projection consistent with their spherical morphology. The dispersion of the TS-AgNP onto a C/Cu TEM support grid was tailored to enable clear differentiation between individual particles. Particle size distributions of 4.9 ± 1.5 nm (batch 2, n = 188, averaged from two different regions of the TEM grid) (Figure 4.3c) and 4.2 ± 0.7 nm (batch 5, n = 285) (Figure 4.3d) were similar / of the same order of magnitude as literature examples of DDM stabilised AgNP [2]. Similarly, Figure 4.4a presents a TEM micrograph of octanethiol (OM) stabilised AgNP (again, dispersed onto a C/Cu support), returning a particle size distribution of 5.3 ± 0.8 nm (n = 311). Further, the particle size and size distribution data for starting DDM stabilised AgNP templates, measured directly from TEM micrographs, was found to be in good agreement with a value of 5.4 nm ± 1.1 nm for DDM stabilised TS-AgNP obtained from dynamic light scattering (DLS) investigations.

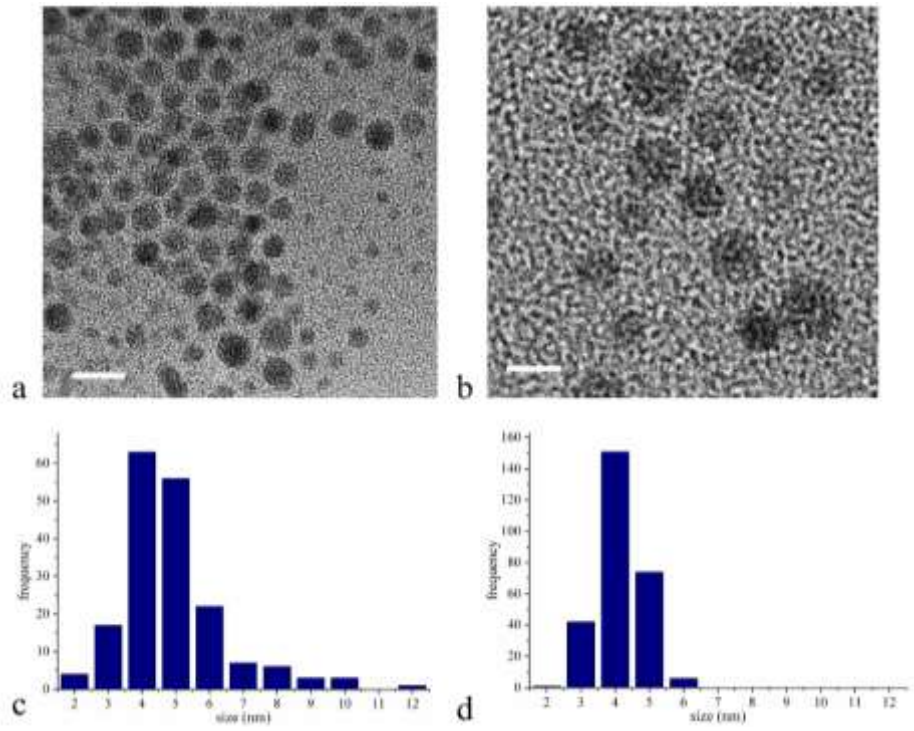

Figure 4.3 Representative (a,b) bright field, diffraction contrast TEM images showing starting AgNP templates; and (c,d) corresponding particle size histograms for DDM stabilised AgNP (images were contrast enhanced). (a) Batch 2 (scale bar 10 nm); (c) average diameter 4.9 ± 1.5 nm (n = 188). (b) Batch 5 (scale bar 5 nm); (d) average diameter 4.2 ± 0.7 nm (n = 285).

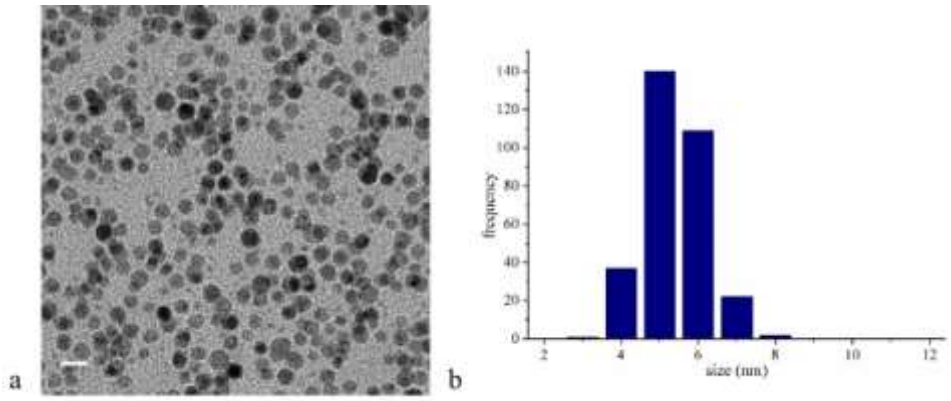

Figure 4.4 TEM micrograph of: (a) Octanethiol stabilised AgNP (scale bar 10 nm), and; (b) associated particle size distribution histogram (5.3 ± 0.8 nm, n = 311), (0.5 mg / 1 ml hexane).

Figure 4.5a presents a selected area diffraction (SAED) pattern from TS-AgNP typical of a random distribution of many small, crystalline Ag grains, consistent with published SAED data for (DDM-stabilised) AgNP (Figure 4.5b) [3].

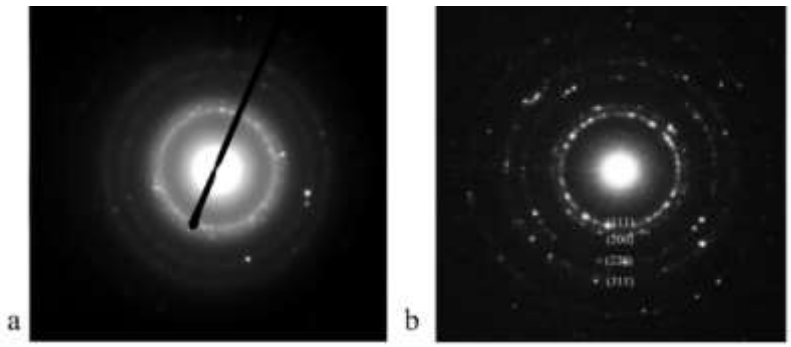

Figure 4.5 SAED pattern for (a) DDM-stabilised TS-AgNP and; (b) example SAED of TS-AgNP from literature with assigned crystal planes for metallic Ag [3].

Figure 4.6 presents a representative UV/vis spectrum for DDM stabilised AgNP in solution (1.0 mg / mL cyclohexane), taking the form of a single absorbance peak with maximum at ~ 440 nm. Indeed, single absorbance peaks were observed for all DDM stabilised AgNP samples, consistent with the presence of spherical nanoparticles: energy of the surface plasmon resonance (SPR) depends on the size and shape of the nanoparticles and since spheres present the same radius in all directions, they give rise to a single SPR; in contrast, anisotropic-shaped NP would give rise to more than one plasmon resonance [4]. Furthermore, a relatively narrow peak width is indicative of a narrow size distribution [2].

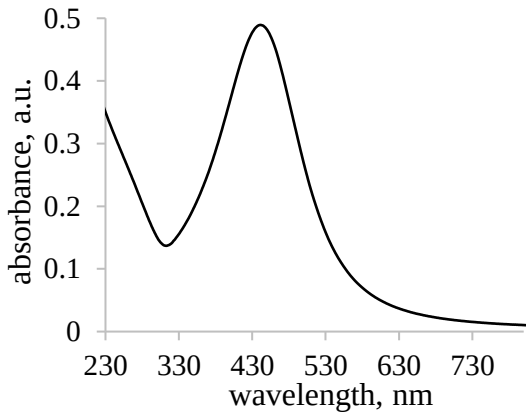

Figure 4.6 UV/vis spectrum for DDM stabilised AgNP. The presence of a discrete, single peak (maximum ~ 440 nm) is characteristic of spherical nanoparticles and indicative of a narrow particle size distribution [2].

The Fourier transform infrared (IR) spectrum for TS-AgNP (Batch NP002), presented in Figure 4.7, is indicative of the presence of thiol and alkane functional groups [5]; *e.g.* the band observed at 719 cm^{-1} is consistent with the presence of thiol functional groups. In addition, band positions attributable to the alkane chain (at ~ 2900 and ~1400 cm^{-1}) are typical of DDM bonded to AgNP and not to the presence of free thiol molecules. In particular, the alkane CH_2 symmetric and asymmetric stretching bands usually observed in DDM IR spectra at 2853 and 2924 cm^{-1}, respectively, were slightly shifted to 2847 and 2916 cm^{-1}, whilst expected twisting-rocking and wagging bands of DDM in the ~1150 - 1400 cm^{-1} region were observed at 1378 and 1468 cm^{-1}, respectively. The latter CH_2 scissoring band position is typical for all trans zig-zag chains of DDM stabilising AgNP [2]. Notably, bands due to aromatic carbon functional groups around 1600 cm^{-1} were not observed; hence the starting TS-AgNP was non-graphitic.

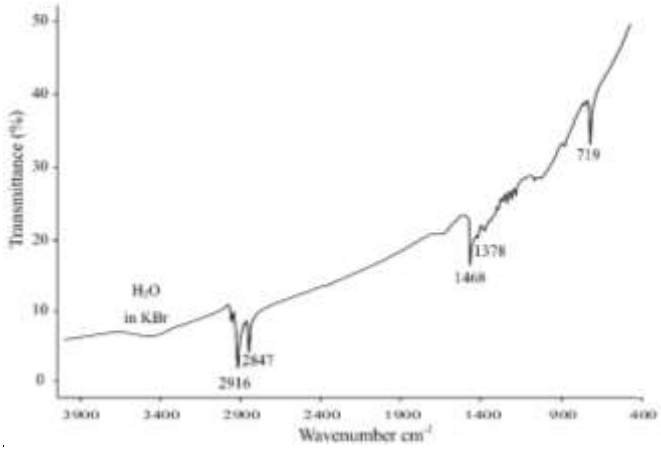

Figure 4.7 FTIR spectrum for TS-AgNP (NP002) consistent with the presence of alkane (~2900 and ~1400 cm^{-1}) and thiol (719 cm^{-1}) functional groups of DDM bonded to the surface of AgNP [2]. The absence of a signature due to aromatic carbon functional groups confirmed the starting TS-AgNP to be non-graphitic

Complementary NMR spectroscopy investigations of as-synthesised TS-AgNP and as-purchased DDM also confirmed the presence of alkane thiol stabilised AgNP, consistent with the FTIR data. Figure 4.8a presents a spectrum for AgNP stabilised by DDM, with peaks at 0.9 ppm and ~ 1.2 – 1.6 ppm being assigned to the terminal methyl group and unbranched alkane chain, respectively.

Indeed, the NMR spectrum for DDM in solution (Figure 4.8b) constitutes evidence for DDM being bonded to Ag in the TS-AgNP, since peaks at 1.6 and 2.4 ppm that are present in the DDM spectrum are not observed in the TS-AgNP spectrum, due to alterations to relaxation times associated with nuclei bonded (or close) to the AgNP core. These NMR spectra were found to be consistent with published data [6, 7]. In particular, peaks were absent in the region associated with aromatic functional groups (6 - 9 ppm); again confirming that the starting TS-AgNP was non-graphitic.

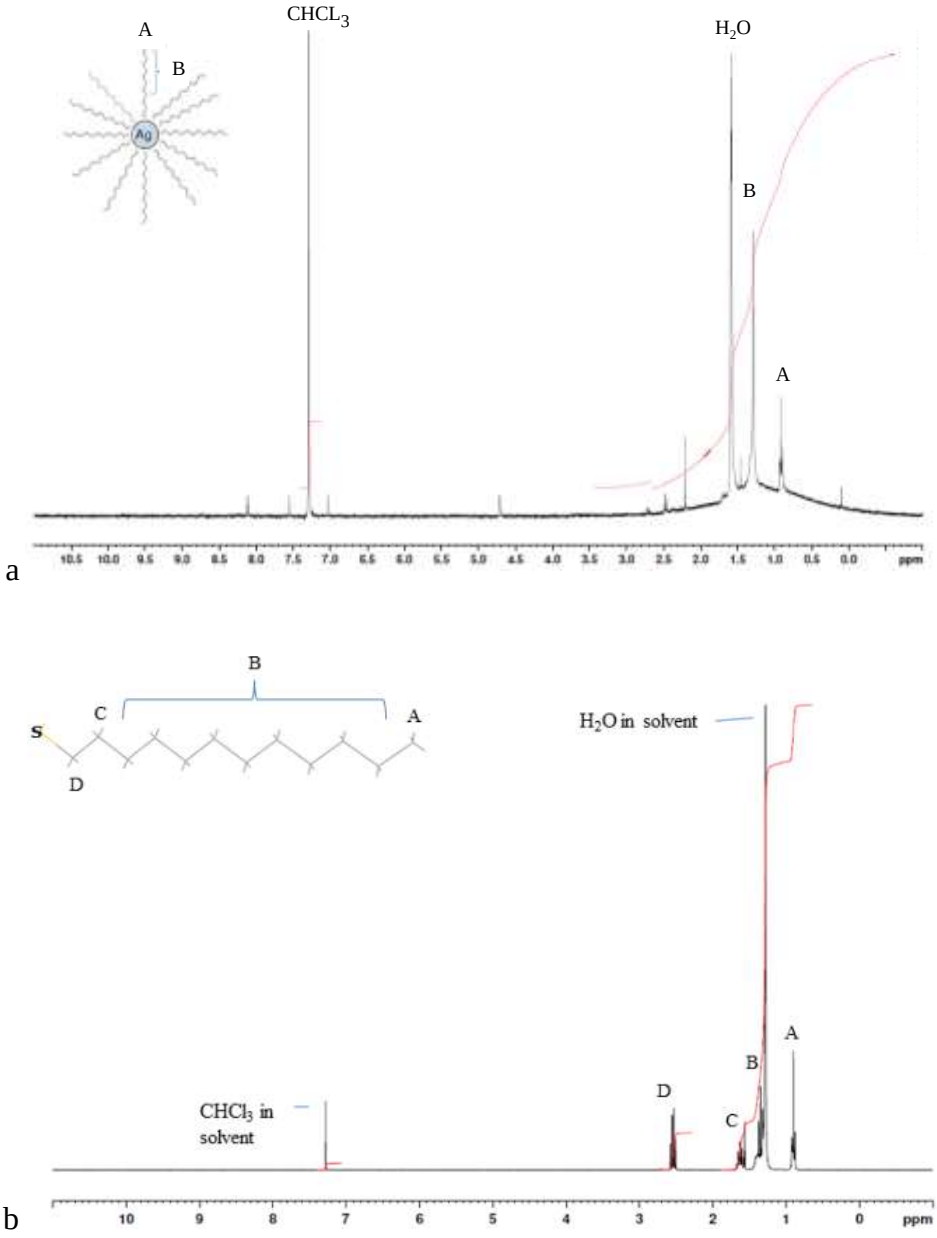

Figure 4.8 ^{1}H NMR spectra and peak assignments [2] of: (a) DDM stabilised AgNP, comparable with; (b) DDM. Both spectra are consistent with literature examples [3], note the H_20 peak shift attributable to changes in hydrogen bonding.

In summary, characterisation of as-synthesised TS-AgNP confirmed the structure to be an FCC Ag core; acting as a template for the alkane thiol carbon source, bonded to the Ag surface. For the case of DDM, a *trans* zig-zag configuration is adopted (Figure 4.9).

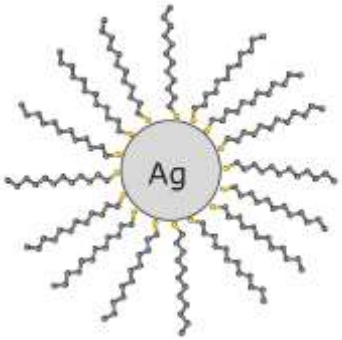

Figure 4.9 Schematic of TS-AgNP starting material for HCNS production, consisting of a DDM stabilisation layer bonded to an FCC AgNP core (not to scale).

Having thoroughly characterised the TS-AgNP starting materials, the next section reports on issues for the deposition of TS-AgNP onto suitable TEM supports, as required for both *in situ* and *ex situ* heating experiments.

4.3 Deposition of TS-AgNP onto supports

Figures 4.10a,b present a TEM micrograph and particle size histogram for OM stabilised AgNP, dispersed from a briefly sonicated solution (0~ 30 s, 5 mg / 1 ml hexane), indicating the presence of spheroidal particles with a measured particle size distribution of 8.1 ± 2.3 nm, (n = 199). Comparison with AgNP from the same batch dispersed from a non-sonicated solution (*e.g.* Figure 4.4), indicated that this simple stage of sample handling had had a significant effect on the distribution / agglomeration of TS-AgNP, with all processing parameters (except the sonication step) being kept the same in these two cases. Indeed, in general, it was found that the sonication of AgNP samples tended to return larger average particle sizes, with broader size distributions [8].

Further, Figure 4.11a illustrates the effect of 5 minutes of sonication time on a dispersion of OM stabilised AgNP, with pronounced agglomeration observed,

compared to samples dispersed in the absence of sonication, Figure 4.11b, which show smaller, discrete AgNP.

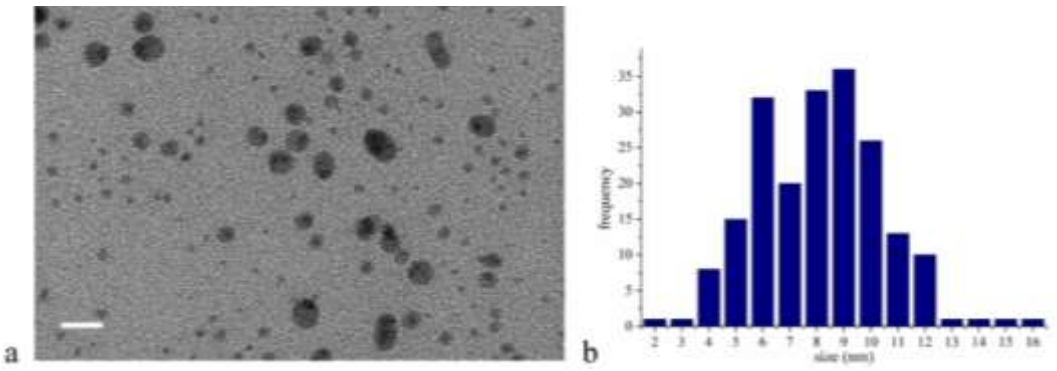

Figure 4.10 TEM micrograph of: a) Octanethiol stabilised AgNP (scale bar 20 nm) with; b) associated particle size distribution histogram (average diameter 8.1 ± 2.3 nm, n = 199), (following sonication for 30 s, Cu / C).

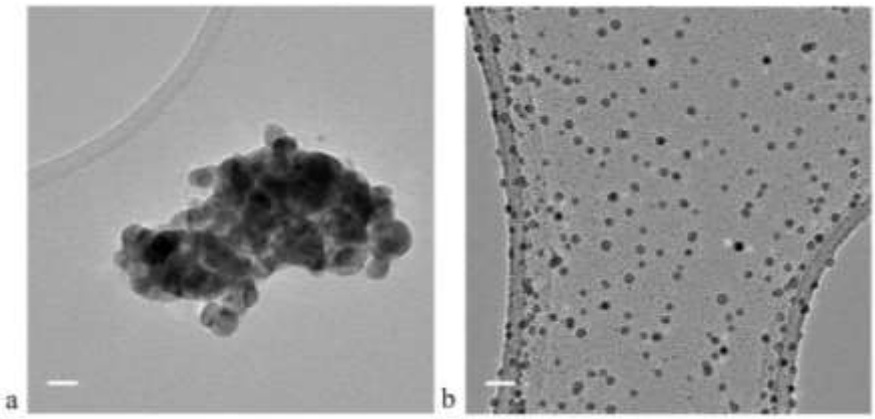

Figure 4.11 TEM images of TS-AgNP stabilised with octanethiol (0.5 mg / 1 ml $CHCl_3$, one drop cast); (a) solution sonicated for 5 minutes and; (b) no sonication. (Scale bars 20 nm).

Interestingly, Figure 4.12 presents conventional bright field, diffraction contrast TEM images of TS-AgNP dispersed from either cyclohexane (Figure 4.12a,c), or from cyclohexane with 30% DDM (Figure 4.12b,d). In this case, it is evident that the

solution has had a significant effect on the NP distribution, purely as a consequence of process of the dispersion. After drying on the TEM support grid, the AgNP dispersed from cyclohexane showed a broadly bimodal size distribution (4 ± 1.5 nm) (Figure 4.12c) and a random dispersion across the grid. Conversely, samples dispersed from cyclohexane in the presence of excess DDM showed a much narrower, single size distribution (3 ± 0.6 nm) and regions of highly ordered superlattices, with close packing (Figure 4.12b), indicative of a surfactant effect [9].

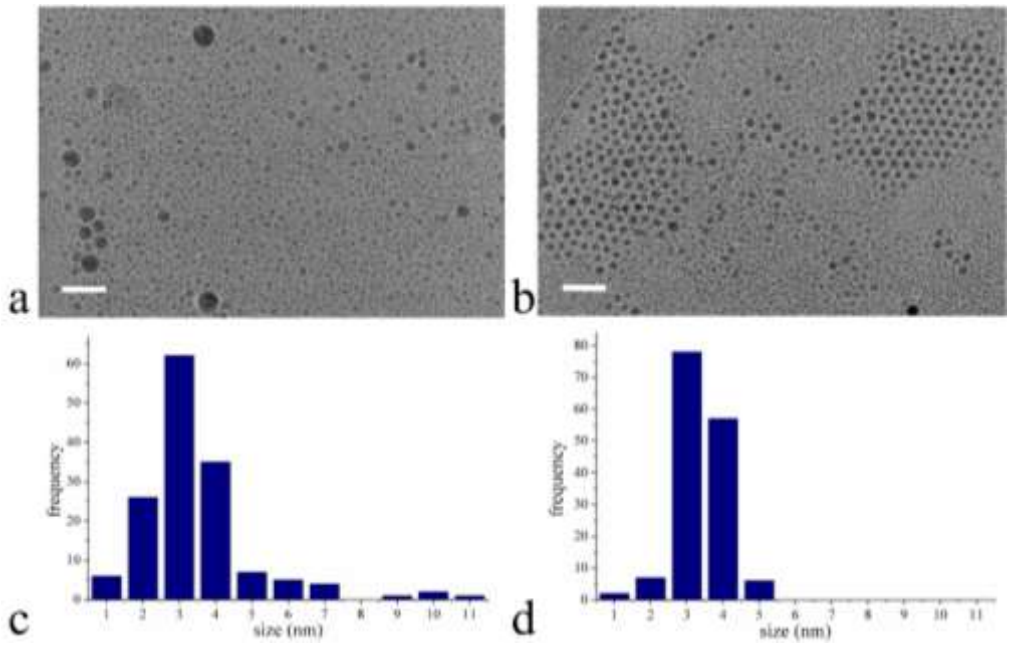

Figure 4.12 TEM micrographs and particle size histograms of TS-AgNP dispersed from (a, c) cyclohexane; and (b, d) cyclohexane in the presence of dodecanethiol, respectively, (scale bars 20nm).

Further, to enable *ex situ* heating experiments, TS-AgNP were deposited onto multi walled carbon nanotubes (MWCNT) by shaking (15 minutes) and brief sonication (3.6 mg TS-AgNP and 3.9 mg MWCNT in 1.5 ml cyclohexane), followed by isolation by filtration. Figure 4.13a presents a low magnification, diffraction contrast TEM

image of TS-AgNP decorated MWCNT, illustrating the nanoparticle dispersion on carbon nanotube edges. Figure 4.13b shows a higher magnification phase contrast image of the TS-AgNP / MWCNT; with TS-AgNP clearly identifiable at the external surfaces of the MWCNT, relative to the electron-optic axis, demonstrating that TS-AgNP could be observed directly without contributions from the support, *i.e.* effectively free-standing.

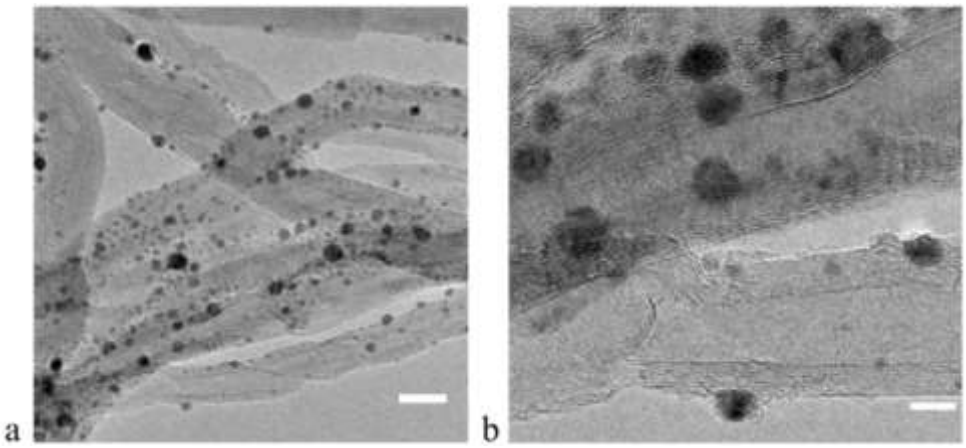

Figure 4.13 TEM micrographs of TS-AgNP deposited onto MWCNT: (a) At low magnification, showing the dispersion of NP on MWCNT (scale bar 20 nm) and; (b) at higher magnification, revealing TS-AgNP relative to the support (scale bar 5 nm).

In summary, it became evident that a systematic approach was needed for sample processing and handling throughout these experimental investigations, recognising that even the simple process of dispersing AgNP samples onto support grids could affect the particle sizes and size distributions returned; whilst additional thiol within solution acted to influence the spatial arrangements of AgNP on the supports. Accordingly, it is emphasised that AgNP were not sonicated, prior to drop casting, for all subsequent experiments reported on here.

4.4 Thermal protocol development

As-synthesised TS-AgNP on various support materials were characterised prior to, during and after *in situ* thermal processing, each performed within a single TEM session to enable the direct observation of transformation processes. For example, Figure 4.14a shows a conventional, bright field TEM image of TS-AgNP (BN/Au support), before thermal processing. The projected dark speckle corresponds to crystalline, spherical AgNP, closely distributed on a BN flake support. Conversely, Figure 4.14b shows a similar site, recorded during the early stages of thermal processing, *i.e.* once the temperature was established at 850°C (Gatan 652 DT holder); demonstrating rapid loss of AgNP from most regions, and the retention of some localised regions showing signs of AgNP agglomeration.

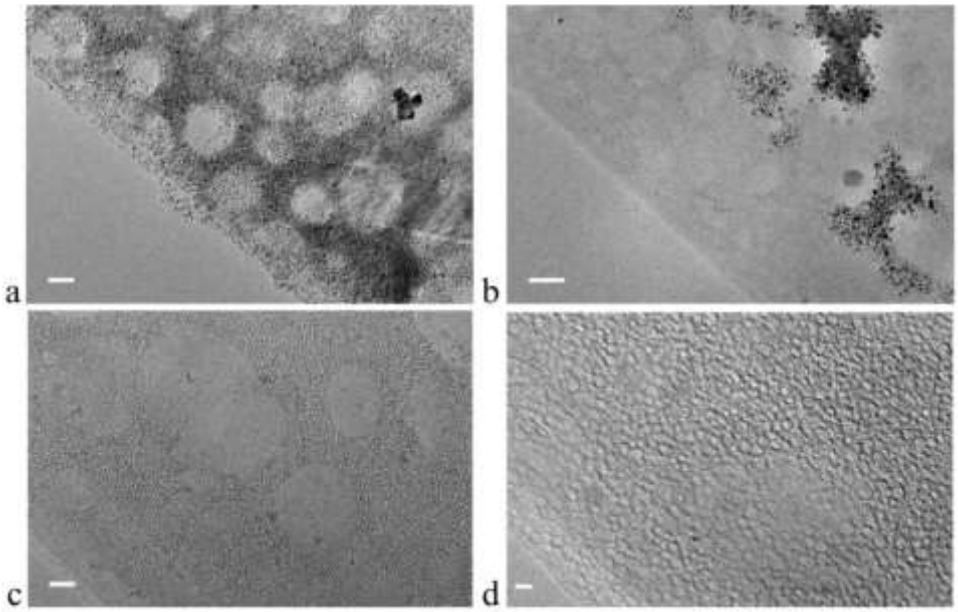

Figure 4.14 Bright field TEM micrographs of: (a) TS-AgNP at ambient temperature and; (b) at 850°C, after rapid heating, showing loss of significant amounts of AgNP, and some signs of residual, localised agglomeration (scale bars 20 nm). Following 15 minutes hold at 850 °C: (c) Complete removal of Ag was observed (scale bar = 20 nm); and (d) at higher magnification, closely packed < 10 nm sized, hollow shell structures became visible (scale bar 10 nm) (BN/Au support).

Further, Figure 4.14c presents a low magnification, bright field TEM image recorded at the conclusion of thermal processing (850 °C, 15 minutes hold). In this case, a complete absence of AgNP was apparent, whilst faint, circular structures had become visible on the BN support. Indeed, the complete removal of AgNP from this field of view was observed in real time, as detailed later. The higher magnification image of Figure 4.12d shows the < 10 nm sized products in more detail, consistent with the development of spheres having hollow interiors. It is commented that thermal drift of the TEM sample holder, compounded by the non-homogeneity of the BN flake support, was an issue during thermal processing prohibiting ease of recording of identical locations at both ambient *and* elevated temperatures. Nevertheless, the size and size distribution of hollow structures formed as a consequence of thermal processing appear broadly the same as that of the TS-AgNP before thermal processing (Figure 4.14a,b).

Similar thermal processing experiments for TS-AgNP using BN/Mo supports yielded similar results. Figure 4.15a presents a low magnification, bright field, diffraction contrast image of starting TS-AgNP recorded at room temperature, with dark speckle corresponding to spherical, crystalline AgNP dispersed over the support material, along with a few larger agglomerations. Conversely, Figure 4.15b shows the < 10 nm sized, hollow structures formed and complete removal of the AgNP following a 15 minutes hold at 850°C (Gatan 652 DT holder). Further, Figures 4.15c,d show TEM micrographs from the same field of view, imaged during the hold stage at 850°C, ~ 2 s apart, illustrating rapid reduction in the number of AgNP observed in real-time, once the correct conditions had become established (four individual NP are highlighted in both images as points of reference). Although these two images are from the same

field of view, overall, some image differences become evident, reflecting slight distortion of the support material at elevated temperature.

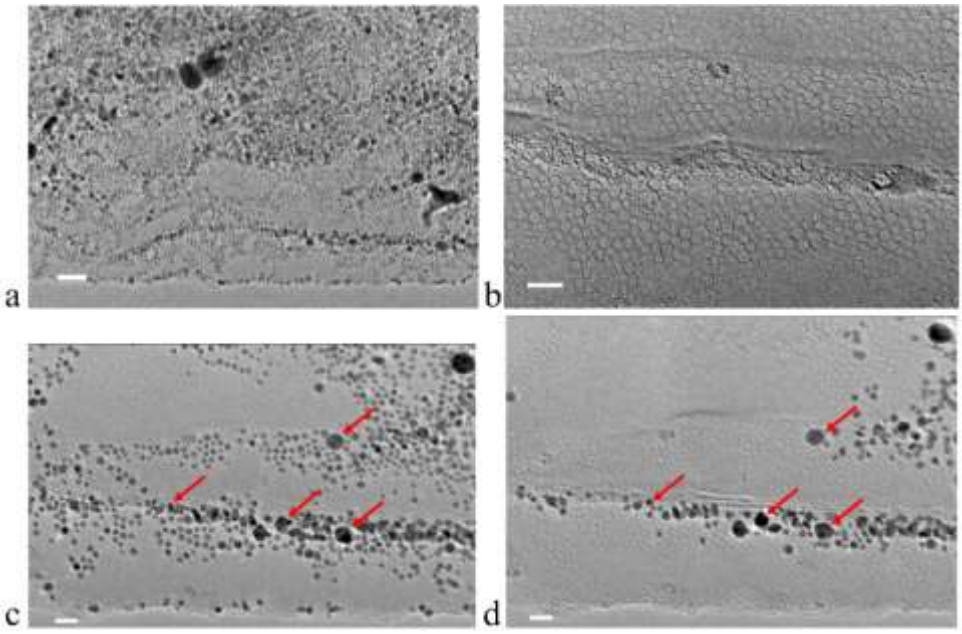

Figure 4.15 Bright field, diffraction contrast TEM images of: (a) TS-AgNP at ambient temperature (scale bar = 500 nm) and; (b) resultant spherical, hollow structures formed after rapid heating to 850°C and a hold time of 15 minutes (scale bar 20 nm). (c, d) TEM images recorded during the hold at 850°C, recorded 2 s apart, indicating rapid removal of the AgNP, once appropriate conditions were established, being replaced by the hollow shell structures (arrows provide a visual guide) (scale bars 20 nm; BN/Mo support).

It is noted that the TEM micrographs of Figures 4.14a and 4.15a relate to TS-AgNP starting materials dispersed onto BN flakes on either Au or Mo TEM grids, leading to the production of strikingly similar, spherical, hollow reaction products, following thermal processing (rapid heating to 850°C and a 15 minutes hold). All other parameters remained constant, *i.e.* the source TS-AgNP starting material, the heating system, temperature, rate of heating, and hold time.

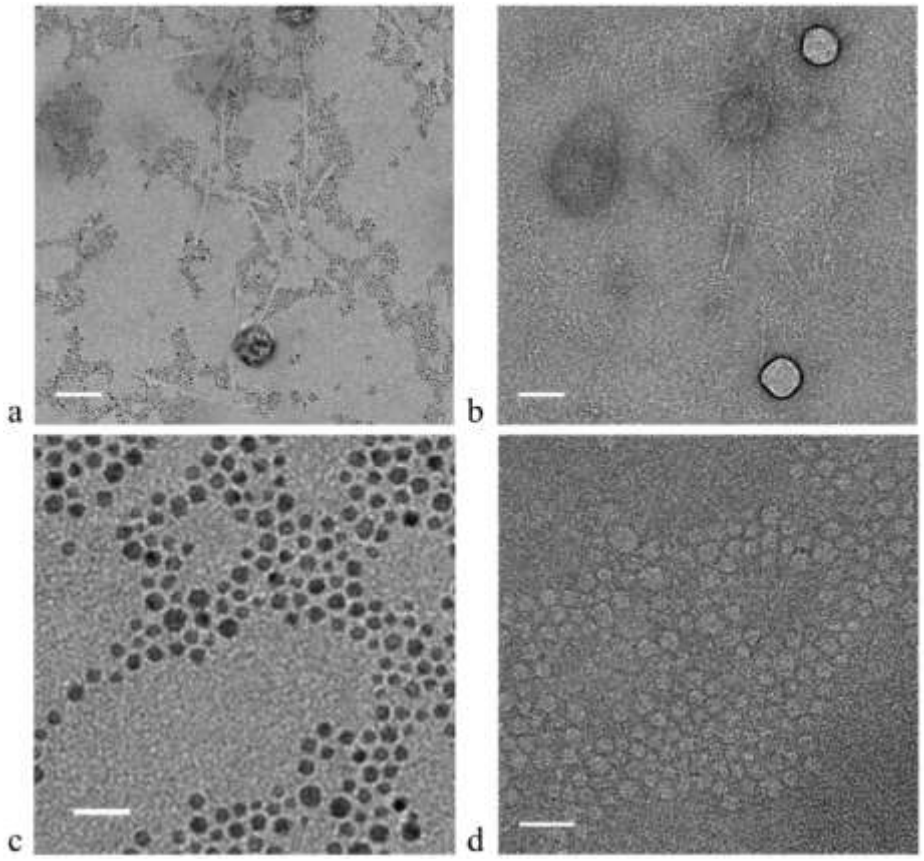

Figure 4.16 Low magnification TEM images of: (a) TS-AgNP ($S_{i3}N_3$ MEMS support) at 23 °C and; (b) hollow shell products produced at 650°C (scale bars 100 nm). (c) Higher magnification, conventional bright field image showing individual, < 10 nm sized TS-AgNP (at 23 °C); and (d) Higher magnification, bright field image recorded at 650 °C, showing details of the hollow shell structures, of commensurate size to the starting TS-AgNP, and the complete absence of Ag (scale bars 20 nm).

Figure 4.16 illustrates the TS-AgNP starting materials and hollow shell products formed at a lower processing temperature of 650°C, with a fast heating rate (23°C to 650°C in 3.29s, at 179°C/s), using a MEMS based heating system (DENSolutions; SH30). Figure 4.16a presents a low magnification, bright field contrast TEM image of TS-AgNP dispersed onto the planar $S_{i3}N_3$ MEMS support of the heating chip, at 23°C, consistent with results presented previously for spherical AgNP, whilst Figure 4.16b shows the resultant structures formed after rapid heating to 650°C, with starting

material and reaction products again appearing coincident on the support. (The presence of a few ~ 100 nm sized patches of contamination in these images collected at 23°C and at 650°C was also evident, and while useful as points of reference, it is noted that such contamination was highly unusual.) Figure 4.16c presents a high magnification TEM image recorded at 23°C, prior to heating, showing the dispersion of discrete, spherical, < 10 nm sized TS-AgNP on the support. Figure 4.16d, presents a high magnification TEM image of the products formed following rapid heating to 650°C, showing hollow structures (circular in projection) with similar morphology and size to the starting material, along with the absence of Ag. However, it is noted that there were some spatial variations in the loss of Ag across the support under these processing conditions.

Figure 4.17 presents further experimental data for thermal processing TS-AgNP, with rapid heating to 850°C (at 92°C/s), using the MEMS heating holder, to ensure complete removal of Ag, whilst allowing images of the same location before and after thermal processing, to be obtained (in this case, no contamination was evident). Accordingly, Figure 4.17a shows a bright field, diffraction contrast TEM image of the starting TS-AgNP (Si_3N_4 MEMS chip), recorded at room temperature (RT), revealing the crystalline AgNP, comprising spheres of average size 6.6 ± 1.4 nm (Figure 4.15c). Conversely, Figure 4.17b shows the same field of view, imaged at 850°C, following rapid *in situ* heating. In this case, the resultant hollow structures were revealed, again matching the positions of the starting TS-AgNP, whilst exhibiting a slightly larger average size of 8.9 ± 1.7 nm (Figure 4.17d).

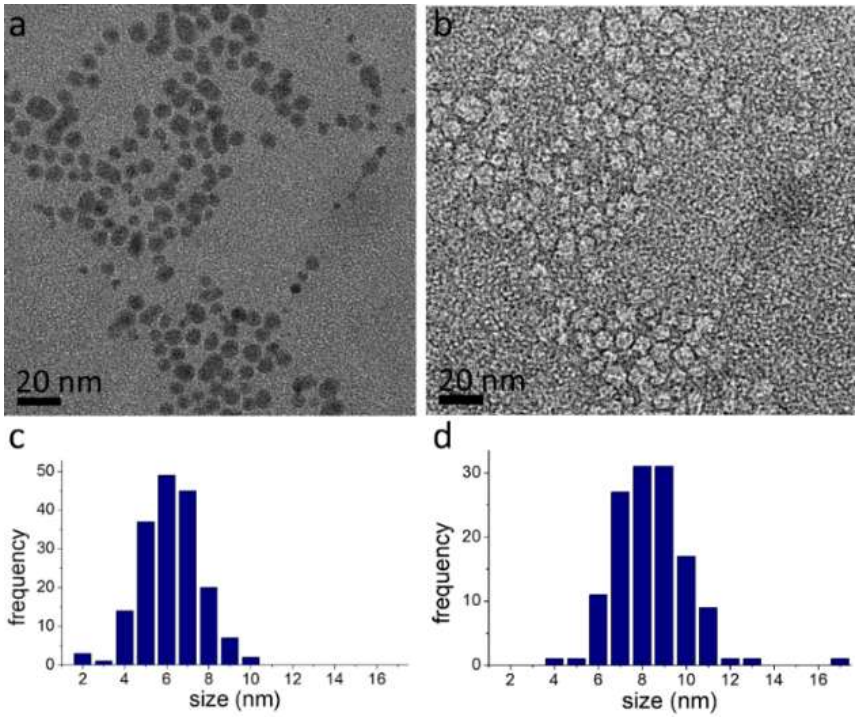

Figure 4.17 Bright field, diffraction contrast TEM micrographs of: (a) TS-AgNP / Si_3N_4 before rapid *in situ* heating to 850°C (at 92°C/s); and (b) the resultant hollow structures, imaged at 850°C. (Scale bars 20 nm). Particle size histograms: (c) Before thermal processing (corresponding to AgNP); and (d) after thermal processing (corresponding to hollow shell structures formed).

Complementary, wide field of view energy dispersive spectroscopy (EDS) investigations (Figure 4.18) confirmed the presence of Ag within the starting templated structures, whilst indicating its near complete removal from the product. In addition, carbon remains on the support material, with low levels of sulphur; with other peaks are attributable to the support material or residuals from the solvent (Si, N, O and Cl), the presence of oxygen may tentatively be ascribed to oxidation of the silicon nitride support material at elevated temperatures [10].

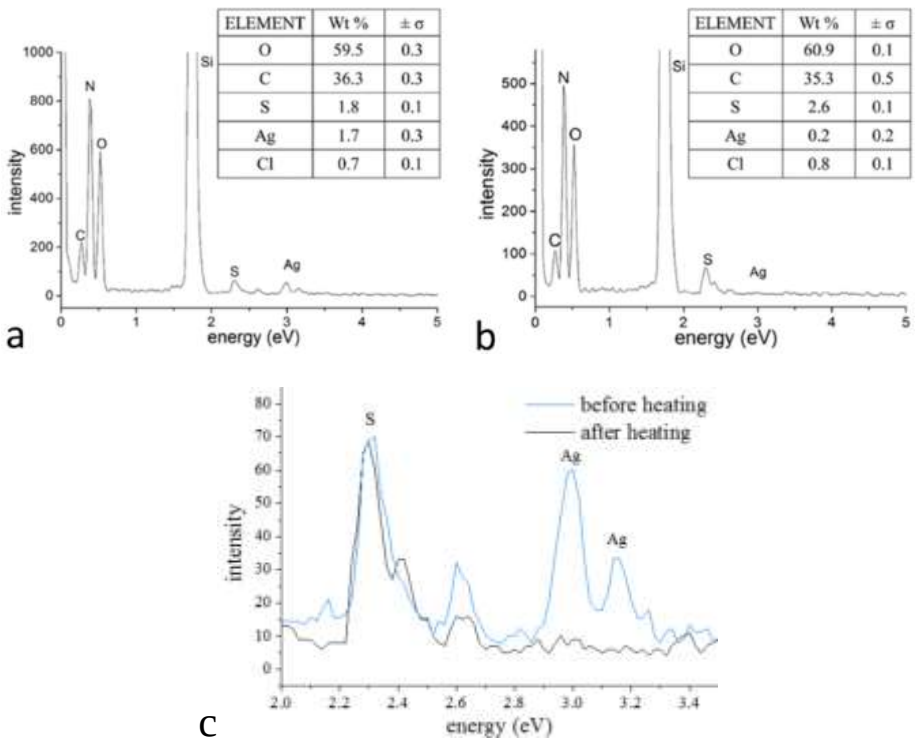

Figure 4.18 Wide field of view EDS spectra (recorded at RT) for TS-AgNP dispersed onto a planar Si_3N_4 MEMS support: (a) Before and (b) after thermal heating to 850°C (at 92°C/s), indicating the retention of C and S. (c) Comparison of the two spectra, over the range 2 - 3.4 eV, demonstrates the near complete removal of Ag from the carbon product.

Further, Figures 4.19a,b present high magnification, TEM images of these developed hollow carbon nanoshells (HCNS), in this case recorded 8 days after processing, at RT, confirming the stability of the resultant structures. The majority of these particles comprised complete, distinct carbon shells, being spherical in nature and hollow, consistent with the complete removal of the AgNP template. It is noted that a small proportion of these HCNS particles appeared to be fragmented (Figure 4.19a, arrowed), indicative of a heating rate effect on their formation.

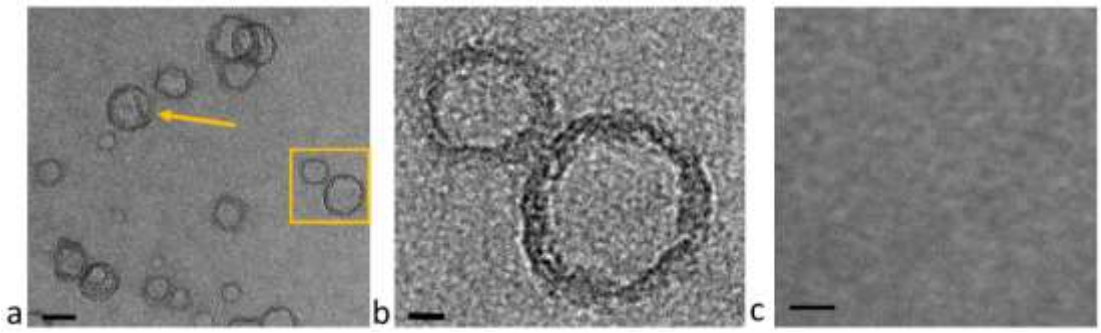

Figure 4.19 High resolution TEM micrographs providing a more detailed view of the resultant HCNS structures (imaged at 100kV at RT). (a) Discrete HCNS and example fragmented HCNS (arrowed, scale bar 20 nm); and (b) higher magnification image (scale bar = 5 nm) of region indicated by box in (a). (c) Bright field TEM image of Si_3N_4 'blank' window, demonstrating the underlying, flocular structure of this support material (scale bar 20 nm).

Furthermore, Figure 4.19c shows a bright field TEM image of an as-supplied Si_3N_4 MEMS window, the structure of this support material is evident, limiting detailed morphological and structural investigations of the deposited TS-AgNP and HCNS products. Hence, to gain improved imaging and insight into the development of these HCNS structures, TS-AgNP were deposited onto MWCNT supports (TS-AgNP@MWCNT), the tilting of which allowed discrete NPs to be imaged edge-on to the support, *i.e.* effectively free standing, without contribution from the background material. It was found that furnace heating of TS-AgNP@MWCNT *ex situ* produced morphologies commensurate with the HCNS structures formed *in situ*. For example, Figure 4.20a presents a high magnification image of an individual TS-AgNP decorated MWCNT, illustrative of the amorphous thiol coated AgNP prior to thermal processing, whilst Figure 4.20b unambiguously demonstrated the formation of a hollow carbon shell (following *ex situ* heating at 850°C for 3 h).

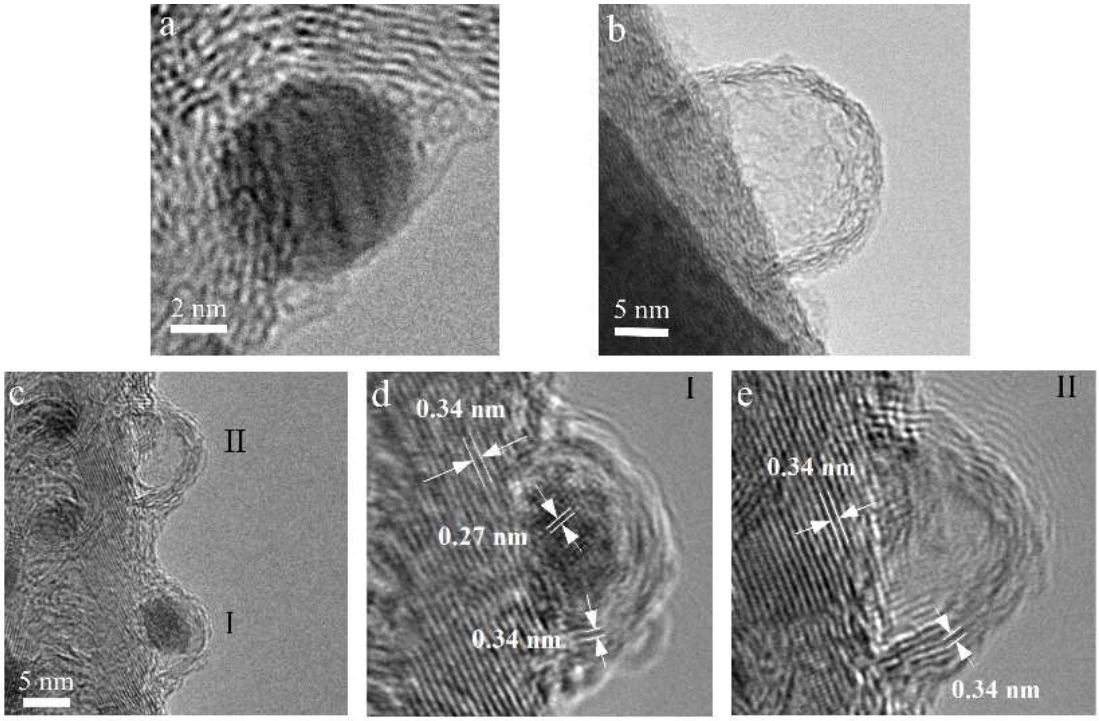

Figure 4.20 High magnification, phase contrast TEM micrographs of: (a) TS-AgNP@MWCNT before *ex situ* heating at 850°C for 3 h; (b) resultant HCNS, imaged at RT. (c) Phase contrast TEM images showing (d) Ag templated (I) and (e) hollow (II) graphitic carbon shell structures (G-HCNS).

In particular, the TEM images of Figure 4.20c, recorded under flat focus conditions, illustrates two neighbouring NPs which were (I) Ag-filled and (II) hollow. The phase contrast image of Figure 4.20d, recorded under conditions of slight defocus, showed the development of an irregular, graphitic shell surrounding the AgNP (*i.e.* G-AgNP); whilst Figure 4.20e confirmed the graphitic nature of the resultant hollow shell structure (G-HCNS). The HCNS walls comprised typically four layers on average, with graphitic spacing 0.34 nm [11]. Further, Figure 4.21 presents a complementary tilt series view of similar HCNS products, confirming their spherical nature, and illustrating their hollow interiors. It is noted that the graphitic walls of hollow carbon shell nanostructures form prior to removal of the AgNP template, at elevated

temperature [12], consistent with the catalytic activity of Ag during carbon shell formation [13].

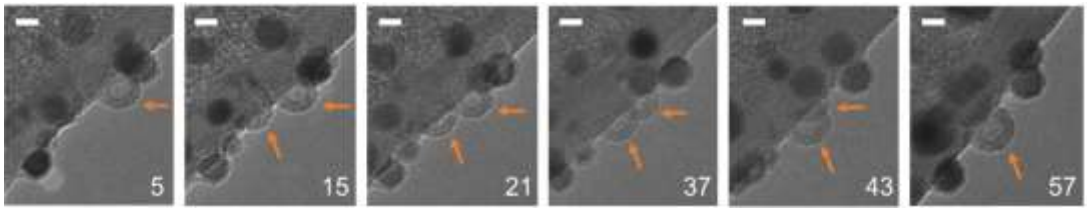

Figure 4.20 TEM tilt series, showing structures produced from the *ex situ* thermal processing of TS-AgNP on MWCNT (850°C for 3 h), illustrating the spherical nature of the HCNS product, tilt angle in degrees (scale bars 10 nm). JEOL 2100F operating at 100 kV.

The HCNS illustrated in Figures 4.16 and 4.17 have very similar appearances, whilst noting the AgNP starting materials are stabilised with different alkane thiols; OM and DDM, respectively.

4.5 Bulk characterisation of hollow carbon products

4.5.1 Raman Spectroscopy

Figure 4.19 presents a first order Raman spectrum acquired from HCNS products formed from TS-AgNP on Si_3N_4 supports, thermally processed *in situ* at 850°C, with a fast heating rate. Data collection and interpretation were performed by Dr G. Rance. The general peak shapes illustrated and weak intensity features in the second order spectra (data not shown), associated with combination modes and overtones are consistent with the formation of highly disordered graphitic carbon in HCNS products.

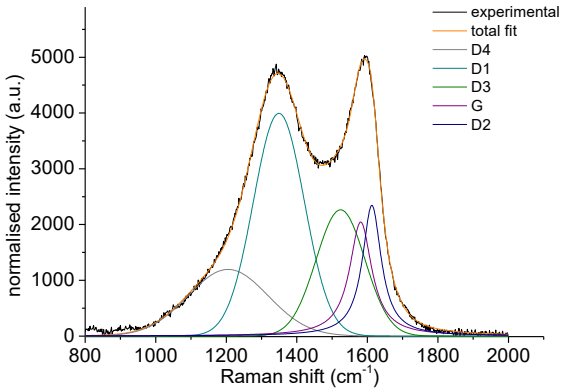

Figure 4.19 First order Raman spectra (λ_{ex} = 532 nm) from hollow carbon structures confirming the disordered graphitic nature of the products; the spectrum has been baseline-corrected using a third-order polynomial subtraction and fit using a five-band model analogous to reported methods, [14] (χ^2 = 2.3) *Data collection and analysis performed by Dr G. Rance.*

Table 4.1 First order Raman bands assignment [14, 15,16] (vs = very strong, s = strong, m = medium, w = weak).

Band [a]	**Raman shift / cm^{-1}**	**Proposed vibrational mode assignment**
G	1581 s	Ideal graphitic lattice (E_{2g} symmetry)
D1 (D)	1349 vs	Disordered graphitic lattice (A_{1g} symmetry)
D2 (D')	1613 s	Disordered graphitic lattice (E_{2g} symmetry)
D3 (D", A)	1524 m	Amorphous carbon
D4 (I)	1205 m	Disordered graphitic lattice (A_{1g} symmetry), polyenes, ionic impurities

[a] alternative band designations of earlier studies are bracketed.

The spectra is dominated by two broad, overlapping features centred around 1350 and 1580 cm^{-1}, nominally attributable to the defect (D) and graphite (G) bands, respectively. Although the intensity ratio (I_D:I_G) of these bands has frequently been used to quantify disorder in graphitic nanostructures, results are often unreliable for more disordered graphitic structures, such as these < 10 nm HCNS. This unreliability arises due to a number of factors; ambiguities associated with the use of peak heights

or areas to calculate I_D:I_G ratios; the non-linearity of the I_D:I_G relationship and inter-defect distance within the graphitic lattice itself [16]. Additionally, it is also probable that this spectral region comprises of a superposition of at least five different contributions. Therefore, to analyse the spectrum four Lorentzian-shaped bands (G, D1, D2, D4) and a Gaussian-shaped band (D3) were carefully deconvoluted, Table 4.1, [14]. Intensity ratios of both the D1 to G bands (I_{D1}:I_G =3.08) and D3 to G bands (I_{D3}:I_G = 1.68), relating to the ratios of disorder - order in graphitic domains and to amorphous carbon - graphitic domains, respectively, are both high, providing quantitative evaluation of these highly disordered graphitic carbon structures.

4.5.2 X-Ray Photoelectron Spectroscopy

Figure 4.20 presents XPS spectra from HCNS products formed from TS-AgNP on Si_3N_4 supports, thermally processed to 850 °C. The Ag 3d and C 1s peaks are presented, indicating trace amounts of Ag (0.15 At %) with the broad peak ~ 285 eV, suggesting carbon is present in two chemical states, likely to include a graphitic contribution, expected at 284.4 eV [17]. However, due to support tomography, signal contributions from regions at the edge of support windows could not be excluded and confound further analysis.

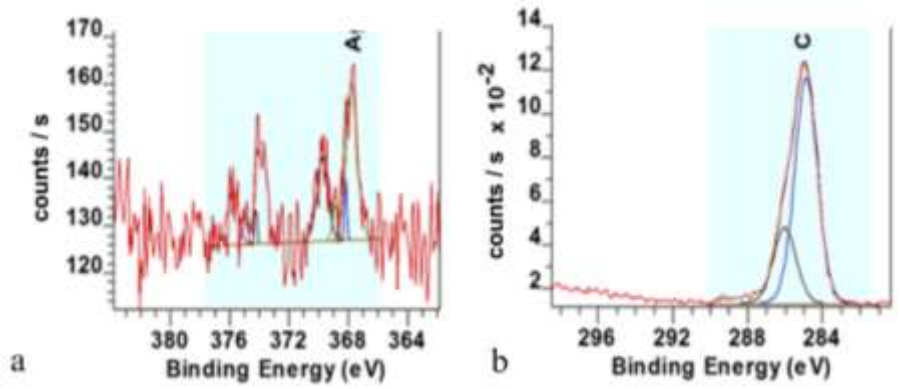

Figure 4.20 XPS for TS-AgNP on Si_3N_4, heated to 850°C (a), the Ag 3d peak suggests trace amounts of Ag remain, and; (b), the C 1s peak indicates the presence of carbon, with peak broadness suggesting two components, with a graphitic contribution, however, contributions due to adventitious carbon confound further analysis. *Data collection and interpretation by Dr E. Smith.*

4.6 Discussion

Discrete, < 10 nm sized HCNS have been formed from the single-step, thermal processing of TS-AgNP, by *ex situ* heating on a MWCNT support, or as observed in real time via *in situ* TEM on BN flakes (Au or Mo grid), or Si_3N_4 MEMS supports. The identical location of the HCNS product with the starting dispersion of TS-AgNP, as observed during *in situ* TEM thermal processing, provides direct evidence for the templated formation of HCNS on AgNP (Figure 4.15). In particular, the size of these HCNS particles (8.9 ± 1.7 nm for the sample set shown here) is defined by, and slightly larger than, the size of the AgNP template (6.6 ± 1.4 nm), as compared with the previous smallest HCNS reported to date of ~20 nm, that have a significant size distribution of 20 – 40 nm [58].

Most of the HCNS product, formed *in situ* comprised complete spheres, with the occasional observation of partially fragmented spheres (Figure 4.17), suggesting an

effect of variable localised temperature, or rate of heating, on their formation. Nevertheless, the defining features for the product, *i.e.* hollow interior and < 10 nm sized spheres are clearly evident (Figure 4.13). For the case of structures observable free from background contributions at the edges of MWCNT supports (Figure 4.17), HCNS interlayer spacings commensurate with graphitic spacings (0.34 nm) [11] were observed, whilst noting that these structures are likely to be disordered [19] because of their very pronounced curvatures.

With regard to the HCNS products processed *in situ*, definitive visual evidence for graphitisation could not be obtained, BN flakes were damaged by the electron beam when attempting HCNS imaging at higher magnifications (Figures 4.14, 4.15), [20], whilst products on planar Si_3N_4 supports (Figures 4.16, 4.17), were considered to be compromised by the morphology and thickness of the support, combined with the very high levels of curvature associated with such < 10 nm sized shells, acting to mask the structural details of the developed shell walls. However, indirect evidence from complementary Raman spectroscopy confirmed the presence of highly disordered graphitic domains for samples processed *in situ* (Table 4.1); with high intensity peak ratios indicating the presence of both disordered and graphitic carbon (I_{D1}:I_G = 3.08) [14]), suggesting that HCNS graphitisation at elevated temperature is not MWCNT template specific. The presence of sp^3 carbons is additionally tentatively suggested by XPS data for these HCNS products on Si_3N_4 supports, while the absence of graphitic carbons in TS-AgNP starting materials was illustrated by both IR and NMR data.

Whilst a contribution from the support material on graphitisation cannot be discounted, it is considered that the process of graphitisation is thermally induced and catalysed by Ag [13] in this instance. Further, the ability to form commensurate

HCNS structures by *ex situ* furnace heating of TS-AgNP (Figure 4.13) confirms that this thermally mediated process is not governed by electron beam effects. Indeed, once formed, the HCNS appear to be very stable.

Accordingly, it is proposed that the formation of HCNS, from the thiol stabilising layer of TS-AgNP, proceeds via thermally driven dehydrogenation [21], with the crosslinking of alkane chains, the transformation of sp^3 to sp^2 carbon during graphitisation, and finally Ag template removal (Figure 4.21). Indeed, the appearance of carbon shells surrounding AgNP (Figures 4.12b,c and Figure 4.17c), during both *in situ* and *ex situ* heating experiments, demonstrates that the development of carbon shells proceeds at the surfaces of AgNP, in advance of template removal. Hence, it is considered that the AgNP core acts both as a physical template for HCNS and catalyses the formation of carbon shells [22]. The residual presence of small amounts of Ag within some of the developed HCNS, indicative of incomplete processing, is also consistent with the removal of AgNP after shell formation. It is suggested that Ag migrates through the shells via structural defects [23]. With regard to the EDS observation of low S levels within the product, this heteroatom is known to terminate unsaturated vacancies at graphitic domain edges, resulting in thermodynamic stabilisation [24].

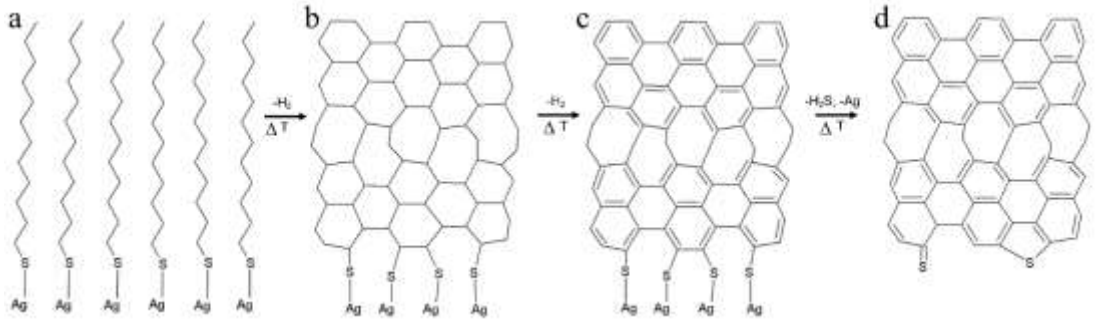

Figure 4.21 Proposed schematic mechanism for HCNS formation during rapid thermal processing (TP-1), up to 850°C: (a) Surface of thiol stabilised AgNP; (b) cross-linking of alkane chains; (c) graphitisation; and (d) loss of AgNP template to leave a stabilised HCNS product.

The formation of HCNS, catalysed and templated by AgNP, may be similar to CNT formation at the surface of metal NP during chemical vapour deposition (CVD) [25]. The development of graphitic structures, defined by NP diameter, occurs in both cases, however during CVD CNT formation the carbon source is replenished, but HCNS are formed from thiol stabilised AgNP starting materials, and the amount of carbon is limited. Although CNT formation mechanisms are debated [26], a simplified, general atomistic mechanism is considered to proceed from the high temperature decomposition of a carbon precursor, the C atoms from which then diffuse onto and dissolve into a metal NP catalyst [27]. When the concentration of C in the metal NP is sufficiently high, carbon networks form at the NP surface, additional diffused C atoms integrate into these structures, resulting in CNT growth. Despite the solubility of C in Ag being extremely low [28], this metal has been shown to catalyse the formation of single-walled CNT at suitably high temperatures (~800°C) [29]. This may possibly be explained by thermally induced advantageous changes in carbon adsorption, atom mobility, bulk and surface diffusion [26] contributing to the catalytic effect.

Spatial variations in the nature of the HCNS product were evident for both *ex situ* and *in situ* processed samples, suggesting a combination of effects relating to individual NP size, temperature and heating rate. For example, the close proximity of filled and empty nanoshells processed *ex situ* (Figures 4.17c,d,e and Figure 4.18) is considered indicative of a subtle NP size effect; whilst samples processed on BN support flakes *in situ* showed examples of well-defined HCNS and regions of partially processed TS-AgNP at the onset of heating, possibly arising due to a temperature (thermal conduction / thermal gradient) effect, from a combination of position on the BN support flake and support thickness, with the almost complete removal of Ag over a few seconds.

With regard to the aggregation of TS-AgNP (Figure 4.11) after sonication, this is also due to localised effects, with acoustic cavitation inside bubbles producing very high localised temperatures and pressures; additionally, collapsing bubbles produce shock waves, influencing localised energetics and producing NP aggregation [30].

For the purpose of materials control and the potential for scale-up, and from a wider reaction kinetics perspective, it is recognised that further work is needed to separate out the competing roles of temperature, heating rate, template size and support material on the development of these HCNS products.

The formation of bespoke HCNS (of sizes > 70 nm) has been achieved to date via the use of multi-step processing, *e.g.* carbon coating of hard template materials, necessitating a synthetic step and thermal treatment, in advance of chemical template removal. Here, we have demonstrated that thiol stabilised AgNP, can be transformed into < 10 nm sized HCNS, using a facile one-step thermal process. This approach provides for excellent size control of the HCNS product via appropriate AgNP

template selection. The addition of DDM to TS-AgNP solutions at the sample preparation stage prior to drop casting, promotes self-assembly and produces narrower AgNP size distributions, leading to the formation of commensurate HCNS after thermal processing, however, for particle size determination addition of DDM requires acknowledgment.

4.7 Conclusions

The formation of < 10 nm sized HCNS from one-step thermal processing of TS-AgNP has been demonstrated on different support materials. The resulting product has a hollow appearance and disordered graphitic walls, which form prior to thermally induced removal of Ag.

Discrete, < 10 nm sized HCNS structures have been formed from TS-AgNP via heat induced transformation, using a facile one-step process, by either *ex situ* heating on a MWCNT support, or *in situ* heating within a TEM on BN flake or Si_3N_4 MEMS support. Direct evidence for the templated formation of predominantly complete, spherical HCNS on AgNP under rapid heating to > 650 °C is presented, with the size of the resultant HCNS being slightly larger than that of the AgNP template. These very stable HCNS exhibited clearly the twin characteristics of hollow interiors and highly disordered, sphere wall graphitisation. It is proposed that the HCNS formation mechanism, from the thiol stabilising layer of TS-AgNP, proceeds via thermally driven dehydrogenation, with crosslinking of alkane chains and transformation of sp^3 to sp^2 during graphitisation, in advance of AgNP template removal. Accordingly, the AgNP core acts both as a physical template for HCNS and catalyses the graphitisation

of carbon. Spatial variations in the development of the reaction product reflects predominantly a competition between the thermal transformation of the TS-layer and loss of the AgNP template effect. It is considered that one-step thermal processing of thiol stabilised AgNP provides for excellent size control of the HCNS product, via appropriate AgNP template selection.

References

1 Kora, A. J., Beedu, S. R., Jayaraman, A., *Size-controlled green synthesis of silver nanoparticles mediated by gum ghatti (Anogeissus latifolia) and its biological activity*, Org. Med. Chem. Lett. (2012) 2 pp17.

2 Kang, S. Y., Kim, K., *Comparative Study of Dodecanethiol-Derivatized Silver Nanoparticles Prepared in One-Phase and Two-Phase Systems*, Langmuir (1998) 14 pp226-230.

3 Gonzalez-Carter, D. A., Leo, B. F., Ruenraroengsak, P., Chen, S., Goode, A. E., Theodorou, I. G., K Chung, K. F., Carzaniga, R., Shaffer, M. S. P., Dexter, D. T., Ryan, M. P., Porter, A. E., *Silver nanoparticles reduce brain inflammation and related neurotoxicity through induction of H_2S-synthesizing enzymes*, Nature, Sci. Rep. (2017) 7 pp42871.

4 Mayergoyz, I. D., (2013). *Plasmon resonances in nanoparticles*. (World Scientific series in nanoscience and nanotechnology; v. 6). Singapore; London.

5 Williams, D. H. and Fleming, I., (1989) *Spectroscopic Methods in Organic Chemistry*, McGraw-Hill. (4th ed., rev. ed.). London.

6 Hasan, M., Bethell, D., Brust, M., *The Fate of Sulfur-Bound Hydrogen on Formation of Self-Assembled Thiol Monolayers on Gold: ^1H NMR Spectroscopic Evidence from Solutions of Gold Clusters*, J. Am. Chem. Soc., (2002) 124 (7) pp1132–1133.

7 Hostetler, M. J., Wingate, J. E., Zhong, C. J., Harris, J. E., Vachet, R. W., Clark, M. R., Londono, J. D., Green, S. J., Stokes, J. J., Wignall, G. D., Glish, G. L., Porter, M. D.. Evans N. D., and Murray, R. W., *Alkanethiolate gold cluster molecules with core diameters from*

1.5 to 5.2 nm: Core and monolayer properties as a function of core size, Langmuir (1998) 14(1) pp17-30.

8 Perkas, N., Amirian, G., Applerot, E., Efendiev, Y., Kaganovskii, A., Ghule V., Chen B-J., Ling, Y.-C., Gedanken, A., *Depositing silver nanoparticles on/in a glass slide by the sonochemical method*, Nanotechnology, (2008) 19 pp43.

9 Watts, J. A., Fay, M. W., Khlobystov, A. N., Brown, P.D., *Effect of TEM grid deposition method on the dispersion of thiol-stabilised nanoparticles*, J. Phys. Conf. Ser. (1997) 902, 1.

10 Filla, J., Aguzzoli, C., Sonda, V., Farias, M. C. M., Soares, G. V., Baumvol, I. J. R., Figueroa, C.A., *Nanoscale friction of partially oxidized silicon nitride thin f*ilms, Surf. Coat. Tech. (2011) 205 pp4528-4531.

11 Iijima, S., Yudasaka, M., Yamada, R., Bandow, S., Suenaga, K., Kokai, F., Takahashi, K., et al., *Nano-aggregates of single-walled graphitic carbon nano-horns*, Chem. Phys. Lett., (1999) 309 (3-4) pp165-170.

12 Kim, S., Song, Y., Heller, M. J., *Seamless aqueous arc discharge process for producing graphitic carbon nanostructures*, Carbon (2017) 120 pp83-88.

13 Endo, O., Nakamura, M., Amemiya, K., Ozaki, H., *Graphene nanoribbons formed from n-alkane by thermal dehydrogenation on Au(111) surface*, Surf. Sci. (2015) pp44-48.

14 Sadezky, A., Muckenhuber, H., Grothe, H., Niessner. R., Pöschl, U., *Raman microspectroscopy of soot and related carbonaceous materials: Spectral analysis and structural information*, Carbon (2005) 43 (8) pp1731-1742.

15 Ferrari, A., Robertson, J., *Interpretation of Raman spectra of disordered and amorphous carbon*, Phys. Rev. B (2000) 61 (20) pp14095-14107.

16 Cançado, L. G., Jorio, A., Martins, E. H., Stavale, F., Achete, C.A., Capaz, R. B., Moutinho, M. V. O., Lombardo, A., Kulmala, T. S., Ferreira, A. C., *Quantifying defects in graphene via Raman spectroscopy at different excitation energies*, Nano letters (2011) 11 (8) pp3190-6.

17 Mérel, P., Tabbal, M., Chaker, M., Moisa, S., Margot, J., *Direct evaluation of the sp^3 content in diamond-like-carbon films by XPS,* Appl. Surf. Sci. (1998) 136 (1–2) pp105-110.

18 Xu, F., Tang, Z., Huang, S., Chen, L., Liang, Y., Mai, W., Zhong, H., Fu. R., Wu, D., *Facile synthesis of ultrahigh-surface-area hollow carbon nanospheres for enhanced adsorption and energy storage,* Nature Comm. (2015) 6 7221 pp1-10.

19 Banhart, F., The role of lattice defects in the formation of new carbon structures under electron irradiation, J. Electron Microsc. (2002) 51 (1) pp189-194.

20 Alem, N., Ermi, R., Kisielowski, C., Rossell, M. D., Garnett, W., Zettl, A., *Atomically thin hexagonal boron nitride probed by ultrahigh-resolution transmission electron microscopy*, Phys. Rev. B (2009) 80 pp155425.

21 Shih, J-J., Kuo, K-H., Yang, C-M., Lin, J-L., Fan, L-J., Yang, Y-W., *Thermal dissociation of $HSCH_2CH_2OH$ on Cu(1 1 1),* Surface Science, (2008) 602 (21) pp3266-3271.

22 Yaakob, Y., Yusop, M. Z. M., Takahashi, C., Rosmi, M. S., Kalitaa, G., Tanemura, M., *In situ transmission electron microscopy of Ag-incorporated carbon nanofibers: the effect of Ag nanoparticle size on graphene formation,* RSC Adv. (2015) 8 (**5)** pp5647-5651.

23 Banhart, F., Redlich, P., Ajayan, P.M., *The migration of metal atoms through carbon onions*, Chem. Phys. Lett. (1998) 292 (4) pp554-560.

24 Chuvilin, A., Bichoutskaia, E., Gimenez-Lopez, M. C., Chamberlain, T. W., Rance, G. A., Kuganathan, N., Biskupek, J., Kaiser, U., Khlobystov, A. N., *Self-assembly of a sulphur-terminated graphene nanoribbon within a single-walled carbon nanotube*, Nat. Mater. (2011) 10 (9) pp687-692.

25 Yoshida, H., Takeda, S., Uchiyama, T., Khono, H., Homma, Y., *Atomic-Scale In-situ Observation of Carbon Nanotube Growth from Solid State Iron Carbide Nanoparticles,* Nano Lett. 8, 7 (2008) pp2082-2086.

26 Juornet, C., Picher, M., Jourdain, V., *Carbon nanotube synthesis: from large-scale production to atom-by-atom growth,* Nanotechnology 23 (2012) 142001.

27 Gohier, A., Ewels, C. P., Minea, T. M., Djouadi, M. A., Carbon nanotube growth mechanism switches from tip- to base-growth with decreasing catalyst particle size, Carbon 46 (10) (2008) pp1331-1338.

28 Karakaya, I., Thompson, W. T., *The Ag-C (Silver-Carbon) System*, Bull. Alloy Phase Diagr. 3 (1988) pp226-227.

29 Takagi, D., Homma, Y., Hibino, H., Suzuki, S., Kobayashi, Y., Single-Walled Carbon Nanotube Growth from Highly Activated Metal Nanoparticles, Nano Letters 6 (12) (2006) pp2642-2645.

30 Suslick, K. S., Price, G. P., *Applications of ultrasound to materials chemistry*, Annu. Rev. Mater. Sci. (1999) 29 (1) pp295-326.

5.0 Effects of heating regime on structures of HCNS

5.1 Introduction

In Chapter 4, it was shown that hollow, < 10 nm sized, graphitic carbon nanoshells could be produced by heating TS-AgNP to temperatures > 650°C, with fast heating rate, either *in situ* within a TEM (on BN or Si_3N_4 supports), or *ex situ* on multi-walled carbon nanotube (MWCNT) supports. This Chapter considers the influence of various process parameters on the products formed, with specific attention given to the effects of heating rate, as outlined in Table 5.1.

Table 5.1 Overview of parameters to investigate the effect of heating rate on HCNS formation.

TS-AgNP size / nm	Support	Heating system	Heating rate / °C.s^{-1}	Initial temp / °C	Final temp / °C	Hold time / minutes
3.4 ± 0.9	FLG / Mo	Gatan *in situ*	**~ 14**	23	850	-
5.0 ± 1.5	GO / Cu	Gatan *in situ*	**~ 18**	23	750	-
				750	850	~ 20
4.1 ± 1.4	GO / Cu	Gatan *ex situ*	**~ 14**	23	850	5
6.7 ± 2.4	MWCNT	muffle furnace *ex situ*	**~ 20**	20	850*	180
6.6 ± 1.4	Si_3N_4	MEMS *in situ*	**92**	23	850	-
6.6 ± 1.4	Si_3N_4	MEMS *in situ*	**1.5**	23	650	-
			2	650	900	-

**Pre-set furnace temperature, hence ramp rate was estimated.*
FLG = few layered graphene flakes, GO = Graphene oxide flakes.

The effects of support materials on HCNS production, the process of removal of Ag templates at elevated temperature, and aspects of localised processing variability are also considered. Further, attention is given to variations in the approach to *ex situ* heating. Accordingly, Section 5.2 presents data obtained from the heating of TS-AgNP to 750 or 850°C, at an intermediate heating rate of ~ 10°C/s, using a Gatan heating stage (652 double tilt) *in situ* within the TEM. Complementary to this, Section 5.3 details the *ex situ* heating of TS-AgNP to 850°C, either using the Gatan heating stage (~ 10°C/s), or placed in a muffle furnace (850°C) with samples sealed under vacuum inside a quartz ampoule. Section 5.4 then reports on the more controlled *in situ* MEMS (DENSolutions; SH30) processing of TS-AgNP, with fast (~100°C/s) and slow (~1°C/s) heating rates.

5.2 Heating TS-AgNP at ~ 10°C/s (*in situ* TEM; Gatan sample holder)

Figure 5.1a presents a low magnification image of TS-AgNP stabilised with an equimolar mixture of 1-dodecanethiol (DDM) and 11-(*1H*-pyrrol-1-yl)undecane-1-thiol (PUT) deposited (0.5 mg / 1 mL cyclohexane and 10% DDM, solution filtered) onto few-layered graphene (FLG) flakes / Mo grid (prepared in-house). At 23°C prior to thermal processing at 850°C (~ 14°C/s; Gatan holder), the presence of small, (3.4 ± 0.9 nm, n = 103) discrete, spherical TS-AgNP are shown to be distributed across the support. Conversely, bright field imaging at 850°C (Figure 5.1b) revealed the development of a foam-like material, with some broadly circular, hollow structures at the support edges (25.5 ± 1.6 nm; n = 7), along with substantially larger agglomerations of AgNP (~ 20 – 80 nm). The relatively large size of both residual

AgNP and irregular, hollow / foam structures after heating, compared to the TS-AgNP starting material, constitutes evidence for Ostwald ripening of the Ag templates [1] prior to C-shell/foam formation, and is suggestive of the combined effects of inefficient heat transfer and support inhomogeneity.

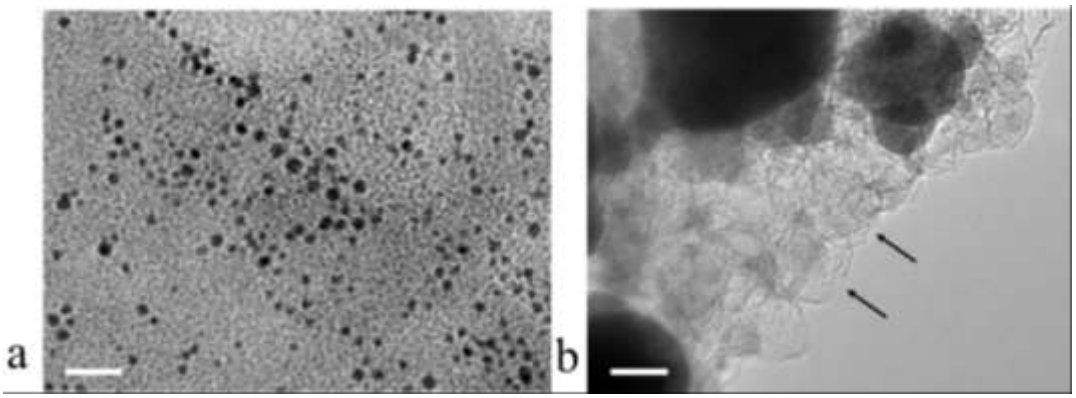

Figure 5.1 (a) Low magnification, bright field TEM image of TS-AgNP (FLG / Mo) at 23°C, and; (b) higher magnification image showing the development of a foam-like material at the support edges, with some irregular, hollow structures imaged at 850°C (arrowed), and large (20 – 80 nm), dark regions identified as Ag (scale bars 20 nm).

Further, Figure 5.2a presents a low magnification TEM image of TS-AgNP (DDM/PUT) on a graphene oxide (GO)/Cu (EMResolutions) support (0.5 mg / 1 ml cyclohexane and ~1% DDM, solution filtered), at 23°, prior to heating (~ 18°C/s, Gatan holder), commensurate with previous examples for starting spherical TS-AgNP templates (5.0 ± 1.5 nm, n = 59). Complementary, conventional bright field imaging at 750°C (Figure 5.2b) showed the HCNS products formed (9.1 ± 1.5 nm, n = 66), along with some residual, larger AgNP (15.6 ± 2.6 nm, n = 14). Figure 5.2c, now imaged at 850°C (~ 18°C/s), after a ~ 2 minute hold, similarly showed the developed HCNS products, and the near complete removal of Ag from the field of view. Notably, the GO support appeared intact at this stage of processing at elevated temperature, however, imaging after ~ 20 minutes of hold at 850°C (Figure 5.2d) showed evidence for the degradation of the GO support, with the appearance of holes (arrowed).

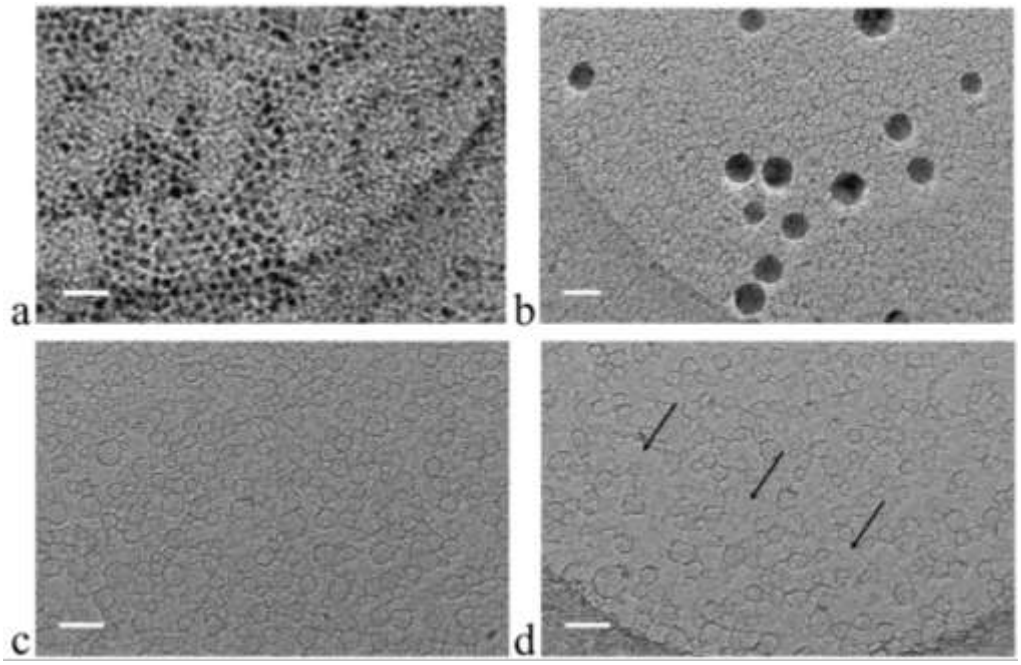

Figure 5.2 Bright field TEM images of TS-AgNP (GO/Cu), prior to and during thermal processing: (a) Low magnification image at 23°C showing starting TS-AgNP (scale bar 50 nm); and higher magnification images (b) recorded at 750°C, illustrating the formation of HCNS with some large, residual AgNP; (c) HCNS imaged at 850°C (~ 2 minutes hold), showing near complete removal of Ag and; (d) sample imaged at 850°C (~ 20 minutes hold), confirming the stability of the HCNS product but also showing the onset of degradation of the GO support (holes arrowed) (scale bars 20 nm).

Since commercially available GO/Cu TEM supports afforded better integrity than the in-house prepared Graphene supports, at elevated temperatures, GO/Cu grids were employed for complementary *ex situ* heating experiments (Gatan holder), as compared with further *ex situ* heating of TS-AgNP on MWCNT supports (muffle furnace).

5.3 Heating TS-AgNP at ~ 10°C/s (*ex situ*; Gatan sample holder *cf* muffle furnace)

To complement the *in situ* TEM investigations, *ex situ* experiments were performed using two different heating systems; the first involved the Gatan TEM sample holder

under *ex situ, in vacuo* conditions (heated to 850°C; ~ 14°C/s); the second, a laboratory furnace, with samples sealed inside quartz ampoules *in vacuo* (*i.e.* placed into a pre-heated oven at 850°C).

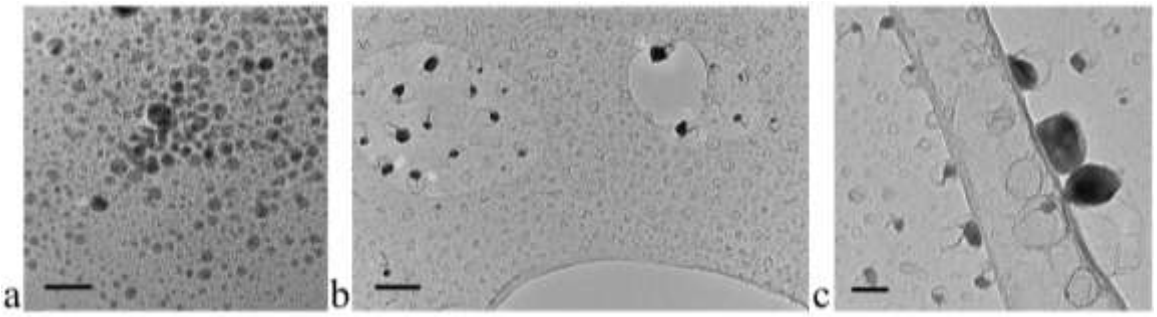

Figure 5.3 Bright field TEM images of: (a) TS-AgNP prior to heating *ex situ* at 850°C (scale bar 20 nm); (b) overview of HCNS products formed after heating, imaged at 23°C (9 days after processing), exhibiting a broad range of sizes / morphologies, and the retention of some larger AgNP (scale bar 100 nm); and (c) residual AgNP located to the sides / within disrupted oval hollow C structures (scale bar 20 nm).

Figure 5.3a presents a bright field TEM image of TS-AgNP (DDM/PUT) (GO/Cu, 0.5 mg / 1 ml cyclohexane and ~1% DDM) at 23°C, showing the starting, small, circular TS-AgNP (DDM/PUT) (4.1 ± 1.4 nm, n = 156). Figure 5.3b shows the products formed from the *ex situ* heating of TS-AgNP (Gatan holder; 850°C, at ~ 14°C/s, 5 minutes hold, $1x10^{-8}$ bar), imaged at 23°C (9 days after processing). In this case, the products comprised 9.9 ± 5.0 nm (n = 156) HCNS with a broad size distribution (3 – 38 nm), and disrupted morphologies, with the retention of some residual Ag (19.9 ± 7.9, n = 23), associated with these hollow carbons, suggesting incomplete processing. Further, Figure 5.3c, imaged at higher magnification, illustrates details of the associations between these irregular, hollow carbon structures, and the residual, larger AgNP. Observations of these structures in different projections confirmed the residual AgNP to be located to the sides / on the interior

surfaces of these ovoid carbon structures. It is noted that this sample and support were notionally the same as for the example presented in Figure 5.2.

Conversely, Figure 5.4 presents a phase contrast TEM image of TS-AgNP deposited onto MWCNT supports (C/Cu, 0.5 mg / 1 mL cyclohexane), illustrating the nanoparticle dispersion on carbon nanotube edges before heating *ex situ*, inside a quartz ampoule under vacuum (~ 7 x 10^{-8} bar), within a muffle furnace pre-set to 850°C (180 minutes). In contrast, Figure 5.4b imaged under conditions of slight defocus (~ 10 days after processing) shows the development of irregular graphitic HCNS (I) on the MWCNT walls, in close proximity to the formation of graphitic carbon shells surrounding AgNP (II). Hence, it is recognised that the formation of graphitic carbon shells can precede AgNP template removal. In this case, the heating time had been extended to allow for sufficient radiative thermal heating from the furnace, through the ampoule, to the sample.

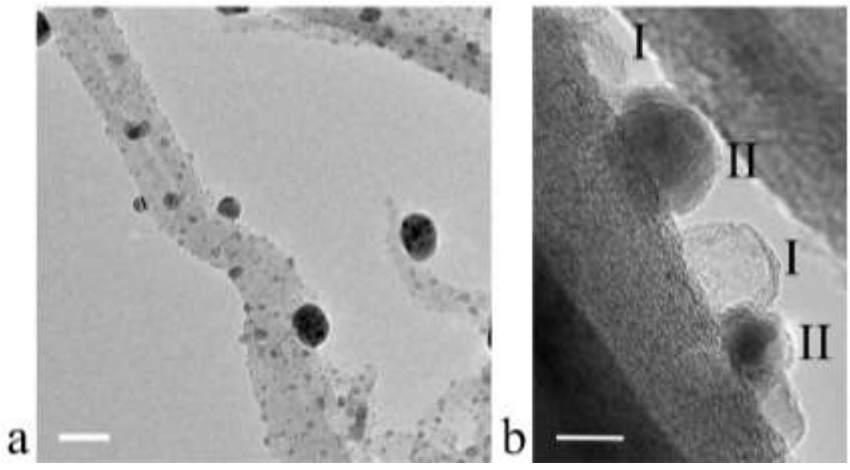

Figure 5.4 Bright field TEM micrographs of: (a) TS-AgNP@MWCNT before *ex situ* heating to 850°C for 3 h (scale bar 20 nm); and (b) higher magnification phase contrast image showing resultant HCNS (I) adjacent to Ag templated CNS structures (II), imaged at RT (~ 10 days after processing; scale bars 10 nm).

Based on the variability in these heating experiments, an *in situ* TEM MEMS heating holder approach was adopted, to give better control over the processing conditions and heating rate in particular; recognising that limited temperature control was afforded by the Gatan and furnace heating systems, which were not able to achieve heating rates above ~ 18°C/s.

5.4 Heating TS-AgNP at ~ 100°C/s and ~ 1°C/s (*in situ* TEM; MEMS heating holder)

To better understand the effect of heating rate on HCNS formation, two very different heating procedures were adopted. Firstly, rapid heating from room temperature to 850°C (92°C/s), Thermal Protocol 1 (TP-1), and secondly, slow heating from 23°C to 650°C (1.5°C/s, hold time 2 minutes), then slow heating from 650°C to 900°C (2°C/s), Thermal Protocol 2 (TP-2).

Figure 5.5a presents a bright field, diffraction contrast TEM image of the starting TS-AgNP dispersed onto the planar Si_3N_4 support of a MEMs heating chip, (0.5 mg / 1 ml $CHCl_3$) recorded at 23°C. The AgNP (7.0 ± 1.4 nm, n = 84) were crystalline, and again circular in projection, consistent with spherical NP. Conversely, Figure 5.5b shows the same field of view (contrast enhanced) at 850°C, following rapid *in situ* heating (TP-1). In this case, the resultant HCNS structures were revealed, precisely matching the positions of the starting TS-AgNP, whilst exhibiting slightly larger sizes (8.4 ± 1.4 nm, n = 84).

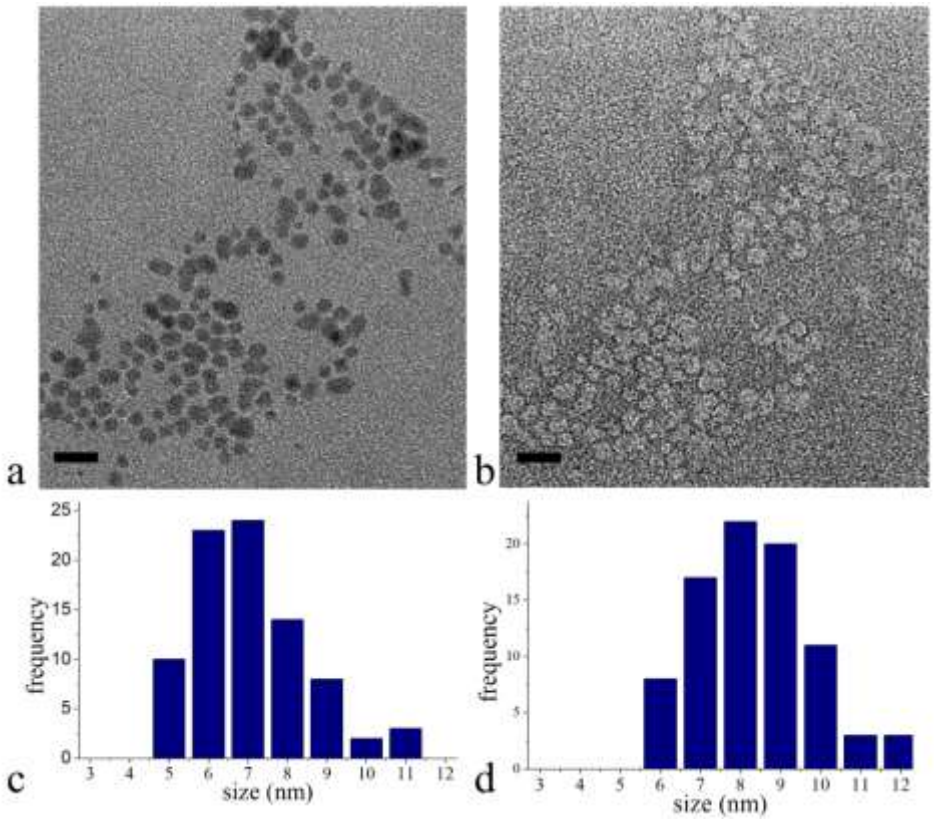

Figure 5.5 Bright field, diffraction contrast TEM micrographs of: (a) TS-AgNP / Si_3N_4 before rapid *in situ* heating to 850°C (TP-1); (b) the resultant HCNS products, imaged at 850°C (contrast enhanced; scale bars 20 nm); and size distribution (c) prior to heating (7.0 ± 1.4 nm, n= 84) and (d) after heating (8.4 ± 1.4 nm, n = 84).

Conversely, Figure 5.6 presents images of the reaction products formed from the same TS-AgNP starting material (0.5 mg / 1 ml $CHCl_3$), following *in situ* thermal processing with a very slow, two-stage heating rate up to 900°C (TP-2). In this case, there was a very high degree of variability in the product across the centralised support windows of the MEMS heating chip, with a mixture of amorphous, lacy carbon (Figure 5.6a) interspersed with inhomogeneous (large shell) carbon structures (Figure 5.6b) and large accumulations of Ag (Figure 5.6c). In particular, no small, discrete HCNS structures were evident. At low magnification (Figure 5.6d), the relative associations of lacy carbon, adjacent to large agglomerations of Ag, became apparent.

These data sets demonstrated that heating rate is critical for the formation of well-defined HCNS structures.

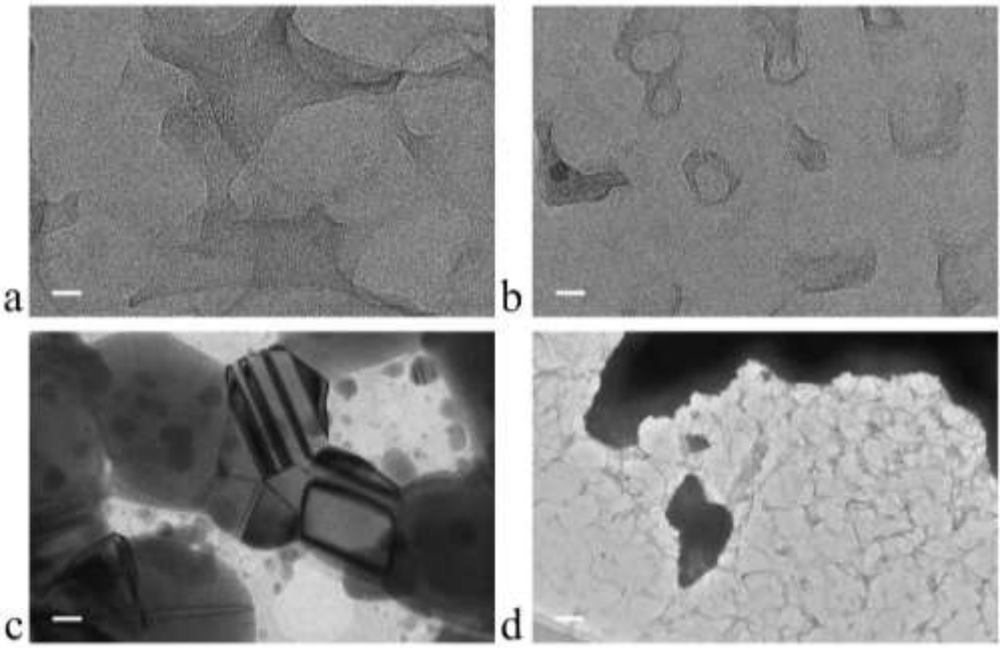

Figure 5.6 TEM images showing the variety of products formed upon heating TS-AgNP to 900°C (slow, 2-stage heating rate, TP-2). Phase contrast images of: (a) lacey carbon and; (b) inhomogeneous (large shell) carbon structures (scale bars 20 nm). (c) Diffraction contrast image showing Ag agglomeration / grain growth (with twin bands) (scale bar 20 nm); and (d) low magnification image showing relative associations of large accumulations of Ag and lacey carbon products (scale bar 200 nm).

Further, dark-field scanning TEM (STEM) and associated EDS data from TS-AgNP, thermally processed at slow heating rate (TP-2), recorded at 23°C after heating, illustrated significant variations in the product (Figure 5.7). In particular, C and S were found to be absent from regions containing large agglomerations of Ag.

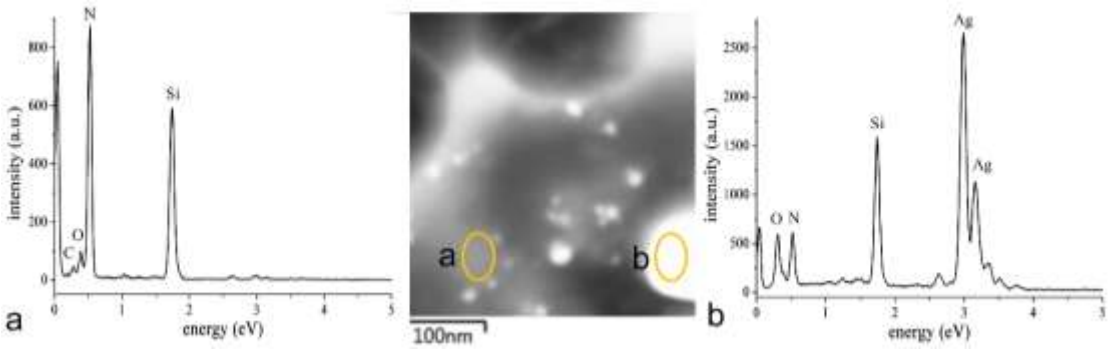

Figure 5.7 Dark field STEM and associated EDS data from regions a & b (circled), showing significant variation in the products formed and localised accumulations of Ag, following thermal processing of TS-AgNP under slow heating rate conditions (TP-2). *Data collection by Dr Mike Fay.*

Figure 5.8 presents a first order Raman spectrum acquired from products formed from TS-AgNP thermally processed on Si_3N_4 supports at 850°C with slow heating rate (TP-2). The general peak shapes presented and weak intensity features in the second order spectrum (data not shown) are consistent with the formation of highly disordered graphitic carbon. The presence of two broad, slightly overlapping bands around 1350 and 1595 cm^{-1} were attributed nominally to the defect (D) and graphite (G) bands, and four Lorentzian-shaped bands (G, D1, D2, D4) and a Gaussian shaped band (D3) were deconvoluted carefully (Table 5.2), as described previously in Section 4.5.1 [3].

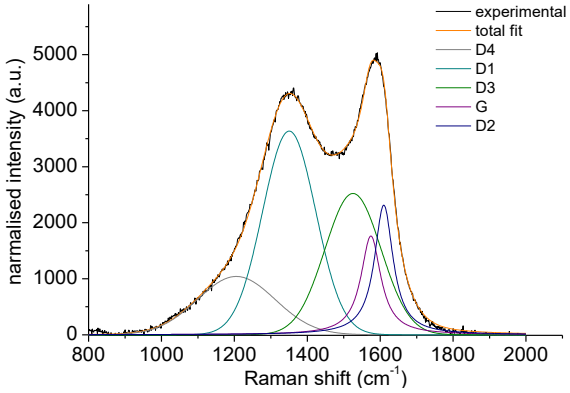

Figure 5.8 First order Raman spectrum (λ_{ex} = 532 nm) obtained in the range 800-2000 cm^{-1} from a TS-AgNP sample thermally processed using slow heating rate (TP-2), confirming the disordered graphitic nature of the products. The spectrum has been normalised to the intensity of the G band (results from TP-1), baseline-corrected using a third-order polynomial subtraction and fit using a five-band model analogous to that described previously [2] (χ^2 = 2.4). *Data collection and analysis performed by Dr Graham Rance.*

Table 5.2 First order Raman band assignments [2, 4]

Band [a]	**Raman shift / cm^{-1}**	**Proposed vibrational mode assignment**
G	1574 s	Ideal graphitic lattice (E_{2g} symmetry)
D1 (D)	1350 vs	Disordered graphitic lattice (A_{1g} symmetry)
D2 (D')	1610 s	Disordered graphitic lattice (E_{2g} symmetry)
D3 (D", A)	1525 m	Amorphous carbon
D4 (I)	1205 m	Disordered graphitic lattice (A_{1g} symmetry), polyenes, ionic impurities

[a] *alternative band designations of earlier studies are in parantheses (vs = very strong, s = strong, m = medium).*

This first order spectrum from TS-AgNP heated to 850°C with slow heating rate (TP-2) (Figure 5.8), while notably very similar to the spectrum obtained from TS-AgNP heated to 850°C with fast heating rate (TP-1) (Figure 4.19), presents subtle differences, yielding information regarding the relative amounts of amorphous and

disordered graphitic C present. A shift in the position of the apparent G band from ~1590 to ~1595 cm^{-1} for carbon structures formed using TP-1 and TP-2, respectively, may be rationalised tentatively by either: (a) Plasmonic heating, or charge transfer effects, due to the presence of residual Ag in close proximity to the carbon structures formed using a slow heating rate, resulting in a red shifted G band or; (b) differences in the curvature of the obtained nanostructures. Also noted, are differences in the relative intensities of the apparent D and G bands. Further, evaluation of peak areas for deconvoluted bands provided quantitative information regarding the extent of disorder and amorphous C in the structures formed from heating TS-AgNP, whilst the intensity ratio (as peak area) of the D1 and G bands (I_{D1}:I_G) was high for products formed using both TP-1 or TP-2 (I_{D1}:I_G = 3.08 and 3.77, respectively), with the value for structures formed under slow heating rates (TP-2) being larger. In addition, the intensity ratio (as peak area) of the D3 and G bands (I_{D3}:I_G) was also high and significantly higher for structures obtained with a slower heating rate compared to HCNS formed with a fast heating rate (I_{D3}:I_G = 2.76 and 1.68, respectively). Both of these ratios indicate that carbon structures formed from heating TS-AgNP using slow heating rates contain slightly less graphitic C, in conjunction with more amorphous carbon contributions, when compared to HCNS formed using faster rates of heating, indicating that heating rate strongly influences the extent of graphitisation of the carbon products formed, consistent with observations from TEM.

By way of brief summary overview, Table 5.3 now provides a precis of the data sets from Sections 5.2 to 5.4, summarising the effect of heating rate on TS-AgNP and the products formed. A very rapid heating rate (~ 100°C/s) was found to be essential for the formation of well-defined HCNS, marginally larger (~ 2 nm) than the starting TS-

AgNP. In contrast, slower heating rates (~ 1°C/s) did not lead to the production of HCNS, but to more amorphous, lacy carbon structures. Intermediate heating rates (~ 10°C/s, obtained using the Gatan TEM heating holder, *in situ* and *ex situ*) led to the formation of larger, more irregular HCNS structures, with significant ripening and presence of residual AgNP, indicative of a combination of coarsening and incomplete processing.

Table 5.3 Summary of heating rate effects on HCNS formation from TS-AgNP.

TS-AgNP size / nm	Support	Heating system	Heating rate / °C.s^{-1}	Max temp / °C	Hold time / minutes	AgNP size / nm	HCNS size / nm
6.6 ± 1.4	Si_3N_4	MEMS	**1.5**	650	-	> 100	none
			2	650 - 900	-		
4.1 ± 1.4	GO / Cu	Gatan *ex situ*	**~ 14**	850	5	19.9 ± 7.9 inside HCNS	9.9 ± 5.0, 3 – 38 nm
3.4 ± 0.9	FLG/ Mo	Gatan *in situ*	**~ 14**	850	-	20 - 80	17.3 ± 6.1
5.0 ± 1.5	GO / Cu	Gatan *in situ*	**~ 18**	750	-	15.6 ± 2.6	9.1 ± 1.5
				750 - 850	20	none	none-
6.7 ± 2.4	MWCNT	muffle furnace	**~ 20**	850	180	~ 12	~ 12
6.6 ± 1.4	Si_3N_4	MEMS	**92**	850	-	none	8.9 ± 1.7

5.5 Localised variations of HCNS products

Some localised variations were observed for products formed under both *ex situ* and *in situ* processing conditions, on different support materials. For example, for the case of HCNS formed *ex situ* on MWCNT, instances of the close proximity of templated CNS and HCNS were observed (Figure 5.9a), indicative of some localised variability

in the activation of this transformation process. Furthermore, localised variability was observed also during *in situ* thermal processing to 850°C (fast heating rate, TP-1), depending on NP position relative to the MEMS Si_3N_4 support windows. For example, Figure 5.9b shows a distribution of distinct HCNS on the electron transparent window of a Si_3N_4 MEMS chip (I), whilst an array of larger, CNS encapsulated AgNP (II) decorated the edge of the support window. Further, it is noted that AgNP (23.3 ± 4.2 nm, n = 6) in this instance were significantly larger than the starting TS-AgNP (6.6 ± 1.4 nm, Figure 4.17a,c), indicative of Ostwald ripening [1].

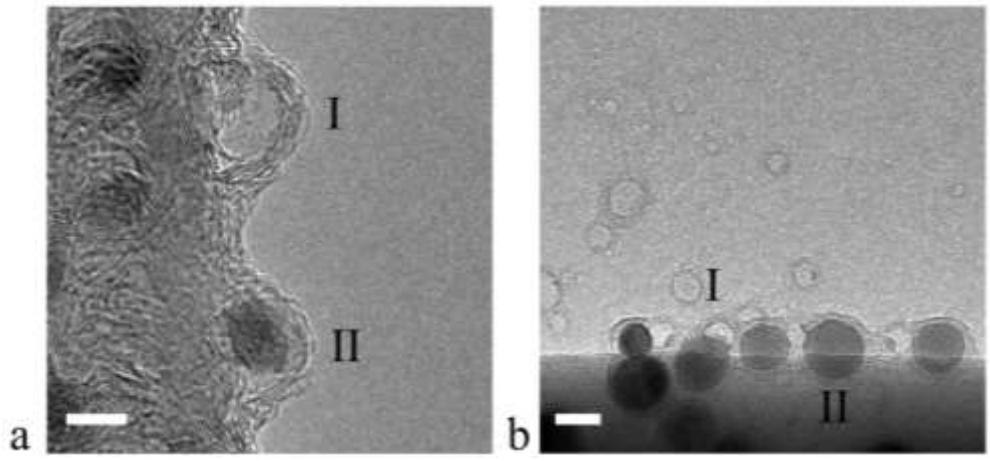

Figure 5.9 Products formed from TS-AgNP after heating; (a) *ex situ* on MWCNT (850°C, at ~ **20**°C / s), showing HCNS (I) in close proximity to Ag templated CNS (II) (scale bar 5 nm) and; (b) TS-AgNP (TP-1) processed *in situ* on Si_3N_4, MEMS support showing HCNS (I) adjacent to CNS encapsulated AgNP (II) located on thicker regions of support (scale bar 20 nm). Both images were recorded at RT, following rapid heating to 850°C.

Further, Figure 5.10 presents example phase contrast TEM images of partially processed TS-AgNP on a Si_3N_4 MEMS chip heated to 850°C (TP-1), representing a region where activation for the process was retarded. Figure 5.10a shows a range of intermediate products, including completely hollow CNS (11.0 ± 4.3 nm, n=9) with a

wide size range (6 – 18 nm), *i.e.* significant larger than the starting TS-AgNP (6.6 ± 1.4 nm). Ag templated CNS (17.4 ± 3.1 nm, n = 16) were also larger than the starting NP, and nearly twice the diameter of hollow CNS from within the same field of view, suggesting AgNP ripening in advance of HCNS formation. Figure 5.10b recorded at higher magnification, shows an example AgNP (axes of ~ 20.3 – 25.0 nm in projection) within a hollow carbon structure (~ 22.2 nm diameter). The location of residual Ag within templated CNS appears consistent for all structures within the field of view, not evenly distributed through the CNS, but pinned to interior surfaces, minimising the free Ag surface volume, with a mostly faceted appearance. The phase contrast image, Figure 5.10c, indicates that the CNS adopts a graphitic structure (spacing 0.34 nm [5]) in advance of Ag loss.

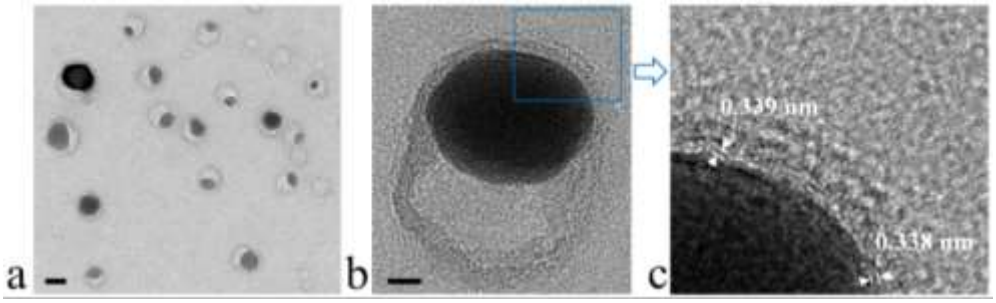

Figure 5.10 Phase contrast images showing: (a) Incompletely processed TS-AgNP, nominally at 850°C (TP-1) on a Si_3N_4 MEMS chip (scale bar 20 nm) and; (b) residual AgNP within an individual CNS (scale bar 5 nm); and (c) templated CNS walls with developed graphitic spacings [5].

All these observations are consistent with the suggestion that localised thermal effects influence the onset and progression of the HNCS transformation process, with heating rate leading to a competition between AgNP ripening and HCNS production.

5.6 Loss of Ag templates at elevated temperature

Figures 5.11a-d present phase contrast TEM time-lapse images for an AgNP on a Si_3N_4 support, recorded at 650°C (at ~ 2°C / s), showing rapid reduction of AgNP size, and removal of Ag, with no accumulations of Ag observed on the Si_3N_4 support at the end of heating (noting that thicker regions of the support could not be observed by TEM). In this instance, the reduction in AgNP size was not continuous, but occurred via abrupt steps, accompanied by a faceted appearance, commensurate with Figure 5.10a. Theoretical calculations suggest the cleaving of facets, followed by sublimation would be energetically favourable for < 20 nm AgNP [6]. Indeed, the presence of lattice fringes, corresponding to Ag(111) [7], observed during NP size reduction, indicated continuous crystallinity arising from solid Ag, with changing lattice orientations due to the elevated temperature [8]. The absence of a liquid phase provides further evidence for the removal of Ag via sublimation. The experimental heating protocol in this instance was chosen to appraise the removal of Ag only, and not the formation of HCNS. However, it is recognised that the encapsulation of Ag by CNS may influence the process of Ag template removal.

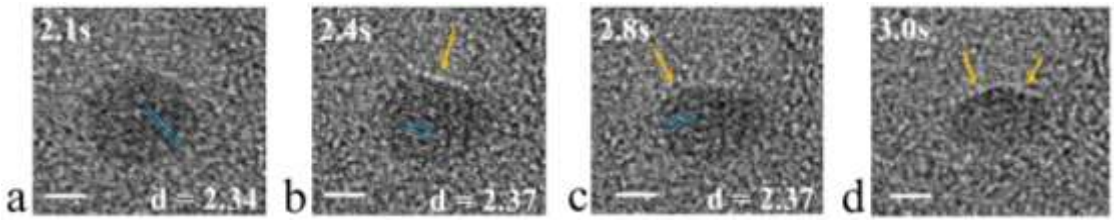

Figure 5.11 Time-lapse, phase contrast images of an AgNP (Si_3N_4 support), recorded at 650°C, indicative of a step wise, faceted reduction in AgNP size (indicated by arrows), consistent with literature examples for sublimation (scale bar 2 nm) [6]. Values for d_{hkl}, in Å, measured between the blue lines, correspond to Ag(111) [7]. *Images collected with assistance from Dr M. Fay.*

Figure 5.12 presents a complementary TEM time-lapse series showing the step-wise loss of Ag observed within CNS, whilst heating AgNP (stabilised with DDM and PUT, at 750°C, ~ 18°C / s, 15 minutes, GO/Cu). For the case of the structure (arrowed) overhanging the edge of the support, a distinct deflation of the hollow structure occurred during imaging, in contrast to the size retention and more stable morphologies of CNS on the support material in close proximity. In this example, the ~ 20 nm sized structure formed was not entirely stable under these conditions. Further, step-wise removal of Ag was observed when located within CNS, demonstrating that carbon encapsulation did not affect this Ag loss process.

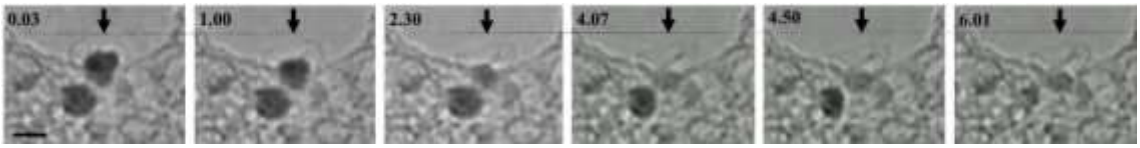

Figure 5.12 Time-lapse series of conventional bright field TEM images showing the step-wise removal of Ag from within HCNS, and slight collapse of an unsupported hollow carbon structure (arrowed; line added to enable for direct comparison between images) adjacent to supported HCNS which do not change size (scale bar 10 nm, time in s).

These data sets (Sections 5.2-5.5) demonstrate that heating rate has a substantial effect on the formation of stable < 10 nm sized HCNS, when heating TS-AgNP on a variety of support materials, with some localised product variations when processed *in situ* and *ex situ*.

5.7 Discussion

The demonstration of well-defined, < 10 nm sized graphitised HCNS from the one step thermal processing of TS-AgNP was described in Chapter 4, achieved via *in situ* TEM or *ex situ* thermal processing with fast heating rate. Indeed, most of the HCNS products formed *in situ* under fast heating conditions (TP-1, ~100°C/s) comprised complete spheres (Figure 5.5), with the location of HCNS products being identical to the TS-AgNP starting material, demonstrating the templated formation of HCNS on AgNP. Further, direct evidence for the graphitisation of HCNS walls, at elevated temperature, was provided by *ex situ* heating of TS-AgNP on MWCNT supports, whilst Raman spectroscopy provided indirect evidence for the graphitic nature of HCNS products formed *in situ* on Si_3N_4 supports. The HCNS structures formed were defined by, and slightly larger than the starting thiol stabilised, AgNP templates.

The data sets presented in the present Chapter demonstrate the importance of heating rate on the formation of well-defined HCNS (and hence, G-HCNS). In particular, the thermal processing of TS-AgNP under very slow heating rate conditions (TP-2; ~1°C/s) *in situ* did not yield uniform HCNS, leading instead to the development of a carbon-foam like product and large agglomerations of Ag. In this case, it is considered that the steady diffusion of Ag under conditions of slow heating rate resulted in a degradation of the NP templating effect, due to agglomeration and grain growth, in turn acting to disrupt the formation of HCNS, leading instead to the development of foam-like lacey, amorphous, non-homogeneous carbon structures (Figures 5.6a,b,d). In addition, localised, large accumulations of Ag (Figures 5.6c Figure 5.7) constitute evidence for the ripening of AgNP, with a concomitant decrease in catalytic activity and product graphitisation [9]. Indeed, complementary Raman spectroscopy

demonstrated decreased levels of graphitic ordering within slowly heated *in situ* TS-AgNP (I_{D1}:I_G = 3.77, consistent with increased disorder), as compared to samples processed *in situ* under fast heating rate conditions (I_{D1}:I_G = 3.08).

Investigations at intermediate heating rates (broadly represented at ~ 10°C/s, as an order of magnitude) provided a number of valuable insights into the formation mechanisms and kinetics for HCNS structures, in competition with the processes of AgNP ripening and template removal. For example, the development of ~ 9 nm sized HCNS products and ~ 16 nm sized residual AgNP from ~ 5 nm sized TS-AgNP starting materials (Figures 5.2b&c, *in situ,* Gatan holder, 750°C, ~18°C/s) constitutes clear evidence for the ripening of AgNP prior to HCNS formation; and the continued ripening of residual AgNP after HCNS formation. Additionally, the commensurate formation of ~ 10 nm sized HCNS and ~ 20 nm sized residual AgNP from ~5 nm sized starting material (Figures 5.3a&b, *ex situ,* Gatan holder, 850°C, ~14°C/s) provides further evidence. The implication being that HCNS formation followed by rapid AgNP template loss occurs only when a critical set of localised, thermal conditions have been established. It is anticipated that disruption to the AgNP templates, under conditions of intermediate heating rate, would produce a less well-graphitised HCNS product. (Complementary Raman spectroscopy data was not obtained for this intermediate sample set due to the graphitic nature of the GO supports used.)

Figure 5.13 presents a broad summary of the effects of fast, intermediate and slow heating rates (~100, ~10 and ~1°C/s, respectively) on the development of carbon products from thermally processed TS-AgNP, illustrating the effect of competition between HCS development and the diffusion of Ag across the support.

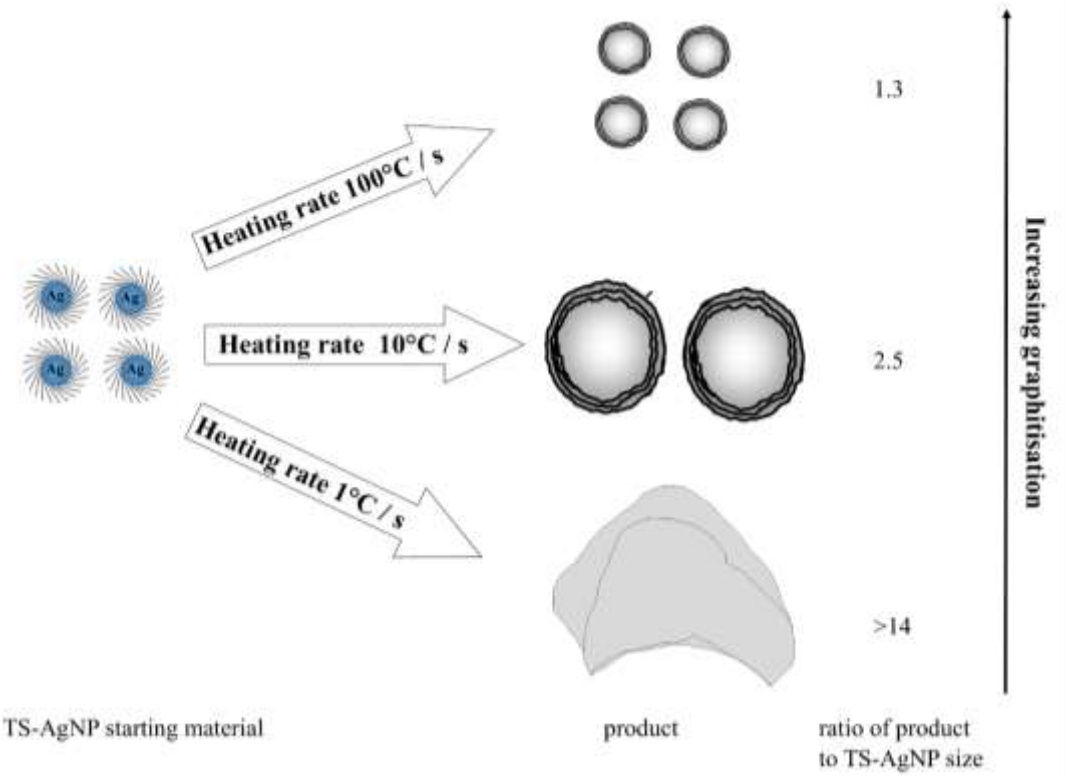

Figure 5.13 Overview of the effect of heating rate on the development of carbon products from thermally processed TS-AgNP, at > 650°C. A fast heating rate (~100°C/s) led to the formation of well-defined G-HCNS, with size / size distribution defined by the starting TS-AgNP; an intermediate heating rate (~10°C/s) led to the formation of larger, more disrupted (& presumably less-well graphitised) HCNS products, associated with a process of co-operative ripening of the AgNP templates at elevated temperature; whilst a low heating rate (~1°C/s) led to the formation of foam-like or lacy, amorphous carbon structures and large agglomerations of Ag, but no HCNS.

The rate of heating not only affected HCNS formation, but also produced a marked disruption in the AgNP templates which were rendered ineffective under particular conditions. At fast heating rates (~100°C/s), small AgNP remained after HCNS products had formed and are removed during a process of sublimation, before particle ripening can occur, as evidenced by the absence of Ag and the formation of HCNS products commensurate with the size and size distribution of the TS-AgNP starting material. At slower heating rates (~10°C/s), competition between the dynamic

processes of HCNS formation and Ag diffusion across the support is evidenced by the appearance of larger AgNP, which remain on the support due to the increase in their size, and to the formation of HCNS products which must be templated by larger AgNP. At the slowest heating rates, diffusion of Ag proceeds in preference to HCNS formation, leading to the development of increasingly larger AgNP, in conjunction with particle coalescence, which result in the formation of large aggregations of silver, which are not removed during heating. Figure 5.14 provides an overview the role rate of heating has on AgNP.

It is considered that at fast heating rates (~ 100°C/s) thiol molecules bonded to the Ag surface become dehydrogenated, thermally driven, but catalysed by stable AgNP templates. In this case, HCNS formation then proceeds rapidly and in preference to diffusion of Ag from TS-AgNP and particle migration. Following cross-linking of carbon chains and graphitisation, observed at temperatures > 600°C [10], the formation of HCNS progresses, with Ag then being lost upon continued heating (Figure 5.5). The presence of lattice fringes and facet development during AgNP loss (Figures 5.11 & 5.12) constitute evidence for the removal of Ag by a process of sublimation, rather than melting [6]; whilst noting the Gibbs-Thomson equation predicts a melting point for AgNP substantially below the 650°C used for these experiments (*e.g.* 250 °C for 5 nm diameter AgNP [11]). Additionally, temperatures experienced by AgNP are likely to be higher than experimental measurements recorded from the heating furnace, due to electron beam induced heating effects, particularly the case for isolated NP [6].

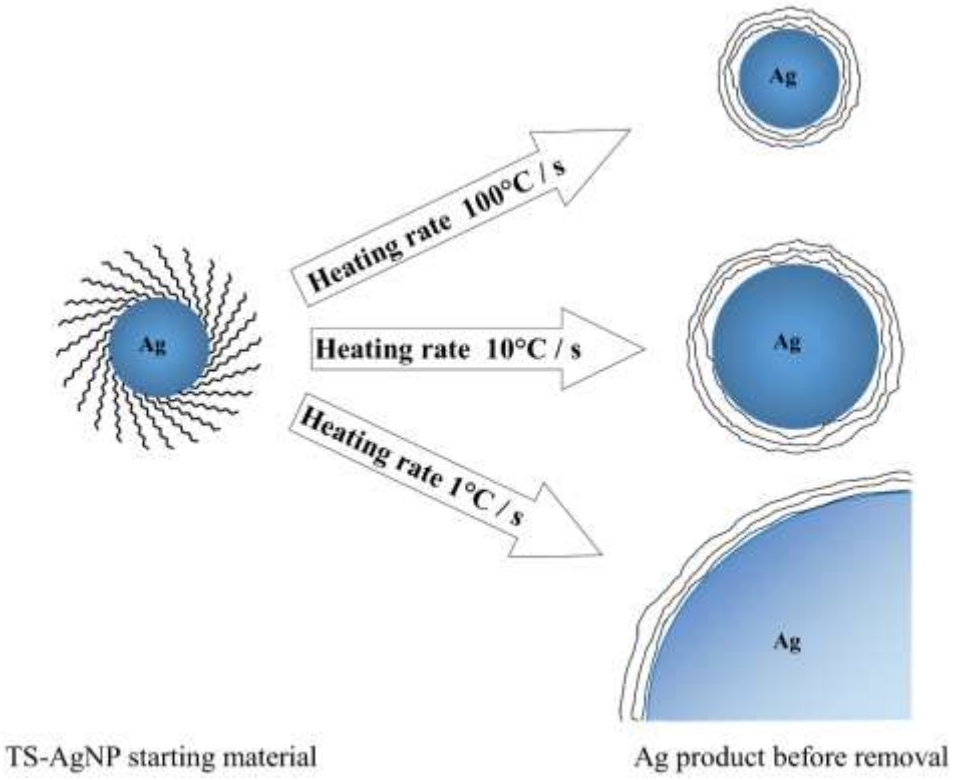

Figure 5.14 Overview of heating rate effect on AgNP ripening in competition with the formation of HCNS, from thermally processed TS-AgNP at > 650°C. A fast heating rate (~100°C/s) led to the formation of well-defined HCNS without change of the AgNP template, with the size / size distribution of the product being defined by the starting TS-AgNP, in advance of the removal of the AgNP template by sublimation. An intermediate heating rate (~10°C/s) led to Ostwald ripening of AgNP (and retention of the thiol surfactant stabilisation layer) in advance of the formation of larger, more disrupted HCNS products (and retention of some larger AgNP in the event of continued ripening). A low heating rate (~1°C/s) led to the near complete disruption of the AgNP templates, with the development of very large agglomerations of Ag which were not removed at elevated temperatures, and hence did not produce any HCNS products.

At intermediate heating rates of ~ 10°C/s, the onset of dehydrogenation, cross-linking and graphitisation of thiol molecules occurs when temperatures are sufficiently high. However, prior to this, Ag molecules have sufficient time to diffuse across the support material during the process of Ostwald ripening [12] (and by implication, thiol surfactant stabilisation molecules are also transported). In particular, consumption of

the smallest TS-AgNP may occur preferentially [13], leading to the production of larger TS-AgNP templates which effectively retards the onset of HCNS production, as evidenced by the formation of HCNS ~ 2.5 times the size of the TS-AGNP starting material, and the presence of even larger, residual AgNP on the support (Figure 5.2b). A corresponding reduction in catalytic activity would be expected for larger AgNP, hence it is anticipated that the extent of product graphitisation would also be decreased. In addition, larger AgNP have higher melting points compared to smaller AgNP (Gibbs–Thomson equation), commensurate with the observed retention of the largest AgNP. Hence, competition between thermally activated dynamic processes, leading to AgNP growth in advance of HCNS formation, are reflected in the differences in products observed for fast and intermediate heating rates (~ 100°C/s and ~ 10°C/s).

At the slowest heating rates (~ 1°C/s), AgNP ripening processes dominate over HCNS production, with the eventual formation of very large (> 100 nm) accumulations of Ag over the support. The transformation of thiol molecules during this process instead produces a variable foam-like or lacy carbon product over the support, echoing the processes of template movement, increasing NP size and retarded catalytic activity following preferential loss of AgNP. The retention of large agglomerations of Ag is expected, as the melting point of bulk Ag (962°C) exceeds the processing temperatures used here. Accordingly, the formation of graphitised HCNS is not promoted under conditions of very slow heating rate.

The radial temperature distribution across the MEMS support heating spiral provided conveniently for the observation of partially processed products (Figure 5.10). In particular, it was noted that the body of residual Ag remained pinned to the interior surfaces of templated CNS, rather than spreading throughout the structure, this

configuration providing for the smallest Ag surface volumes, resulting in the lowest free surface energy formations [14]. In this context, it is noted that the localised temperature across the window could be up to ~ 300°C lower than the set temperature of 850°C [15].

Indeed, there were various subtle spatial variations in the nature of the HCNS products, in the case of both *in situ* and *ex situ* processed samples, suggesting a combination of effects relating to individual NP size, temperature and heating rate (& support, environment *etc*). By way of example, the close proximity of filled and empty nanoshells processed *ex situ* (Figure 5.9b,c) was considered indicative of a subtle NP size effect; whilst samples processed *in situ* under conditions of fast heating showed examples of well-defined HCNS and regions of partially processed TS-AgNP, depending on the location of the MEMS Si_3N_4 window, *e.g.* with larger encapsulated AgNP at the window edge (Figure 5.9b) being attributed to localised Ostwald ripening, indicative of localised thermal transport or particle size differences.

In practice, HCNS structures were consistently and reproducibly formed, with very similar morphologies on the following support materials: BN flakes deposited onto Au or Mo TEM grids; GO or graphite on Cu or Mo grids; Si_3N_4 MEMS heating chips; and MWCNT, accordingly, it is suggested that the support materials do not actively participate in the HCNS formation process, but do provide a physical support (*e.g.* as evidenced by the change in shape observed for partially, unsupported HCNS (Figure 5.12). Nevertheless, there were caveats associated with each of the support materials investigated, *e.g.* for the case of BN flake supports, in-house deposition produced limited, inhomogeneous coverage of the TEM grids, and carbon contaminants present from the solvents required for the deposition process confounded *in situ* TEM spectroscopy. The thickness and morphology of Si_3N_4 MEMS heating chips

compromised detailed TEM imaging of HCNS graphitic walls. In the case of TS-AgNP deposited onto MWCNT, direct comparison of identical locations was not possible, as *ex situ* heating was required. Further, for the case of GO/Cu supports, an initial, lower, hold temperature of 750°C (suggested by the TEM grid manufacturer) was used to preserve the GO TEM support, but was found not to be sufficient to remove AgNP templates after HCNS formation. Fortunately, a higher temperature of 850°C could be established without immediate breakdown of the support (provided the hold time was limited to a few minutes), allowing HCNS products free of Ag to be formed.

Previously, the formation of distinct HCNS (> 70 nm) was achieved via the use of multi-step processing, *e.g.* carbon coating of hard template materials, necessitating a synthetic step and thermal treatment, in advance of chemical template removal. Here, it has been demonstrated that TS-AgNP, can be transformed into < 10 nm sized HCNS, using a facile one-step thermal process, provided a very fast heating rate is used. This approach provides for excellent size control of the HCNS product via appropriate AgNP template selection. However, for the purpose of materials control and the potential for scale-up, and from a wider reaction kinetics perspective, it is recognised that further work is needed to separate out the competing roles of temperature, heating rate, template size and support material on the development of these HCNS products.

5.8 Conclusions

The formation of HCNS products from the heating of TS-AgNP at > 650°C is found not to be dependent on the support material, for the many examples illustrated above. Spatial variations in the development of the reaction product reflects predominantly a competition between the thermal transformation of the TS-layer and the kinetics of Oswald ripening, in advance of loss of the AgNP template. In particular, a fast heating rate is found to be critical for the formation of well-defined graphitic <10 nm sized HCNS, whilst intermediate heating rates lead to larger HCNS, following AgNP ripening. Very slow heating rates give rise to a more variable product, comprising lacy, amorphous, non-homogeneous carbon structures with decreased levels of graphitic ordering.

References

1 Bastus, N.G., Comenge, J., Puntes, V., *Kinetically Controlled Seeded Growth Synthesis of Citrate-Stabilized Gold Nanoparticles of up to 200 nm: Size Focusing versus Ostwald Ripening*, Langmuir (2011) 27(17) pp11098-11105.

2 Sadezky, A., Muckenhuber, H., Grothe, H., Niessner, R., Pöschl, U., *Raman microspectroscopy of soot and related carbonaceous materials: Spectral analysis and structural information*, Carbon (2005) 43 (8) pp1731-1742.

3 Ferrari, J., Robertson, J., *Interpretation of Raman spectra of disordered and amorphous carbon,* Phys. Rev. B (2000) 61(20) pp14095-14107.

4 Cançado, L.G., Jorio, A., Martins, E. H., Stavale, F., Achete, C.A., Capaz, R.B., Moutinho, M. V. O., Lombardo, A., Kulmala, T. S., Ferreira, E.H.M., *Quantifying defects in graphene via Raman spectroscopy at different excitation energies*, Nano Letters (2011) 11(8) pp3190-6.

5 Iijima, S., Yudasaka, M., Yamada, R., Bandlow, S., Suenaga, K., Kokai, F., Takahashi, K., et. Al. *Nano-aggregates of single-walled graphitic carbon nano-horns*, Chem. Phys. Lett. (1999) 309 (3-4) pp165-170

6 Asoro, M. A., Kovar, D., Ferreira, P. J., *In situ transmission electron microscopy observations of sublimation in silver nanoparticles*, ACS Nano (2013) 24 7(9) pp7844-52

7 Zhao, X., Zhang, J., Wang, B., Zada, A., Humayun, M., *Biochemical Synthesis of Ag/AgCl Nanoparticles for Visible-Light-Driven Photocatalytic Removal of Colored Dyes*, Materials 8 (2015) pp2043-2053

8 Rankin, J., Sheldon, B. W., *In situ TEM sintering of nano-sized ZrO 2 particles*, Mater. Sci. Eng. A, (1995) 204 (1) pp48-53.

9 Gangula, P., Karanam, M., Janardhana, C., Rao, A. M.,. *Catalytic reduction of 4-nitrophenol using biogenic gold and silver nanoparticles derived from Breynia rhamnoides*, Langmuir (2011) 27 (24) pp15268-74.

10 Endo, O., Nakamura, M., Amemiya, K., Ozaki, H., *Graphene nanoribbons formed from n-alkane by thermal dehydrogenation on Au(111) surface*, Surf. Sci. (2015) pp44-48.

11 Menamparambath, M. M., Amjal, C. M., Kim, K. H., Yang, D., Roh, J., Park, H. C., Kwak, C., Choi, J-Y., Baik, S., *Ag nanowires decorated with Ag nanoparticles for low-haze flexible transparent conductive films*, Sci. Rep. (2015) **5** pp16371.

12 Thanh, N. T. K., Maclean, N., Mahiddine, S., *Mechanisms of nucleation and growth of nanoparticles in solution*, Chem. Rev. (2014) 114 (15) pp7610-7630

13 Hansen, T., Delariva, A., Challa, S., Datye, A., *Sintering of catalytic nanoparticles: Particle migration or Ostwald ripening?* Acc. Chem. Res. (2013) 46 (8) pp1720-30.

14 Garruchet, S., Politano, O., Salazar, J. M., Hasnaoui, A., Montesin, T., *An empirical model for free surface energy of strained solids at different temperature regimes*, Appl. Surf. Sci. 252 (15) (2006) pp5384-5386.

15 Niekiel, F., Kraschewski, S. M., Muller, J, Butz, B., Spieker, E., *Local temperature measurement in TEM by parallel beam electron diffraction*, Ultramicroscopy (2017) 176 pp161-169

6.0 Formation of hollow carbon nanoshells containing F or N heteroatoms

6.1 Introduction

The development of < 10 nm sized hollow carbon nanoshells (HCNS), formed from the heating of thiol stabilised Ag nanoparticles (TS-AgNP), and the importance of a fast heating rate for the synthesis (providing for effective control over HCNS size and extent of graphitisation), have been demonstrated in Chapters 4 and 5. This Chapter is concerned with the potential for the incorporation of heteroatom species into the HCNS structures, *i.e.* F or N atoms, via the thermal processing of TS-AgNP stabilised with either fluorinated thiols, or thiols containing nitrogen functional groups (Summary overview presented in Figure 6.1). Section 6.2 reports on the addition of fluorine to TS-AgNP and the HCNS products formed, whilst Section 6.3 reports on the challenges of incorporating nitrogen.

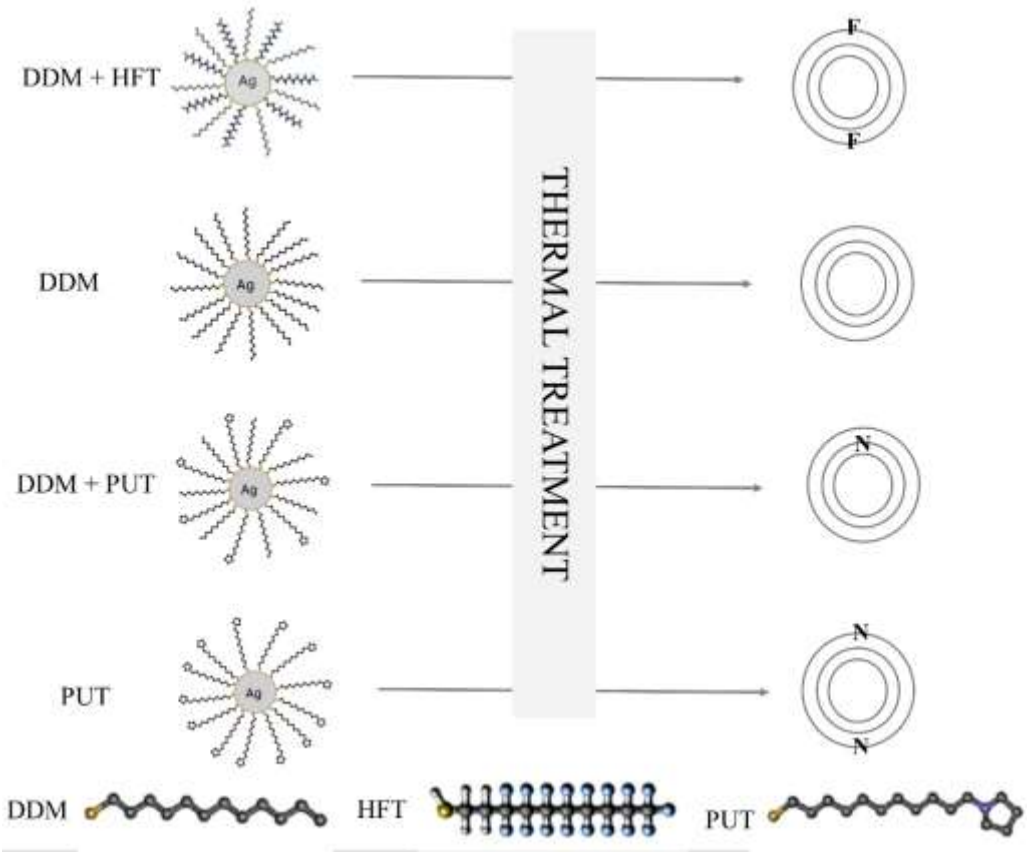

Figure 6.1 Overview of HCNS products formed from the heat treatment of TS-AgNP containing F or N heteroatoms.

Heteroatom incorporation was investigated, as a precursor to the more formal doping of graphitised HCNS products. F and N were chosen for investigation because they are both substitutional dopants, able to replace H or C, respectively, with minimal structural disruption due to their size similarities. In the case of N, the electronic structure of graphitic carbon materials, such as multi-walled carbon nanotubes (MWCNT) will be modified due to the electron donating effect of the lone electron pair, shifting the Fermi level to the valence bands, creating MWCNT with metallic characteristics [1] and modifying chemical reactivity [2]. Similarly, the electronegativity of F may also modify the band gap and thus electronic structure when added to carbon materials [3], leading to improved catalytic or electronic properties, F is known to impart other properties to materials, such as hydrophobicity

[4], ultra-low friction [5], and is a promising MRI agent, with a sensitivity similar to ^{1}H, but having no background signal *in vivo* [6]. The heteroatom containing AgNP sample sets investigated in this Chapter are summarised in Table 6.1, giving the different and relative amounts of thiols employed and sample names. Samples were heated *in situ* with a rapid heating rate using the MEMS holder (850°C; ~ 100°C/s, Si_3N_4), with one sample heated with the Gatan holder (850°C; ~ 18°C/s, Graphene Oxide (GO)/Cu); additionally, two N-containing TS-AgNP supported on MWCNT were heated *ex situ* (850°C, at ~ 20°C/s), as summarised in Table 6.2.

Table 6.1 TS-AgNP starting materials synthesised from different thiol mixtures, with heteroatom amounts given as a percentage of the stabilising layer, excluding the AgNP core.

Sample name	**Stabilising layer / %**	**Thiol / %**			
		DDM	**PUT**	**HFT**	**OM**
F-AgNP	F 47.3	50	0	50	0
TS-AgNP	none	100	0	0	0
N2-AgNP	N 1.6	75	25	0	0
N3-AgNP	N 3.1	50	50	0	0
N4-AgNP	N 4.4	25	75	0	0
N5-AgNP	N 5.5	0	100	0	0
TS-AgNP	none	0	0	0	100

HFT = 3,3,4,4,5,5,6,6,7,7,8,8,9,9,10,10,10-heptadecafluoro-1-decanethiol;
DDM = 1-dodecanethiol;
PUT = 11-(1H-pyrrol-1-yl) undecane-1-thiol, ($C_{15}H_{27}NS$);
OM = 1-octanethiol.

In particular, it is noted that the addition of heteroatoms into TS-AgNP affected the dispersion of AgNP in solvents, which presented significant challenges for sample dispersion onto the TEM supports, as required for thermal processing. Hence, Table 6.3 summarises the dispersion conditions used for each sample set.

Table 6.2 TS-AgNP starting materials (with heteroatom amounts given as a percentage of the stabilising layer excluding the AgNP core) and heating experiments performed (temperature and rate of heating).

Sample name	Stabilising layer / %	Heating System / support	Temperature / °C	Heat rate / °C/s
F-AgNP	F 47.3	MEMS / Si_3N_4	850	~ 100
TS-AgNP	none	MEMS / Si_3N_4	850	~ 100
TS-AgNP	none	Furnace / MWCNT	850	~ 20
N2-AgNP	N 1.6	MEMS / Si_3N_4	850	~ 100
N3-AgNP	N 3.1	MEMS / Si_3N_4	850	~ 100
N3-AgNP	N 3.1	Gatan / (GO/Cu)	850	~ 20
N3-AgNP	N 3.1	Furnace / MWCNT	850	~ 20
N4-AgNP	N 4.4	MEMS / Si_3N_4	850	~ 100
N5-AgNP	N 5.5	MEMS / Si_3N_4	650 - 1000	~ 100
N5-AgNP	N 5.5	Furnace / MWCNT	850	~ 20

Table 6.3 TS-AgNP starting materials, synthesised from different thiol mixtures (heteroatom amounts given as a percentage of the stabilising layer and excludes the AgNP core) with summary of the dispersion conditions onto TEM supports (altered by the addition of F and varying amounts of N).

Sample name	Stabilising layer / %	Dispersion conditions			
		Solvent	Sonication	Support	Drops cast
F-AgNP	F 47.3	hexane*[a]	N	GO/Cu	1
F-AgNP	F 47.3	ethanol	N	Si_3N_4	5
F-AgNP	F 47.3	cyclohexane*[b]	5 min	C/Cu	5
N2-AgNP	N 1.6	cyclohexane	N	GO/Cu	5
N2-AgNP	N 1.6	chloroform	N	GO/Cu	5
N2-AgNP	N 1.6	toluene*[b]	Y	Si_3N_4	5
N3-AgNP	N 3.1	cyclohexane	N	C/Cu	5
N3-AgNP	N 3.1	toluene*[b]	Y	Si_3N_4	1
N3-AgNP	N 3.1	cyclohexane**[c]	N	GO/Cu	5
N4-AgNP	N 4.4	acetone	N	Si_3N_4	1
N5-AgNP	N 5.5	cyclohexane*[b]	Y	GO/Cu	5
N5-AgNP	N 5.5	chloroform	N	Si_3N_4	1
TS-AgNP	none	chloroform	N	Si_3N_4	5
TS-AgNP	none	hexane	N	C/Cu	5

**[a]F-AgNP did not dissolve, but were suspended by fluid agitation, with immediate drop casting;*

**[b]Sonication required due to sample insolubilities in these solvents;*

**[c] ~ 1 % DDM added, solution filtered.*

6.2 Production of HCNS from fluorinated AgNP

This section reports initially on the characterisation of starting TS-AgNP, synthesised from a mixture of 1-dodecanethiol (DDM) and 3,3,4,4,5,5,6,6,7,7,8,8,9,9,10,10,10-heptadecafluoro-1-decanethiol (HFT) (50:50); leading on to a description of the

dispersion of fluorinated AgNP (F-AgNP) onto support materials; followed by a description of the HCNS products formed by thermal processing.

6.2.1 Characterisation of starting F-AgNP

As-synthesised F-AgNP samples (Section 3.2.1) were characterised to confirm the nature of (and presence of F within) the starting materials. Attention was given to the overall morphology and chemistry of the samples, with emphasis on the AgNP template and the F-doped carbon source, *i.e.* thiol stabilising layer. Starting F-AgNP samples were evaluated using a combination of XRD, TEM and UV/vis spectroscopy, with chemistry investigated further using the complementary technique of NMR spectroscopy.

Figure 6.2 presents XRD data for F-AgNP (50:50 DDM:HFT), returning peaks at 2θ = 38.4°, 43.8°, 64.6°, 77.2° and 82° corresponding to {111}, {200}, {220}, {311} and {222} lattice planes of Ag, respectively [7]. Again, comparison with the standard powder diffraction card of the Joint Committee on Powder Diffraction Standards (JCPDS) silver file (No. 004–0783) confirmed the presence of face centred cubic metallic Ag (similar in shape and peak positioning to the DDM stabilised AgNP sample described in Section 4.2, but with the intensity halved in this example. However, the peak shapes were broader than expected, compared to DDM stabilised AgNP, and exhibited slight asymmetries, suggesting at least a bimodal size distribution [8].

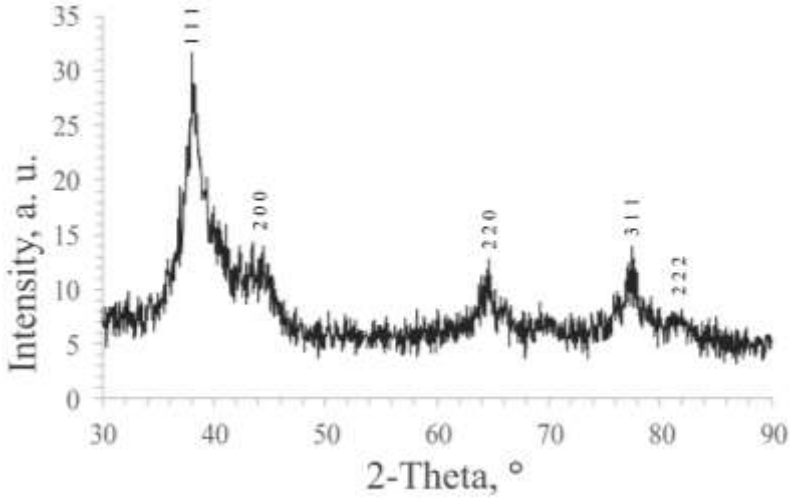

Figure 6.2 XRD data for AgNP stabilised with 50:50 DDM:HFT, with appropriate Miller indices, commensurate with fcc Ag.

Figure 6.3a presents a bright field, diffraction contrast TEM image of 50:50 DDM:HFT stabilised AgNP (GO/Cu, 0.5 mg / ml, *mixed* with hexane, without sonication), with dispersion conditions onto the grid tailored to enable clear differentiation between individual NP (*cf.* Section 6.2.2, Figure 6.7, F-AgNP in cyclohexane, sonicated). Dark, spheroidal F-AgNP were clearly observed, with overall size distribution 4.0 ± 2.8 nm, n = 205 (Figure 6.3b), reflecting a mixture of very small (~ 3 nm) and some larger NP (up to ~ 30 nm), *i.e.* the F-AgNP size distribution was poly-dispersed, consistent with the indications from XRD data, which indicated *at least* a bimodal size distribution. The addition of the fluorinated thiol to the AgNP stabilising layer was implicated in this distribution. Indeed, the dispersion in solvents of F-AgNP differed significantly from TS-AgNP, with the former found to disperse in relatively polar solvents, such as ethanol and acetone (results not shown), but not readily in non-polar solvents such as hexane. Complementary EDS investigation indicated the presence of C, Ag, F and S at levels of 66.5, 17.0, 11.6 and 4.9 at%, respectively,

(Figure 6.3c), from the field of view shown (Figure 6.3d); *i.e.* confirming the presence of F in the starting material, (carbon at% values include support contributions).

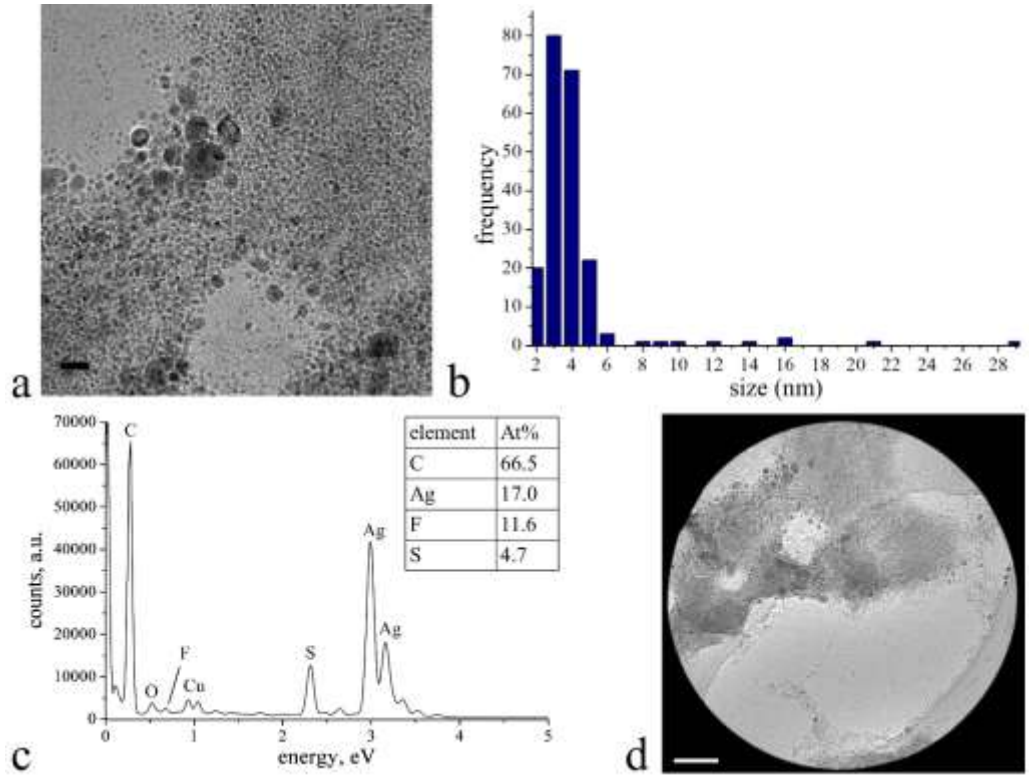

Figure 6.3 (a) Bright field, diffraction contrast TEM image showing starting F-AgNP (GO/Cu, 0.5 mg / hexane, no sonication; scale bar 20 nm) with associated (b) size distribution plot (4.0 ± 2.8 nm); and (c) EDS data confirming the presence of F in the AgNP starting material, from field of view in (d), scale bar 100 nm.

Further, Figure 6.4 presents a dark field scanning TEM (STEM) image, in conjunction with EDS mapping, from F-AgNP (Si_3N_4 MEMS chip, 0.5 mg / mL ethanol), showing F to be associated with C, S and Ag, and hence, uniformly distributed throughout the sample. In this case F-AgNP were deposited from ethanol, as the sample was not soluble in hexane.

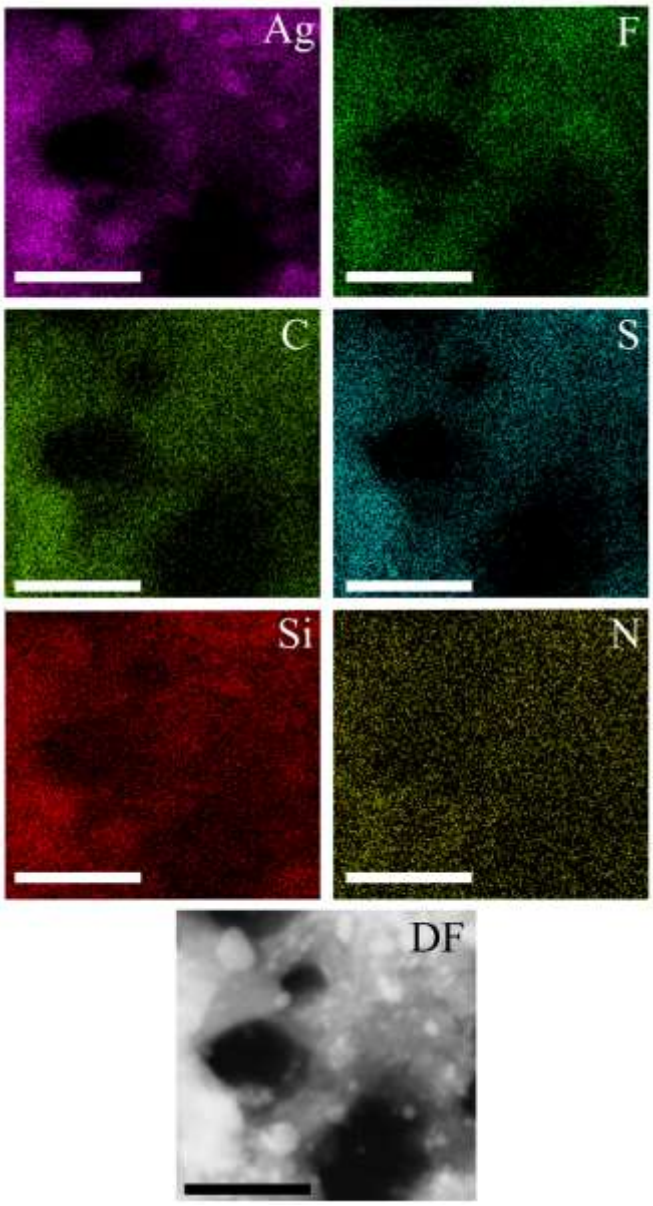

Figure 6.4 Dark field STEM image (DF) and EDS chemical mapping of F-AgNP (Si_3N_4 MEMS chip, 0.5 mg / mL ethanol) showing the distribution of F to match closely C, S and Ag throughout the sample (scale bars 250 nm). *Data collected by Dr Mike Fay*.

Figure 6.5 presents a representative UV/Vis spectrum from the starting F-AgNP (1.0 mg / ml ethanol), taking the form of a broad absorbance peak at 462 nm, with a shoulder at 237 nm, and a possible absorbance peak around ~ 287 nm (arrowed). This could arise from anisotropic shaped NP [9], or a non-monodispersed distribution of spherical F-AgNP, in accordance with XRD and TEM data.

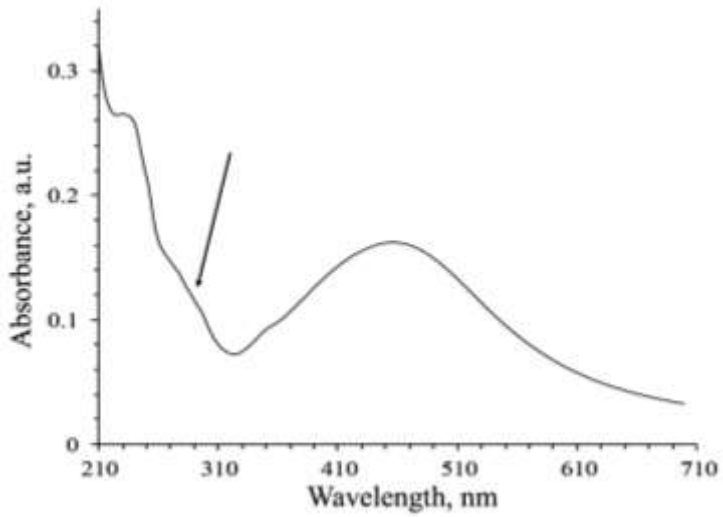

Figure 6.5 UV / Vis spectrum for starting F-AgNP, exhibiting peaks at 227 and 462 nm, and possibly ~ 287 nm, (arrowed), consistent with TEM and XRD data, indicating at least a bimodal NP size distribution.

Further, Figures 6.6a,b present ^{19}F NMR spectra for F-AgNP and as purchased HFT, respectively, indicating unambiguously the presence of F in the AgNP, consistent with the EDS data. Although many aspects of ^{19}F NMR spectroscopy are similar to ^{1}H NMR, resonance frequencies experienced by ^{19}F nuclei include a paramagnetic contribution from p-electrons which dominate over diamagnetic contributions and produce resonances shifted substantially downfield, compared to ^{1}H or ^{13}C, up to -270 ppm. Indeed, the spectra were consistent with that expected for HFT, with the peak at -82 ppm (t) assigned to the terminal $–CF_3$ group, and peaks at -114, -122, to 127 ppm, being attributable to the $–CF_2$- chain [10], with limited dispersion of F-AgNP in d_6-acetone leading to noisy spectra.

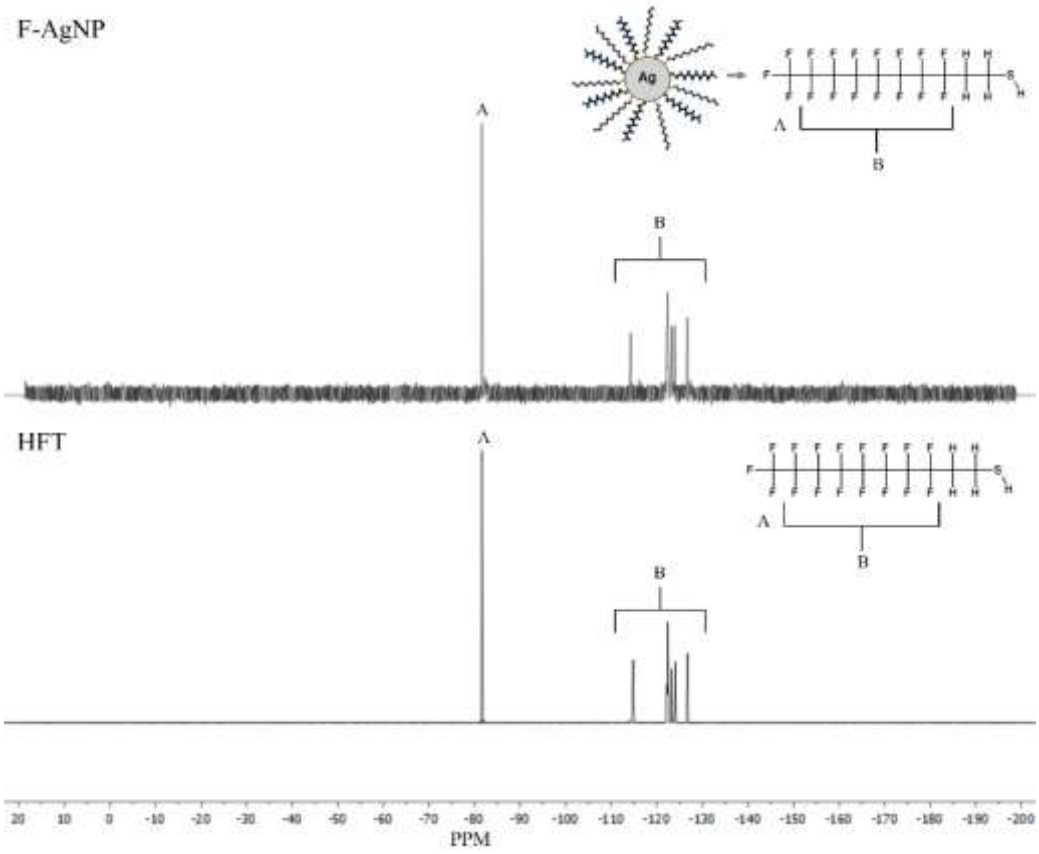

Figure 6.6 ^{19}F NMR spectra for: (a) F-AgNP stabilised with a mixture of 50:50 HFT:DDM, unambiguously indicating the presence of fluorine (acetone-d_6), consistent with perfluorinated alkane chains [10], and; (b) HFT (as purchased, acetone-d_6) for comparison.

6.2.2 Dispersion of F-AgNP onto support TEM grids

For comparison, Figures 6.7a,b present TEM images of starting F-AgNP (C/Cu; 0.5 mg/ml cyclohexane, sonicated 15 minutes, several drops cast, drying naturally between additions), showing a tendency for the formation of connected, large clusters of NP. Choice of solvent for deposition in this instance was guided by previous experiments for AgNP samples, stabilised with dodecanethiol; sonication was commonly performed to ensure dissolution, prior to the experiments investigating the effect of sonication on AgNP samples in suspension, as reported on in Chapter 4.3. The higher magnification image of Figure 6.7b allowed individual NP to be identified.

This contrasts with samples deposited in the absence of sonication from one drop of AgNP (agitated and mixed well, but not dissolved in hexane) (Figure 6.3a) which did not show evidence for such large clusters. However, the formation of self-assembled structures mediated by F, and aggregation of F-NP, are consistent with literature [11, 12], inevitably presenting challenges for discrete HCNS formation. Figure 6.7d presents a selected area electron diffraction (SAED) pattern from F-AgNP, typical of a random distribution of many small, crystalline Ag particles, consistent with published SAED data for (DDM-stabilised) AgNP (Figure 6.7e) [13].

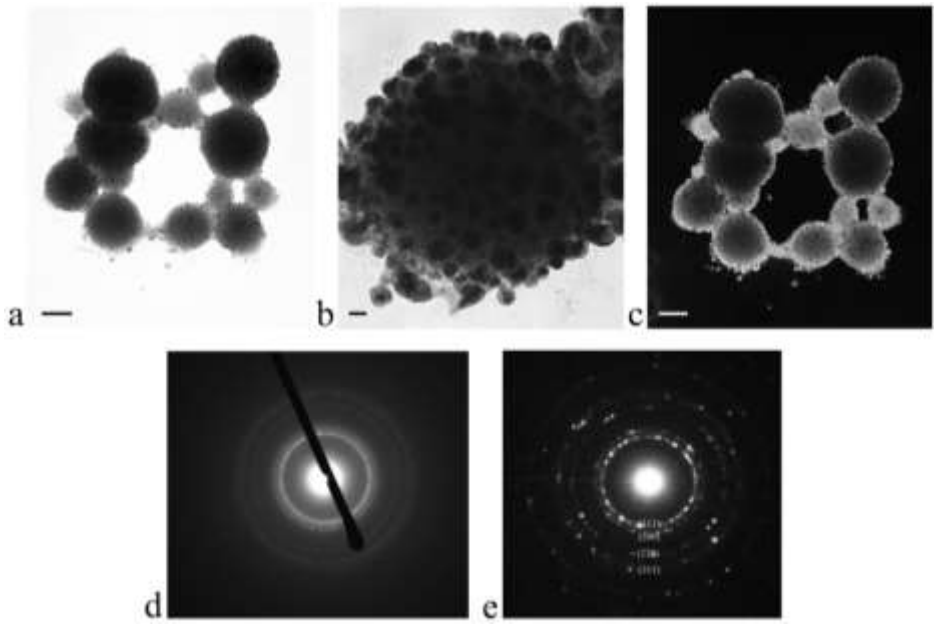

Figure 6.7 TEM images of AgNP stabilised with 50:50 DDM:HFT, dispersed from cyclohexane, showing: (a,b) Connected, highly clustered, distributions of particles (scale bars 200 & 20 nm, respectively); and (c) associated dark field image (scale bar 200 nm); (d) complementary diffraction pattern confirming the presence of Ag and; example SAED of AgNP from literature with assigned crystal planes for fcc Ag [13].

6.2.3 Thermal processing of F-AgNP

The formation of HCNS from F-AgNP was achieved *in situ* with a rapid heating rate using the MEMS holder (TP-1; ~ 100°C/s). Figure 6.8a presents an image of the starting F-AgNP and the HCNS product after rapid thermal processing (850°C, TP-1, Si_3N_4), from a region providing for the discrimination of individual F-AgNP allowing for direct comparison between starting material and HCNS formed (Note: F-AgNP were not soluble in hexane or cyclohexane and to avoid sonication, the sample was drop cast from ethanol solution, (0.5 mg / 1 ml ethanol, 5 drops cast)), however, most of the sample comprised large agglomerations (Figure 6.9a)). The relative location of products and starting material provided direct evidence for the formation of HCNS from the F-AgNP, with the size distribution of the HCNS product (7.6 ± 2.8 nm) slightly larger than the starting F-AgNP (7.2 ± 2.8 nm).

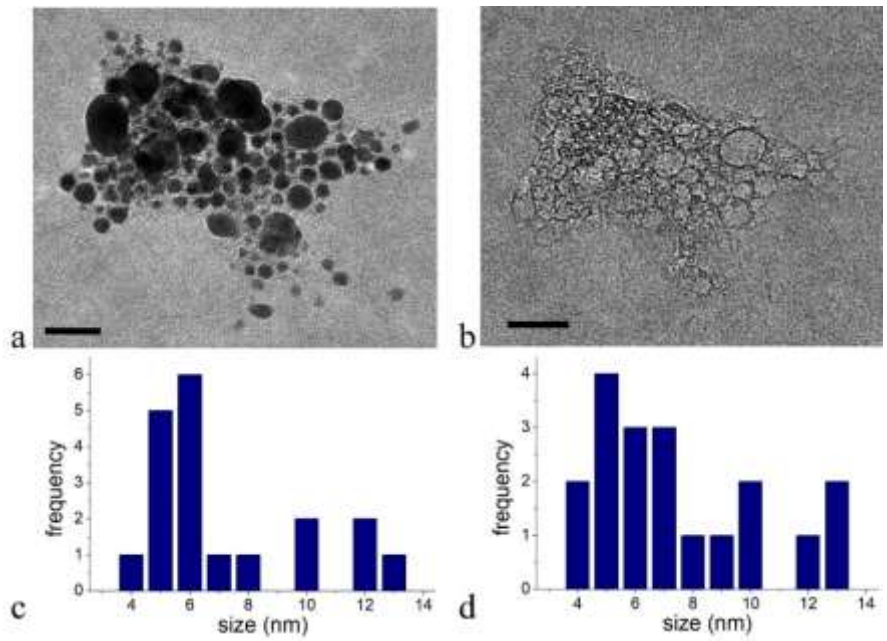

Figure 6.8 TEM images (contrast enhanced) of: (a) Starting F-AgNP; and (b) HCNS products after rapid thermal processing (TP-1; dispersed from ethanol, Si_3N_4 MEMS chip, scale bars 20 nm), returning size distributions of: c) 7.2 ± 2.8 nm; and d) 7.6 ± 2.8 nm, respectively (n = 20).

The low magnification TEM image of Figure 6.9a, providing a wide field of view, illustrates the large F-AgNP agglomerations or superstructures more typically observed on the Si_3N_4 support window, which produced large HCNS and C foam-like structures following rapid heating (Figure 6.9b). However, and most notably, complementary EDS confirmed the presence of F in the HCNS / foam products, after thermal processing of F-AgNP, detected at low levels ~ 0.5 at%, along with C, Ag and S at levels of 97.2, 1.8 and 0.5 at%, respectively (Figure 6.10a), from the field of view indicated (Figure 6.10b).

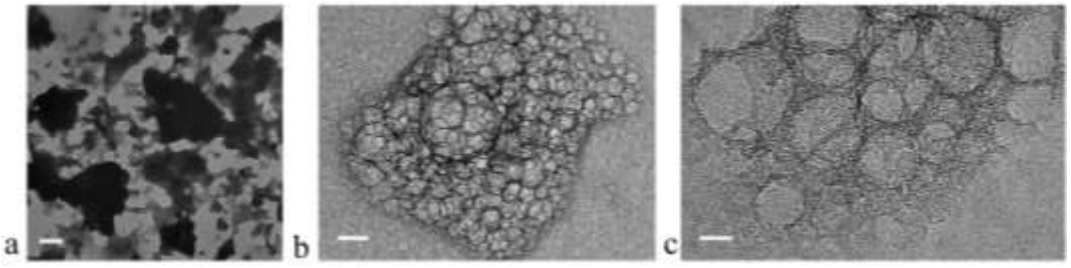

Figure 6.9 (a) Low magnification image of large agglomerations of starting F-AgNP on the MEMS support, prior to rapid heating (TP-1, 850°C, scale bar 200 nm, dispersed from ethanol); and (b,c) developed HCNS and C foam-like structures, following the loss of Ag templates (scale bars 20 & 10 nm, respectively; images contrast enhanced).

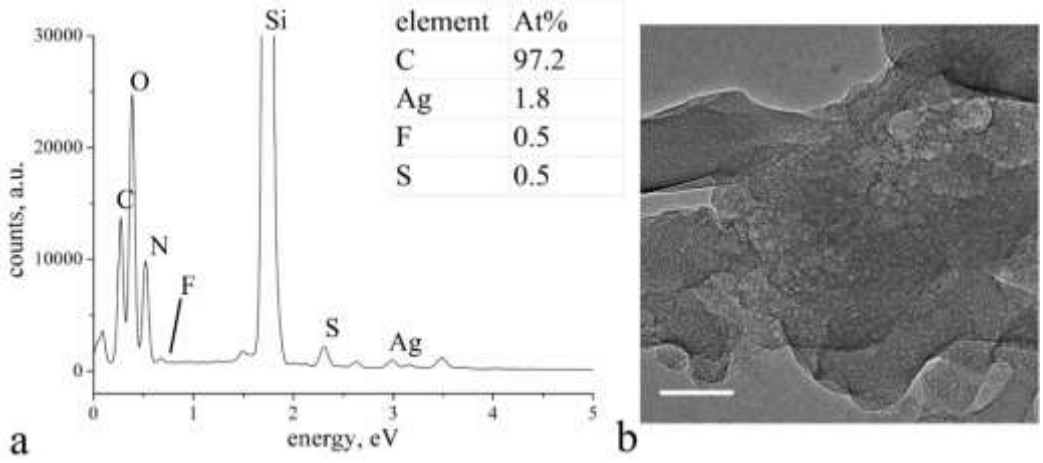

Figure 6.10 F-AgNP, after heating to 850°C (TP-1) on Si_3N_4: (a) EDS data confirming the presence of trace amounts of F (0.5 at%) in the HCNS product, along with C, Ag and S, from the field of view in image (b), (scale bar = 50 nm).

Further, Figure 6.11 presents a first order Raman spectrum acquired from products formed from heating F-AgNP on Si_3N_4 (850°C, at ~ 100°C/s). The general peak shapes are consistent with a highly disordered graphitic carbon.

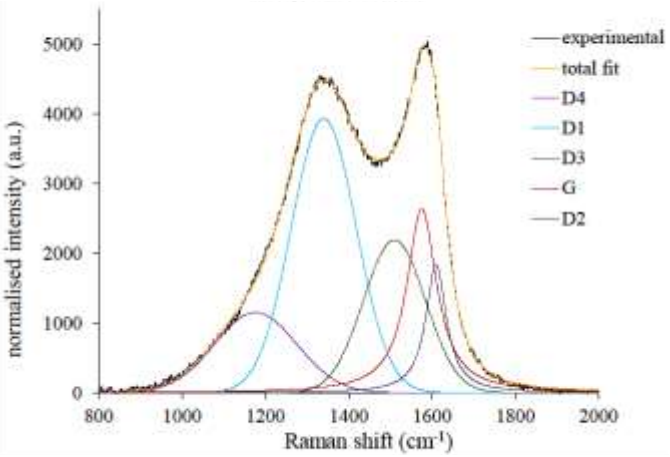

Figure 6.11 First order Raman spectrum (λ_{ex} = 532 nm) obtained in the range 800-2000 cm^{-1} from F-AgNP heated to 850°C (at ~ 100°C/s), confirming the disordered graphitic nature of the product. The spectrum was normalised to the intensity of the G band (*cf.* results from TP-1, Figure 4.19), baseline-corrected using a third order polynomial subtraction and fit using a five-band model, analogous to that previously described [14] ($\chi 2 = 2.0$). *Data collection and analysis performed by Dr Graham Rance.*

Table 6.4 First order Raman band assignments [14, 16].

Band [a]	**Raman shift / cm^{-1}**	**Proposed vibrational mode assignment**
G	1576s	Ideal graphitic lattice (E_{2g} symmetry)
D1 (D)	1340 vs	Disordered graphitic lattice (A_{1g} symmetry)
D2 (D')	1610 s	Disordered graphitic lattice (E_{2g} symmetry)
D3 (D", A)	1510 m	Amorphous carbon
D4 (I)	1176 m	Disordered graphitic lattice (A_{1g} symmetry), polyenes, ionic impurities

[a] *alternative band designations of earlier studies are in parantheses (vs = very strong, s = strong, m = medium).*

The two broad, slightly overlapping bands around 1345 and 1582 cm^{-1} were attributed nominally to the defect (D) and graphite (G) bands, with four Lorentzian-shaped bands (G, D1, D2, D4) and a Gaussian-shaped band (D3) carefully deconvoluted (Table 6.4), as described in Section 4.5.1 [15].

The first order spectrum presented in Figure 6.11, whilst notably very similar to the spectrum obtained from HCNS (Figure 4.19 and Figure 5.8), presents subtle differences, yielding information regarding the relative amounts of amorphous and disordered graphitic C present. A shift in the position of the apparent G band from ~1590 to ~1582 cm^{-1} for HCNS and F-HCNS, respectively, may be tentatively rationalised by either: (a) Plasmonic heating, or charge transfer effects, due to the presence of residual Ag in close proximity to the carbon structures, resulting in a red shifted G band or; (b) differences in the curvature of the obtained nanostructures, as the F-HCNS are slightly smaller (~ 7.5 nm) compared to HCNS (~ 9 nm), Figure 5.5. Indeed, the relative intensities of the apparent D and G bands appeared to be very similar. Further, evaluation of peak areas for deconvoluted bands provided quantitative information regarding the extent of disorder and amorphous C in the F-HCNS structures, whilst the intensity ratio (as peak area) of the D1 and G bands (I_{D1}:I_G) was high for both F-HCNS or HCNS, (I_{D1}:I_G = 2.25 and 3.08, respectively), with the value for the latter being larger. In addition, the intensity ratio (as peak area) of the D3 and G bands (I_{D3}:I_G) was also high for F-HCNS, and significantly higher compared to HCNS (I_{D3}:I_G = 1.68 and 1.20, respectively). Both of these ratios indicated that F-HCNS structures contained slightly more graphitic C, in conjunction with less amorphous carbon contributions, when compared to HCNS, indicating that the extent of graphitisation of the carbon products formed was not diminished by F-

incorporation into TS-AgNP starting materials, indeed, graphitisation was slightly improved.

Hence, and by way of brief summary, the formation of HCNS containing F heteroatoms was indicated from the *in situ* heating of F-AgNP to 850°C (~ 100°C/s) on Si_3N_4, with the products obtained commensurate with the distribution of F-AgNP starting material on the support, along with the development of foam-type structures formed from connected large clusters of F-AgNP. The introduction of F into TS-AgNP starting materials appeared to slightly improve the extent of HCNS graphitisation.

6.3 Production of HCNS from N-containing TS-AgNP

A set of nitrogen containing TS-AgNP (N-AgNP) samples were synthesised (Table 6.5), using varying additions of DDM and PUT. These were characterised initially before dispersion onto supports and thermal processing to form HCNS.

Note: N-AgNP samples were thermally processed *in situ* on MEMS chips, with fast heating rates, to confirm the development of well-defined G-HCNS products, but inevitably, the presence of Si_3N_4 supports precluded confirmation of the successful incorporation of N heteroatoms into the product. Hence, N-AgNP were also processed *in situ* on GO/Cu with the Gatan system and *ex situ* on MWCNT supports, albeit with the limitations of intermediate heating rates, in order to identify N heteroatoms in the product.

Table 6.5 Overview of starting N-AgNP, synthesised using varying DDM:PUT ratios, thermally processed to produce HCNS.

Sample					**Heating conditions**			
Name	**Stabilising layer / %**	**DDM / %**	**PUT / %**		**System**	**Support**	**Temp / °C**	**Rate / °C/s**
TS-AgNP*	**none**	100	0		MEMS	Si_3N_4	850	~ 100
TS-AgNP*	**none**	100	0		Furnace	MWCNT	850	~ 20
N2-AgNP	**N 1.6**	72	25		MEMS	Si_3N_4	850	~ 100
N3-AgNP	**N 3.1**	50	50		MEMS	Si_3N_4	850	~ 100
N3-AgNP	**N 3.1**	50	50		Gatan	GO/Cu	850	~ 20
N3-AgNP	**N 3.1**	50	50		Furnace	MWCNT	850	~ 20
N4-AgNP	**N 4.4**	25	74		MEMS	Si_3N_4	850	~ 100
N5-AgNP	**N 5.5**	0	100		MEMS	Si_3N_4	650 - 1000	~ 100
N5-AgNP	**N 5.5**	0	100		Furnace	MWCNT	850	~ 20

DDM = 1-dodecanethiol; PUT = 11-(*1-H*-pyrrol-1-yl)undecanethiol.

**The formation of HCNS from DDM stabilised AgNP was shown in Chapters 4 & 5.*

6.3.1 Characterisation of starting N-AgNP & HCNS products

As-synthesised N-AgNP samples (Section 3.2.1) were characterised to confirm the nature of (and presence of N within) the starting materials; with emphasis on the effect of DDM:PUT ratio. Again, attention was given to the overall morphology and chemistry of the samples, *i.e.* the AgNP template and the N-containing carbon source (thiol stabilising layer). Starting N-AgNP samples were evaluated using a combination of XRD, TEM and UV/vis spectroscopy, with chemistry investigated

further using the complementary technique of NMR spectroscopy, to avoid repetition, one example is presented in this results section, with others in appendix A.

The N-AgNP samples were thermally processed *in situ* to at least 850°C, with a fast heating rate (~ 100°C/s, TP-1), on Si_3N_4 MEMS heating chips; with individual data sets to follow, in order of ascending N-content within the stabilising layer. For sample N5-AgNP, fast heating (~ 100°C/s) to 650°C, then 850°C, 950°C and 1000°C, with a hold time at each temperature of 1 minute employed, to allow for collection of data at these temperatures. Raman spectroscopy was performed on all thermally processed N-AgNP samples (Si_3N_4), with spectra and all results presented in Appendix B, and with key results tabulated at the end of this section. Complementary *in situ* thermal processing (850°C / at ~ 20°C/s) of N3-AgNP on GO/Cu (Gatan system) and *ex situ* heating to 850°C (at ~ 20°C/s) was also performed for samples N3-AgNP and N5-AgNP deposited onto MWCNT, sealed under vacuum into quartz ampoules, and imaged at RT ~ 8 days later (in the attempt to identify N within the HCNS products, free of the interference of the Si_3N_4 supports).

6.3.1.1 DDM:PUT ratio of 75:25 (1.6% N)

For nitrogen containing NP with a mixed thiol stabilising layer of DDM:PUT in the proportions 75:25 (N2-AgNP), particle size and appearance were found to be comparable to AgNP stabilised by DDM only, but some N-AgNP agglomeration / grain growth was also apparent. Figures 6.12a,b present TEM images of this mixed thiol stabilised AgNP (0.5 mg / ml cyclohexane, GO / Cu, ~ 5 drops, natural drying between additions), with a spherical NP appearance. The cyclohexane solvent choice was made to enable direct comparisons between TS-AgNP and N-AgNP. Whilst

Figure 6.12b shows significant agglomerations, a narrow size distribution (5.0 ± 1.8 nm, n = 384; range 2 – 18 nm) was found for N2-AgNP, measured from the image free from agglomeration (Figure 6.12c).

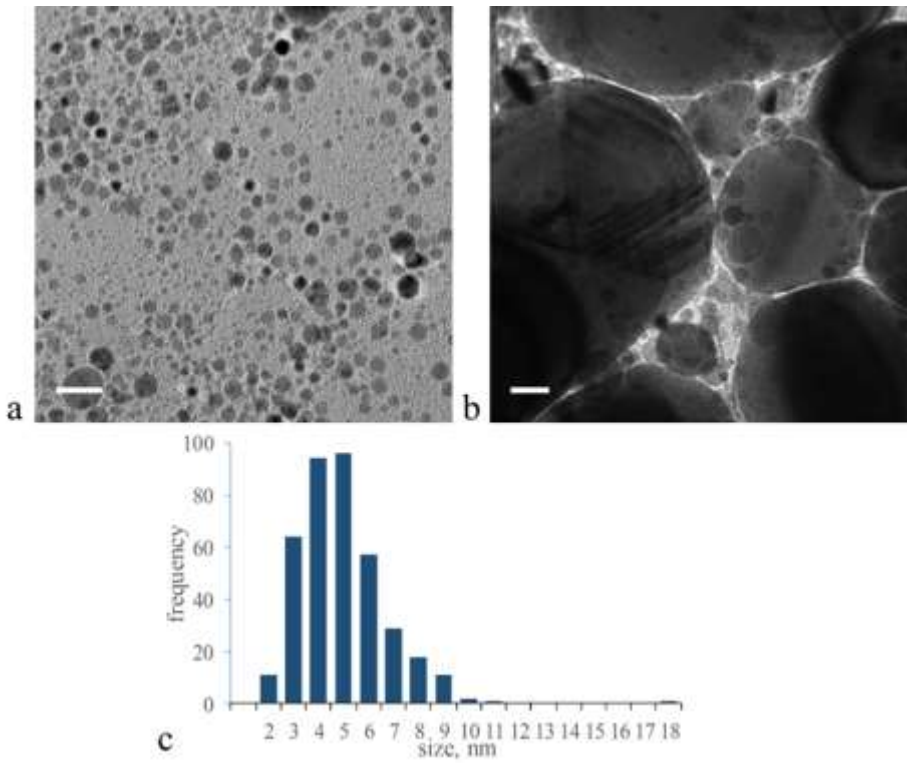

Figure 6.12 TEM data for N2-AgNP (0.5 mg / ml cyclohexane, GO / Cu, ~ 5 drops, natural drying between additions), showing: (a) spheroidal NP; and (b) some regions of pronounced agglomeration, with the presence of twin bands indicative of grain growth (scale bars 20 nm); with (c) size distribution 5.0 ± 1.8 nm, n= 384, range 2 – 18 nm.

Interestingly, Figures 6.13a,b for N2-AgNP deposited from a more polar solvent (GO/Cu, 0.5 mg / ml chloroform, ~ 5 drops, natural drying between additions) showed more evidence for agglomeration / grain growth, promoted by the presence of dipoles in the AgNP stabilising layer due to the presence of pyrrole groups in PUT, and an increased size and size distribution, with a larger range of starting AgNP sizes (9.3 ± 4.7 nm, n = 437; range 2 – 50 nm). The histogram of Figure 6.13c shows this increased morphological variation, compared to samples deposited from cyclohexane

(Figure 6.12c), however, this could arise due to selective dissolution of AgNP, rather than being attributable to a solvent effect.

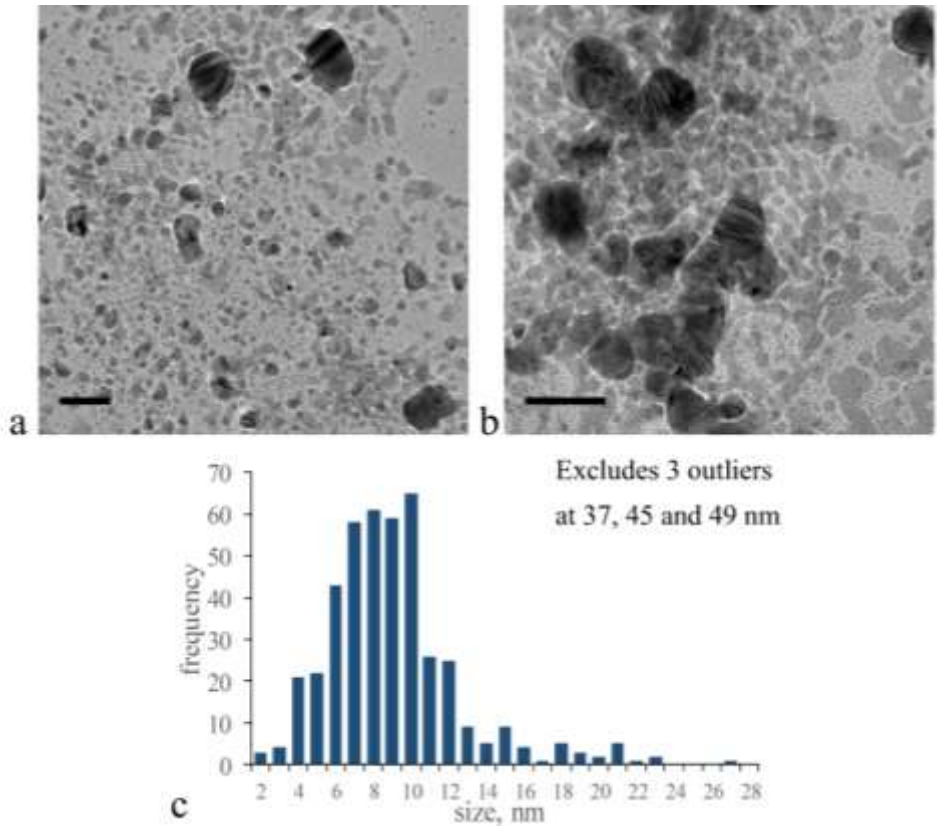

Figure 6.13 TEM data for N2-AgNP (0.5 mg / mL $CHCl_3$, ~ 5 drops, Cu/GO) showing: (a) More varied shapes (compared to TS-AgNP stabilised with DDM) and a broader size distribution (scale bar 50 nm); (b) some significant agglomeration / grain growth of N-AgNP (scale bar 20 nm); and (c) size 9.3 ± 4.7 nm, n = 437; range 2 – 50 nm .

Figure 6.14 presents a representative UV/Vis spectrum for starting N2-AgNP (1.0 mg / ml $CHCl_3$, filtered), taking the form of a narrow absorbance peak at 436 nm, consistent with a monodispersed distribution of spherical AgNP, *i.e.* with a single size distribution and the absence of agglomeration / grain growth, in contrast to TEM data. The difference may be due to sample handling and preparation, with larger agglomerations of N2-AgNP excluded during filtration and perhaps settling prior to, or during, UV/Vis data collection.

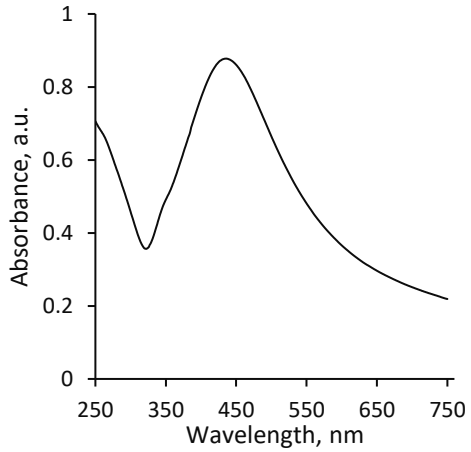

Figure 6.14 UV/Vis spectrum for N2-AgNP with a single peak at 436 nm, consistent with the presence of a narrow size distribution of spherical AgNP.

Figure 6.15a presents a TEM image of the starting N2-AgNP (Si_3N_4 MEMS chip, 0.5 mg / ml toluene, sonicated, 1 drop cast), recorded at RT, showing spherical AgNP (8.67 ± 4.32 nm) whilst the associated histogram (Figure 6.15c) indicates the extent of aggregation / grain growth, possibly attributable to the brief sonication employed to ensure sample dissolution in this instance, with toluene as the solvent in this instance to increase drying times on the support, *i.e.* aiming to discretely disperse NP. Conversely, Figure 6.15b shows the same field of view, imaged at 850°C (heated at ~ 100°C/s, TP-1), with the resultant hollow structures revealed, matching the positions of the starting N2-AgNP, whilst exhibiting a slightly larger size of 9.28 ± 4.92 nm (Figure 6.15d). Both TEM images were contrast enhanced for clarity.

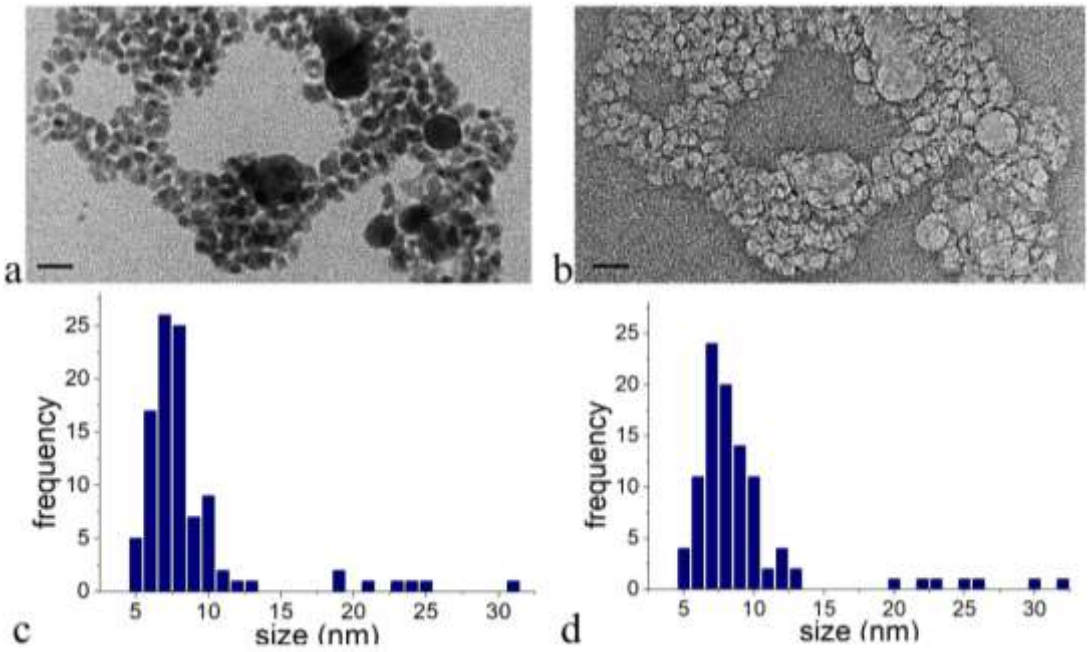

Figure 6.15 TEM micrographs (contrast enhanced) of: (a) N2-AgNP / Si_3N_4, before rapid heating to 850°C (TP-1); and (b) the resultant HCNS, imaged at 850°C (scale bars 20 nm). Associated particle size histograms: (c) Before heating, 8.67 ± 4.32 nm (corresponding to N2-AgNP); and (d) after heating, 9.28 ± 4.92 nm (corresponding to the HCNS products).

Unfortunately, no evidence for the presence of N within these HNCS products was found from EDS of EELS investigations, whilst noting that both the sample amount and nitrogen content were very low. Complementary Raman data for this sample set are presented in Appendix B.

6.3.1.2 DDM:PUT ratio of 50:50 (3.1% N)

Figure 6.16a presents a representative, conventional, bright field, diffraction contrast TEM image of AgNP stabilised with an equimolar mixture of DDM and PUT (N3-AgNP), (C/Cu, 0.5 mg / ml cyclohexane, solution filtered, 200 µm PTFE), revealing the crystalline, spheroidal AgNP, with a particle size distributions of 4.0 ± 1.5 nm (Figure 6.16b) similar / of the same order of magnitude as literature examples for

DDM stabilised AgNP [9]. The associated SAED pattern from N-AgNP (Figure 6.16c) was typical of a random distribution of many small, crystalline Ag grains, consistent with published SAED data for (DDM-stabilised) AgNP (Figure 6.16d) [13].

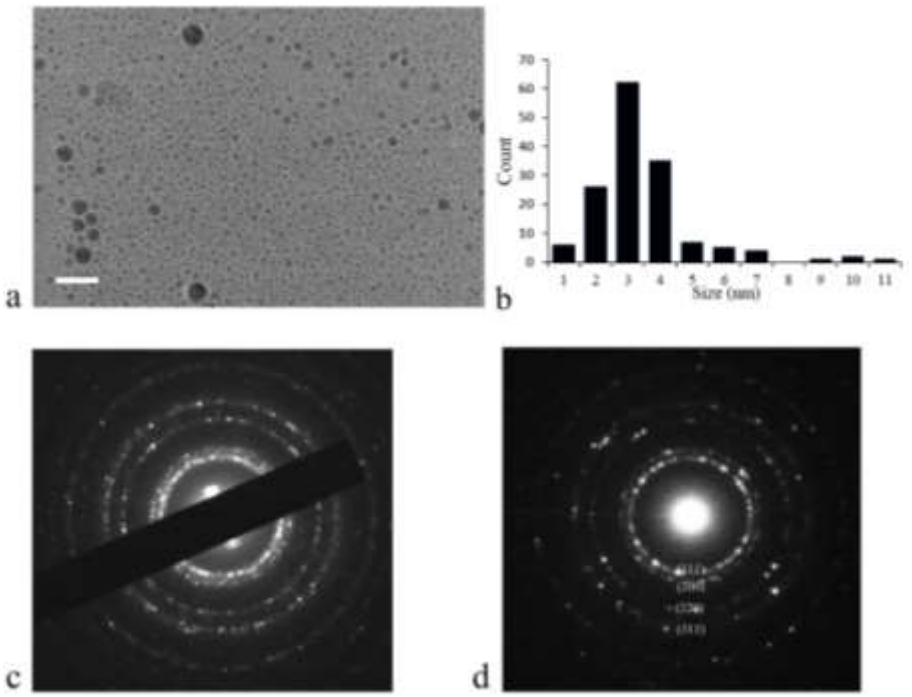

Figure 6.16 Bright field, diffraction contrast TEM image of N3-AgNP stabilised with DDM:PUT 50:50 (scale bar 20 nm), with: (b) Particle size distribution (4.0 ± 1.5 nm) (C / Cu, 0.5 mg / ml cyclohexane). (c) SAED pattern consistent with published diffraction data for DDM-stabilised AgNP (d) [13 Gonzalez]. *Data collected by Dr Mike Fay.*

Figure 6.17 presents a representative UV/Vis spectrum for starting N3-AgNP (1.0 mg / ml cyclohexane), with a narrow absorbance peak at 460 nm, again consistent with a narrow size distribution of spherical AgNP, in accordance with TEM data, noting that the solution was filtered prior to data collection.

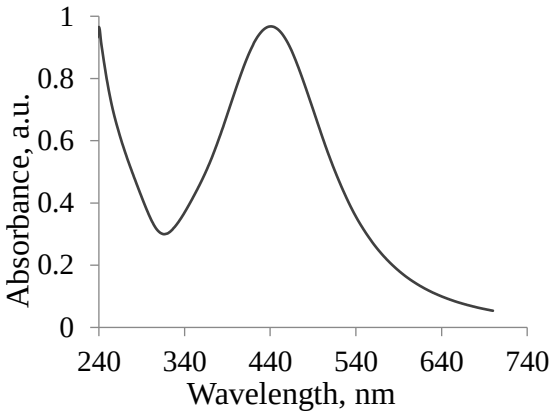

Figure 6.17 UV/Vis results for N3-AgNP with a single, narrow absorbance at 436 nm, consistent with the presence of narrowly size distributed, spherical AgNP.

Complementary NMR spectroscopy investigations of as-synthesised N3-AgNP, and as-purchased DDM and PUT, confirmed the presence of these thiols stabilising the AgNP. Figure 6.18a presents a spectrum for AgNP stabilised by DDM:PUT (50:50), with peaks at 0.9 ppm and ~ 1.2 – 1.6 ppm being assigned to the terminal methyl group and unbranched alkane chain, respectively, whilst the peak at 3.9 ppm was assigned to the alkane chain adjacent to nitrogen, and those at 6.2 and 6.7 ppm to the pyrrole ring [17]. There was found to be a ~ 50:50 mixture of thiols in the NMR spectrum of N3-AgNP, calculated from peak integrals. Indeed, the ^{1}H NMR of DDM and PUT in solution (Figures 6.18b,c, respectively) evidence DDM and PUT were bonded to AgNP, since peaks at 1.6 and 2.4 ppm present in the DDM spectrum were not observed in the N3-AgNP spectrum, due to alterations to relaxation times associated with nuclei bonded (or close) to the AgNP core. In particular, only peaks attributable to the pyrrole functional group were present in the region associated with aromatic functional groups (6 - 9 ppm); confirming that the starting TS-AgNP was non-graphitic.

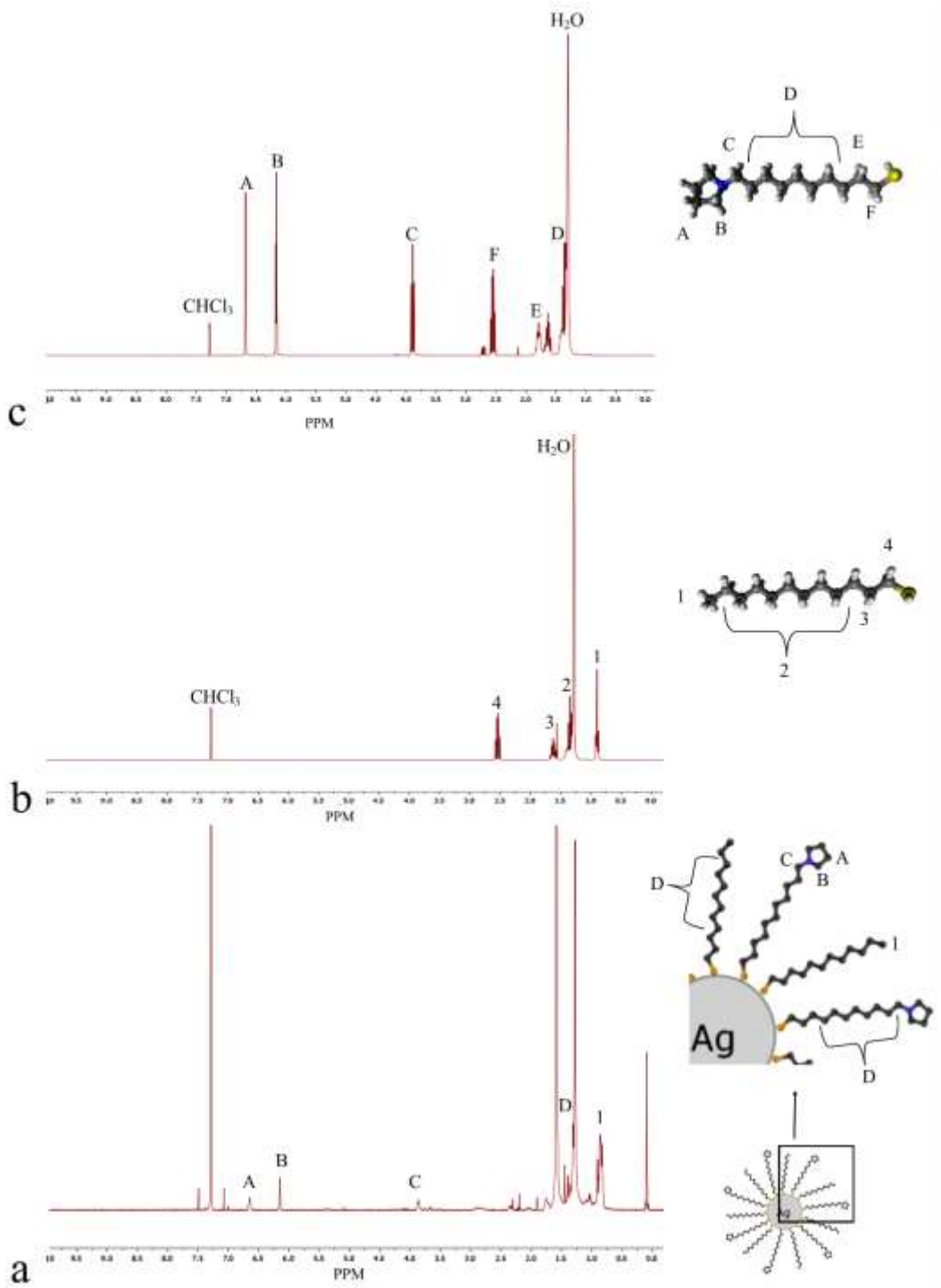

Figure 6.18 [1]H NMR spectra of: (a) N3-AgNP stabilised with DDM:PUT (50:50), with peak assignments and; (b) DDM and; (c) PUT for comparison. The absence of peaks at 2.5 ppm indicate that the thiol molecules are bound to AgNP. Low amounts of dispersed N-AgNP resulted in noisy spectrum. *Note: NMR spectra are measured in frequency units (MHz), but presented in the dimensionless units of PPM to enable comparison between spectra recorded at different field strengths.*

Figure 6.19a presents a bright field, diffraction contrast TEM micrograph of the starting N3-AgNP (Si_3N_4 MEMS chip, 0.5 mg / ml toluene, sonicated, 1 drop cast) at RT, revealing spheroidal AgNP (8.07 ± 3.37 nm) (Figure 6.20c), with toluene as the solvent to increase drying times on this support. Aggregation was observed in this field of view and over the wider MEMS support, again possibly attributable to brief sonication during sample deposition. In contrast, Figure 6.19b shows the same location, imaged *in situ* at 850°C (heated at ~ 100°C/s, TP-1), with HCNS structures (8.52 ± 3.54 nm) (Figure 6.19d) matching the positions of the starting N3-AgNP. Both TEM images were contrast enhanced for clarity.

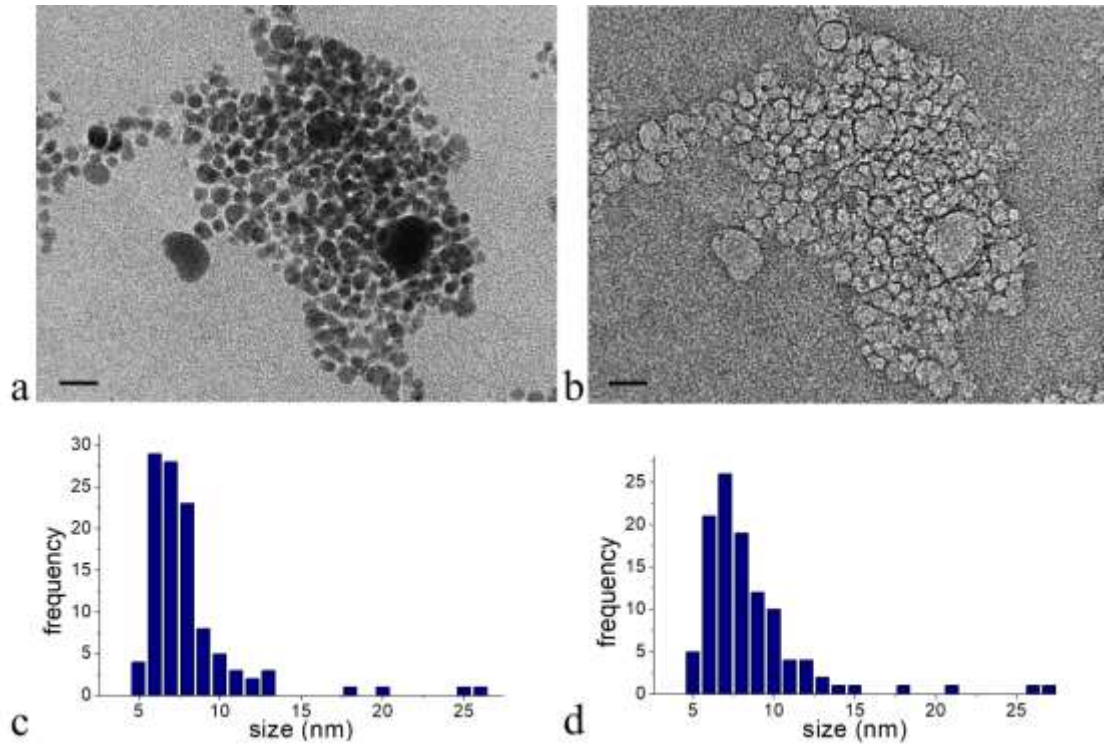

Figure 6.19 TEM micrographs (contrast enhanced) of: (a) N3-AgNP / Si_3N_4 before rapid heating to 850°C; and (b) the resultant HCNS imaged at 850°C (scale bars 20 nm). Particle size histograms: (c) Before heating, 8.07 ± 3.37 nm (corresponding to N3-AgNP); and (d) after heating, 8.52 ± 3.54 nm (corresponding to the HCNS structures formed).

Further, Figure 6.20a presents a low magnification TEM image for N3-AgNP (GO/Cu, 0.5 mg / 1 ml cyclohexane and ~ 1% DDM, solution filtered) at 23°C commensurate with previous examples of spherical N-AgNP, Figure 6.2b recorded at 850°C (at ~ 20°C/s) shows the well-defined HCNS products formed, with removal of Ag from the field of view. Complementary XPS spectra from N3-AgNP (GO/Cu, heated to 850°C, ~ 20°C/s), at 23°C, ~ 8 days later, Figure 6.20c, indicate the presence of carbon (70.2 at%), sulphur (14.1 at%), oxygen (10.2 at%) and nitrogen (5.6 at%).

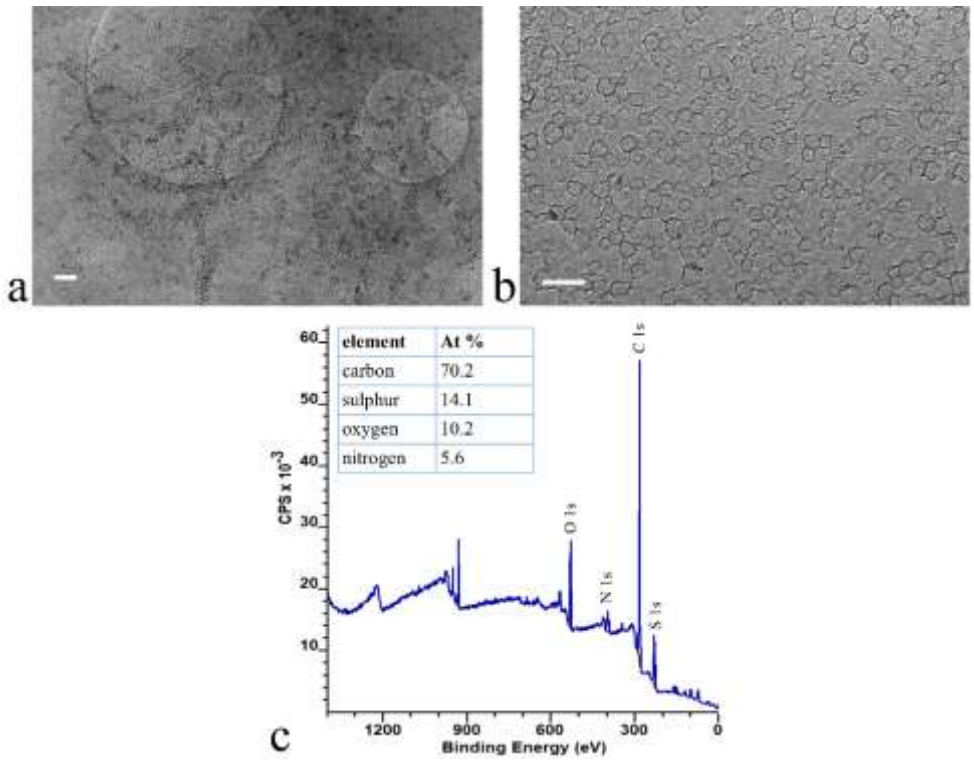

Figure 6.20 TEM images of N3-AgNP (GO/Cu, 0.5 mg / 1 ml cyclohexane and ~ 1% DDM, solution filtered); (a) low magnification image at 23°C showing starting material dispersion and; (b) higher magnification image recorded at 850°C, illustrating the structures formed and removal of AgNP; (c) wide-scan XPS results indicate the presence of carbon, sulphur, oxygen and nitrogen.

Conversely, Figure 6.21 presents phase contrast TEM images for N3-AgNP (DDM:PUT 50:50) deposited onto MWCNT, *ex situ* heated rapidly to 850°C (inserted

into a hot furnace; heated at ~ 20°C/s), recorded at RT (~ 8 days later), revealing a somewhat variable product, reflecting the intermediate heating rate, with foam-like appearance, containing hollow circular or oval regions (~ 10 – 20 nm sized), and some residual AgNP, suggesting incomplete processing (Figure 6.21a). Additionally, Figure 6.21b shows the formation of HCNS, positioned on the edge of MWCNT. It is considered likely that sonication during deposition of N-AgNP onto MWCNT in this instance induced some agglomeration of AgNP in preference to attachment of N-AgNP to CNT, with the resulting carbon structures formed from heating reflecting the more varied morphology of the N-AgNP.

However, EDS and EELS data were unable to provide conclusive evidence for the presence of N within HCNS, again due to the very limited sample amounts (and low anticipated levels of N therein), combined with the presence of residual AgNP and quantities of MWCNT support material.

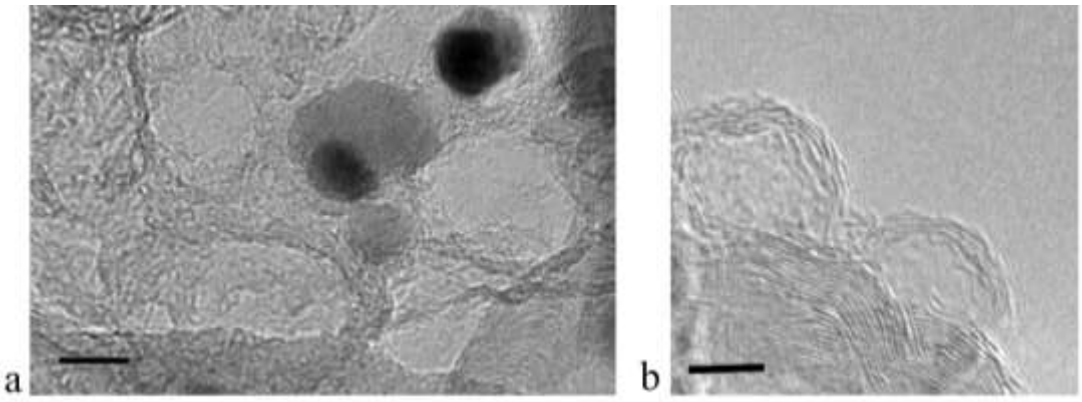

Figure 6.21 Phase contrast TEM images of N3-AgNP deposited onto MWCNT (deposited from cyclohexane), *ex situ* heated to 850°C, recorded at RT (~ 14 days later), show the resultant structures formed: (a) Connected foam-like structure with hollow circular regions adjacent to incompletely processed AgNP (scale bar 10 nm) and; (b) individual hollow carbon structures on the edge of MWCNT (scale bar 5 nm).

6.3.1.3 DDM:PUT ratio of 25:75 (4.4% N)

Figure 6.22a presents a TEM micrograph for AgNP stabilised with DDM:PUT (25:75, N4-AgNP), (0.5 mg / ml acetone, Si_3N_4), showing generally well-defined spherical particles, with a rather broad size distribution, 8.34 ± 3.15 nm (Figure 6.22b), and some larger N4-AgNP. N4-AgNP were soluble in acetone, but not in hexane or cyclohexane (results not shown), hence use of this solvent for TEM deposition in this instance.

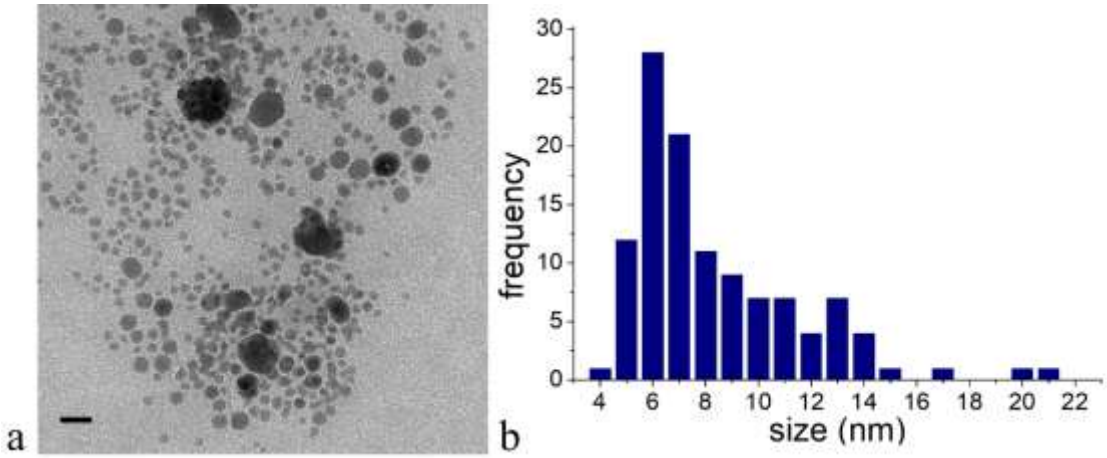

Figure 6.22 TEM micrograph for: (a) Starting N4-AgNP (0.5 mg / ml acetone, Si_3N_4), showing generally well-defined spherical particles, but the presence of more varied morphologies and larger NP (scale bar 20 nm) and; (b) size distribution histogram (8.34 ± 3.15 nm).

Figure 6.23 presents UV/Vis data for N4-AgNP (0.5 mg / ml acetone, solution filtered), displaying an absorbance at 455nm, indicative of spherical NP species with a size distribution consistent with TEM data.

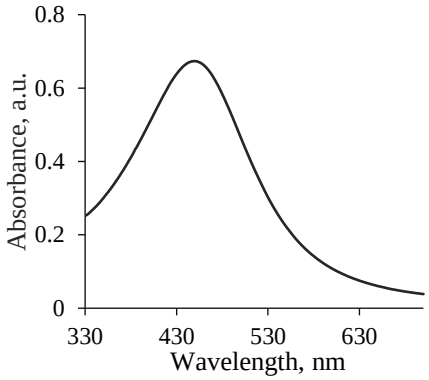

Figure 6.23 UV/Vis spectrum for starting N4-AgNP (0.5 mg /ml acetone), exhibiting a peak maxima ~ 455nm, consistent with TEM data indicating an acceptable NP size distribution.

Complementary NMR spectroscopy investigations of as-synthesised N4-AgNP confirmed the presence of DDM and PUT in the AgNP stabilising layer, the spectrum is presented in Appendix A.

Figure 6.24a shows a TEM micrograph of N4-AgNP (Si_3N_4 MEMS chip, 0.5 mg / ml acetone, 1 drop cast), at RT, revealing mostly spherical AgNP, 8.34 ± 3.15 nm sized (Figure 6.24c), with some aggregation observed. In contrast, Figure 6.24b shows the same field of view, recorded at 850°C (heated at ~ 100°C/s, TP-1), with the HCNS structures matching the positions of the starting material, N4-AgNP, whilst being slightly larger, 9.24 ± 3.43 nm (Figure 6.24d). Both TEM images were contrast enhanced for clarity.

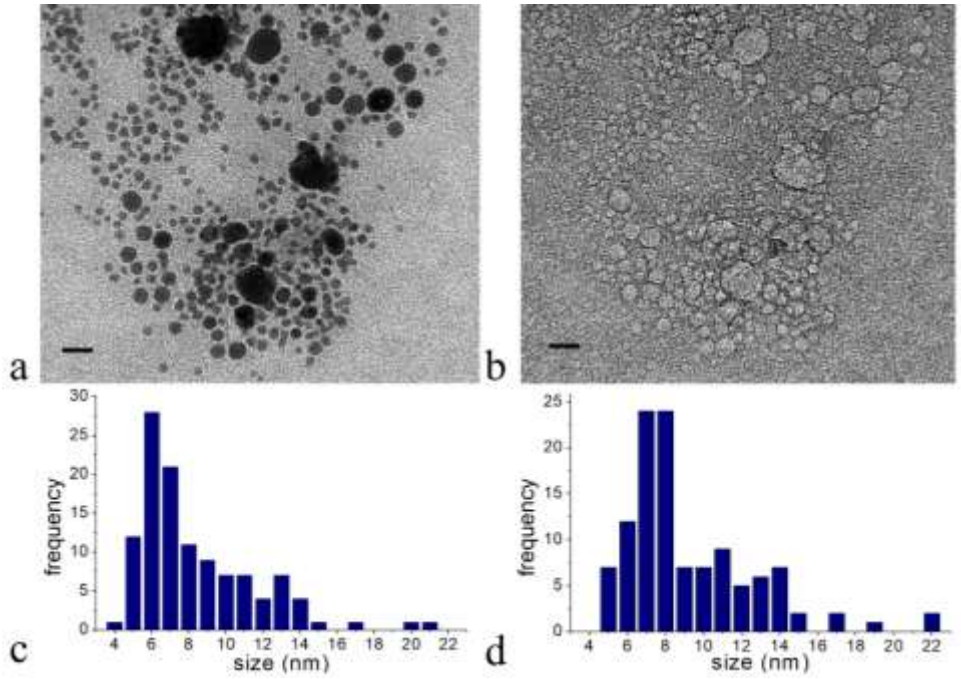

Figure 6.24 TEM micrographs, contrast enhanced, of: (a) N4-AgNP / Si_3N_4 before rapid heating to 850°C; and (b) the resultant HCNS, imaged at 850°C (scale bars 20 nm). Particle size histograms: (c) Before heating, 8.34 ± 3.15 nm (corresponding to N4-AgNP); and (d) after heating 9.24 ± 3.43 nm (corresponding to HCNS structures formed).

6.3.1.4 AgNP stabilised with PUT (5.5% N)

Figure 6.25 presents TEM data and size distribution for AgNP stabilised with PUT (N5-AgNP), revealing spherical AgNP (7.9 ± 2.3 nm, n = 185), with some evidence for agglomeration (GO/Cu, 0.5 mg / ml cyclohexane, 5 minutes sonication). Dispersion in solvents of AgNP stabilised with PUT presented issues for characterisation; TEM sample preparation only required samples suspended in solvent for a brief time, but for UV / Vis spectroscopy and NMR spectroscopy, having intrinsically low sensitivity, samples must remain suspended or dissolved for the duration of the experiment, hence the selection of different solvents for these techniques.

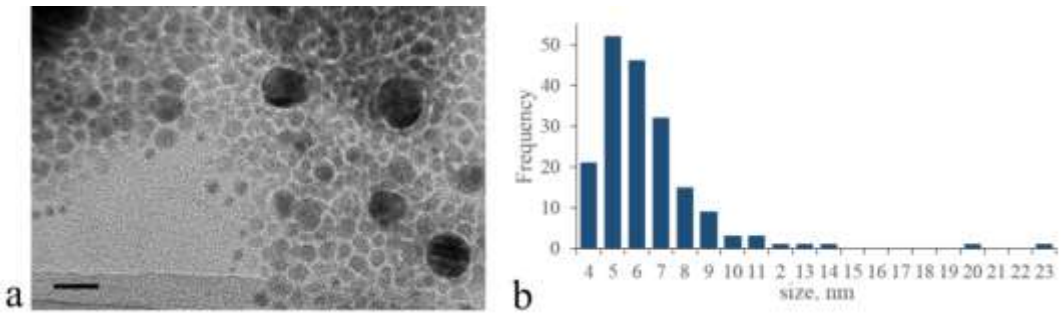

Figure 6.25 TEM image for N5AgNP (0.5 mg / ml cyclohexane, sonicated 5 minutes), showing spherical NP with a somewhat broad size distribution (7.9 ± 2.3 nm, n = 185), and size range 2 – 23 nm.

In contrast, Figure 6.26 presents UV / Vis spectrometry data for N5-AgNP (0.5 mg /ml $CHCl_3$, no sonication) showing a single peak, centred at 441 nm, again indicative of a narrow size distribution, possibly reflecting differences in sample handling.

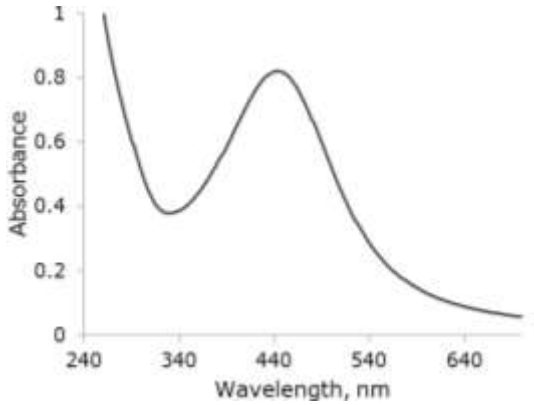

Figure 6.26 UV/Vis spectrum for starting N-AgNP stabilised with PUT (0.5 mg /ml $CHCl_3$), exhibiting a relatively narrow peak centred at 441nm, indicating a narrow NP size distribution.

The presence of PUT in the stabilising layer of N5-AgNP was confirmed by ^1H NMR spectra, presented in Appendix A.

For this experiment, N5-AgNP were heated from RT to 650°C (MEMS heating at ~ 100°C/s), followed by step-wise heating to 850°C, 950°C and 1000°C, with a hold time of 1 minute between steps. Figure 6.27a shows a TEM micrograph of N5-AgNP

(Si_3N_4 MEMS chip, 0.5 mg / ml $CHCl_3$, 1 drop cast) at RT, revealing spheroidal AgNP (8.61 ± 2.91 nm) (Figure 6.27c), with some aggregation observed. In contrast, Figure 6.27b shows the same field of view, recorded at 1000°C, with the HCNS structures matching the positions of the starting N5-AgNP material, whilst being slightly larger (10.03 ± 4.92 nm) (Figure 6.27d).

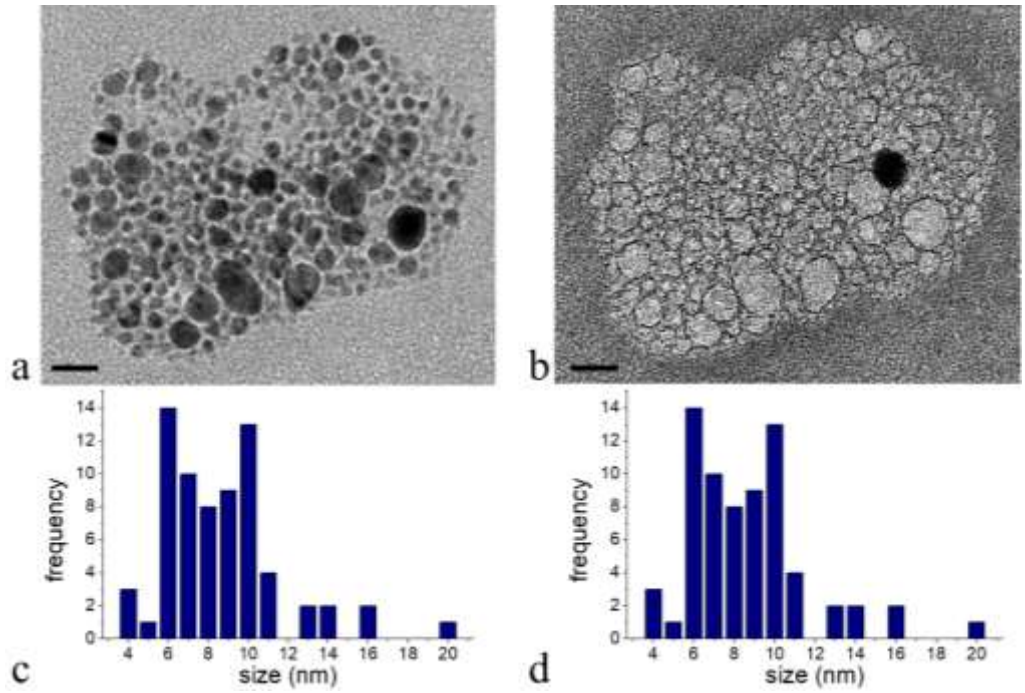

Figure 6.27 TEM micrographs of: (a) N5-AgNP / Si_3N_4 at 23°C before rapid heating to 1000°C; and (b) the resultant HCNS, imaged at 1000°C, contrast enhanced (scale bars 20 nm). Particle size histograms: (c) Before heating, 8.61 ± 2.91 nm (corresponding to N5-AgNP); and (d) after heating, 10.03 ± 4.92 nm (corresponding to HCNS structures formed).

For comparison, Figure 6.28a presents TEM images of N5-AgNP@MWCNT, *ex situ* heated to 850°C (at ~ 20°C/s), recorded at RT (~ 14 days later), again revealing N-AgNP template aggregation in preference to discrete N-AgNP distribution onto MWCNT, whilst noting some associations between MWCNT and N-AgNP. Figure 6.28b shows the formation of relatively amorphous material from these aggregated templates, with individual carbon shells present but difficult to distinguish, again

indicative of the intermediate heating rate used in this instance. Figures 6.28c,d, at higher magnification, show the variability in products obtained and the presence of residual Ag, with few individual CNS formed from N-AgNP at the MWCNT edges. In this case, and notably, complementary EDS data (Figure 6.29) indicated the presence of N (0.4 at%) in the product; note that values for C (97.95 at%) include MWCNT and TEM grid support contributions.

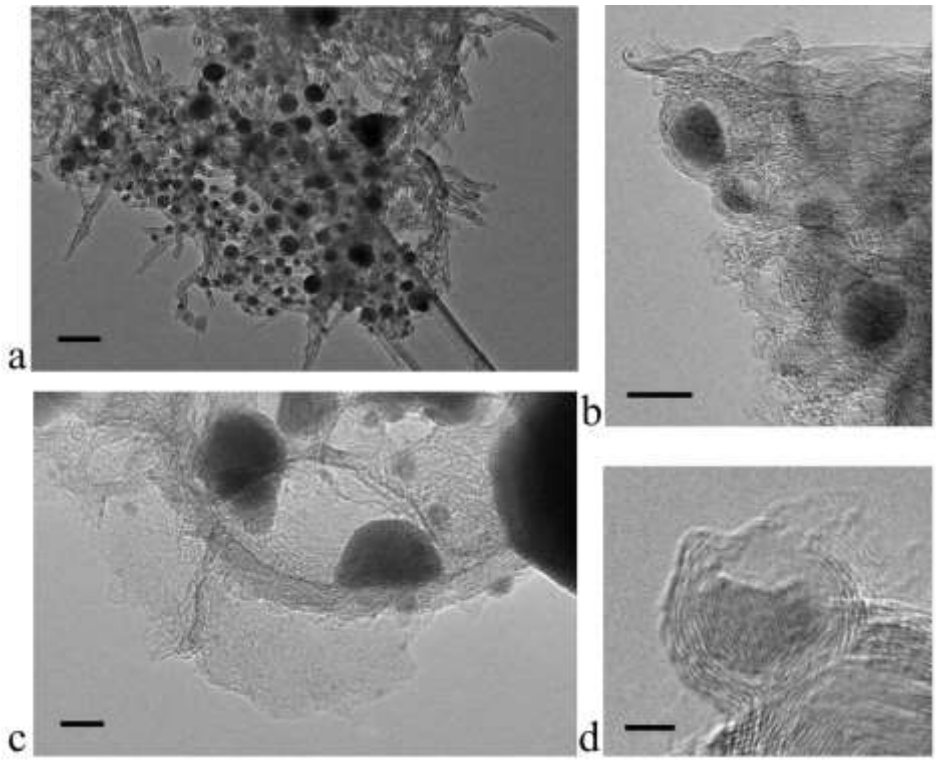

Figure 6.28 TEM images for N5-AgNP deposited (from cyclohexane) onto MWCNT, *ex situ* heated to 850°C, recorded at RT (~ 14 days later), showing the products formed: (a) Aggregated AgNP associated with MWCNT (scale bar 100 nm); (b) connected foam like structure with hollow circular structures and incompletely processed AgNP (scale bar 10 nm). (c) Phase contrast image revealing the variable nature of the product (scale bar 10 nm) and; (d) an individual carbon structure, circular in projection, on the edge of MWCNT (scale bar 5 nm).

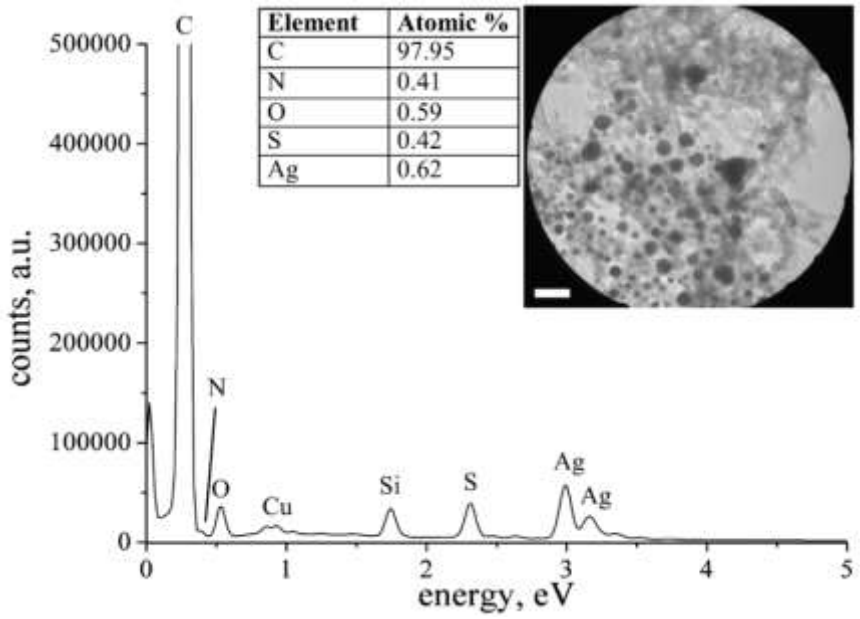

Figure 6.29 EDS data for N5-AgNP@MWCNT heated to 850°C, indicating the presence of N in the product (field of view inset, scale bar 100 nm).

Table 6.6 summarises Raman spectroscopy data for all HCNS formed from heating AgNP starting materials > 650°C (Si_3N_4, at ~ 100°C/s, TP-1); associated spectra and accompanying text for N-HCNS are presented in Appendix B. Careful deconvolution of spectra provide an insight into the degree of graphitisation as analysed by the intensity ratio (as peak area) of the D1 and G bands (I_{D1}:I_G), and amorphous content of products, by the intensity ratio (as peak area) of the D3 and G bands (I_{D3}:I_G).

Table 6.7 summarises the results of all *in situ* and *ex situ* heating of AgNP samples, showing the slightly increased size of HCNS product compared to AgNP starting materials in all cases.

Table 6.6 Presents a summary of Raman spectroscopy results with sample details and sizes, and heteroatom amounts in the stabilising layer.

Sample	**TS-layer / %**	**AgNP size / nm**	**HCNS size / nm**	**G band Raman shift / cm^{-1}**	**D band Raman shift / cm^{-1}**	**I_{D1}:I_G**	**I_{D3}:I_G**	**Rank graphitisation**
TS-AgNP	**none**	6.6 ± 1.4	8.9 ± 1.7	1350	1590	3.08	1.68	6
F-AgNP	**F 47.3**	7.2 ± 2.8	7.6 ± 2.8	1345	1582	2.25	1.20	4
N2-AgNP	**N 1.6**	8.7 ± 4.3	9.3 ± 4.9	1344	1590	1.76	1.08	2
N3-AgNP	**N 3.1**	8.1 ± 3.4	8.5 ± 3.5	1345	1586	2.63	1.50	5
N4-AgNP	**N 4.4**	8.3 ± 3.1	9.2 ± 3.4	1356	1598	1.27	0.41	1
N5-AgNP	**N 5.5**	8.6 ± 2.9	10.0 ± 4.9	1360	1590	1.93	1.37	3

Table 6.7 Comparison of AgNP starting material and HCNS product size distributions, with heteroatom content in the stabilising layer, deposition solvent, support and detection of heteroatoms in HCNS.

Sample	TS-layer / %	Solvent	AgNP size / nm	System / support	Temp / °C	HCNS size / nm	Heteroatom detected
TS-AgNP*	none	chloroform	6.6 ± 1.4	MEMS / Si_3N_4	850	8.9 ± 1.7	-
TS-AgNP*	none	none	**	Furnace / MWCNT	850	**	-
F-AgNP	F 47.3	ethanol	7.2 ± 2.8	MEMS / Si_3N_4	850	7.6 ± 2.8	**Y**
N2-AgNP	N 1.6	toluene (sonicated)	8.7 ± 4.3	MEMS / Si_3N_4	850	9.3 ± 4.9	-
N3-AgNP	N 3.1	toluene (sonicated)	8.1 ± 3.4	MEMS / Si_3N_4	850	8.5 ± 3.5	-
N3-AgNP	N 3.1	none	**	Furnace / MWCNT	850	**	**N**
N4-AgNP	N 4.4	acetone	8.3 ± 3.1	MEMS / Si_3N_4	850	9.2 ± 3.4	-
N5-AgNP	N 5.5	chloroform	8.6 ± 2.9	MEMS / Si_3N_4	650 - 1000	10.0 ± 4.9	-
N5-AgNP	N 5.5	none	**	Furnace MWCNT	850	**	**Y**

**TS-AgNP results from Chapter 4.*

***For AgNP samples deposited onto MWCNT, comparison of sizes prior to and after heating (intermediate heating rate) would not be direct, nor relevant; in addition sampling sizes were very low, and hence this data is excluded.*

6.4 Discussion

Novel AgNP containing F or N have been formed by incorporation of fluorinated or nitrogen-containing thiols into the AgNP stabilising layer during chemical synthesis. The single-step thermal processing of these F-incorporated or N-incorporated AgNP starting materials produced well defined, < 10 nm sized, F-containing or tentatively N-containing HCNS, with product sizes defined by, and slightly larger than, the starting material, thereby illustrating the potential of this paradigm for the synthesis of graphitic HCNS containing heteroatoms. Direct evidence was provided by *in situ* TEM heating experiments on Si_3N_4 supports, with indirect evidence for the graphitisation of heteroatom containing HCNS products provided by complementary Raman spectroscopy.

HCNS products formed from *in situ* heating F-AgNP, retained the defining features of hollow interiors, <10 nm size, and graphitised walls, which were clearly evident (Figures 6.8, 6.11), with products appearing very similar to HCNS formed from alkane thiol stabilised AgNP (Figure 4.12) processed under the same conditions. This was expected, as the substitution of H by F in the thiol layer of AgNP starting materials was not anticipated to disrupt templated HCNS formation [18], or the thermally mediated graphitisation of products. The presence of F in HCNS products, 0.5% at%, was confirmed by EDS (Figure 6.10), from starting materials containing ~ 12 at% F (EDS Figure 6.3 & EDS chemical mapping, Figure 6.4), with F content of HCNS products much lower than the F-AgNP starting materials. Note that the F-AgNP stabilising layer F content tabulated (Tables 6.1 - 6.3, 6.6, 6.7) is much higher, at 47%, than the experimental value (12%) since the former was calculated as % in the stabilising layer *only* and did not take into account the AgNP core, however, the

preferential bonding of alkane thiols [19] to F-thiols may occur, but this was limited by maintaining the total thiol molarity constant during F-doped AgNP synthesis. Accordingly, it is proposed that the removal of F from thiols occurred in conjunction with dehydrogenation during cross-linking of carbon chains and graphitisation of HCNS, both thermally mediated processes, with the retention of some F within HCNS bonded to carbon, either terminating the edges of graphitised domains [20], at structural defects, or within amorphous regions, Figure 6.30, [21]. Indeed, a slightly improved degree of graphitisation was found for products formed from F-AgNP compared to TS-AgNP, heated with the same protocol, (Si_3N_4, 850°C, at ~ 100°C/s), evidenced by analysis of Raman spectroscopy results, with I_{D1}:I_G = 2.25 and 3.08, in the case of F-AgNP and TS-AgNP, respectively, reflecting slightly more graphitic carbon contributions, and I_{D3}:I_G = 1.68 and 1.20, indicating less amorphous carbon contribution in the case of F-doped products.

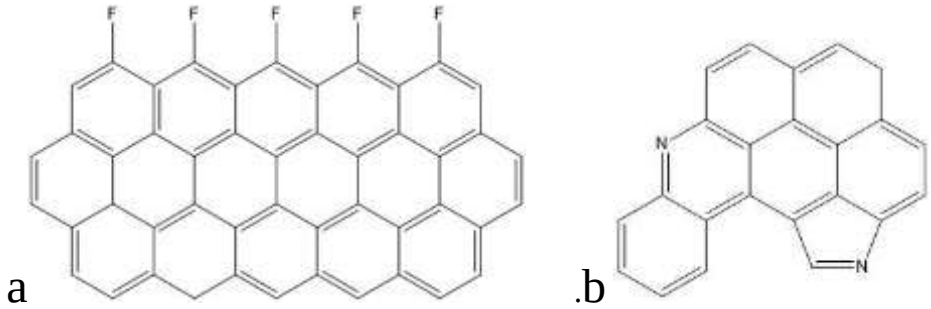

Figure 6.30 F is expected to either (a), terminate graphitic domain edges or bond to C in disordered, amorphous HCNS wall regions, whereas N, if present, may be (b) pyridinic or pyrollic, or may substitute for C within the graphitic lattice.

The general applicability and flexibility of the one-step thermal processing of heteroatom containing AgNP to form HCNS is further evidenced by direct *in situ* observations for the formation of HCNS from thermal processing a range of N-doped

AgNP starting materials (Table 6.5), which show well-defined HCNS products (Figures 6.15, 6.24). The presence of N in HCNS formed *in situ* from N-AgNP could not be confirmed by EDS or EELS, since Si_3N_4 support contributions would mask the low expected levels of N in the small quantities of HCNS on the support. Additionally, XPS was unable to distinguish sample N contributions from the Si_3N_4 chip, however, XPS results at ambient temperature from N3AgNP on GO/Cu (heated to 850°C, Gatan system, ~ 20°C/s) indicated the presence of N at 5.6 at%, but could not confirm the location of nitrogen (Figure 6.20). Further, tentative evidence for incorporation of nitrogen is provided from products formed via *ex situ* thermal processing of N-doped AgNP samples deposited onto MWCNT, (850°C, ~ 10°C/s) with N 0.4 at% detected (EDS, Figure 6.29). The location of N could not be confirmed unambiguously as arising from HCNS products in this region due to the presence of residual AgNP.

As expected, HCNS structures were defined by starting material morphology, size and size distribution, and were slightly larger than the N-AgNP starting materials (Table 6.11), illustrating the good size control of HCNS products obtained with these processing parameters. Slight observed variations in the size differences between starting N-AgNP and HCNS products of 0.4 – 2.3 nm were likely to be attributable to slight differences in attained sample temperatures; there was a pronounced radial temperature gradient across the Si_3N_4 MEMS support [22], as discussed in Chapter 5. Moreover, varying the amount of N-containing thiol in the AgNP stabilising layer from 1.6 – 5.5% N did not compromise HCNS formation (Figures 6.15, 6.19, 6.24 and 6.27) achieved from heating N-AgNP to temperatures > 850°C with a fast heating rate (~ 100°C/s). Accordingly, the presence of the pyrrole functional group within the AgNP stabilising layer was found not to adversely affect HCNS formation. Indeed, complementary Raman spectroscopy results for all HCNS formed from N-containing

AgNP (Table 6.6, Appendix Figures A1.3 – A1.6), suggested that contributions due to graphitic carbon increased slightly, with a concomitant decrease in amorphous contributions, compared to HCNS formed from TS-AgNP, whilst noting the absence of graphitic carbon content in the N-AgNP starting materials, indicated by NMR spectroscopy (Figures 6.18, Appendix A1.1, A1.2). These results are commensurate with HCNS formed from F-AgNP samples.

In the case of *ex situ* N-doped AgNP supported on MWCNT, N-AgNP deposition onto MWCNT walls during sonication proceeded in competition with agglomeration of AgNP (Figures 6.21, 6.28), in contrast to AgNP samples stabilised with only dodecanethiol (Figure 5.4), which disperse discretely along MWCNT walls. Whilst individual HCNS structures on MWCNT edges were observed following thermal processing (850°C, ~ 10°C/s) of N-AgNP@MWCNT (Figure 6.21b), the presence of a variable product, with a foam-type appearance, less well-defined hollow carbon structures and associated residual AgNP (Figures 6.21a, 6.28) provided evidence for the effect of slower rates of heating. The increased AgNP sizes (Figures 6.21a, 6.28a,b,c) after heating, were indicative of ripening processes, which have been shown to compete with HCNS formation at slower heating rates.

Regarding the heteroatom containing AgNP starting materials, these showed poly-dispersed size distributions, compared to AgNP stabilised with alkane thiols (Figure 4.3); both F-AgNP (Figure 6.8) and N-AgNP (Figures 6.13, 6.21, 6.25) displayed a tendency to agglomerate. Combined with changes to dispersion of F-AgNP and N-AgNP, this presented sample deposition and characterisation challenges, table 6.7 summarises the TEM deposition conditions for all N- and F-containing AgNP starting materials.

Table 6.7 Summary of heteroatom containing AgNP samples, and resulting size distributions, along with their respective deposition conditions.

Sample name	Stabilising layer / %	AgNP size / nm	Deposition			
			solvent	sonication	support	drops
F-AgNP	F 47.3	4.0 ± 2.8	hexane*[a]	N	GO/Cu	1
F-AgNP	F 47.3	7.2 ± 2.8	ethanol	N	Si_3N_4	5
F-AgNP	F 47.3	clusters	cyclohexane	5 min	C/Cu	5
N2-AgNP	N 1.6	5.0 ±1.8*[b]	cyclohexane	N	GO/Cu	5
N2-AgNP	N 1.6	8.7 ± 4.3	toluene	Y	Si_3N_4	5
N2-AgNP	N 1.6	9.3 ± 4.7	chloroform	N	GO/Cu	5
N3-AgNP	N 3.1	4.0 ±1.5*[c]	cyclohexane	N	C/Cu	5
N3-AgNP	N 3.1	8.1 ± 3.4	toluene	Y	Si_3N_4	1
N4-AgNP	N 4.4	8.3 ± 3.1	acetone	N	Si_3N_4	1
N5-AgNP	N 5.5	7.9 ± 2.3	cyclohexane	Y	GO/Cu	5
N5-AgNP	N 5.5	8.6 ± 4.9	chloroform	N	Si_3N_4	1
TS-AgNP	none	6.6 ± 1.4	chloroform	N	Si_3N_4	5

** [a] F-AgNP did not dissolve, but were suspended by fluid agitation followed with immediate drop casting.*
** [b] measured from an image taken from a location free from aggregation.*
** [c] sample filtered prior to drop casting.*

Solvent choice initially appeared to influence observed size distributions, however, sample deposition was not constant, but depended on the dispersion characteristics of individual doped AgNP, *e.g.* for suspension in non-polar solvents sonication was required, and in one experiment the AgNP solution was filtered prior to drop casting and one size distribution was measured from a selected area free from agglomeration. For remaining examples, average AgNP size of F- or N- AgNP was 8.4 nm, compared to 6.6 nm for TS-AgNP, which is an increase of > 2 nm, however, the size distribution, evaluated as σ, became much larger (to an average of 3.4 from 1.4 nm for N-AgNP

and TS-AgNP, respectively), reflecting the observed aggregation and the presence of larger heteroatom containing AgNP. Notably, no appreciable size differences were revealed with increasing AgNP N-content (Figures 6.12, 6.19, 6.21 and 6.28).

Increased agglomeration of N-AgNP is considered to be attributable to the lone electron pairs of pyrrole functional groups of PUT in the AgNP stabilising layer, which create dipoles, modifying the electrostatic and steric interactions between individual AgNP, resulting in disruption to the repulsive forces that prevent close contact of individual AgNP, leading to aggregation [23]. The formation of dipoles at N-AgNP surfaces would also be expected to change dispersion characteristics, *e.g.* the observed suspension or dispersion of N-AgNP in polar $CHCl_3$, but not in non-polar solvents such as hexane. Similarly, for AgNP containing F in the stabilising layer, the electronegativity of F is expected to produce dipoles and therefore influence dispersion and tendency for AgNP agglomeration.

Dispersion of mixed thiol metal nanoparticles in solvents may also be dependent on packing of the thiol layer at AgNP surfaces [24, 25], whilst noting that dispersion of F-AgNP in non-organic solvents was initially ascribed to insufficient purification and washing [26]. Indeed, although determination of the relative location and packing of alkane and fluorinated or nitrogen-containing thiols at the AgNP surface was outside the scope of this research, the inclusion of an immiscible binary mixture of alkane thiols (DDM and HFT, or DDM and PUT) may be expected to produce phase segregation at the Ag surface, leading to random or highly ordered thiol arrangements, depending on the choice of thiols and their relative stoichiometry Figure 6.31, [adapted from 19].

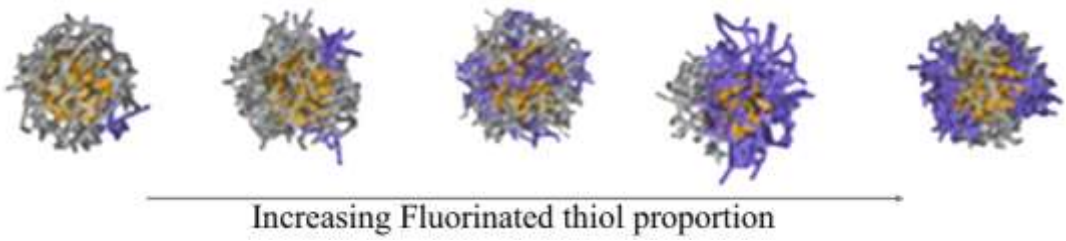

Figure 6.31 Predicted relative packing of (a) thiol (grey) and fluorinate thiol (purple) poly(oxoethylene) chains on AuNP, adapted from [19].

Sample handling in preparation for thermal processing, was influenced by these changes in dispersion, in the case of F-AgNP and N-AgNP, additionally for N-AgNP containing different amounts of N. A range of solvents were required for most F- and N-AgNP, reflecting the dispersion differences, but also requiring the use of sonication in cases where suspension was very limited, acknowledging that agglomeration of AgNP was likely to be induced by this processing step. An alternative method to introduce sufficient sample onto support materials was to drop cast several drops of less well-suspended AgNP, but this did not produce improved size distributions, *e.g.* 9.3 ± 4.7 nm from 5 drops of N2-AgNP, and 8.6 ± 4.9 nm for one drop of N5-AgNP, however, filtration significantly improved size distribution, (4.0 ±1.5 nm for N3-AgNP / cyclohexane). The combination of many interacting factors and competing diffusion effects during TEM grid deposition are graphically represented, Figure 6.32, with the dynamic nature of drying processes suggesting treatment of this system as a complex network [27, 28].

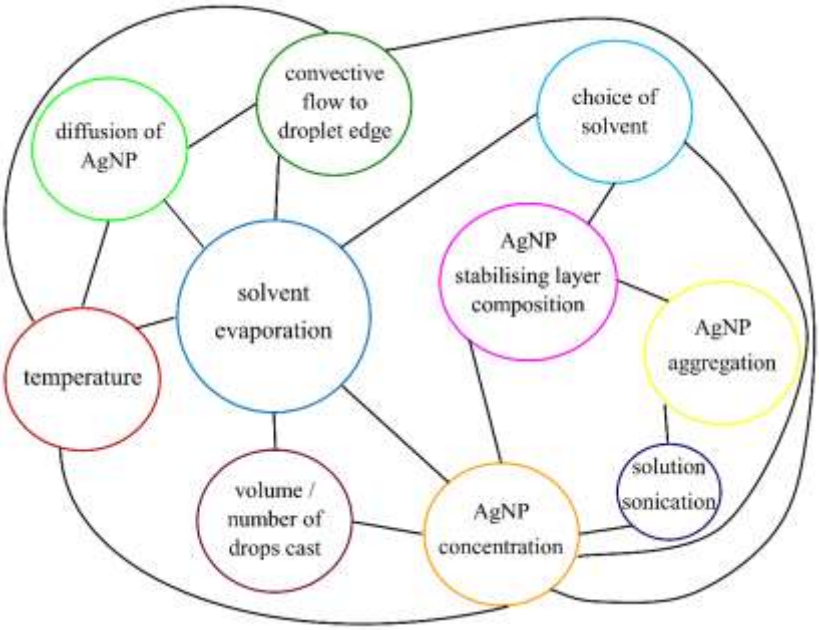

Figure 6.32 Factors influencing AgNP deposition onto TEM grids, lines represent connections between factors.

In addition to the deposition variables, thermal processing F- or N- containing AgNP introduces further processing options for HCNS formation, key variables are represented in Figure 6.33.

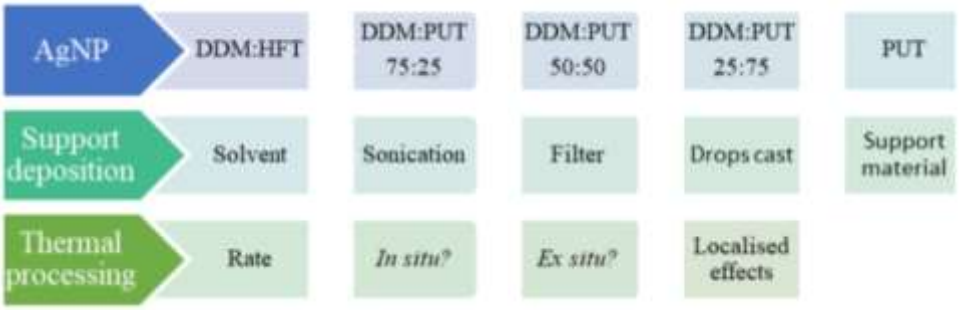

Figure 6.33 Key processing variables influencing HCNS formation from thermal processing of AgNP containing heteroatoms.

Further, since product and starting material morphology are correlated, the self-assembly or agglomeration of heteroatom containing AgNP could provide a facile

route to foam-type or ordered formations of hollow structures. *E.g*. the formation of HCNS foam-type products / larger HCNS, (Figure 6.9), reflect the agglomeration and clustering of starting material F-AgNP templates prior to heating, further, the absence of Ag from within foam-like HCNS (Figure 6.10), suggests heat transfer is efficient throughout these clusters. Indeed, fluorinated thiols have been shown to produce ordered 2D self-assemblies [29] and harnessing this could allow deposition of isolated NP, promote 2D superlattice formation [26], or mediate 3D assembly [18]; following thermal processing these should produce a F-doped HCNS product commensurate with starting material morphology.

6.5 Conclusions

The formation of well-defined heteroatom doped < 10 nm sized graphitic HCNS may be achieved from the one-step thermal processing of AgNP stabilised by ligands containing F or N, with the resulting products reflecting starting material morphology. However, the addition of heteroatoms into AgNP stabilising layers presents challenges for sample handling due to aggregation and changes in dispersion characteristics. The presence of F in HCNS has been demonstrated, but evidence for inclusion of N is more tentative. Good size control of HCNS products was also demonstrated for a range of starting materials, with a fast rate of heating. Mixed thiol stabilised AgNP starting materials therefore present a facile and versatile route for incorporation of heteroatoms into HCNS structures via one-step thermal processing.

References

1 Lee, J. M., Kwon, B-H., Park, H. I., Kim, H., Kim, M. G., Park, J. S., Kim, E. S., Yoo, S., Jeon, D. Y., Kim, S. O., *Exciton Dissociation and Charge-Transport Enhancement in Organic Solar Cells with Quantum-Dot/N-doped CNT Hybrid Nanomaterials*, Adv. Mater. (2013) 25 (14) pp2011-2017.

2 Cruz-Silva, E., Cullen, D. A., Gu, L., Romo-Herrera, J. M., Muñoz-Sandoval, E., López-Urias, F., Terrones, M. et al. *Heterodoped nanotubes: Theory, synthesis, and characterization of phosphorus-nitrogen doped multiwalled carbon nanotubes,* ACS Nano (2008) 2 (3) pp41-8.

3 Pan, H., Feng, Y., Lin, J., *Ab initio study of F-and Cl-functionalized single wall carbon nanotubes,* J Physic: Condensed Matter (2006) 18 (22) pp5175-5184.

4 Bhowmick, .S, Banerji, A., Alpas, A. T., *Friction and adhesion of fluorine containing hydrophobic hydrogenated diamond-like carbon (F-H-DLC) coating against magnesium alloy AZ91,* Surf. Coat. Tech. (2015) 267 (C) pp21-31.

5 Wang, F., Wang, L., Xue, Q., *Fluorine and sulfur co-doped amorphous carbon films to achieve ultra-low friction under high vacuum,* Carbon 96 (2016) pp411-420.

6 Makela, A., Foster, P. J., Imaging macrophage distribution and density in mammary tumors and lung metastases using fluorine-19 MRI cell tracking. Magn. Reson. Med. (2018) 80 (3) pp1138-1147.

7 Kora, A. J., Beedu, S. R., Jayaraman, A., *Size-controlled green synthesis of silver nanoparticles mediated by gum ghatti (Anogeissus latifolia) and its biological activity*, Org. Med. Chem. Lett. (2012) 2 pp17.

8 Uvarov, V., Popov, I., *An estimation of the correctness of XRD results obtained from the analysis of materials with bimodal crystallite size distribution,* Cryst. Eng. Comm. (2015) 17 (43) pp8300-8306.

9 Kang, S. Y., Kim, K., *Comparative Study of Dodecanethiol-Derivatized Silver Nanoparticles Prepared in One-Phase and Two-Phase Systems,* Langmuir (1998) 14 pp226-230.

10 Naud, C., Calas, P., Blancou, H., Commeyras, A., *Synthesis of terminally perfluorinated long-chain alkanethiols, sulfides and disulfides from the corresponding halides,* J. Fluor. Chem. (2000) 104 (2) pp173-183.

11 Yuan, Y., Ge, S., Sun, H., Dong, X., Zhao H., An, L., Zhang, J., Wang, J., Hu, B., Liang, G., *Intracellular Self-Assembly and Disassembly of 19F Nanoparticles Confer Respective "Off" and "On" 19F NMR/MRI Signals for Legumain Activity Detection in Zebrafish,* ACS Nano (2015) 9 (5) pp5117-5124.

12 Song, X., Zhai, J., Wang,Y., Jiang, L., *Fabrication of Superhydrophobic Surfaces by Self-Assembly and Their Water-Adhesion Properties* J. Phys. Chem. B (2005) 109 (9) pp4048-4052.

13 Gonzalez-Carter, D. A., Leo, B. F., Ruenraroengsak, P., Chen, S., Goode, A. E., Theodorou, I. G., K Chung, K. F., Carzaniga, R., Shaffer, M. S. P., Dexter, D. T., Ryan, M. P., Porter, A. E., *Silver nanoparticles reduce brain inflammation and related neurotoxicity through induction of H_2S-synthesizing enzymes*, Nature, Sci. Rep. (2017) 7 pp42871.

14Sadezky, A., Muckenhuber, H., Grothe, H., Niessner, R., Pöschl, U., *Raman microspectroscopy of soot and related carbonaceous materials: Spectral analysis and structural information*, Carbon (2005) 43(8) pp1731-1742.

15 Ferrari, J. Robertson, J., *Interpretation of Raman spectra of disordered and amorphous carbon*, Phys. Rev. B (2000) 61(20) pp14095-14107.

16 Cançado, L.G., Jorio, A., Ferreira, E.H.M., Stavale, F., Achete, C.A., Capaz, R.B., et al., *Quantifying defects in graphene via Raman spectroscopy at different excitation energies,* Nano. Letters. (2011) 11(8) pp3190-6.

17 Williams, D., Fleming, I., Spectroscopic methods in Organic Chemistry, 1989 McGraw Hill Company, New York

18 Shimizu, T. K., Jung, J., Otani, T., Han, Y. K., Kawai, M., Kim, Y., *Two-dimensional superstructure formation of fluorinated fullerenes on Au(1 1 1): A scanning tunnelling microscopy*, ACS Nano (2012) 6 (3) pp2679-2685.

19 Posocco, P., Gentilini, C., Bidoggia, S., Pace, A., Franchio, P., Lucarini, M., Fermeglia, M., Pricl, S., Pasguato, L., *Self-Organization of Mixtures of Fluorocarbon and Hydrocarbon*

Amphiphilic Thiolates on the Surface of Gold Nanoparticles, ACS Nano(2012) 6 8 pp7243-7253

20 Piriz, S., Fernndez-Werner, L., Pardo, H., Jasen, P., Faccio, R., Mombr, L., *Mechanical properties and electronic structure of edge-doped graphene nanoribbons with F, O, and Cl atoms,* Physical Chemistry Chemical Physics, (2017) 19 (32) pp21474-21480.

21 Nair, R., Ren, W., Jalil, R., Raiz, I., Kravets, V. G., Britnell, L., Blake, P., Schedin, F., Mayorov, A. S., Yuan, S., Katsnelson, M. I., Cheng, H. M., et al, *Fluorographene: A Two-Dimensional Counterpart of Teflon*, Small (2010) 6 (24) pp2877-2884.

22 Niekiel, F., Kraschewski, S. M., Muller, J, Butz, B., Spieker, E., *Local temperature measurement in TEM by parallel beam electron diffraction*, Ultramicroscopy (2017) 176 pp161-169

23 Xu, B., Gonella, G., DeLacy, B. G., Dai, H. L., *Adsorption of Anionic Thiols on Silver Nanoparticles,* J. Phys. Chem. C (2015) 119 (10) pp 5454–5461.

24 Centrone, A., Penzo, E., Sharma, M., Myerson, J. W., Jackson, A. M., Marzari, N., Stellacci, F., The role of nanostructure in the wetting behavior of mixed-monolayer-protected metal nanoparticles PNAS (2008) 105 (29) pp9886-9891.

25 Şologan, M., Gentilini, C., Bidoggia, S., Boccalon, M., Pace, A., Pengo, P., Pasquat,L., *Gold nanoparticles protected by mixed hydrogenated/fluorinated monolayers: controlling and exploring the surface features,* J Nanopart. Res. (2018) 20 pp152.

26 Yonezawa, T., Onoue, S., Kimizuka, N., *Formation of Uniform Fluorinated Gold Nanoparticles and Their Highly Ordered Hexagonally Packed Monolayer,* Langmuir (2001) 17 (8) pp2291-2293

27 Strogatz, S. H., *Exploring complex networks*, Nature, (2001) 410 (6825) pp268-276.

28 Boccaletti, S., Criado, R., Romance, M., Torres, J. J., *Introduction to Focus Issue: Complex Dynamics in Networks, Multilayered Structures and Systems*, Chaos (2016) 26 (6) pp065101.

29 DeVries, G. A., Brunnbauer, M., Hu, Y., Jackson, A. M., Long, B., Neltner, B. T., Uzun, O., Wunsch, B. H., Stellacci. F., *Divalent metal nanoparticles,* Science (2007) 315 pp358–361.

7.0 Discussion and critical appraisal

7.1 Introduction

Hollow carbon nanomaterials have multifarious potential applications reflecting their physical nature and functional properties: electrode materials for energy storage and conversion [1], detection of metal ions or small molecules [2], as catalyst materials [3], for drug delivery or imaging [4], or as test-tubes to enable formation of unusual reaction products due to molecular confinement effects [5]. However, limited solubility and tendency to bundle limit the applications of carbon nanotubes (CNT) and nanofibres [6], whilst very limited volumes are afforded by fullerene molecules [7].

Hollow carbon nanoshells (HCNS) may offer solutions to these issues, but are typically ~ 200 nm sized, and synthesised via multi-step processes involving environmentally unfriendly chemical template removal steps [8]. The need for smaller HCNS, e.g. for electrodes with increased cycling rates and ion storage, or as biocompatible storage and release platforms, is recognised [9, 10, 11], but the smallest HCNS formed to date are ~ 20 nm sized, however, these have a large size distribution and size control is limited [12]. Improvements to functional properties, e.g. conductance, of HCNS may be achieved through inclusion of heteroatoms, most commonly N [13].

The formation of much smaller (< 10 nm sized) HCNS, formed from a single-step thermal processing step from thiol stabilised silver nanoparticle (AgNP) starting materials has been demonstrated. The advantages of HCNS formation from stabilised AgNP starting materials include their ability to self-template, the flexibility offered by selection of suitable stabilising agents, and the potential to tailor HCNS sizes in the < 30 nm range, additionally, well-defined, stable products with very thin walls comprising 3 - 4 graphitised layers are produced. Indeed, the rapid formation of graphitised HCNS, and subsequent removal of Ag templates, requires a single heating step for both formation and template removal processes, and provides for good size control of products. Rate of heating was found to be crucial for synthesis of well graphitised < 10 nm sized HCNS products, with slower heating rates producing a more variable, less well-graphitised product, reflecting competition between transformation of the AgNP thiol layer and kinetics of Ostwald ripening of AgNP leading to template degradation. Addition of heteroatoms to AgNP templates has been demonstrated, but presented significant challenges due to agglomeration of AgNP and changes to dispersion in solvents; thermal processing a range of AgNP starting materials containing F or N enabled production of HCNS, but evidence for the inclusion of heteroatoms in products was tentative.

The flexibility of the approach to HCNS formation outlined in this chapter is illustrated in figure 7.1.

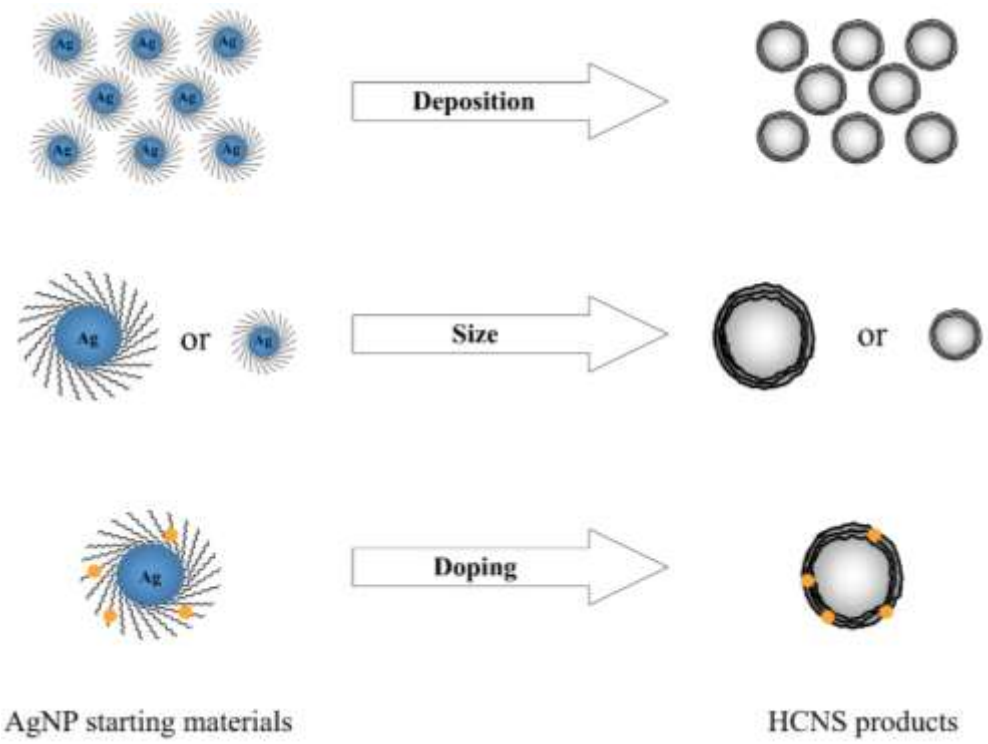

Figure 7.1 Schematic illustrating the flexibility of HCNS formation from one-step thermal processing of AgNP, allowing for a bespoke range of different HCNS, with changes to the relative arrangement of products, HCNS size, and inclusion of heteroatoms (represented as orange circles).

7.2 Processing parameters – heating rate, temperature.

While the formation of HCNS from TS-AgNP was observed during *in situ* thermal processing with both furnace-type (Gatan) and MEMS heating systems, both afford limited temperature measurement accuracy [14], confounded by heating effects due to electron beam – sample interactions producing higher localised temperatures [15].

For the case of *ex situ* heating of TS-AgNP samples deposited onto MWCNT (sealed i*n vacuo* inside quartz ampoules), the furnace was pre-heated to 850°C, however, the temperature at the sample would depend on sample position, *i.e.* contact with the ampoule walls, and vacuum conditions, extended heating times were intended to

ensure the set temperature was attained. Further, heat transfer to samples, for both *in situ* and *ex situ* experiments, may depend on contact between individual AgNP and the support material, with experimentally observed localised variations responsible for significant differences in products obtained, *e.g.* templated and HCNS observed on both MWCNT and Si_3N_4, presenting issues for scale-up purposes.

Lateral movement due to drift and displacement of the TEM support material during heating prevented real-time observations of the transformation of the thiol layers with the Gatan heating system, and locating the same region of interest was not possible at high temperatures; but this system did offer a choice of support materials [16]. In the case of MEMS systems, less lateral movement was apparent, however, due to thermal expansion, the support material bowed significantly [17], again preventing image capture of the transformation process in real-time. Images recorded in the same field of view showing AgNP and HCNS products provided useful data, but improved MEMS heating supports may offer a solution [18]. The absolute temperature at which thiols were transformed to graphitised structures was not therefore determined.

Collecting images of HCNS products on Si_3N_4 supports was very challenging due to the combination of small HCNS size; limited material present, HCNS walls are 3 -4 graphitic layers thick (3 – 4 carbon atoms) and; relatively low sample contrast compared to the support, additionally support morphology presented problems for obtaining detailed structural images of HCNS.

7.3 HCNS characterisation

The incorporation of heteroatoms into AgNP starting materials and F in HCNS has been demonstrated, however, evidence for the inclusion of N within HCNS is tentative. This is an acknowledged weakness of the experimental set-up, reflecting technical difficulties in obtaining EDS data from low sample amounts, low expected quantities of N within the structures and support material contributions. Indeed, the EELS peak due to carbon around 290 eV extends beyond the expected K edge of N at round 400 eV, with simulations indicating that N quantities ~ 3% were below detection levels of the EELS system available. Detection of 3% N would be possible with a direct detection camera [19], noting that EELS in combination with aberration-corrected scanning transmission electron microscopy has identified individual N atoms to be identified within graphene [20].

In the case of the bulk technique of XPS, MEMS support windows were lower than the surrounding support areas, creating problems for data acquisition of HCNS from within these areas, whilst mass spectrometry of HCNS products (on GO/Cu) were not appreciably different to results of blank TEM grids. A preferred option would be to form HCNS free from support materials, allowing for XPS, and also possibly PXRD, NMR and Raman spectroscopy directly on HCNS samples,

7.4 Carbon sources and graphitisation

HCNS formed from TS-AgNP starting materials were experimentally found to be 3-4 graphitic layers thick, with the thiol stabilising layer of AgNP providing the source

of carbon. Calculating the amount of carbon present in TS-AgNP starting materials and of HCNS products, per unit area, was informative.

Alkane thiol molecules are known to self-assemble as an ordered monolayer, chemisorbed on the FCC AgNP {1 1 1} surface [21], illustrated in Figure 7.2. Since the surface density of Ag {1 1 1} is 13.83 Ag nm^{-2} [22], the number of carbon atoms available per unit area will be given by Equation 7.1. Assumptions are that all AgNP surfaces are Ag {1 1 1}, thiols attain complete monolayer coverage and all thiol angles are at a tilt of 0°.

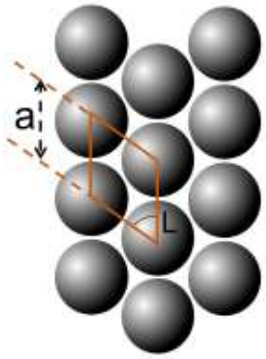

Figure 7.2 Unit cell of Ag (1 1 1), top view of S atoms bonded to surface, 'a' is the unit cell length and 'L' the interior angle.

$$\textit{Carbon atoms } (nm^{-2}) = \textit{Surface density of Ag x Number of C atoms in DDM}$$

$$= \quad 13.83 \times 12$$

$$= \quad 166 \ nm^{-2}$$

Equation 7.1.

For HCNS products the number of carbon atoms per graphitic layer may be derived from knowledge of the graphitic structure, illustrated in Figure 7.3. The unit cell area

may be calculated from Equation 7.2, assuming the HCNS structures comprise defect – free continuous graphene layers.

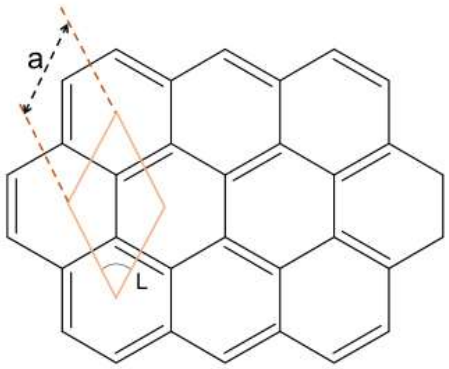

Figure 7.3 Graphene unit cell, with a cell length of 'a' and an interior angle, 'L'.

$$\text{Unit cell area} = a^2 \sin \angle_L$$

$$= (0.246)^2 \times \sin(60)$$

$$= 0.05239 \text{ nm}^2$$

Equation 7.2 The unit cell area of a graphitic layer, 'a' is the unit cell length and the sine of $\angle_L$, the interior angle (60°).

As each graphene unit cell contains two carbon atoms and is one carbon atom thick it follows that:

$$\text{nm}^2 : \text{carbon atoms}$$

$$0.0524 : 2$$

$$1 : x$$

$$1 : 38.2$$

Per HCNS graphitic layer there are 38 carbon atoms / nm^2 and a maximum of 166 carbon atoms / nm^2 available in the starting material. Therefore there are a maximum of 166 / 38 = 4.4 HCNS graphitic layers that could be formed from the AgNP

stabilising thiol carbon source. As the assumption that complete monolayer thiol coverage of Ag surfaces is likely to over-estimate the amount of C starting material, and the HCNS products have a pronounced curvature and must therefore contain defects, the calculated values are both probably inflated. However experimental evidence suggests the presence of 3 – 4 graphitic layers in HCNS formed for DDM stabilised AgNP starting materials, which is in agreement with this calculated value.

7.5 Functional HCNS data

Lack of functional data is a limitation of the experimental work, and therefore any possible applications are merely speculative, based on similar materials or first-principle assumptions. Photoluminescence (PL) spectra obtained for HCNS formed from N-AgNP showing emission around 1.5 – 1.7 eV (λ = 532 nm), however, AgNP are known to have PL properties in this energy range [23], and the presence of residual AgNP could not be excluded, therefore emission from HCNS cannot be confirmed.

Considering the physicality of these < 10 nm sized structures, interior cavities may offer possibility for containment, for gas storage, either H_2 for fuel, Xe which has potential data storage applications, drugs, or other <10nm species for imaging or drug delivery, but initial attempts at filling HCNS were ambiguous and further work is required: since Ag is able to permeate the shell walls and leave the HCNS interiors during template removal, it is not unreasonable to assume that a similar reverse process could also occur. In addition to interior cavities, exterior surfaces present possibilities for functionalisation or attachment with Figure 7.2 illustrating options for attachment or containment.

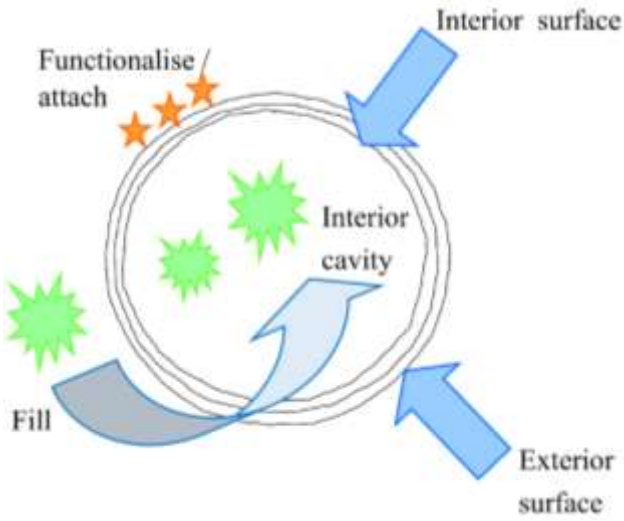

Figure 7.2 Physical features of HCNS could provide for a number of applications.

The very high surface area of HCNS could be exploited for catalysis, but the absorbance and emission characteristics, and electrochemical properties of this material are unknown. The addition of N to HCNS is predicted to alter band gaps of these HCNS, modifying any electrochemical and photoluminescence (PL) properties, and addition of N should shift PL to longer wavelengths (NIR), with use of NIR negating the effect of cellular auto-fluorescence. However, an important consideration is the biocompatibility and toxicology of these HCNS, and safety and environmental issues remain to be determined.

7.6 Starting material synthesis

Synthesis of AgNP stabilised with a mixed thiol layer was performed via a bottom-up approach, Figure 7.3 illustrates the simplicity and flexibility of this approach for formation incorporation of a variety of stabilising ligands.

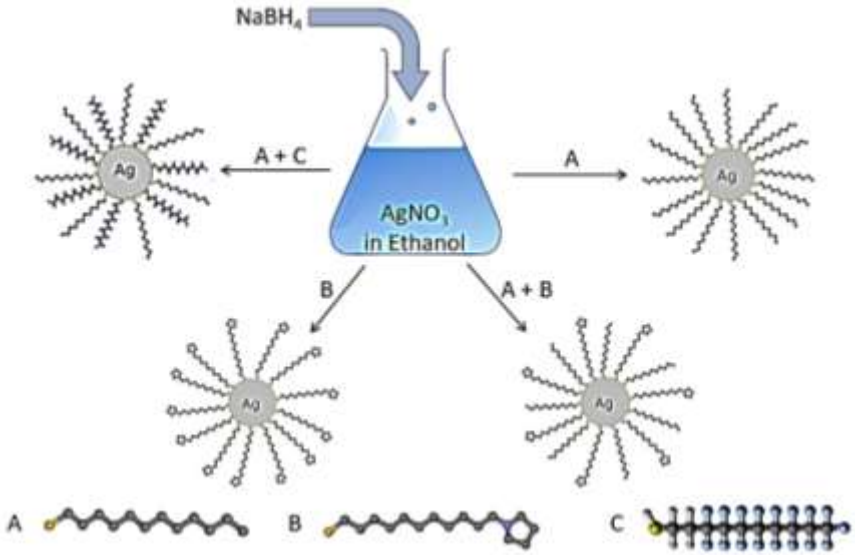

Figure 7.3. AgNP synthesis from the reduction of Ag^+ ions in solution by $NaBH_4$, followed by addition of stabilising ligands allows for the formation of a variety of stabilising layer compositions.

Choice of a modified one-phase Brust-Shiffrin method for AgNP production [24], produces stable AgNP with good size distributions, important for the production of well-defined HCNS, but the reducing agent ($NaBH_4$) is hazardous and not environmentally friendly, therefore greener synthetic approaches may have been more appropriate [25].

Addition of fluorinated and nitrogen containing thiols to AgNP surfaces changed the dispersion of AgNP in solvents and promoted aggregation, presenting significant challenges for sample preparation. This issue could have been addressed by size separation, with centrifugation for example. Alternatively, the addition of surfactant molecules and filtration at the grid deposition stage of sample preparation has been shown to promote superlattice formation for N-AgNP, with narrower size distributions. Since HCNS size and morphologies closely resemble those of the AgNP starting material, the self-assembly of heteroatom containing AgNP could provide a

facile route to HCNS superlattice formation [26], or foam-type formations [27]. Fluorinated thiols, in particular have been shown to have limited solubility, but notably the mixed DDM:HFT thiol stabilising layer appears to confer stable distributions of AgNP suspended in ethanol.

The arrangement of two immiscible thiols at the Ag surface may not be random, as phase separation enables spontaneous organisation of thiols [28], which may produce 'polar singularities' on individual NP, facilitating directional assembly and formation of self-assembled NP chains, at levels as low as (4%) added fluorinated ligand for example, [29], however, this has not been addressed..

Addition of heteroatoms to AgNP starting materials during chemical synthesis does not represent the only method for heteroatom containing HCNS formation, other methods include:

- AgNP ligand exchange, which would require an additional synthetic step and has limited applicability [30, 31].
- Addition of heteroatom containing molecules to AgNP at the support deposition stage, but this was considered unlikely to be easily controllable and would not allow 'dopant' quantities to be pre-defined.
- Post-synthesis functionalisation of AgNP stabilising layers or HCNS [32
-], which necessitates at least one additional synthetic step.

The formation of well-defined HCNS, with good size control has been illustrated, on a variety of supports, providing evidence for the thermally mediated nature of the

transformation of saturated thiols to graphitised products, irrespective of support material. Further, the influence of heating rate was found to profoundly influence products formed in the case of both *in situ* and *ex situ* conditions.

References

1 Fan, Y., Liu, P-F., Huang, Z-Y., Jiang, T-W., Yao, K-L., Han, R., *Porous hollow carbon spheres for electrode material of supercapacitors and support material of dendritic Pt electrocatalyst,* J Power Sources 280 (2015) pp30-38.

2 Liu, T., Qu, L., Qian, K., Liu, J., Zhang, Q., Liu, L., Liu, S., *Raspberry-like hollow carbon nanospheres with enhanced matrix-free peptide detection profile*s, Chem. Comm. 52 (8) (2016) pp1709-1712.

3 Zheng, D., Pang, C., Wang, X., *The function-led design of Z-scheme photocatalytic systems based on hollow carbon nitride semiconductors*, Chem. Comm. 51 (98) (2015) pp17467-17470.

4 Jong, W. H. De., Borm, P. J. A., *Drug delivery and nanoparticles: Applications and hazards*, Int. J Nanomedicine 3 (2) (2008) pp133–149.

5 A. Chuvilin, A., Bichoutskaia, E., Gimenez-Lopez, M. C., Chamberlain, , Rance, G. A., Kuganathan, N., Biskupek, J., Kaiser, U., Khlobystov, A. N., S*elf-assembly of a sulphur-terminated graphene nanoribbon within a single-walled carbon nanotube,* Nature Materials 10 (2011) pp687–692.

6 Okutan, E., Aydın, G. O., Hacıvelioğlu, F., Kılıç, A., Beyaz, S. K., Yeşilot, S.. *Synthesis and characterization of soluble multi-walled carbon nanotube/poly(organophosphazene) composites,* Polymer 52 (5) (2011) pp1241-1248.

7 Jaroš, A., Badri, Z., Bora, P., Bonab, E., Marek, R., Straka, M., Foroutan-Nejad, C., *How Does a Container Affect Acidity of its Content: Charge-Depletion Bonding Inside Fullerenes,* Chem. Eur. J. 24 (17) (2018) pp4245-4249.

8 Chen, A., Wang, Y., Yu, Y., Sun, H., Li, Y., Xia, K., Li, S., *Nitrogen-doped hollow carbon spheres for supercapacitors*, J Mater. Sci. 52 (6) (2017) pp3153-3161.

9 Blinc, R., Arcon, D., Umek, P., Apih, T., Milia F., Rode, A. V., *Carbon nanofoam as a potential hydrogen storage material*, Phys.Status Solidi 244 (11) (2007) pp4308-4310.

10 Chen, A. B., Li, Y. Q., Yu, Y. F., Ren, S. F., Wang, Y. Y., Xia K. C., Li, S. H., *Nitrogen-doped hollow carbon spheres for supercapacitors application*, J. Alloys Compd. 688 (2016) pp878-884.

11 Jong, W. H. De., Borm, P. J. A., *Drug delivery and nanoparticles: Applications and hazards*, Int. J Nanomedicine 3 (2) (2008) pp133–149

12 Huang, Q., Wang, S., Zhang, Y., Yu, B., Hou, L., Su, G., Ma, S., Zou, L.u., Huang, H., *Hollow Carbon Nanospheres with Extremely Small Size as Anode Material in Lithium-Ion Batteries with Outstanding Cycling Stability*, J Phys. Chem. C 120 (6) (2016) pp3139-3144.

13 Zhong, M.J., Kim, E.K., Natesakhawat, S., McGann, J.P., Whitacre, J.F., Matyjaszewski, K., Kowalewski, T., *Nitrogen-rich porous nanocarbon from block copolymer precursors for CO_2 capture and electrocatalysis of oxygen reduction*, Abstr. Pap. Am. Chem. (2012) S 244.

14 Niekiel, F., Kraschewski, S. M., Muller, J, Butz, B., Spieker, E., *Local temperature measurement in TEM by parallel beam electron diffraction*, Ultramicroscopy (2017) 176 pp161-169

15 Asoro, M. A., Kovar, D., Ferreira, P. J., *In situ transmission electron microscopy observations of sublimation in silver nanoparticles*, ACS Nano (2013) 24 7(9) pp7844-52.

16 Kameya, Y., Hayashi, T., Motosuke, M., *Stability of platinum nanoparticles supported on surface-treated carbon black*, Appl. Catal. B 189 (2016) pp219-225.

17 Allard, L.F., Bigelow, W.C., Jose-Yacaman, M., Nackashi, D.P., Damiano, J., Mick , S.E., *A new MEMS-based system for ultra-high-resolution imaging at elevated temperatures*, Microsc. Res. Tech., 72 (2009) pp. 208-215.

18 Van Omme, J. T., Zakhozheva, M., Spruit, R. G., Sholkina, M., Pérez Garza, H. H., *Advanced microheater for in situ transmission electron microscopy; enabling unexplored analytical studies and extreme spatial stability*, Ultramicroscopy 192 (2018) pp14-20.

19 Maigné, A., Wolf, M. (2018) *Low-dose electron energy-loss spectroscopy using electron counting direct detectors,* Microscopy 67 (1) (2018) ppI86-I97.

20 Nicholls, R. J., Murdock, A. T., Tsang, J., Britton, J., Pennycook, T. J., Koos, A., Nellist, P. D., Grobert, N., Yates, J. R., *Probing the bonding in nitrogen-doped graphene using electron energy loss spectroscopy*, ACS Nano, 7 (8) (2013) pp7145-7150.

21 Ozin, G., Arsenault, A. C., (2005) Nanochemistry: A chemistry approach to nanomaterials Royal Society of Chemistry, Cambridge

22 Irving, D. L., Sinnott, S. B., *Relative stabilities of Ag multilayers on GaAs and GaSb determined from ab initio calculations,* Phys. Rev. B 74 (2006) pp195403.

23 Kalishwaralal, K., Deepak, V., Ram Kumar Pandian,S., Kottaisamy, M., Barathmanikanth, S., Kartikeyan, B., Gurunathan, S., *Biosynthesis of silver and gold nanoparticles using Brevibacterium casei,* Colloids Surf. B 77 (2) (2010) pp257-262.

24 Kang, S. Y. and K. Kim *Comparative study of dodecanethiol-derivatized silver nanoparticles prepared in one-phase and two-phase systems,* Langmuir 14 (1) (1998) pp226-230

25 Iravani, S., *Green synthesis of metal nanoparticles using plants,* Green Chem. 13 (2011) pp2638–2650.

26 Yonezawa, T., Onoue, S., Kimizuka, N., *Formation of Uniform Fluorinated Gold Nanoparticles and Their Highly Ordered Hexagonally Packed Monolayer,* Langmuir 17 (8) 2001 pp2291-2293

27 Shimizu, T. K., Jung, J., Otani, T., Han, Y. K., Kawai, M., Kim, Y., *Two-dimensional superstructure formation of fluorinated fullerenes on Au(1 1 1): A scanning tunnelling microscopy,* ACS Nano 6 (3) (2012) pp2679-2685.

28 DeVries, G. A., Brunnbauer, M., Hu, Y., Jackson, A. M., Long, B., Neltner, B. T., Uzun, O., Wunsch, B. H., Stellacci, F., *Divalent metal nanoparticles.* Science 315 (2007) pp358–3.

29 Posocco, P., Gentilini, C., Bidoggia, S., Pace, A., Franchio, P., Lucarini, M., Fermeglia, M., Pricl, S., Pasguato, L., *Self-Organization of Mixtures of Fluorocarbon and Hydrocarbon Amphiphilic Thiolates on the Surface of Gold Nanoparticles* ACS Nano 6, 8, 7243-7253

30 Abdulhalim, L., Kothalawala, N., Sinatra, L., Dass, A., Bakr, O., *Neat and complete: Thiolate-ligand exchange on a silver molecular nanoparticle*. J Am. Chem. Soc. 136 (45) (2014) pp15865-8.

31 Lee, C. M., Jeong, H. J., Kim, D. W., Sohn, M. H., Lim, S. T., *The effect of fluorination of zinc oxide nanoparticles on evaluation of their biodistribution after oral administration*, Nanotechnology. 23 (20) (2012) pp205102.

32 Bianco, A., Kostarelos, K., Prato, M., *Making carbon nanotubes biocompatible and biodegradable, Chemical Communications*, 47 (37) (2011) pp10182-10188.

8.0 Further Work

8.1 Introduction

The formation of hollow carbon shells has been demonstrated, with good size control and well-defined morphology, but there remain many opportunities for further investigations. These are discussed in the following text, beginning with HCNS characterisation and functional properties, moving onto starting materials, and the nature of supports and deposition and ending with suggestions for other hollow carbon morphologies.

8.2 HCNS characterisation and functional properties

The functional properties of these very small HCNS are unknown; similar, but larger, HCNS structures have been shown to have electron donating properties [1], therefore obtaining electrochemical measurements of this material, and of HCNS / carbon nanotube composite materials would allow an assessment of possible catalytic / electrochemistry applications [2]. Additionally, the electrochemistry of N – containing HCNS has not been determined, any effects due to the addition of N to HCNS, designed to modify the band gap of the material and alter electrochemical properties [3], could then be evaluated. Alteration of the band gap of HCNS would also be expected to influence any photoluminescence properties [4], therefore further photoluminescence experiments may also be illuminating, noting that the presence of residual AgNP may confound results. Further functional data acquisition, e.g.

experiments designed to fill HCNS either with metals [5], or with gasses to determine adsorption isotherms [6], will allow the hollow nature of the material to be evaluated.

Determining levels of N within HCNS was not possible, due to the nature of support materials: the simplest solution to this would be to perform experiments to prepare HCNS support-free, possibly by ex-situ heating a sample of AgNP inside a quartz tube under vacuum, similar to experiments already undertaken with AgNP deposited onto carbon nanotubes. This should allow determination of heteroatom amounts within HCNS, through bulk techniques such as XPS, elemental analysis or NMR, or nanoscale techniques such as EDS, if deposited onto a Si support (Si would not withstand the high temperatures required for HCNS formation from AgNP). Obtaining functional data support free may also be advantageous.

8.3 Starting materials

The addition of other heteroatoms, such as B, O or P to HCNS via addition of these elements to AgNP starting material stabilising layers may also be evaluated and AgNP with different morphologies may be synthesised, e.g. cubed, oblong and triangular [7]; since HCNS morphology is template dependant, thermal processing such structures should yield hollow carbon with commensurate shapes. Size control of HCNS has been demonstrated over a very narrow range, this could be extended by thermally processing appropriately sized starting materials.

Issues concerning agglomeration of heteroatom containing AgNP require addressing; speculatively, size selection may be possible through separation techniques such as

centrifugation [8], and filtration may eliminate large agglomerations of AgNP, offering future potential improvements to heteroatom containing HCNS.

8.4 Heating protocols

Repeating thermal processing AgNP on MEMS support chips may yield improved results, as recent design improvements have decreased temperature gradients across the support and better control drift and bulging effects which limit imaging capabilities [9].

Experiments to improve thermal processing, for example to determine optimum temperature and heating duration could be performed, the possibility to save time and energy through the use of microwave heating [10] is a further unexplored field.

8.5 Functionalising HNCS

Investigating superlattice formation, or controlled assembly, particularly of mixed-thiol AgNP, may offer a potential route to arrays, or inter-connected HCNS foams [11], after thermal processing. Thermal processing experiments of similar metallic nanoparticles, e.g Cu NP, Fe NP, Pb NP has also not been performed, and may also lead to HCNS formation. Incomplete processing of thiol stabilised metal NP could be explored as a route to formation of HCNS containing residual metal and therefore forming a composite material and possibilities for further functionalisation of these HCNS with organic molecules, metals or metal ions remain unexplored [12]. Lastly, feasibility studies to determine if very fast heating protocols could enable formation

of HCNS from template free starting materials, potentially overcoming existing issues maintaining structural integrity during the heating process [13].

References

1 Kumar, P., Boukherroub, R., Shankar, K. *Sunlight-driven water-splitting using two-dimensional carbon based semiconductors,* J Mater. Chem. A, (2018) 6 (27) pp12876-12931.

2 Gawande, M. B., Goswami, A., Asefa, T., Guo, H., Biradar, A., Peng, D., .Zboril, R., Varma, R., *Coreshell nanoparticles: Synthesis and applications in catalysis and electrocatalysis,* Chem. Soc. Rev. (2015) 44 (21) pp7540-7590.

3 Zhang, N., Liu, F., Xu, S. D., Wang, F. Y., Yu, Q., Liu, L., *Nitrogenphosphorus co-doped hollow carbon microspheres with hierarchical micromesomacroporous shells as efficient electrodes for supercapacitors, J Mater. Chem. A (2017) 5 (43)* pp22631-22640.

4 Li, X., Yu, J., Jaroniec, M., *Hierarchical photocatalysts,* Chem. Soc. Rev. (2016) 45 (9) pp2603-2636.

5 Cao, K., Zoberbier, T., Biskupek, J., Botos, A., McSweeney, R. L., Kurtoglu, A., Stoppiello, C. T., Markevich, A. V., Besley, E., Chamberlain, T. W., Kaiser, U., Khlobystov, A. N., *Comparison of atomic scale dynamics for the middle and late transition metal nanocatalysts,* Nat. Commun. (2018) pp3382.

6 Lakhi, K., Park, D., Singh, G., Talapaneni, S., Ravon, U., Al-Bahily, K., Vinu, A., *Energy efficient synthesis of highly ordered mesoporous carbon nitrides with uniform rods and their superior CO 2 adsorption capacity,* J Mater. Chem. A (2017) 5 (31) pp16220-16230.

7 Mceachran, M., Kitaev, V., *Direct structural transformation of silver platelets into right bipyramids and twinned cube nanoparticles: Morphology governed by defects,* Chem. Comm. (2008) (44) pp5737-5739.

8 Arvizo, R., Bhattacharyya, S., Kudgus, R., Giri, K., Bhattacharya, R., Mukherjee, P., *Intrinsic therapeutic applications of noble metal nanoparticles: Past, present and future*, Chem. Soc. Rev. (2012) 41 (7) pp2943-2970.

9 Van Omme, J. T., Zakhozheva, M., Spruit, R. G., Sholkina, M., Pérez Garza, H. H., Advanced microheater for in situ transmission electron microscopy; enabling unexplored analytical studies and extreme spatial stability, Ultramicroscopy 192 (2018) pp14-20.

10 Hung, C. T., Yu, N., Chen, C. T., Wu, P. H., Han, X., Kao, Y. S., Liu, S. B., *Highly nitrogen-doped mesoscopic carbons as efficient metal-free electrocatalysts for oxygen reduction reactions*, J Mater. Chem. A (2014) 2 (47) pp20030-20037.

11 Lin, T., Chen, I., Liu, F., Yang, C., Bi, H., Xu, F., Huang, F., *Nitrogen-doped mesoporous carbon of extraordinary capacitance for electrochemical energy storage*, Science (2015) 350 (6267) pp1508-13.

12 Benzigar, M., Talapaneni, S., Joseph, S., Ramadass, K., Singh, G., Scaranto, J., Ravon, U., Al-Bahily, K., Vinu, A., *Recent advances in functionalized micro and mesoporous carbon materials: Synthesis and applications*, Chem. Soc. Rev. (2018) 47 (8) pp2680-2721.

13 Hong, M., Chen, J., Zhang, M., Huang, X., Xu, Q., *High-frequency fabrication of discrete and dispersible hollow carbon spheres with hierarchical porous shells by using secondary-crosslinking pyrolysis*, RSC Adv. (2016) 6 (20) pp16141-16149.

Conclusions

The main achievements were to have discovered that heating < 10 nm sized thiol stabilised Ag nanoparticles (TS-AgNP) produces well-defined hollow carbon nanoshells (HCNS) that reflect the starting material size and morphology *only* at very fast heating rates. MEMS thermal processing of AgNP on Si_3N_4 supports, *in situ* inside a TEM provided direct evidence for the templated formation of HCNS from TS-AgNP, from the same field of view, with *ex situ* heating on carbon nanotube supports revealing the graphitic nature of the HCNS walls. Slower rates of heating produced evidence for the competition between HCNS formation and AgNP ripening processes (both thermally mediated) that were reflected in the formation of larger HCNS products, and the presence of AgNP much larger than the AgNP starting material size. The slowest rates of heating were found to produce a significantly variable product consisting of large accumulations of Ag and lacy, disrupted carbon structures exhibiting decreased levels of graphitisation.

HCNS structures were slightly larger than the size of AgNP starting materials, with good size control of products demonstrated and a mechanism was proposed for graphitisation of the AgNP thiol layer, templated and catalysed by AgNP. Whilst the flexibility of this synthetic route was demonstrated by the formation of well-defined HCNS from a range of AgNP starting materials containing F or N in the thiol stabilising layer: evidence for the presence of F has been presented, but evidence for the inclusion of N was more tentative.

Whilst obtaining TEM images of AgNP starting materials was routine, the HCNS samples formed at high temperatures were extremely difficult to locate due to low sample amounts on Si_3N_4 support windows, the very small size of the HCNS and background support morphology. This challenge was overcome by significantly under-focussing the electron beam, producing Fresnel fringes at HCNS edges, once the structures were located, the focus was adjusted to record clear images of the HCNS.

The synthesis and characterisation of novel AgNP, stabilised by a binary mixture of alkane thiol and fluorinated thiol was successfully achieved; notably, these AgNP were soluble in ethanol. Further, a range of N-containing mixed thiol AgNP were synthesised and characterised, indicating that incorporation of varying amounts of N to AgNP stabilising layers is achievable. Introduction of highly electronegative F atoms, and electron donating pyrrole groups at the AgNP surface produced agglomeration, which was found to be influenced by sample handling during TEM deposition procedures. Sonication of AgNP suspensions was found to increase levels of AgNP agglomeration, particularly for mixed-thiol AgNP, however this could provide a route to form foam-type HCNS products via heating processes. The appearance of AgNP may also be influenced by addition of surfactant molecules, which reduce observed AgNP agglomeration.

Appendix A: NMR and Raman spectroscopy data supplementary to chapter 6

Results presented here include supplementary NMR data from N-AgNP and Raman spectroscopy of HCNS products formed from thermal processing N-AgNP on Si_3N_4 MEMS supports. *Raman spectroscopy data collection and analysis performed by Dr Graham Rance.*

A 1.0 NMR spectroscopy

Spectra are presented for AgNP stabilised with DDM:PUT ratio of 75:25 (4.4% N) and AgNP stabilised with PUT (5.5% N), with peak assignments [1]. The ^{1}H NMR of DDM and PUT in solution were provided in Figures 6.18b,c, respectively, for comparison.

A1.1 results for AgNP stabilised with DDM:PUT ratio of 75:25 (4.4% N)

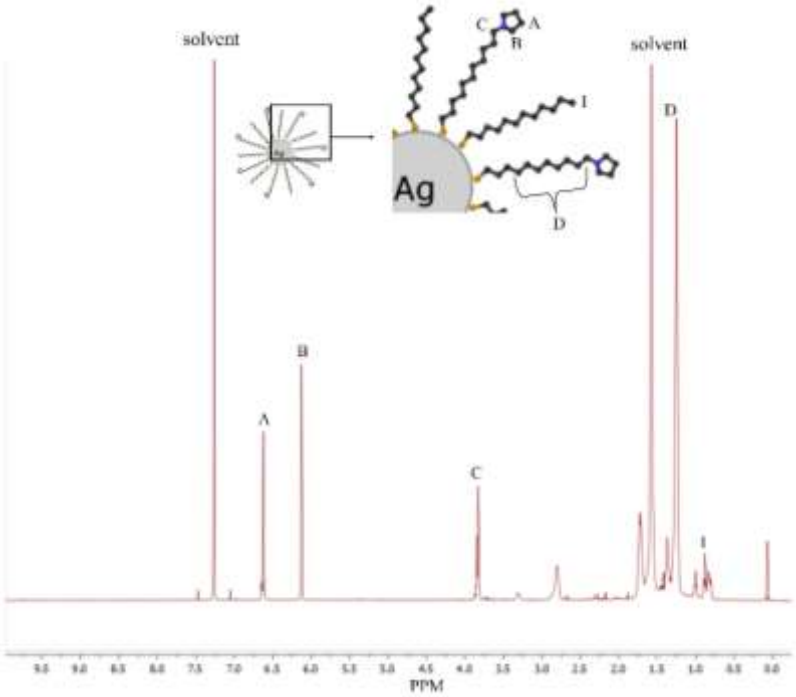

Figure A1.1 1H NMR of N4-AgNP (2 mg / 4 ml acetone-D6), with peak assignments confirming the presence of alkane and pyrrole functional groups, around 1 – 2 and 6 – 7 ppm,

respectively, and the absence of graphitic contributions (the peak around 2.75 ppm is a contaminant).

A1.2 results for AgNP stabilised with PUT (5.5% N)

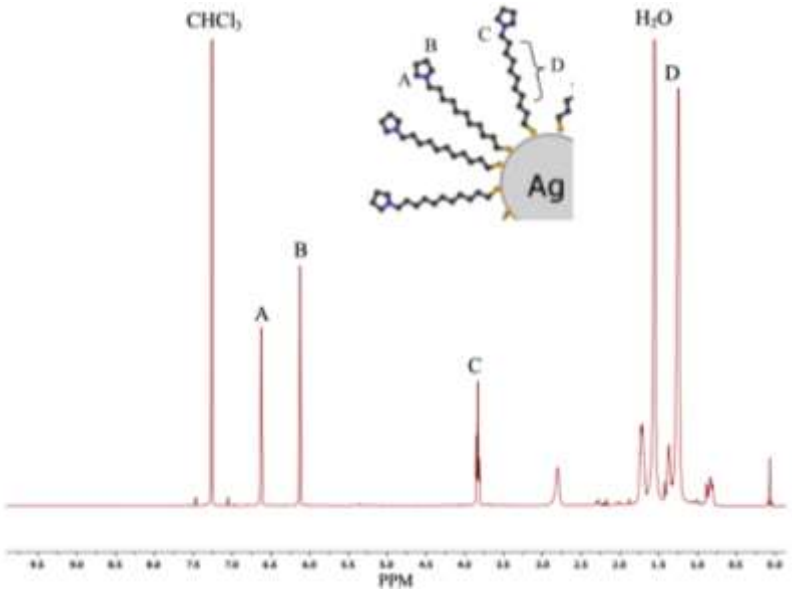

Figure A1.2 ^{1}H NMR of AgNP stabilised with 11(1H-pyrrol-1-yl) undecane thiol, indicating: (a) The presence of a pyrrole functional group (peaks at 6.1 and 6.6 ppm), adjacent to an alkane group (peak at 3.8ppm), and an alkane chain (peaks at lower field 1-1.8 ppm), the peaks at 7.26 ppm, 1.56 ppm and 1.25 ppm were attributed to residual hydrogenated chloroform, and to water and ethanol residual contaminants, respectively (2).

A 2.0 Raman spectroscopy

For all spectra, the two broad, overlapping bands around 1300 and 1600 cm^{-1}, nominally attributed to the defect (D) and graphite (G) bands, were carefully deconvoluted with four Lorentzian-shaped bands (G, D1, D2, D4) and a Gaussian-shaped band (D3), (Table A1), as described previously in Section 4.5.1 [3]. All first order spectra were normalised to the intensity of the G band (of results from TP-1, figure 4.19), baseline-corrected using a third order polynomial subtraction and fit using a five-band model analogous to that previously described, [4]. The first order spectra presented here were very similar, and notably very similar to the spectrum

obtained from HCNS (Figure 4.19) and F-HCNS (Figure 6.11), with general peak shapes consistent with a highly disordered graphitic carbon material, but with subtle differences reflecting a small change in degree of graphitisation and amorphous carbon content.

Table A1 First order Raman band assignments [4, 5].

Band [a]	**Raman shift / cm^{-1}**	**Proposed vibrational mode assignment**
G	1585 s	Ideal graphitic lattice (E_{2g} symmetry)
D1 (D)	1348 vs	Disordered graphitic lattice (A_{1g} symmetry)
D2 (D')	1609 s	Disordered graphitic lattice (E_{2g} symmetry)
D3 (D", A)	1521 m	Amorphous carbon
D4 (I)	1213 m	Disordered graphitic lattice (A_{1g} symmetry), polyenes, ionic impurities

[a] *alternative band designations of earlier studies are in parantheses (vs = very strong, s = strong, m = medium).*

A2.1 Thermally processed AgNP stabilised with DDM:PUT ratio of 75:25 (1.6% N)

Figure A1.1 presents a first order Raman spectrum acquired from products formed from heating N2-AgNP on Si_3N_4 (850°C, at ~ 100°C/s). The apparent G band is positioned ~1590 cm^{-1}, the same value as HCNS (sized ~ 9 nm), and higher than F-HCNS (~1582 cm^{-1}; sized ~7.5 nm) tentatively suggesting differences in the curvature of the obtained nanostructures may be responsible, rather than plasmonic heating, or charge transfer effects. Additionally, it is noted that the relative intensities of the apparent D and G bands appear to differ for "doped-HCNS" compared to "undoped HCNS". Further, evaluation of peak areas for deconvoluted bands indicate the intensity ratio (as peak area) of the D1 and G bands (I_{D1}:I_G) was high for both HCNS formed from heating N2-AgNP (850°C; at ~ 100°C/s) or HCNS, (I_{D1}:I_G = 1.76 and

3.08, respectively), with the value for the latter being larger. In addition, the intensity ratio (as peak area) of the D3 and G bands (I_{D3}:I_G) was also high for products formed from heating N2-AgNP, and significantly higher compared to HCNS (I_{D3}:I_G = 1.01 and 1.68, respectively). Both of these ratios indicate that HCNS structures produced from N2-AgNP contain slightly more graphitic C, in conjunction with less amorphous carbon contributions, when compared to HCNS, indicating that the extent of graphitisation of the carbon products formed is not diminished by N-doping of AgNP starting materials, indeed, graphitisation was slightly improved.

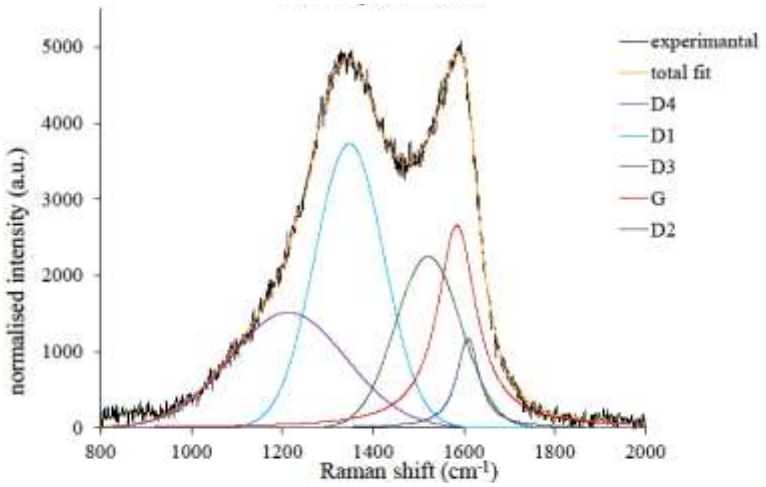

Figure A1.3 First order Raman spectrum (λ_{ex} = 532 nm) obtained in the range 800-2000 cm^{-1} from N2-AgNP heated to 850°C (at ~ 100°C/s), confirming the disordered graphitic nature of the products, ($\chi 2$ = 1.7).

A2.2 Thermally processed AgNP stabilised with DDM:PUT ratio of 50:50 (3.1% N)

Figure A1.4 presents a first order Raman spectrum acquired from products formed from heating N3-AgNP on Si_3N_4 (850°C, at ~ 100°C/s), the two broad, slightly overlapping bands around 1345 and 1586 cm^{-1}, attributed nominally to the defect (D) and graphite (G) bands. The apparent G band for these ~8.5 nm sized structures is

positioned ~1586 cm^{-1}, marginally lower than the ~ 1590 value obtained for HCNS (sized ~ 9 nm), but higher than F-HCNS (~1582 cm^{-1} sized ~7.5 nm) again supporting the suggestion that size differences may be responsible for the shift. Indeed, I_{D1}:I_G = 2.63 and I_{D3}:I_G 1.50, are consistent with previous results.

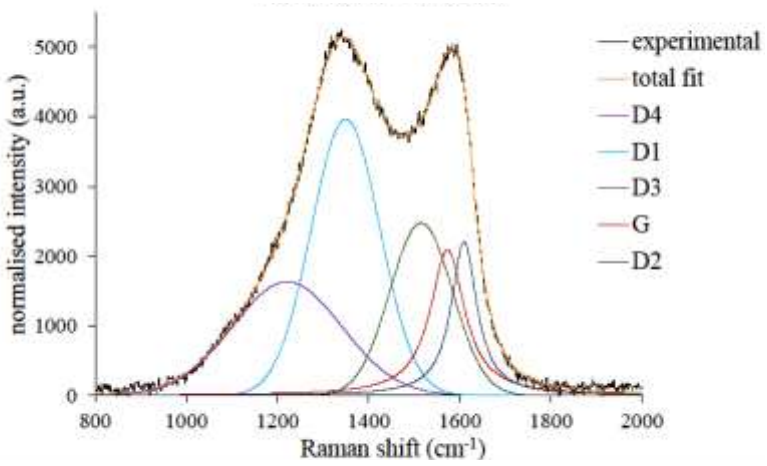

Figure A1.4 First order Raman spectrum (λ_{ex} = 532 nm) obtained in the range 800-2000 cm^{-1} from N3-AgNP heated to 850°C (at ~ 100°C/s), confirming the disordered graphitic nature of the products, ($\chi 2$ = 2.0).

A2.3 Thermally processed AgNP stabilised with DDM:PUT ratio of 75:25 (4.4% N)

Figure A1.5 shows a first order Raman spectrum acquired from products formed from heating N4-AgNP on Si_3N_4 (850°C, at ~ 100°C/s), with the two broad, slightly overlapping bands around 1356 and 1598 cm^{-1}, were attributed nominally to the defect (D) and graphite (G) bands. The apparent G band for these ~9 nm sized structures positioned at ~1598 cm^{-1}, again consistent with the suggestion that size differences may be responsible for the slight observed shift between samples. Indeed, I_{D1}:I_G = 1.27 and I_{D3}:I_G = 0.41 values for the HCNS structures produced from heating N4-AgNP (850°C, at ~100°C/s) were also consistent with the formation of graphitised HCNS, similar to the previous two examples of HCNS formed from N-doped AgNP.

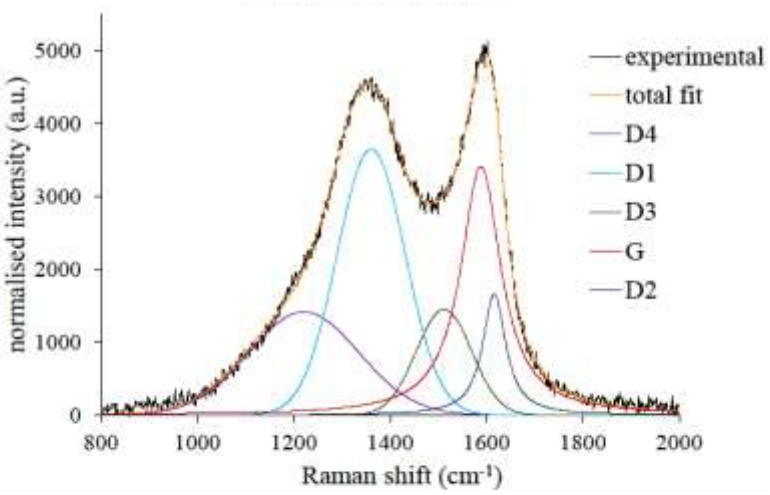

Figure A1.5 First order Raman spectrum (λ_{ex} = 532 nm) obtained in the range 800-2000 cm^{-1} from N4-AgNP heated to 850°C (at ~ 100°C/s), confirming the disordered graphitic nature of the products, ($\chi 2 = 1.7$)

A2.4 Thermally processed AgNP stabilised with PUT (5.5% N)

Figure A1.6 shows a first order Raman spectrum acquired from products formed from heating N5-AgNP on Si_3N_4 (850°C, at ~ 100°C/s), with the two broad, slightly overlapping bands around 1360 and 1590 cm^{-1}, were attributed nominally to the defect (D) and graphite (G) bands The apparent G band for these ~10 nm sized structures positioned at ~1590 cm^{-1}, not consistent with the previous results, which showed a correlation between increasing HCNS size and increasing G band wavenumber. Indeed, I_{D1}:I_G = 1.93 and I_{D3}:I_G 1.37 values for the HCNS structures produced from heating N5-AgNP (850°C, at ~100°C/s) were consistent with all previous examples of graphitised HCNS formed form N-doped AgNP.

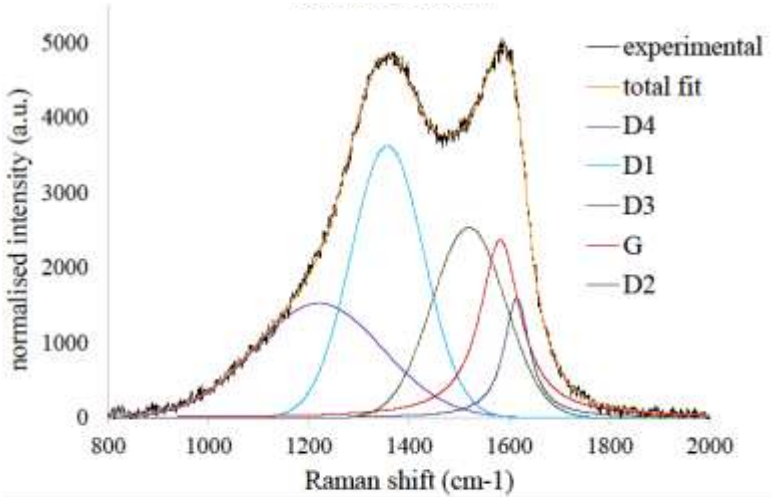

Figure A1.6 First order Raman spectrum (λ_{ex} = 532 nm) obtained in the range 800-2000 cm^{-1} from N5-AgNP heated to 850°C (at ~ 100°C/s), confirming the disordered graphitic nature of the products, ($\chi 2 = 1.3$).

References

1 Williams, D., Fleming, I., Spectroscopic methods in Organic Chemistry, 1989 McGraw Hill Company, New York

2 Fulmer, G. R., Miller, A. J. M., Sherden, N. H., Gottleib, H. E., Nudelman, A., Stoltz, B. M., Bercaw, J. E., Goldberg, K. I., *NMR Chemical Shifts of Trace Impurities: common Laboratory Solvents, Organics, and Gases in Deuterated Solvents Relevant to the Organometallic Chemist,* Organometallics 29 (2010) pp2176–2179

3 Ferrari, J. Robertson, J.,*Interpretation of Raman spectra of disordered and amorphous carbon,* Phys. Rev. B 61(20) (2000) pp14095-14107

4 Sadezky, A., Muckenhuber, H., Grothe, H., Niessner, R., Pöschl, U., *Raman microspectroscopy of soot and related carbonaceous materials: Spectral analysis and structural information,* Carbon 43(8) (2005) pp1731-1742.

5 Cançado, L.G., Jorio, A., Ferreira, E.H.M., Stavale, F., Achete, C.A., Capaz, R.B., et al., *Quantifying defects in graphene via Raman spectroscopy at different excitation energies,* Nano. Letters. 11(8) (2011) pp3190-6.

Appendix B selection of stabilising thiols for AgNP syntheses

Chemical synthesis of silver nanoparticles (AgNP) involving two or more stabilising ligands has been used to tune functional properties of AgNP [1], designed to result in good spatial distribution of these heteroatoms within the final product [2].

B 1.0 Selection of alkane thiol for stabilising AgNP

For mixed thiol synthesis of AgNP, 1-dodecanethiol (DDM, $C_{12}H_{25}S$), was selected as this stabilising ligand has been widely documented to produce stable AgNP, with a narrow size distribution [3], Figure B1.0. For mixed thiols the second thiol was required to have a similar chain length to DDM, minimising preferential bonding effects due to differing chain lengths, since longer chain thiols bond with Ag in preference to shorter chain alkane thiols.

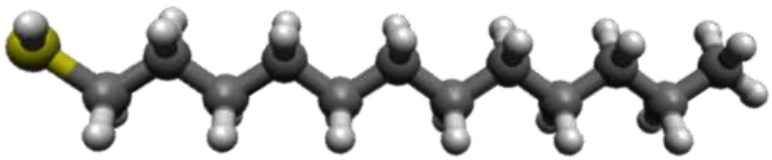

Figure B 1.0 Structure of 1-dodecanethiol, DDM, $C_{12}H_{25}S$.

B 2.0 Selection of Fluorinated alkane thiol

The choice of fluorinated thiol to add to the DDM stabilising layer was carefully considered and the fluorotelomer 1H, 1H, 2H, 2H-perfluoro-1-decanethiol (synonym 3,3,4,4,5,5,6,6,7,7,8,8,9,9,10,10,10-heptadecafluoro-1-decanethiol, HFT,

$C_{10}H_5F_{17}S$), was selected due to structural similarity and chain length compared with DDM Figure B1.1.

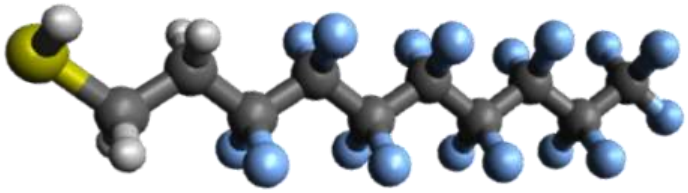

Figure B 1.1 Structure of 1H, 1H, 2H, 2H-perfluoro-1-decanethiol, HFT, $C_{10}H_5F_{17}S$.

B 3.0 Selection of Nitrogen containing alkane thiol

From a range of nitrogen containing thiols, 11-(1H-pyrrol-1-yl) undecane thiol (PUT, $C_{15}H_{27}NS$), Figure B1.2, was selected since the alkane chain length is similar to that of DDM. As the nitrogen atom is protected by the pyrrole ring, it was anticipated that the self-assembly of surfactant at the Ag surface would not be inhibited by Ag-N bond formation in competition with Ag-S bonding, possible in the case of a molecule with a terminal nitrogen atom.

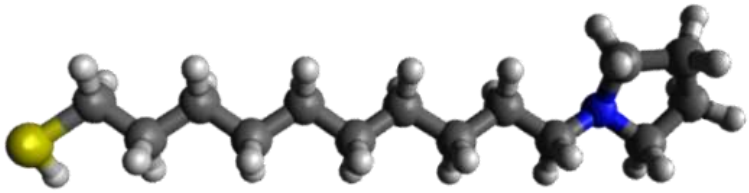

Figure B 1.2 Structure of 11-(1*H*-pyrrol-1-yl) undecane-1-thiol, PUT, $C_{15}H_{27}NS$.

References

1 Stewart, A., Zheng, S., Mccourt, M., Bell, S., *Controlling assembly of mixed thiol monolayers on silver nanoparticles to tune their surface properties*, ACS Nano 6 (5) (2012) pp3718-26.

2 Zabet-Khosousi, A., Zhao, L., Pálová, L., Hybertsen, M. S., Reichman, D. R., Pasupathy, A. N., Flynn, G. W., *Segregation of Sublattice Domains in Nitrogen-Doped Graphene*, J Am. Chem. Soc. 136 (4) (2014) pp1391-1397.

3 Kang, S. Y., Kim, K., *Comparative Study of Dodecanethiol-Derivatized Silver Nanoparticles Prepared in One-Phase and Two-Phase Systems,* Langmuir 14 (1998) pp226-230.